Characterising on-surface processes with spatial and temporal resolution: Porphyrins and Phthalocyanines

Matthew Edmondson, MSci (Hons)

Thesis submitted to the University of Nottingham
for the degree of Doctor of Philosophy

School of Physics and Astronomy
University of Nottingham
March 2023

Abstract

The fundamental interactions between molecules and atoms create the many wonderful biological, chemical and physical processes that allow the world as we know it to exist. One possible approach to investigate these interactions is to constrain specific molecules to a two-dimensional plane then, by employing various surface-sensitive techniques, one can characterise the observed behaviour while accurately controlling experimental conditions. Having a full understanding of these processes will allow us, in principle, to create complex structures from simple molecular 'building-blocks'.

Within this thesis, the self-assembly and chemical interactions of porphyrins and phthalocyanines are explored on metal surfaces under ultra-high vacuum (UHV). To perform this research, surface-sensitive techniques are used in the form of a combination of scanning tunnelling microscopy (STM), and photoelectron spectroscopy techniques which include: X-ray photoelectron spectroscopy (XPS), normal incidence X-ray standing wave (NIXSW) and near-edge X-ray absorption fine structure (NEXAFS).

Porphyrin molecules are the basis for a number of vitally important biological molecules (specifically heme - the precursor to haemoglobin which carries oxygen in red blood cells). By adding functional groups to this molecule, different interactions and/or processes are available. Phthalocyanines have a similar structure to porphyrins, and therefore, have similar interactions and reactivity profiles, however, they are not typically found in nature. These molecules are interesting candidates for surface-confined investigations due to their rich chemistry.

Within this thesis, several molecule-substrate systems are characterised, with a view to understanding key concepts of on-surface reactivity. Tetraphenylporphyrins (TPP) are deposited onto Au(111) surfaces, where self-assembled close-packed structures are formed. These structures are influenced by the surface reconstruction, herringbone reconstruction, of Au(111) and therefore, the TPP molecules have preferential island growth sites on the surface. By varying the surface temperature we characterise this TPP-surface interaction and find energy barriers, via Arrhenius analysis, to diffusion events for TPP within the *fcc* or *hcp* regions of the surface.

Upon annealing TPP on Au(111), intramolecular reactions can occur, which change the structure and properties of the molecule. The molecules are no longer able to self-assemble into close-packed assemblies. Upon heating further, TPP self-metalates with a Au atom incorporated into the macrocycle cavity. Using STM, XPS, NIXSW and NEXAFS we characterise each stage of the reaction, providing an in-depth chemical and structural characterisation of the on-surface process.

TPP can be functionalised by the addition of bromine atoms on the phenyl rings. This unlocks the formation of chains created by individual TPP species, via the Ullmann-type coupling reaction. We investigate each stage of the reaction with STM, and characterise the electronic states of the molecular species. Within this work, we find that we are able to spectroscopically differentiate between TPP and various Br_xTPP species ($x = 0 \rightarrow 4$). Chain formation occurs at a lower temperature than the ring-closing reaction within the TPP molecule leading to covalently coupled chains consisting of ring-closed TPP. We find that self-metalated TPP chain species are subsequently formed at higher annealing temperatures.

The interaction of gas molecules with metalated species is a route towards sequestering pollutant species (CO, CO_2 and NO_x). Here we study, iron phthalocyanine which is shown to produce well-ordered on-surface assemblies on Ag(111). We investigate using STM and XPS, the effect on the molecular overlayer when dosing gases (CO, O_2 and H_2O) at near ambient pressures. We find that there is no interaction between the H_2O and FePc at room temperature whilst dosing up to 7 mbar of H_2O pressure. We found that a combined STM and XPS characterisation is a powerful analytic tool to determine any induced surface changes.

The results presented within this thesis provide insight into on-surface reactions and processes between molecules. The combination of scanning probe microscopy and photoelectron spectroscopy studies provides a detailed chemical and structural characterisation of on-surface synthesis. This quantitative approach allows the mechanisms of interactions to be probed in terms of activation barriers and structural changes for individual reaction steps. By employing a synergistic range of surface science techniques the fundamental mechanisms can be understood, providing a route to influencing and ultimately controlling chemical reactions at surfaces.

List of Publications

- *Order, disorder, and metalation of tetraphenylporphyrin (2H-TPP) on Au(111),* **Matthew Edmondson**, Eleanor S. Frampton, Chris J. Judd, Neil R. Champness, Robert G. Jones and Alex Saywell. ***Chem. Commun.***, 2022, **58**, 6247-6250.
- *Molecular Diffusion and Self-Assembly: Quantifying the Influence of Substrate hcp and fcc Atomic Stacking,* **Matthew Edmondson** and Alex Saywell. ***Nano Lett.***, 2022, 22, 20, 8210–8215.
- *Using polycyclic aromatic hydrocarbons for graphene growth on Cu(111) under ultra-high vacuum,* Benedikt P. Klein, Matthew A. Stoodley, **Matthew Edmondson**, Luke A. Rochford, Marc Walker, Lars Sattler, Sebastian M. Weber, Gerhard Hilt, Leon B. S. Williams, Tien-Lin Lee, Alex Saywell, Reinhard J. Maurer, and David A. Duncan. ***Appl. Phys. Lett.*** 2022, 121, 191603.
- *Porphyrin-Fused Graphene Nanoribbons Synthesized in Solution*, Qiang Chen, Alessandro Lodi, Heng Zhang, Alex Gee, Hai Wang, Fanmiao Kong, Michael Clarke, **Matthew Edmondson**, Jack Hart, James O'Shea, Wojciech Stawski, Jonathan Baugh, Akimitsu Narita, Alex Saywell, Mischa Bonn, Klaus Müllen, Lapo Bogani and Harry L. Anderson. (*Manuscript under review*).
- *Ullmann coupling and subsequent ring-closing/metalation of Br_2TPP on Au(111),* **Matthew Edmondson**, Michael Clarke, Nathan Andersen, Neil R. Champness and Alex Saywell. (*Manuscript in preparation).*

Acknowledgements

I am forever grateful to my supervisor, Alex, who provided me with the opportunity to study such a fascinating and complex field. His continuous support and guidance has enabled me to grow within the PhD to be so much more than when I started. I will always appreciate the long discussions we have had about STM, photoelectron spectroscopy, and science more broadly. He is a wonderful academic and a credit to the Physics department.

I would also like to thank my secondary supervisor, Philip, for the many discussions about my work, his help during the installation of the POLAR system, and his enthusiasm for nanoscience, which is infectious!

I have met some great people along the way... Chris and Ellie were incredibly welcoming to the group and gave me a thorough introduction to the research; I really value their continued friendship. I thoroughly enjoyed our trip to Regensburg, Michael, and your assistance with the POLAR has been invaluable. Oli, I really appreciate all of our 'meal deal' lunches/discussions over the PhD! I enjoyed joining the wider nanoscience group that included Filipe and Alex A, as they provided me with a friendly introduction to the SPM systems in rooms A103/A104. It has been a pleasure working alongside other members of the nanoscience group, and those in C20, both past and present.

I want to thank my sisters, Louise and Rebecca, without whom I would not be the person I am today, and my parents for all the support they have given me up to this point and beyond!

I would also like to thank Hannah's side of the family, Helen, Daven, Christine and Roy for their encouragement.

Finally, I want to thank Hannah. Your unwavering support has been truly inspirational. Without you, I am not sure I would have been able to do this. You always help me whenever I need it. We will always have each other.

Contents

1 Introduction 1

1.1 Overview of this thesis 3

2 Studying on-surface processes 5

2.1 Molecules and their on-surface self-assembled structures 5

2.1.1 Van der Waals interactions 6

2.1.2 Hydrogen Bonding 8

2.1.3 Halogen bonding 9

2.1.4 Other types of surface ordering 10

2.1.5 Ullmann-type coupling 12

2.2 Porphyrins 15

2.2.1 TPP absorption characteristics 16

2.2.2 Thermally induced on-surface reactivity of TPP 22

2.2.3 Metalation of TPP 24

2.2.4 Thermally induced covalent coupling 31

2.2.5 Ullmann-type coupling of TPP 32

2.3 Phthalocyanines 33

2.4 Overview of the literature 37

3 Experimental techniques, methods and materials 38

3.1 Scanning tunnelling microscopy 38

3.1.1 Quantum mechanical tunnelling 39

3.1.2 Tersoff-Hamann theory 41

3.1.3 dI/dV spectroscopy 46

3.1.3.1 Energy resolution of states due to Fermi level . . 48

3.1.4 STM feedback modes 49
3.1.5 STM movement 51
3.1.6 STM Tips 53
3.1.7 Sources of noise within SPM 55
3.1.8 STM summary 57
3.2 Photoelectron spectroscopy 59
3.2.1 XPS 59
3.2.1.1 From kinetic energy to binding energy 60
3.2.1.2 Chemical sensitivity 61
3.2.1.3 Surface sensitivity 61
3.2.1.4 Shake-up and shake-off features 63
3.2.1.5 Peak fitting 65
3.2.2 NAP-XPS 65
3.2.3 NEXAFS 66
3.2.4 NIXSW 69
3.2.5 Sources of photons 74
3.2.5.1 Lab based sources 74
3.2.5.2 Synchrotron source 75
3.3 LEED 76
3.4 UHV experimental setup 78
3.4.0.1 Omicron UHV STM-1 system 78
3.4.0.2 Scienta Omicron POLAR STM/AFM low-temperature system 79
3.5 Surfaces 80
3.5.1 Surface reconstruction of Au(111) 80
3.5.2 Surface preparation 82
3.5.3 Surface summary 83
3.5.4 Molecular deposition 84
3.6 Summary 85

4 Self-assembly and diffusion of tetraphenylporphyrin on Au(111) 86
4.1 Self-assembly on Au(111) 86
4.2 Experimental methods 88

    4.2.1 Performance of STM under elevated sample temperatures . 88
    4.2.2 Drift over time at elevated temperatures 90
    4.2.3 Comparison of cooldown rate of counter-heated and normal samples 90
  4.3 Self-assembly for low coverages of TPP 91
  4.4 Kinetic and thermal effects on the self-assembly of TPP on Au(111) 98
  4.5 Island shape/formation at elevated temperatures 101
  4.6 Arrhenius analysis of individual TPP 103
    4.6.1 Image processing 103
    4.6.2 Tip influence on the molecules 109
  4.7 Conclusion 109

5 STM characterisation of Br_xTPP 111
  5.1 Motivation 112
  5.2 Experimental methods 113
    5.2.1 dI/dV spectra of Au(111) 114
    5.2.2 Comparison of numerical differentiation to lock-in dI/dV . 116
  5.3 TPP/Br_xTPP: Characterisation of molecular packing and structure, based on STM topography 117
    5.3.1 Confirming the presence of Br_xTPP 117
    5.3.2 Close-packed structures with halogen bonds 117
    5.3.3 Single-row structures 120
    5.3.4 How to distinguish between Br_xTPP species 121
  5.4 Scanning tunnelling spectroscopy to identify Br_xTPP species . . . 122
    5.4.1 STS characterisation of individual TPP 122
    5.4.2 Individual Br_2 TPP 124
    5.4.3 STS and differential conductance maps as a method of chemical identification 127
  5.5 Characterisation of Ullmann-type coupling 130
    5.5.1 250°C anneal 130
      5.5.1.1 Summary of 250°C anneal 133
    5.5.2 300°C anneal 133
      5.5.2.1 STS characterisation of the reaction products . . 135

5.5.3 325°C anneal 136
    5.5.3.1 dI/dV of polymers 138
        5.5.3.1.1 dI/dV of ring-closed TPP species 138
        5.5.3.1.2 dI/dV of 'saddle' shaped TPP species . 138
5.6 Self-metalation of TPP within covalently coupled chains 141
5.7 Conclusion 142

6 Order to disorder and self-metalation of tetraphenylporphyrin 145
6.1 Motivation 146
    6.1.1 Previous STM characterisation of TPP on Au(111): work by the Nottingham Nanoscience group 146
6.2 Photoelectron and LEED investigations 148
    6.2.1 LEED data: characterisation of close-packed and diffuse structures 149
    6.2.2 XPS data: chemical environments 152
    6.2.3 NEXAFS data: a 'fingerprint' of self-metalation 156
    6.2.4 XSW data: structural characterisation 160
        6.2.4.1 Considerations whilst fitting NIXSW data 160
        6.2.4.2 Close-packed structural analysis 162
        6.2.4.3 Diffuse structural analysis 164
        6.2.4.4 Metalated structural analysis 165
    6.2.5 Comparison of NIXSW data 167
6.3 Conclusion 169

7 NAP gas dosing on FePc on Ag(111) 170
7.1 Motivation 171
7.2 Experimental methods 172
7.3 Characterisation of deposited FePc using scanning tunnelling microscopy 173
7.4 X-ray photoelectron spectroscopy 176
    7.4.1 C 1s Spectra 177
        7.4.1.1 Multilayer 177
        7.4.1.2 Annealed monolayer 178

7.4.1.3 Monolayer 179
7.4.2 N 1s Spectra 181
7.4.3 Fe 2p Spectra 181
7.4.4 Near ambient pressure of gas dosing 183
7.4.4.1 CO dosing 184
7.4.4.2 H_2O dosing 187
7.4.4.3 O_2 dosing 188
7.5 Summary 189

8 Conclusion 191

8.1 Summary of findings 191

A Diffusion TPP 195

A.1 Surface features alter herringbone reconstruction 195
A.2 Full sized image of TPP 1000 nm 195
A.3 Full sized images of TPP VT-STM measurements 195

B FePc on Ag(110) 199

B.1 Introduction and Motivation 199
B.2 Experimental methods 202
B.3 Results 202
B.4 Conclusion 207

Chapter 1

Introduction

My first introduction to the nanometre scale world was through the genre of science fiction (namely the TV programmes and films of Star Trek). These fictional worlds piqued my interest in the ideas of 'nanofabrication' and the use of 'nanobots' to build, repair and improve the world at the atomic/molecular level. Alas, those technologies are still squarely for the future. In the here and now, the idea of 'building' atomic-scale structures on surfaces is a reality, but is very limited in scope and application. Richard Feynman's talk titled "There's Plenty of Room at the Bottom" [1], delivered in 1959, could be described as the 'starting pistol' to decades of research at the nanoscale. He suggested that it would be possible to write many volumes of literature on the head of a pin, but posed the question of how we could do this and how would we read it. The 'bottom-up' approach of manipulating individual atoms was postulated by Feynman as the precursor to the production of materials with interesting properties. In the 'bottom-up' approach, chemical and physical forces are used to assemble small simple units (such as atoms or small molecules) into larger more elaborate structures that have desirable properties.

The debate around how we could build nanodevices began around 2001. K. Eric Drexler suggested that molecular machines could manipulate individual atoms or molecules to form molecular materials or devices. However, R. Smalley had an opposing view and argued that fundamental physical forces would prevent such devices from becoming a reality. The macroscopic view that Drexler took assumes that the nanoscale 'world' works in a similar way to conventional mechanics, but is that valid? Humans, in general, do not intuitively understand the nanoscale in the same way as the macroscale, as we cannot correlate it to everyday experiences. An example of this is the colour of gold: we see it as a darkish yellow colour, and when making smaller items, the colour it displays is still the same. This is true until the gold material is sufficiently small (nanoscale), where the colour changes to red. The quantum confinement of states has fundamentally changed one of gold's most ubiquitous properties.

Some of the challenges raised by Feynman have been solved, such as atomic manipulation, but some remain out of reach, just like the nanobots within Star Trek. The invention of the scanning tunnelling microscope (STM), along with many other associated scanning probe techniques, has allowed for the manipulation of single atoms and molecules to form structures from the 'bottom-up'. STM uses an atomically sharp tip to image the surface and can be used to physically move atomic scale features on-surface. Using an STM, atoms (xenon atoms on a nickel surface) were manipulated to write words on the surface as shown by Eigler *et al.* [2]. Further work by IBM created the well-known 'A Boy and His Atom' animation out of the same xenon and nickel surface, showing that although difficult, manipulation to form desired structures was possible. The manipulation of CO on Cu(111) was also shown to be able to create logic gates [3]. Indeed, it is also possible to create single bits using single atoms to create the highest density storage media [4]. If we were only limited to 'direct manipulation' of on-surface features, it would take far too long to fabricate our desired structure. Nanoscience research has shown it is possible to create large molecular structures on the surface from smaller molecules, truly emphasising the 'bottom-up' approach to nanotechnology. Nature has found a way to automate this process, such that living organisms can exist. If we could harness the reactions that nature has found and tailor them to our needs, could we create the devices that we want?

1.1 Overview of this thesis

Within this thesis, the on-surface processes and interactions of porphyrins and phthalocyanines are characterised using various surface-sensitive techniques; with a view to 'watching' and understanding atomic-scale processes. Chapter 2 details key developments in surface science that are relevant to the topics explored in the rest of the thesis. The principles by which supramolecular chemistry operates, examples of reactions on surfaces, and how researchers have used surface-sensitive techniques to characterise the mechanisms are explored.

Chapter 3 will detail the theoretical and experimental concepts used in the surface-sensitive characterisation techniques. The chapter will focus on STM as the main method within this thesis to 'view' the reactions and self-assembly of molecules on metal surfaces under ultra-high vacuum and at low temperatures. Furthermore, photoelectron spectroscopy techniques used within this thesis are described, such as X-ray photoelectron spectroscopy (XPS), normal incidence X-ray standing wave (NIXSW), and near-edge X-ray absorption fine structure (NEXAFS). This chapter concludes with explanations/descriptions of the experimental apparatus used in this research.

Chapter 4 will describe the packing structure of tetraphenylporphyrin (TPP) on Au(111) and how packing positions on the surface are determined by the diffusion of the porphyrin. Despite TPP on Au(111) being a well-studied system, specific sites for the formation of self-assembled islands have not been well explored. Using variable and low-temperature STM, the diffusion of TPP on the surface is viewed and characterised to find the energy barrier to diffusion for molecules in two distinct regions of the surface; the face-centred cubic (*fcc*) or hexagonal close-packed (*hcp*) regions, which differ only in their vertical atomic stacking.

Chapter 5 details the investigation into brominated tetraphenylporphyrin (Br_xTPP) on Au(111). The Br_xTPP molecules (similar to TPP) form self-assembled close-packed structures on the surface. These assemblies appear to be driven by the bromine atom with a halogen bond between bromine atoms. We identify differences in the electronic properties of the Br_xTPP as $x = 0 \rightarrow 4$ and use this to spatially identify the Br_xTPP in a differential conductance map for each x value. We also characterise the surface and electronic states as the surface is annealed and forms covalently coupled TPP chains. Further annealing reveals that the covalently coupled chain TPP species undergo the same ring-closing reaction detailed in Chapter 6. Finally, annealing to a higher temperature yields self-metalation of the chain TPP species.

Chapter 6 will detail the order to disorder transition of tetraphenylporphyrin (TPP) on Au(111). Upon annealing close-packed TPP, the surface structure is no longer close-packed and has become disordered. Using photoelectron spectroscopies and low energy electron diffraction we characterise the on-surface reactions occurring. We show that a ring-closing reaction has occurred that reduces the molecule-molecule reaction to cause the transition to disorder. Upon heating further we found evidence for the formation of self-metalation of the TPP species to form Au-TPP.

Chapter 7 will describe iron phthalocyanine gas dosing experiments on Ag surfaces. Iron phthalocyanine produces on-surface assemblies on Ag(111). The effects on the molecular overlayer when dosing gases (CO, O_2 and H_2O) at near ambient pressures are investigated using STM and XPS. We find no interaction between the H_2O and FePc at room temperature and up to 7 mbar of H_2O pressure. The gases of CO and O_2 were dosed, but we found that contaminants within the gas phase complicated the analysis of the interactions.

Finally, Chapter 8 provides a summary of the work presented within this thesis and highlights the key findings.

Chapter 2

Studying on-surface processes

2.1 Molecules and their on-surface self-assembled structures

Solution-phase chemistry has allowed a plethora of molecular species to be synthesised with atomic precision. Such molecules are typically formed from covalently bonded atoms, which may be arranged to form different structures driven by the inherent chemistry of the constituent atoms. Generally, many pathways to the synthesis of a molecule exist, each with its own advantages/disadvantages. Importantly, molecules do not usually exist in isolation and interactions between molecules can form larger structures made from discrete quantities of molecules. These supramolecular structures are formed by the intermolecular forces between molecules. Such forces are generally weaker than covalent bonding but can give rise to complex structures. Examples of these forces include, but are not limited to: hydrogen bonding, halogen bonding, metal coordination, hydrophobic forces, Van der Waals forces, $\pi - \pi$ stacking and electrostatic effects. Supramolecular structures are readily found within solution-based chemistry, see Lehn's Nobel lecture [5], and they are fundamental to the operation of biological systems (double helix structure formed by DNA).

The same principles can be applied to molecules on surfaces, although the complexity of the structures has been limited to 2D, with characterisation made possible by using surface-sensitive techniques. The formation of the complex structures observed is similarly driven by intramolecular forces that result in unique geometric arrangements. The study of the observed self-assembly and/or reactions can lead to insights about each of the molecular systems, which in turn may allow us to improve efficiency and selectivity [6]. Molecular self-assembly could also be exploited to form specific systems with desirable properties (e.g porous structures to trap molecules) [7]. To study self-assembled molecules on surfaces, one common analysis technique is to use scanning tunnelling microscopy (STM). Optical microscope resolution is limited by the wavelength of light, which is not sufficient to resolve atomic-scale features. STM allows for high spatial resolution information to be seen in the form of an image, or topography, of the surface and molecules. STM is based on quantum mechanical tunnelling (discussed in Chapter 3), but the general concept is that tunnelling occurs into the empty states from filled states between the tip and surface structures. The tunnelling varies spatially based on topography and the states available for tunnelling, which allows for the identification of molecular positions. In the next section, I will introduce some of the most important interactions for self-assembled structures.

2.1.1 Van der Waals interactions

At the atomic and molecular level, the Van der Waals (vdW) force describes a collection of intermolecular and/or atomic interactions that are relatively weak compared to covalent bonds, hydrogen bonding and metal-organic bonding. In a simplification of the electronic structure, we assume that around each atom or molecule exists an ‘electron cloud’ corresponding to the probability of electrons, due to orbitals of the atom or the formation of bonds within molecules, being present in this region. An instantaneous dipole can arise for a single atom when the electron cloud around the nucleus is not symmetric, this provides asymmetric shielding to the nucleus resulting in a dipole that has a more negatively charged (δ^-) side, with the other side being more positively charged (δ^+). Where this dipole exists in a molecule as a result of a difference in electronegativity between two atoms, this results in the formation of a permanent dipole. The positive and negatively charged ends of two separate dipoles can attract (dipole-dipole interaction, see Figure 2.1a). It is also possible for the dipole to induce a dipole in a

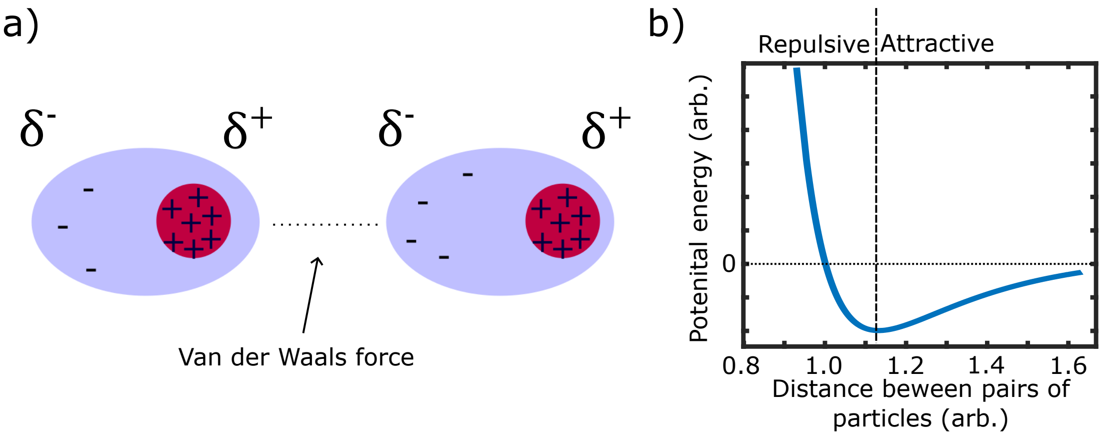

Figure 2.1: (a) Van der Waals forces between two objects due to the formation of a dipole on each object. (b) The Lennard-Jones potential shows longer-range attractive forces that become strongly repulsive at shorter distances. The force experienced by the particles can be obtained from the derivative of the potential.

'neutral' atom, due to the negative end of the dipole repulsing the electron cloud away in a neutral object (with the closest side to the inducing dipole becoming relatively more positive), or vice versa, by attracting the cloud (the closest side to the inducing dipole becomes more negative). This leads to an induced dipole-dipole interaction. Furthermore, a neutral atom can instantaneously form a dipole (at any given time there is a non-uniform electron distribution) and therefore induce another neutral atom to become a dipole (instantaneous dipole-dipole interaction). VdW interactions are inherently an attractive force, although atoms/molecules cannot get too close to each other due to the Pauli exclusion principle, and therefore, the forces become strongly repulsive at shorter distances. The attractive Van der Waals forces and strongly repulsive Pauli exclusion forces are generally approximated by the well-known Lennard-Jones potential [8]. The Lennard-Jones equation is given by the potential energy equation,

$$V(r) = 4\epsilon\left[\left(\frac{\sigma}{r}\right)^{12} - \left(\frac{\sigma}{r}\right)^{6}\right], \tag{2.1}$$

where the energy ϵ defines the lowest potential energy of the curve (bottom of the well), σ defines the distance at which the potential between the particles is zero and r is the distance between the pairs of particles. The $1/r^{12}$ defines the repulsive term due to Pauli repulsion at short distances, and the $1/r^{6}$ term defines the attractive forces between the particles.

Although these forces are weak, the ordering of on-surface structures can occur and even be driven by these interactions. A change in the packing of on-surface molecules was seen in the work reported by Gao *et al.* as a result of altering the Van der Waals interaction forces [9]. The vdW interactions between the molecule-surface/molecule-molecule could be altered by adding flexible alkyl chains to obtain enhanced in-plane molecule-molecule adhesion due to the increased contact surface area between molecules [9]. This resulted in various packing structures present on the surface. VdW forces have no directional preference, but the shapes of the molecules drive the formation of ordered surfaces due to increased interactions.

2.1.2 Hydrogen Bonding

The covalent bonding of hydrogen to electronegative atoms (such as N, O or F) forms a highly polar covalent bond. The electronegative atom (X) has a large partial negative charge δ^{-}, whereas the hydrogen (H) has a large partial positive charge δ^{+}. Electrons are shared between the δ^{-} and δ^{+} species to form a weak bond. This is given by: $\mathrm{X}^{\delta^{-}}\text{–}\mathrm{H}^{\delta^{+}} \cdots \mathrm{X}^{\delta^{-}}$ ("–" represents a covalent bond and "$\cdots$" represents the hydrogen bonding). The formed hydrogen bond is directional due to the symmetry of the orbitals on the δ^{+} and δ^{-} charged atoms.

An example of hydrogen bonding that drives molecular ordering is that of PTCDI and melamine on Ag(111), as reported by Judd *et al.* [10] (based on previous studies including Theobald *et al.* [11] and Perdigão *et al.* [12]). In Figure 2.2a, a diagram of the interaction between a melamine molecule (left) and a perylene-3,4,9,10-tetracarboxylic-3,4,9,10-diimide (PTCDI) molecule (right) is shown, with the hydrogen bonding indicated between the H$\cdots$N and H$\cdots$O atoms within these molecules. Due to the threefold symmetry of the melamine molecule, it can act as a 'triangle vertex' and the two-way symmetry of the PTCDI molecule allows it to act as a 'rod' as shown within Figure 2.2b. This model shows that the hydrogen bonds act to self-assemble the molecules into a hexagonal structure on the surface (see Figure 2.2b-c) [10]. The STM results show this hexagonal structure (see Figure 2.2c), however, there are occasionally defects within this packing mode that appear not to be hexagonally shaped due

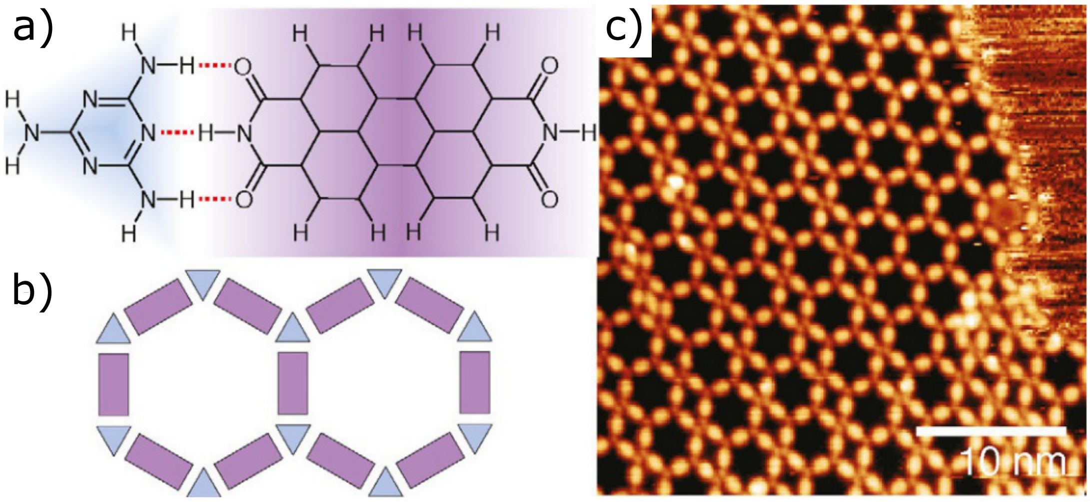

Figure 2.2: (a) Diagram showing melamine (left) and PTCDI (right) interacting via hydrogen bonds between the H···N and H···O atoms. The melamine molecule has threefold symmetry, compared to the twofold symmetry of PTCDI. (b) The symmetry of melamine allows it to act as a triangular vertex, whereas PTCDI acts as a rectangular rod. These molecules form a hexagonal structure due to self-assembly driven by the hydrogen bonds between melamine and PTCDI. (c) STM image shows this hexagonal packing mode. STM image parameters $V_{\text{sample}} = 1.8$ V, $I_{\text{set}} = 50$ pA and T = 300 K. Taken from Judd *et al.* [10].

to variations in local stoichiometry (too few of one of the molecules to form the hexagonal structure) or due to kinetic trapping of other species.

2.1.3 Halogen bonding

Halogen atoms are widely recognised as sites of high electron density due to the high inherent electronegativity of the atom (defined as the ability to attract electrons towards itself). The electron density surrounding the halogen atom is anisotropically distributed when covalently bonded to another atom. This distribution of electrons leads to regions of the halogen atom that have a lower electron density. This distribution is seen in Figure 2.3a, where orthogonal to the R-X bond exists a δ^- charge, compared to along the same axis as the R-X bond where there is a δ^+ charge (termed σ-hole). This charge distribution leads to two types of halogen bonding, shown in Figure 2.3b between two halogen atoms labelled ‘X’. In type 1, the bonding is directed such that it occurs at the same

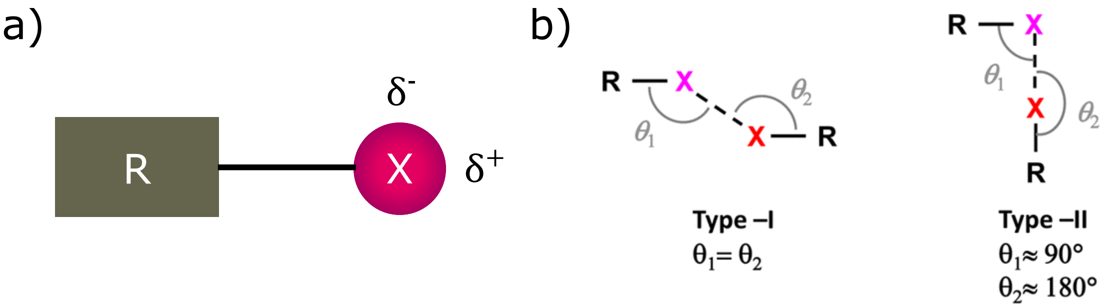

Figure 2.3: (a) Halogen atom 'X' covalently bonded to another atom 'R'. This shows the anisotropically distributed electron density of the halogen atom resulting in δ^+ and δ^- charges on each side of the atom. (b) Shows the possible bonding types observed for halogen bonding. Taken (b) from Cavallo *et al.* [13].

angle for each halogen relative to covalently bonded other atom 'R'. In type 2, this bonding occurs perpendicular to each halogen, such that the δ^+ charge interacts with the δ^- charge. Interested readers are directed to Cavallo *et al.* [13] for a thorough review of halogen bonding; also, see Tschakert *et al.* [14] for a recent investigation into halogen bonding with BrparaImeta-TP and IparaBrmeta-TP molecules on Cu(111) and Au(111).

2.1.4 Other types of surface ordering

There are several interactions that may drive on-surface self-assembly. Self-assembly of molecules on surfaces can also be achieved by metal-organic coordination. Adatoms (surface-confined single atoms) of transition metals can participate in the formation of supramolecular structures. The '*d*' type orbitals of these metals are shielded from the nucleus by the core electrons, allowing for coordination bonds to form with organic molecules. Typically oxygen or nitrogen atoms within molecules take part in the coordination, and these are highly directional bonds due to the lone pair of electrons present for these species. This is a widely studied field [15], however, a good example of self-assembly into a metal-organic coordination network (MOCN) is reported by Dmitriev *et al.* [16] for the co-deposition of 1,2,4-benzene tricarboxylic acid (TMLA - see Figure 2.4a inset) and Fe onto Cu(100). Initially, TMLA forms close-packed structures on the surface (see Figure 2.4a when no Fe is deposited). When Fe is deposited on top of

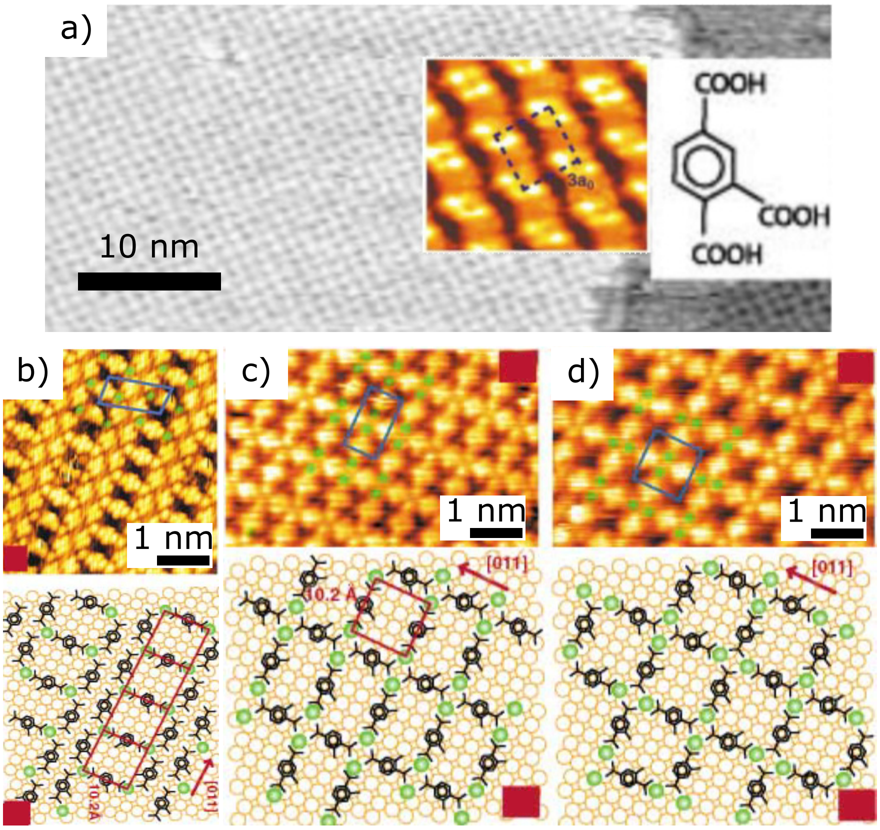

Figure 2.4: (a) Self-assembly of 1,2,4-benzenetricarboxylic acid (see inset) on Cu(100) as reported by Dmitriev *et al.* [16]. Upon the deposition of Fe atoms onto the close-packed organic overlayer MOCNs are formed. When insufficient Fe is deposited, not all of the molecules interact with the Fe atoms (b). In (c) and (d) when the ratio of TMLA to Fe is 1:1, two phases of MOCNs are observed on the surface. STM image parameters: T = 300 K. Taken from Dmitriev *et al.* [16].

the organic layer, MOCNs are formed due to the interaction between the Fe and the carboxyl groups on the TMLA (see Figure 2.4b-d). Altering the ratio of the Fe to TMLA alters the structure of the assembled MOCNs [16]. In Figure 2.4b, insufficient Fe is present on the surface, and therefore some TMLA does not fully interact with the Fe atoms on the surface as the TMLA is partly close-packed with itself. Where the ratio of TMLA to Fe is 1:1, two phases of the MOCN are formed (rectangle and square see Figure 2.4c-d) [16].

2.1.5 Ullmann-type coupling

The formation of covalent bonds between molecules can directly link multiple molecules into a single polymer species. A subset of this coupling is the Ullmann reaction, which in solution chemistry is a type of covalent coupling reaction between two aryl halides (aryl = functional group of an aromatic ring [see phenyl ring], halide = halogen atom covalently or ionically bonded to a less electronegative atom or molecule) [17], where the coupling reaction is catalysed by copper. The accepted mechanism for this reaction involves the formation of an organometallic (specifically organocuprate) intermediate through the loss of the halogen on one of the aryl halides. Through the process of oxidative addition (Cu charge decreased by $2e^-$), the second aryl halide is also bonded to the Cu atom along with the second aryl halide's halogen atom. Finally, reductive elimination (the charge is decreased by -2 on the Cu) occurs whereby the two aryl groups are now bonded by a covalent bond directly with no additional bonds to the halogen or Cu atom. In solution, other metals have been found to be able to act as the catalyst for this coupling reaction in place of Cu (such as Ni or Pd) [18], and these metals often require lower temperatures and/or less harsh conditions [17].

On-surface chemistry also displays coupling reactions (e.g. Ullmann-type coupling see Figure 2.5a) that follow a similar reaction pathway as the Ullmann coupling reaction in solution [19, 20]. The exact on-surface mechanism for this Ullmann-type coupling is disputed (or more than one reaction may be possible under specific conditions), with the interacting metal atom being in the surface layer (Figure 2.5b mechanism 1) [21,22], or as an adatom (Figure 2.5b mechanism 2) [10, 23, 24]. In both mechanisms shown in Figure 2.5b, (i) the molecules are adsorbed to the surface, then in (ii) each of the molecules forms an organometallic intermediate with either the surface or an adatom. It is reported that in the case of interaction with surface atoms in mechanism 1, the molecules would tilt to form this intermediate [22]. Finally, in part (iii) a covalent bond is formed between the two molecules. This reaction is also not limited to Cu surfaces, and a wide variety of atomic species are able to form via Ullmann-type coupling reaction [10, 19].

Depending on surface energetics, organometallic intermediates can exist as stable entities, and intermediate metal coordination can stabilise the overlayer

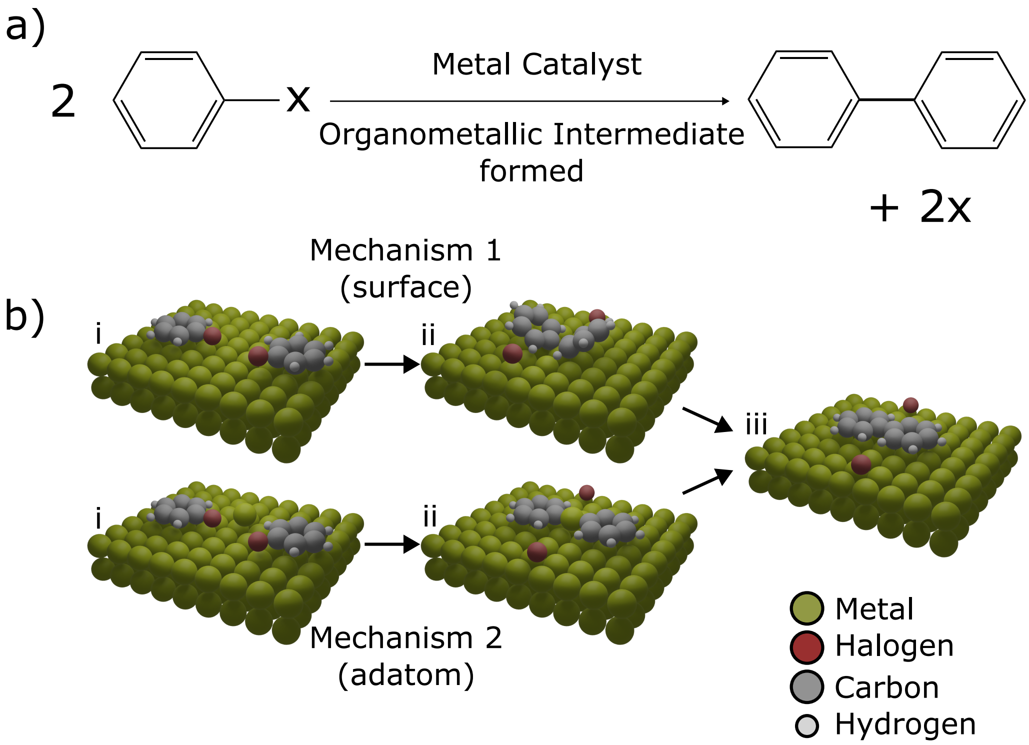

Figure 2.5: (a) Simplified reaction pathway for Ullmann type coupling. Two aryl halides (X denotes halogen) react using a metal catalyst during which an organometallic intermediate is formed. The product of this reaction is that the two molecules are now covalently bonded together and the halogens are adsorbed on the surface. (b) Shows the reaction pathway but split by the two reaction mechanisms suggested (1-surface atom meditated reaction, 2-adatom meditated reaction). Steps i, ii and iii match each step in (a). Rendered (b) using Blender.

structure to form a self-assembled structure [24]. This is shown in the case of 1,4-dibromobenzene on Cu(110) as reported by Di Giovannantonio *et al.* [20]. In this study, upon deposition, the 1,4-dibromobenzene forms an organometallic intermediate with the Cu substrate (see Figure 2.6i). The surface is ordered by the Cu atoms as they are interacting with the phenylene units to form a phenylene-Cu chain. The organometallic intermediate differs from that seen due to metal coordination assembly as the latter does not involve halogens (coordinate bonds form between metal and ligands to form large supramolecular structures that do not have a further reaction pathway). Di Giovannantonio *et al.* reported that once annealed, the structure of the self-assembled 1,4-dibromobenzene changes to that seen in Figure 2.6ii, now the benzene rings are covalently bonded to each

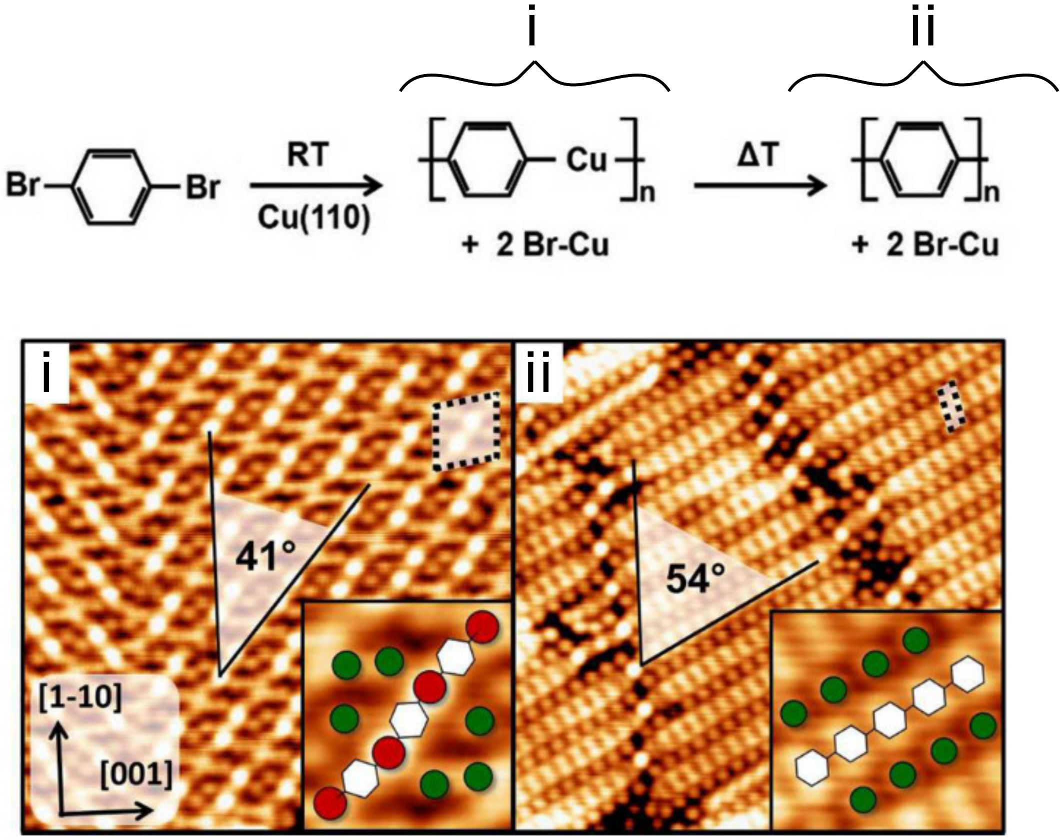

Figure 2.6: Top: Shows a reaction pathway for 1,4-dibromobenzene on Cu(110). Upon deposition, the 1,4-dibromobenzene forms an organometallic intermediate (see i, and see STM image below) with the Cu surface. Upon annealing the surface to 500 K, the reductive elimination reaction and the benzene rings are now covalently bonded as graphene nanoribbons (see ii, and see STM image below). Bottom: white hexagons = benzene, red circles = Cu atoms and green circles = bromine atoms. STM image parameters V_{sample} = 0.02 V, I_{set} = 500 pA and T = 300 K. Taken from Di Giovannantonio *et al.* [20].

other to form graphene nanoribbons (having undergone the reductive elimination reaction). In the annealed reacted state, it is shown that the bromine atoms are still present on the surface [20]. In further work by Galeotti *et al.* [25], the effect of how the choice of halogen atom on the 1,4-dihalobenzene altered the reaction rate, reaction temperature and the length of the formed structures was explored. This showed that the reactivity of halogens is ordered as such: Ar-I > Ar-Br > Ar-Cl due to the strength of the bond with the carbon atom [25]. Halogens in the above example stay on the surface and become involved in the close-packed structure. Halogens may also alter the reactivity of the substrate; in the case of Au(111) additional adatoms present on the surface following the reaction have been attributed to the presence of halogens on the surface [26, 27].

2.2 Porphyrins

Porphyrin-based molecules are found within nature, as part of chlorophyll [28], or within the red blood heme group [29]. Surface science research into porphyrin macrocycles has attempted to mimic some behaviours in biological systems, but has not yet fully realised the range of applications possible. The ability of a porphyrin to incorporate a metal atom in the centre of the molecule allows for it to act as a catalyst [30], as a gas sensor [31] and even as porphyrin-sensitised solar cells [32].

The molecular category of a 'porphyrin' is quite broad, as it describes the addition of other moieties and/or functional groups onto the foundation of porphine macrocycles. Porphines (shown in Figure 2.7a) are flat molecules consisting of four pyrrole-type rings (two pyrrolic -NH- and two iminic =N-) joined together with methine groups (=CH-). The porphine is an example of a conjugated π-system as a result of overlapping p orbitals, this provides additional stability to the molecule. A wide variety of potential substitutions onto the porphine molecule can form a porphyrin [33]. One of the more commonly studied variants is the tetraphenylporphyrin (2H-TPP), whereby phenyl rings are added in place of hydrogen at the methine groups on the porphine (see Figure 2.7b). The addition of these rings produces intramolecular steric repulsion (nonbonding interactions, see Pauli repulsion, that influence the shape and reactivity of the molecule) between hydrogens on the rings and the porphine [34]. The resulting molecule deforms to become saddle-shaped, whilst the phenyl rings have some rotational freedom (see Figure 2.7c for two side views of the molecule) [34]. The π-conjugation is further enhanced by the rotation of the phenyl rings and saddle-shaped deformations [34]. Many studies have focused on the interaction/reactions of 2H-TPP following various surface treatments on different substrate materials, some of these studies are described in the next few sections. The use of STM and

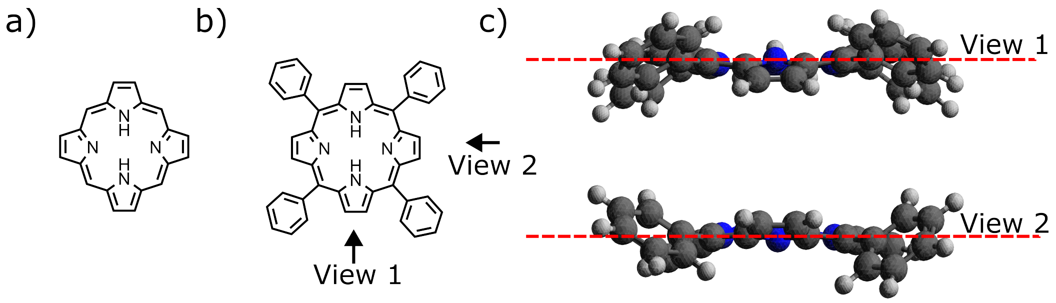

Figure 2.7: (a) Porphine molecule. (b) The addition of phenyl rings on the methine groups of the porphine produces the 2H-TPP molecule shown. When a metal is incorporated into the TPP molecule, the four nitrogen atoms interact with the metal atom. (c) Due to intramolecular steric repulsion and interactions with the surface, the 2H-TPP porphine core becomes saddle-shaped; the phenyl rings also have rotational freedom. In view 1, the pyrrolic (-NH-) group is angled such that the two hydrogen atoms, on that ring, are lower (compared to the central red line) than the nitrogen atom. In view 2, the iminic (=N-) group is angled such that the two hydrogen atoms, on that ring, are higher (compared to the central red line) than the nitrogen atom. The ball and stick shown models in (c) were modelled using energy minimisation (universal force field) within Avogadro which shows a rough estimate of the saddle shape.

photoelectron spectroscopy-based techniques to characterise these interactions is well established [33,35]. The next few sections will discuss details of major scanning tunnelling microscopy and X-ray photoelectron spectroscopy studies that characterise porphyrins with a focus on tetraphenylporphyrins.

2.2.1 TPP absorption characteristics

TPP, like other molecules, can be relatively easily deposited onto surfaces within ultra-high vacuum by thermal sublimation from a crucible. The coverage, temperature, substrate, and the inclusion of a metal centre in the TPP can all vastly alter the properties of the absorbed TPP in terms of self-assembly, chemistry and conformation [33].

For example, in the excellent study by Buchner *et al.* [36] many experiments were conducted to test the adsorption of TPP species on Ag(111). Cobalt TPP was deposited on Ag(111) with the substrate held at room temperature and various coverages were formed by varying the deposition time (and therefore the total CoTPP on the surface). The surface was then characterised with the sample held at room temperature. For surface coverages of ∼0.05 monolayers (ML), the CoTPP was only visible at the step edges of the Ag terraces (see Figure 2.8a). The coverage was then increased to ∼0.4 ML. In addition to step edge absorption, CoTPP was now present in close-packed islands (see Figure 2.8b). Some streaking within the image indicates mobile molecules with motion faster than the acquisition time of the STM. In Figure 2.8c, a multilayer showed square CoTPP ‘terraces’. A monolayer was produced by annealing the multilayer, which desorbed the additional layers (not in contact with the Ag) from the surface due to weaker absorption between CoTPP - CoTPP layers than CoTPP - Ag layers. The CoTPP monolayer surface had a square unit cell with a lattice constant of 1.40 ± 0.05 nm, however, due to tilting of the CoTPP by 25-30° within the multilayer with respect to the surface plane, the lattice constant of the multilayer reduces to 1.25±0.05 nm. Due to impurities (2H-TPP) in the source material, the close-packed islands appear to have differing apparent heights within the monolayer coverage (darker features in Figure 2.8d). Within the same study, Buchner *et al.* [36] also co-deposited FeTPP and 2H-TPP onto Ag(111) (see Figure 2.8e).

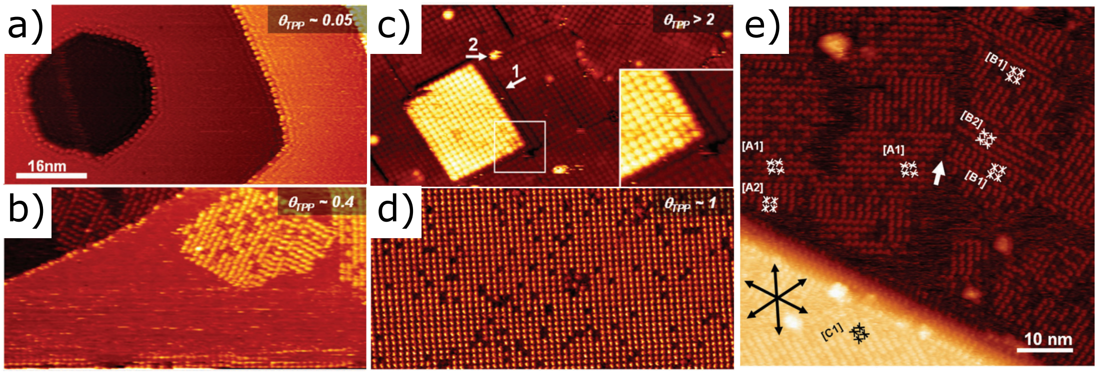

Figure 2.8: (a-d) Different coverages of CoTPP on Ag(111) as characterised by room temperature STM. (a) ∼ 0.05 monolayer (ML) where the CoTPP absorbs at step edges, (b) ∼ 0.4 ML also forms close-packed islands with diffusing molecules present, (c) >2 ML (square growth mode) of multilayers of CoTPP and (d) ∼ 1.0 ML, close-packed CoTPP with darker impurities attributed to 2H-TPP. (e) Co-deposited FeTPP (forms close-packed islands) and 2H-TPP (remains diffuse). Taken from Buchner *et al.* [36].

This showed close-packed islands of FeTPP, surrounded by diffuse 2H-TPP that does not form close-packed islands at room temperature in STM. It is clear that changes to the coverage of the molecular overlayer can lead to different adsorption characteristics. Furthermore, the addition of a metal centre to the TPP can allow for close-packing of the metal-TPP at room temperature, compared to the 2H-TPP which does not form close-packed islands at room temperature. Close-packed islands of TPP in this case are formed due to Van der Waals forces between the TPP molecules, and the formation of CH-π interactions between molecules further stabilises island formation. It is likely that the addition of a metal centre alters the vdW interactions to the surface, and increases the strength of the CH-π interactions.

Similarly, Au is well known to be less reactive than Ag and therefore has fewer interactions with adsorbed species, although the self-assembly of 2H-TPP on each of these metals is similar [33]. Sub-monolayer coverages of 2H-TPP deposited onto Au(111) form close-packed islands at 5 K with a square unit cell [33, 37, 38]. Within the study by Mielke *et al.*, two types of 2H-TPP are identified using STM at 5K at different bias values [37]. As discussed later (in Chapter 3), different bias values between the tip and sample allow for control of the range of local densities of states (LDOS) which can be accessed. At 1.0 V, there are clearly 'darker' and 'brighter' TPP (see Figure 2.9a), based on their apparent height (dark is lower and bright is higher). At bias values other than 1.0 V, shown in Figure 2.9a (0.5 V and 1.5 V), there is little to no discernible difference in topography. To find the LDOS for each of the two types of TPP molecules, dI/dV spectra (in Figure 2.9b) were employed to show that the lowest unoccupied molecular orbital (LUMO) states of the bright TPP were at 1.0 V, whereas the dark TPP had LUMO states at 1.5 V. The proportion of bright/dark TPP varied depending upon the preparation/surface anneal temperature. Bright TPP were able to be generated by using the STM tip to push a dark TPP over and onto an adatom [37]. This indicates that bright TPP species are the result of them sitting atop an adatom. Annealing of Au is known to increase the number of adatoms (absorbed surface atoms above the main surface layer) present on the surface [39, 40]. The difference in spectra between bright and dark TPP was

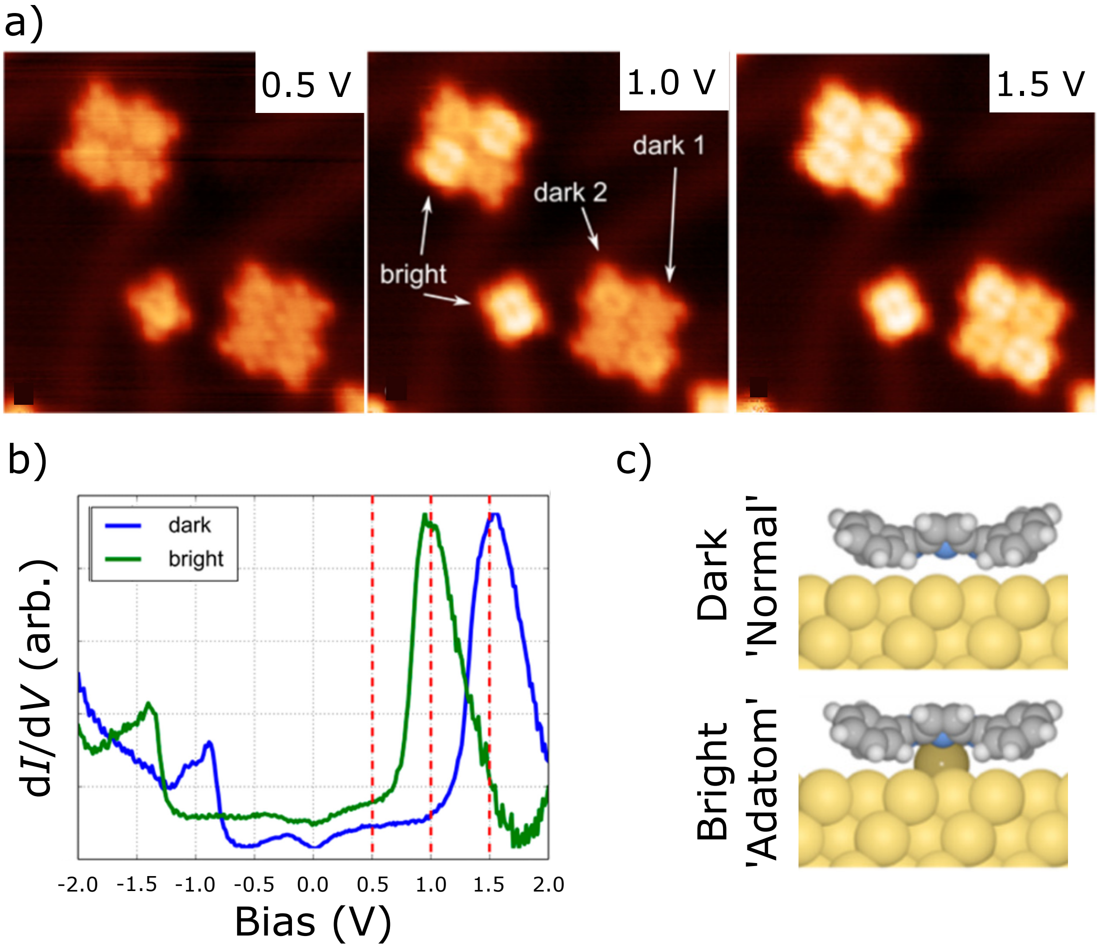

Figure 2.9: (a) STM images of TPP islands on Au(111) at different bias values measured at 5 K. At 0.5 V, there is no perceivable difference in topography. At 1.0 V, some TPP appear brighter (higher), attributed to TPP absorbed on top Au adatoms. There are two different topographies of the 'dark' TPP attributed to two alternative saddle absorption positions [37]. At 1.5 V, all TPP appear brighter. (b) dI/dV spectra show that the LDOS of the bright and dark TPP are different. (c) The difference between the bright and dark TPP is attributed to adatom TPP as calculated by DFT. Adapted (now shown as sample bias - the original work is tip biased) from Mielke *et al.* [37]

calculated using density functional theory (DFT), using the two geometries for bright (adatom) and dark TPP as shown in Figure 2.9c. The absorption position of the TPP is able to influence the LDOS within the molecule, showing that absorption could have implications for the possible reactivity of the molecule on the surface due to the shifting of chemical states. Furthermore, the requirement of low temperatures for close-packed island formation of 2H-TPP highlights the relatively low molecule-molecule interaction (due to the CH-π interaction and vdW forces being lower) compared with that of metalated-TPP.

With what are traditionally considered more reactive metallic substrates, such as Cu, the deposition of 2H-TPP onto the surface provides different adsorption behaviour [41]. As reported by Buchner *et al.*, when TPP is deposited onto a Cu(111) surface at room temperature, no close-packed islands are formed, but rather the TPP stays as isolated molecules on the surface (see Figure 2.10a) [41]. These molecules are specifically absorbed (and aligned) on one of the three symmetry-equivalent $\langle 110 \rangle$ directions of the surface (the absorption of the TPP is shown along one of those axes in Figure 2.10a inset). This strong absorption can be explored by X-ray photoelectron spectroscopy (XPS). It showed that there is an increased interaction with the Cu surface atoms by the iminic nitrogen environment compared to that seen on other metals (Au or Ag). These interaction differences are shown by binding energy shifts between the iminic and pyrrolic nitrogens: 2.1 eV in a bulk multilayer of TPP, 2.0 eV for a monolayer of TPP on Ag(111) or Au(111) and 1.5 eV for a monolayer of TPP on Cu(111) (see Figure 2.10b). This interaction can be seen as a strong localised bond between the Cu and iminic nitrogen which is not present on other metals (Au or Ag).

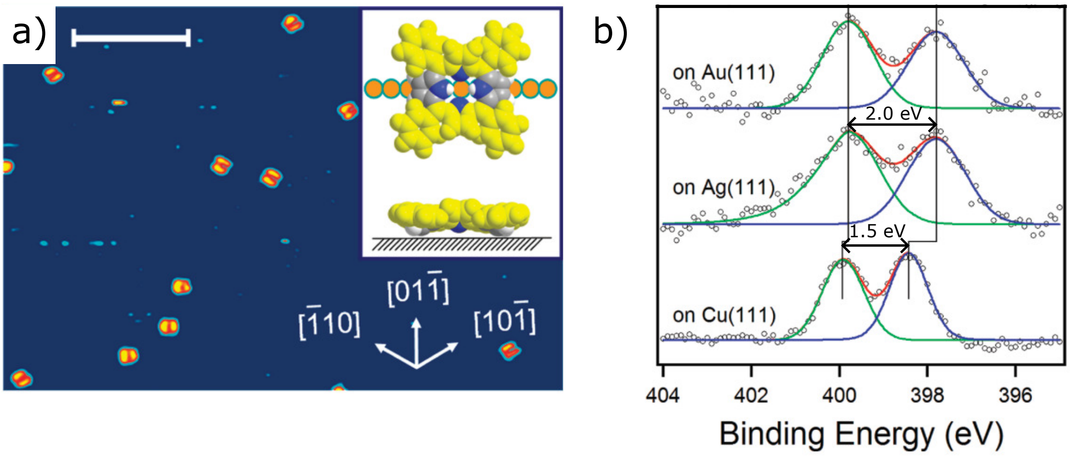

Figure 2.10: (a) STM image showing the surface in blue, and the TPP absorbed along specific surface directions. (b) XP spectra of the N 1*s* environment for 2H-TPP on Au(111), Ag(111) and Cu(111). The two nitrogen environments iminic (=N-, blue) and pyrrolic (-NH-, green) are shown. On Cu(111) the strong interaction between the iminic and the Cu reduces the N 1*s* peak difference to 1.5 eV, compared to Ag and Au at 2.0 eV. Taken from Buchner *et al.* [41]

In an extension to the XPS work, Buchner *et al.* found that at 280 K, the TPP are stationary on the surface (i.e no thermally induced diffusion is observed - see Figure 2.11) [41]. Upon heating the sample to 300 K, the TPP started to become mobile, (in Figure 2.11b-c the coloured dots indicate detected positions of the TPP which are observed to vary over time) the TPP diffuse along one of the three symmetry-equivalent directions $\langle 110 \rangle$ of the surface (directly dependent upon the initial aligned position) [41]. Further heating allowed the TPP to change angular orientation (rotate) to another one of the $\langle 110 \rangle$ directions as seen by Figure 2.11d where rotational diffusion has allowed non-linear motion to occur.

Quantitative information on diffusion events can be obtained since these on-surface processes can be defined as an activated process (when considering transition state theory TST) [43–45]. An energy barrier E_b to the process occurring

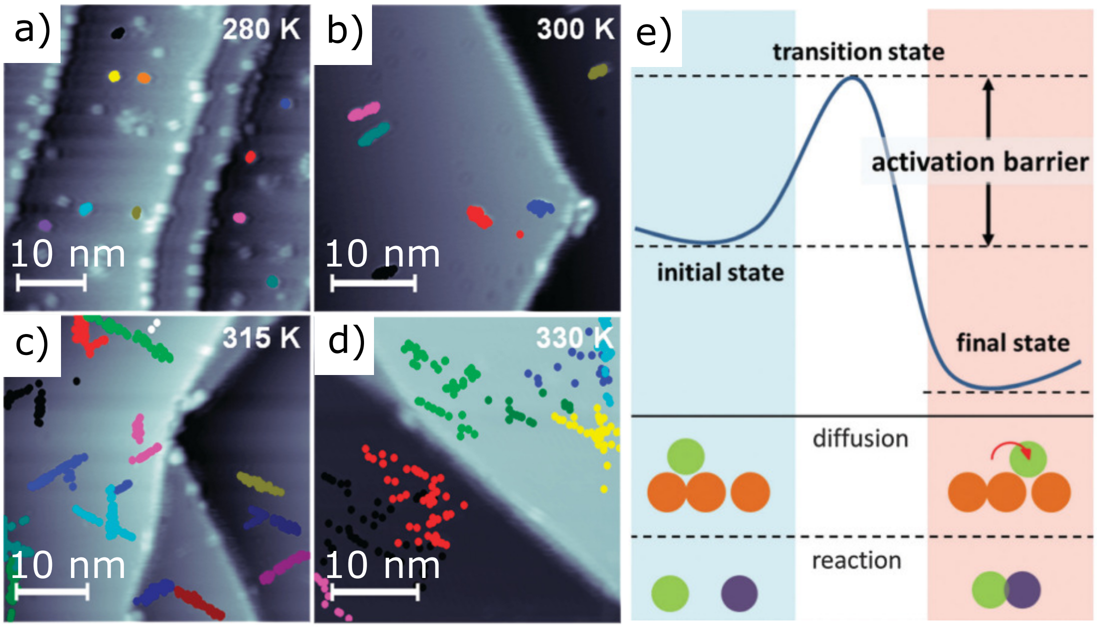

Figure 2.11: (a-d) STM images showing the diffusion of TPP on Cu(111) over time. Each colour represents a tracked TPP, and each dot shows one of the positions of the TPP. At 280 K (a) the TPP seldomly diffuses. At 300 K (b), more diffusion is occurring but is limited to along the surface planes. At 315 K (c), a higher rate of linear diffusion is occurring and seldomly rotates to a different direction. At 330 K (d), the rate of rotational diffusion is higher. (e) Shows the energy barrier assumption for a process to occur. Adapted from (a-d) Buchner *et al.* [41] and (e) taken from H. Marbach and H.-P. Steinrück [42].

must be overcome (see Figure 2.11e) [42]. As the surface/molecules gain more thermal energy, by increased temperature, the probability of the molecule having sufficient energy to overcome the energy barrier increases. This is formalised by the Arrhenius equation that describes the rate r of a process occurring at a specific temperature T. The Arrhenius equation is given by:

$$r = A \exp\left(-\frac{E_\mathrm{b}}{k_\mathrm{b}T}\right), \tag{2.2}$$

where A is the pre-exponential factor and k_b is the Boltzmann constant. In the study by Buchner *et al.* the rate for the linear diffusion and rotation was found at various temperatures and used to determine the energy barrier for the diffusion and rotational processes to occur. It was reported that linear diffusion had an energy barrier of 0.71±0.08 eV, whereas rotation had an energy barrier of 1.28±0.12 eV [41].

The self-assembly into close-packed islands of 2H-TPP on Ag(111) or Au(111) cannot be seen in STM at submonolayer coverages unless cryogenic temperatures are used, however, the inclusion of a metal atom into the TPP (such as Co or Fe) allowed close-packed islands to form at room temperature. Depending on how the TPP interacts with the surface, this can alter the molecules' LDOS in the case of TPP sitting atop an adatom on Au(111). Or in the case of TPP on Cu(111), greater interaction with the surface atoms can increase the energy barrier to diffusion or rotation. Characterising the absorption, diffusion and self-assembly properties of molecules on surfaces is fundamental to our understanding of the interactions possible. Indeed, as discussed above, small changes in molecular structure can tune molecule-molecule and molecule-substrate interactions and lead to changes in the electronic structure of the surface-confined species. It leads to questions such as: how could we design the molecule or substrate to drive supramolecular structures that provide desirable properties?

2.2.2 Thermally induced on-surface reactivity of TPP

Other on-surface processes can be activated by elevated temperatures, such as intra-molecular reactions between different parts of a single molecule. As reported by Wiengarten *et al.*, monolayer coverages of 2H-TPP deposited onto Ag(111)

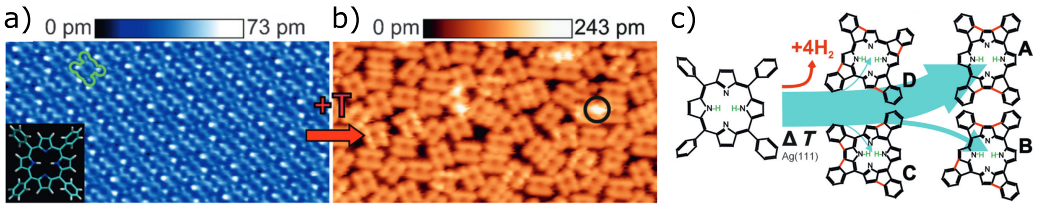

Figure 2.12: (a) Close-packed 2H-TPP on Ag(111). (b) Ring-closed TPP shown following an anneal to 560 K for 30 minutes. Instead of being ordered like the close-packed version, this is now a disordered molecular overlayer. (c) Shows the possible reaction pathways as determined by DFT. Arrows show the relative quantity of each product made. Taken from Wiengarten *et al.* [46].

form close-packed islands (see Figure 2.12a). Upon annealing the surface to 560 K for 10 minutes, the TPP was no longer closely packed and was disordered (see Figure 2.12b) [46]. It was proposed that the TPP had undergone a 'ring-closing' reaction, whereby parts of the phenyl rings and the pyrrolic/iminic carbons lose hydrogen and react together in a cyclodehydrogenation and ring-closing reaction. Bonds are now formed between the phenyl rings and the carbons on the porphine ring. This changes the fundamental 'saddle' shape of the TPP and therefore the interaction between TPP on the surface is weaker (likely caused by the removal of the CH-π interaction that was stabilising the close-packed islands). The possible products of this reaction are shown in Figure 2.12c, as calculated by density functional theory (DFT).

Whilst our investigation of Chapter 6 was underway, Lu *et al.* reported the same cyclodehydrogenation and ring-closing reaction of 2H-TPP on Au(111) for sub-monolayer coverages [38]. Within their work, the 2H-TPP is deposited onto Au(111) which yielded a unit cell of 1.28±0.05 nm by 1.33±0.5 nm with an angle between the two vectors of 87±0.5°. The surface was annealed to 573 K for 30 minutes then cooled to LHe temperatures. This produced the ring-closed TPP on the surface (see Figure 2.13), and using constant height frequency shifted non-contact atomic force microscopy (nc-AFM) with a CO functionalised tip, bond-resolved images of each of the ring-closed TPP products were produced. These bond-resolved images show the formation of the bonds between phenyl rings and the porphine rings. The products were counted and the total percentage of each

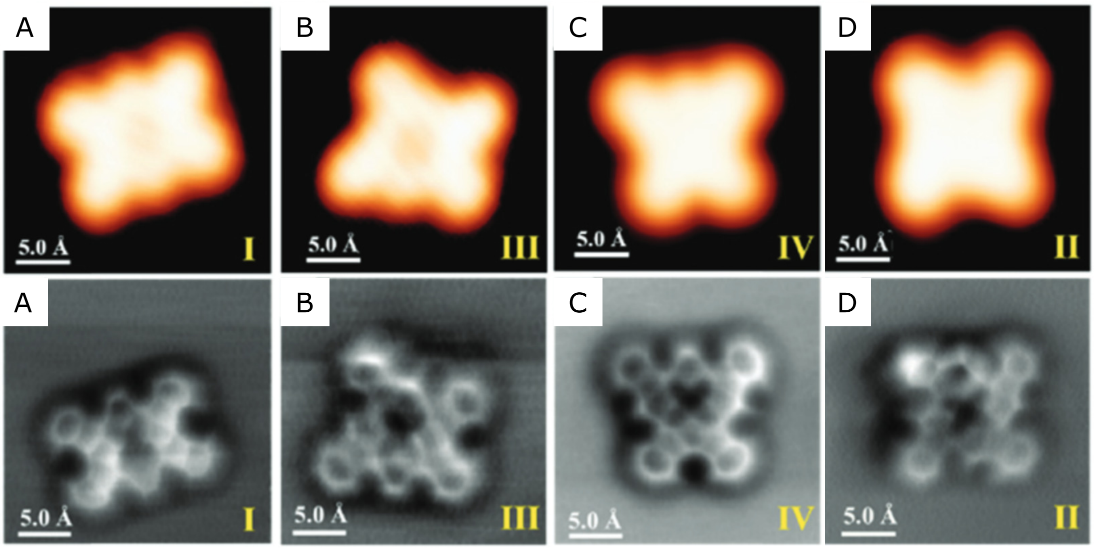

Figure 2.13: SPM images of the four TPP anneal products (A, B, C, D) produced by annealing TPP on Au(111) (See Figure 2.12c). Top: Constant current STM feedback topography image. Bottom: CO functionalised tip scanning in constant height nc-AFM mode detecting changes in frequency response. Taken from Lu *et al.* [38].

product was determined to be: A = 57%, B = 21%, C = 5% and D = 17%. Both Wiengarten *et al.* and Lu *et al.* rely on DFT to determine which form of the TPP is most likely based on the energy barrier pathway to each product.

2.2.3 Metalation of TPP

One of the potential applications of surface-confined synthesis is to identify novel routes to the formation of particular species using on-surface reactions rather than solution-phase chemistry. As previously discussed, the inclusion of a metal atom within the porphyrin centre can allow a variety of other properties and applications to emerge [33]. Due to a strong interaction between Cu(111) and the nitrogen core of the 2H-TPP [41], when the surface is annealed to 490 K, the TPP species sequesters a Cu atom from the substrate into the macrocycle core of the molecule and results in a metalated species as reported by Diller *et al.* [47]. Evidence for this can be seen due to the formation of a single nitrogen (N 1*s*) environment in XPS (see Figure 2.14 - where the two N 1*s* environments, iminic and pyrrolic, form a single environment upon self-metalation). This provides a chemical signature for the type of TPP species present. Scanning probe

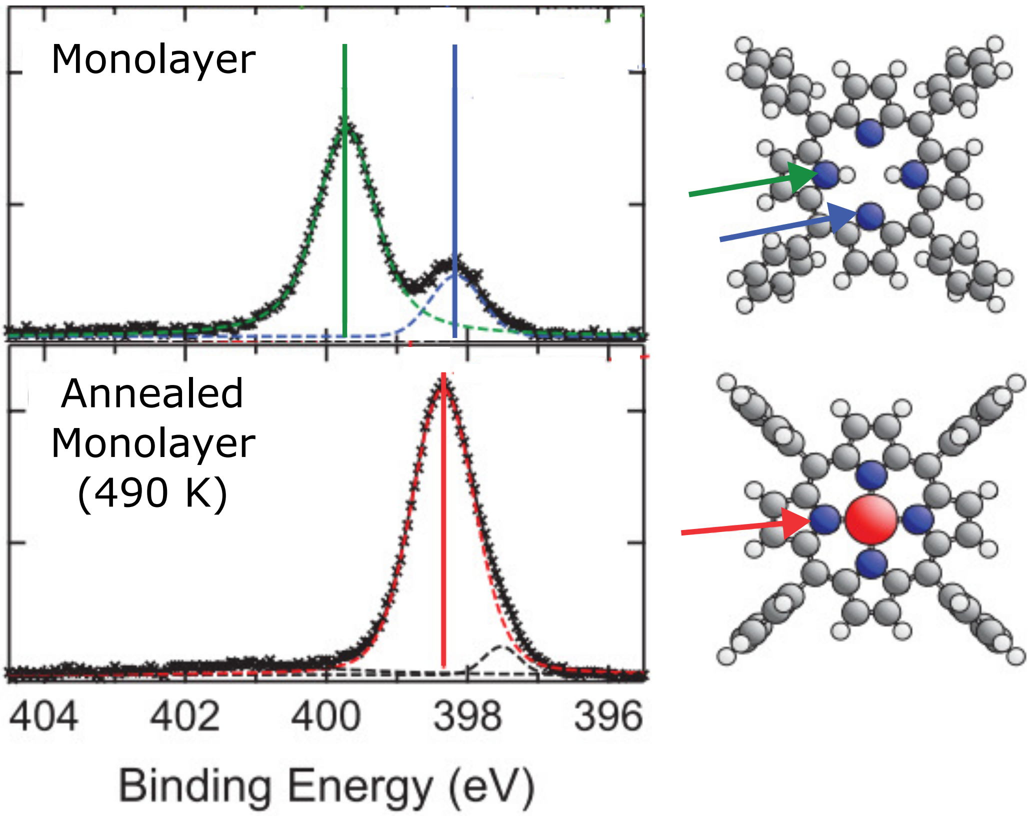

Figure 2.14: XP spectra of a monolayer of 2H-TPP on Cu(111), before and after annealing to 490 K for 30 minutes. Initially, the spectra show two clear environments (pyrrolic -NH- at 399.8 eV and iminic =N- at 398.2 eV). Upon annealing, this forms a single environment main peak at 398.4 eV attributed to the formation of a CuTPP species. Taken from Diller *et al.* [47].

microscopy would be able to provide additional spatial information.

The use of NEXAFS allows for more specific probing of the unoccupied molecular orbitals which will provide information on the bonding state of the molecule. In the self-metalation of TPP on Cu(111), NEXAFS was used (in combination with DFT to predict peak positions) to determine whether the formation of the single N 1*s* environment was the result of metalation or dehydrogenation of the iminic nitrogen (see Figure 2.15). The comparison of the N K-edge spectra to the DFT showed that nitrogen was bonded to a Cu atom following the 490 K anneal [47]. Furthermore, a comparison of C K-edge NEXAFS showed that following the 490 K anneal, there was no change in NEXAFS spectra which indicated that no cyclodehydrogenation/ring-closing reaction had occurred (see Figure 2.15).

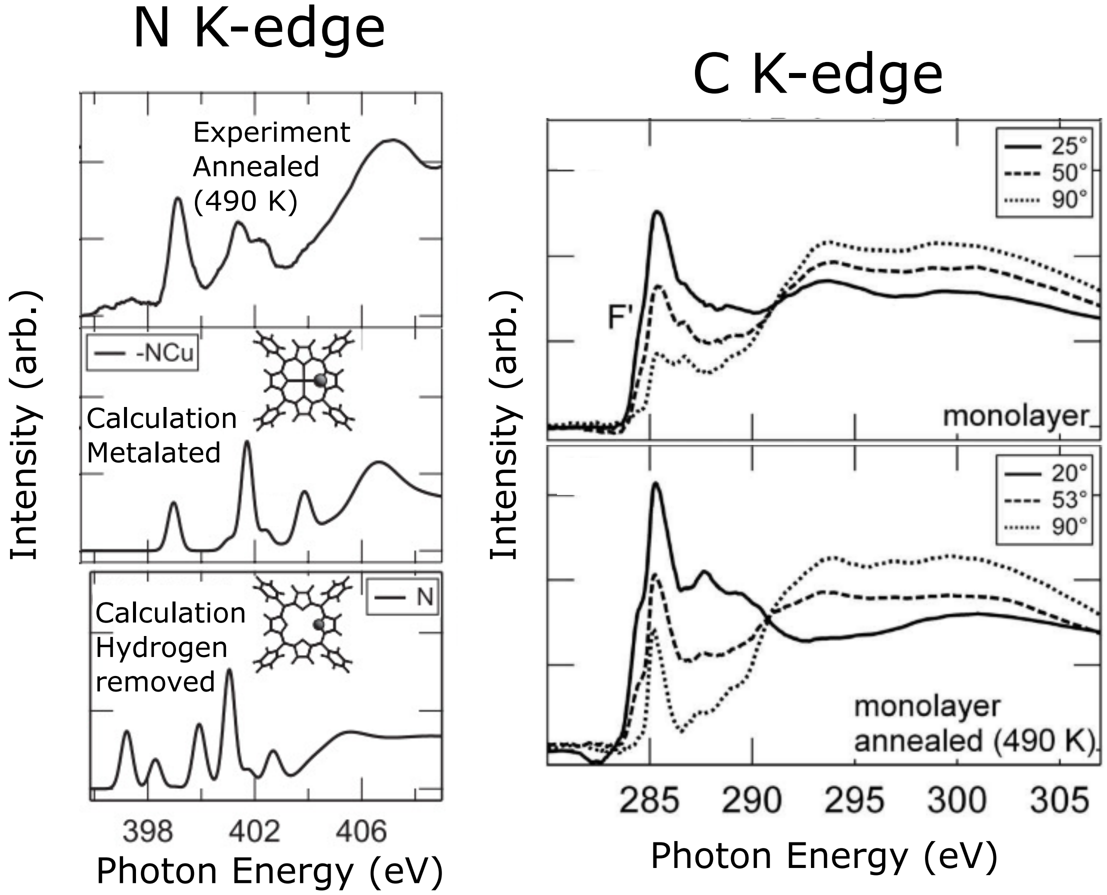

Figure 2.15: N K-edge (annealed) experimental data is shown, with two calculated spectra for either the CuTPP or dehydrogenated nitrogen environment (see inset chemical structures). A comparison of the peak locations in the spectra indicates the experimental spectra best matches the metalated calculation. C K-edge shows the NEXAFS data taken before and after the anneal. A simple comparison between the two preparations shows similar structures. The π^* region at $\sim$285 eV shows a strong intensity peak in both preparations. This indicates little to no change in the carbon features (assigned to a lack of ring-closing). Taken from Diller *et al.* [47].

This reaction was further characterised using various STM, and other photoelectron spectroscopy measurements [48–50]. These results show it is possible to create a new molecule via a novel route using on-surface chemistry.

A similar reaction was reported on Au(111) with fluorinated TPP (denoted as 2H-4FTPP - see Figure 2.16a for the reaction pathway) [49]. The fluorine atoms on 2H-4FTPP are attached at the *para* position on the phenyl rings as shown in Figure 2.16a. Fluorine is an electronegative atom and has been shown

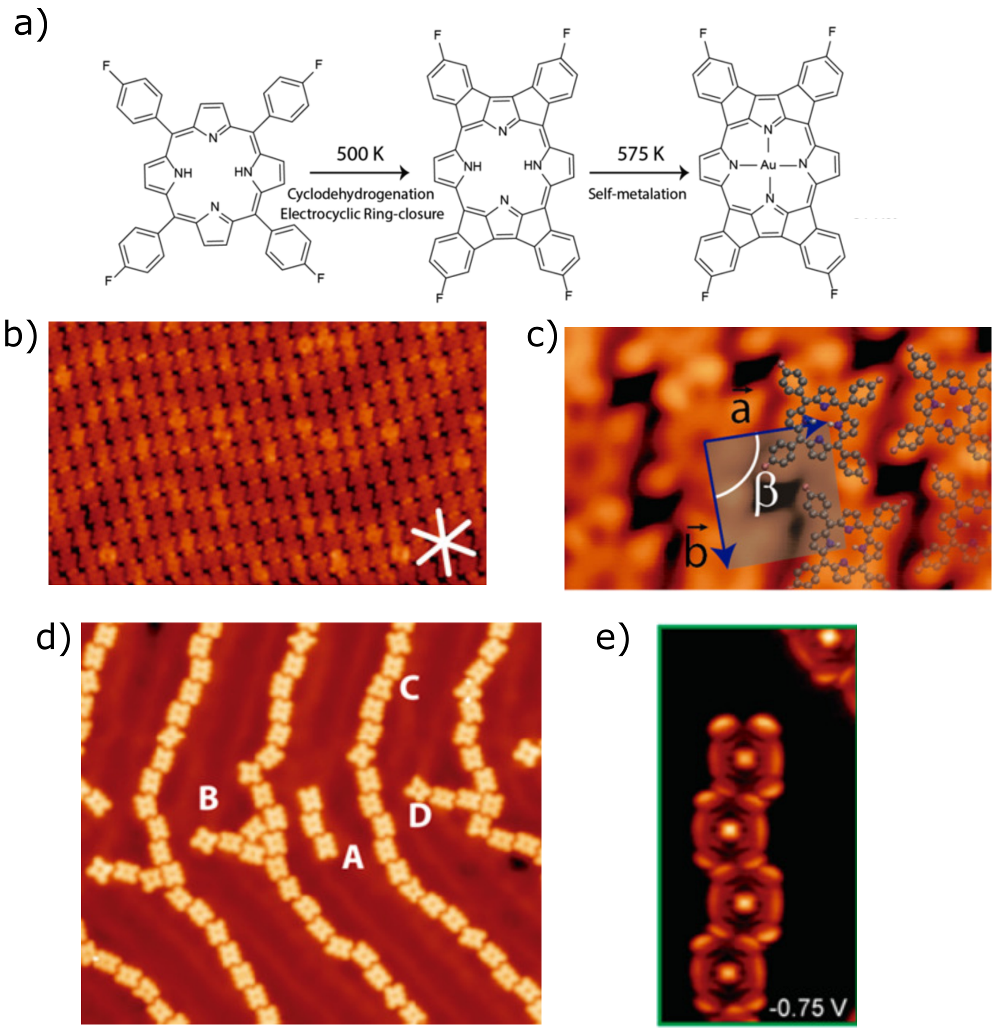

Figure 2.16: (a) Reaction pathway of 2H-4FTPP on Au(111) to self-metalated 4FTPP species. Initially, upon deposition, the close-packed islands are formed (b) and the unit cell of the islands are (c) 1.44±0.05 nm × 1.40±0.05 nm and an angle between the vectors of 92±1°. (d) Annealing to 500 K produces ring-closed 4FTPP. The 4FTPP align into 'chains', likely due to the electronegative fluorine providing a strong dipole interaction. (e) dI/dV mapping of the ring closed 4FTPP shows that the highest occupied molecular orbitals at −0.75 eV are localised at the four fluorine atoms and the porphine cavity. Taken from Cirera *et al.* [49].

to modulate the electronic properties of molecules without structural deformation due to its small atomic radii [49]. Within this experiment, Cirera *et al.* reported that when 2H-4FTPP is deposited onto Au(111) it forms a close-packed structure, see Figure 2.16b-c (similar to 2H-TPP packing on Au(111)), with two vectors of length 1.44±0.05 nm × 1.40±0.05 nm and an angle between the vectors of 92±1°.

Despite the presence of fluorine, the highest occupied molecular orbital (HOMO) and lowest unoccupied molecular orbital (LUMO) states are present at −0.9 eV and 1.6 eV respectively, with the HOMO-LUMO gap reported to be 2.5 eV; similar to the 2.4 eV reported for 2H-TPP on Au(111) [37]. This indicates that the fluorine does not appear to have a strong influence on the electronic states of the molecule [49].

Upon annealing to 500 K, the 2H-4FTPP undergoes the same ring-closing reaction described by Lu *et al.* [38] and Wiengarten *et al.* [46], forming ring-closed planar 2H-4FTPP species as shown in Figure 2.16d. Cirera *et al.* report that the planar 2H-4FTPP species self-assemble due to intermolecular C-H$\cdots$F-C interactions between molecules (see Figure 2.16d). These self-assembled structures appear as porphyrin-based one-dimensional supramolecular wires. The electronic structure of the 2H-4FTPP, as measured by dI/dV spectra, show that the HOMO and LUMO states are now present at −0.75 eV and 0.65 eV respectively. The HOMO-LUMO energy gap is now 1.4 eV, which is 1 eV lower than the non-planarised version of the molecule. Spatial dI/dV maps (see Figure 2.16e) of the planarised molecule show the HOMO state at −0.75 eV is localised at the peripheral fluorine ends of the molecule and the cavity within the porphine ring. The filled state shown in the LUMO shows the reactivity potential of those locations on the molecule. In combination with DFT, species on-surface can be identified using dI/dV spectra.

As shown by Wiengarten *et al.* [46] incomplete planarisation of the molecule from the saddle shape can occur. This is seen as brighter features within the STM topography in constant current mode (see Figure 2.12). This was also explored by Cirera *et al.* [49], and is shown within nc-AFM as a large variation in heights (larger Δf compared to surrounding regions) between fully ring-closed 2H-4FTPP (Figure 2.17a-c right three molecules), half-closed 2H-4FTPP (Figure 2.17a-c left two molecules) and three-quarters ring-closed 2H-4FTPP (Figure 2.17a-c centre molecules).

Further heating of the planarised 2H-4FTPP to 575 K, leads to a similar reaction to that reported by Diller *et al.* [47], whereby one of the Au atoms from the surface is incorporated into the porphyrin core (see Figure 2.18a step at 575 K).

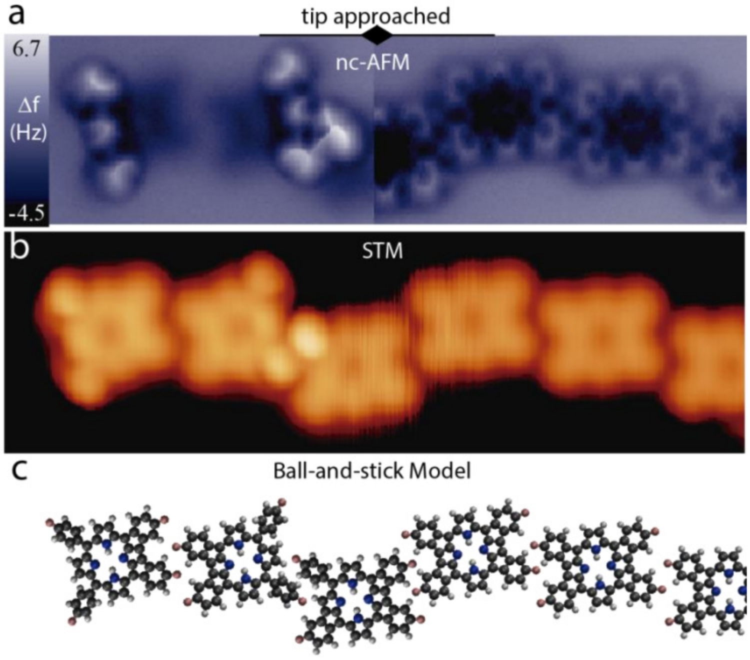

Figure 2.17: Showing 2H-4FTPP after the 500 K anneal to form ring-closed species. The left two molecules are half ring-closed, the middle molecule three quarters ring-closed and the right three molecules are fully ring-closed. (a) Constant height nc-AFM image showing relatively flat ring-closed molecules, with the bright features indicating partial ring-closed 2H-4FTPP. In STM (b) incomplete ring-closing only appears as a slightly brighter feature. (c) Shows the model of the molecules in images a-b. Taken from Cirera *et al.* [49]

STM analysis reveals that non-metalated 2H-4FTPP appears to have an empty cavity in the centre of the molecule (see Figure 2.18a). In comparison, the metalated 4FTPP species has a 'brighter' centre where the Au atom now is covalently bonded to the nitrogen atoms within the porphine ring (see Figure 2.18b). Using nc-AFM, the metalated 4FTPP fits with an expected model, where the four nitrogen atoms are equally interacting with the new metal core. In contrast to the non-metalated 2H-4FTPP, nc-AFM does not show the same interaction between all four nitrogen atoms. In Figure 2.18c-d, the H$\cdots$F interactions are shown in both STM constant current mode and nc-AFM with a CO functionalised tip, interestingly, the metalation of the 4FTPP species does not change the 'chain-like' formations. The electronic structure of the Au-4FTPP, as measured by dI/dV measurements, shows that the HOMO and LUMO states are now present at

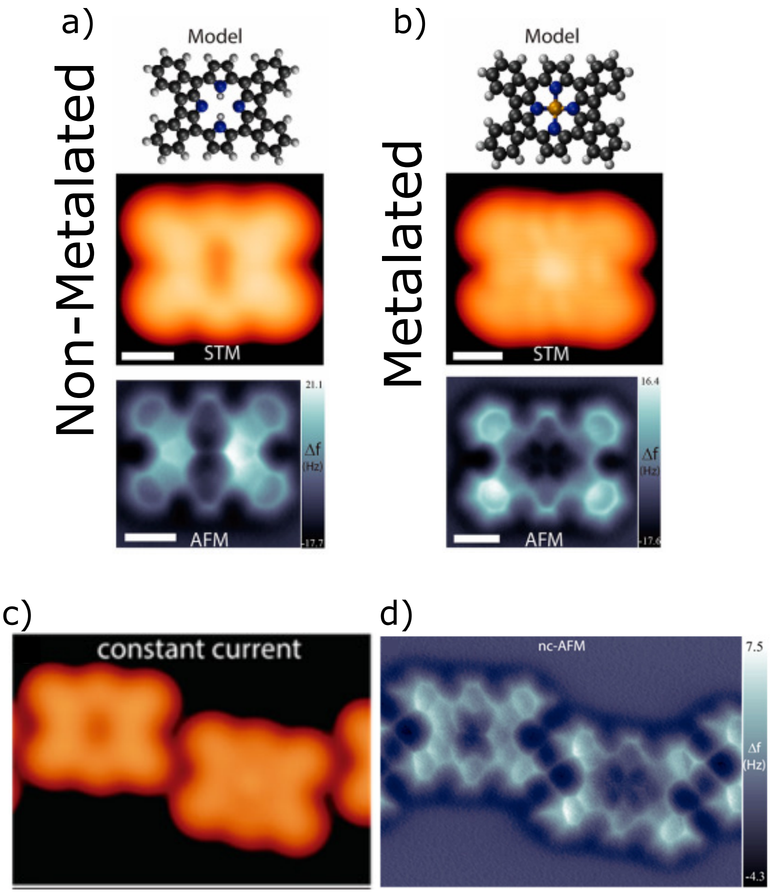

Figure 2.18: A comparison of (a) non metalated 4FTPP and (b) metalated 4FTPP, with the model, STM and nc-AFM images. The STM image shows a bright core of the Au-4FTPP compared to the empty cavity of the 2H-4FTPP. (c) STM image and (d) nc-AFM image show the interaction between the molecules that forms the non-covalent ‘chain’. The lines between molecules (apparent inter-molecular bonds) are likely to be image artefacts and not the result of highly localised electron density above the atoms as is the case with covalent bonding (see great discussion on nc-AFM in [51]). Taken from Cirera *et al.* [49].

−1.2 eV and 0.65 eV respectively giving a HOMO-LUMO gap of 1.85 eV. Figure 2.18c-d also shows that self-metalation of the 2H-4FTPP species does not occur to all molecules, indeed it is reported that after 30 minutes of annealing, ∼20% of the molecules became metalated. The spatial and chemical resolution provided by scanning probe techniques means that they are powerful characterisation tools for single-molecule reactions.

2.2.4 Thermally induced covalent coupling

As an extension to the previous section, work by Cirera *et al.* found that further heating of the planarised and self-metalated Au-4FTPP species (not all species were metalated and some remain as 2H-4FTPP) to 625 K resulted in the activation of the porphyrin's peripheral C-F and C-H bonds [49]. This results in the loss of the fluorine and one of the adjacent hydrogen from each of the fluorine sites from the molecule. These activated molecules then covalently bond with other activated molecules at either the empty fluorine or hydrogen sites. The remaining activated site that is not involved in the covalent bond is hypothesised to be passivated by residual hydrogen [49]. Such a bond is shown between two metalated TPP species in Figure 2.19.

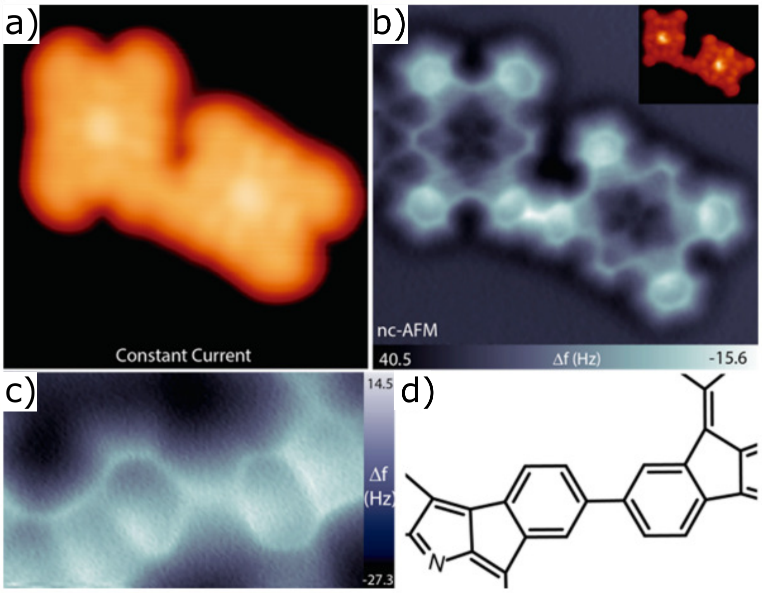

Figure 2.19: Heating 2H-4FTPP to 625 K forms covalently bonded TPP. (a) STM image showing the Au-TPP species as a chain, (b) shows this in bond resolved nc-AFM. A close-up of the bond in nc-AFM is shown in (c), with the skeletal drawing of the bond shown in (d). Taken from Cirera *et al.* [49]

2.2.5 Ullmann-type coupling of TPP

As already discussed, Ullmann-type coupling can be performed on-surface by thermally activating the dissociation of halogen atoms on molecules, such that the molecules form an organometallic intermediate, and then finally covalently bond together. Creating atomic scale molecular electronics [52] by utilising covalent bonds [53] for efficient electron transport [54] is a key goal by using a 'bottom-up' approach to the building of devices.

One of the first Ullmann-type coupling reactions to make extended molecular architectures on-surface was reported by Grill *et al.* Here, Ullmann-type coupling reactions can be performed on Au(111) with brominated TPP [55]. The bromine atoms were present at the *para* position on the phenyl rings attached to the porphine molecule, as shown in Figure 2.20a-c for different quantities of bromine (BrTPP, Br_4TPP and Br_4TPP). Brominated TPP was deposited by thermal sublimation (crucible at 550 K) onto the Au(111). The surfaces were characterised with an STM at 7 K. Upon deposition, the brominated TPP forms close-packed structures on the surface, similar to other TPP on Au(111) [38]. The surface was then annealed and the Ullmann-coupling reaction occurred which is termed method 1. A variety of preparations were made, for the mono-, bi-, and tetra-brominated TPP (BrTPP, Br_2TPP and Br_4TPP). The result of annealing each of the preparations is shown in Figure 2.20. The BrTPP preparation (see Figure 2.20a and d) produced dimers of the TPP molecules (two TPP molecules covalently bonded together). The Br_2TPP preparation allowed for the formation of long chains of covalently bonded TPP molecules (see Figure 2.20b and e). This demonstrates how molecular structure can be used to control reaction products. The Br_4TPP produced a grid of bonded TPP molecules (see Figure 2.20c and f).

Alternatively, the bromine atoms can be dissociated during deposition within the crucible by heating to 610 K (method 2). The exact process of when and how these activated TPP then form chains with this method is not discussed, but likely due to the requirement of needing to form an organometallic intermediate with the surface in the Ullmann coupling reaction, we can therefore assume the reaction likely occurred on the surface. Due to enhanced diffusion, method 1 was found to be more effective in forming chains, likely due to the enhanced diffusion

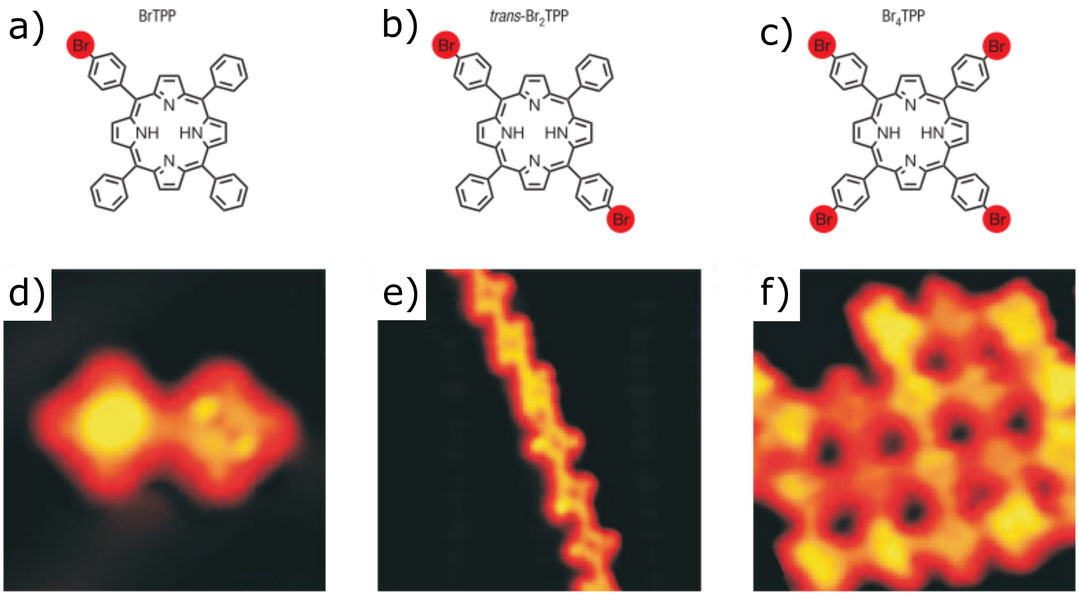

Figure 2.20: (a-c) Chemical structures of the brominated TPP, with 1, 2 and 4 bromine atoms bonded in the *para* position of the phenyl rings. Upon annealing each of these structures, Ullmann-type coupling occurs and (d) dimers, (e) chains and (f) grids of covalently bonded TPP molecules are formed. Taken from Grill *et al.* [55].

upon heating the surface. By altering the starting position of the brominated molecules within the reaction, the chain formation dynamics could be tuned to create longer or shorter chains, showing control of the formed products.

2.3 Phthalocyanines

Phthalocyanines share a similar general structure to that of the porphine and porphyrins (see Figure 2.21). The underlying macrocyclic core of a phthalocyanine is a porphyrazine unit; where porphyrazine differs from a porphine by replacing four of the carbons linking the pyrrole groups with nitrogen atoms. The addition of four benzene groups directly onto the pyrrole groups form the phthalocyanines, which unlike porphyrins, are not found in nature. Since phthalocyanines share the same extended conjugated π-system as porphyrins, they are generally used as dyes or pigments [56]. Other uses of phthalocyanines and their metal complexes include but are not limited to: oxidation catalyst [57, 58], organic light-emitting diodes [58, 59] and photodynamic cancer therapy [60]. Therefore, being able to

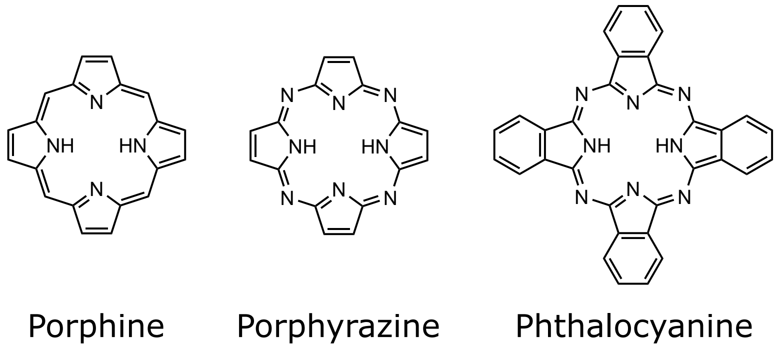

Figure 2.21: Comparison of porphine, with porphyrazine and phthalocyanine.

produce ordered arrays of such materials (on 2D surfaces) is relevant to future device design and manufacture.

On surfaces, phthalocyanines generally form close-packed structures in a similar way to porphyrins. These self-assembled structures are driven by weak interactions such as van der Waals and hydrogen bonding [33]. Furthermore, phthalocyanines (Pc) show similar *general* on-surface properties and/or chemistry as porphyrins, for example, self-metalation of Pcs, tilting upon the growth of multilayers, but also gas adsorption etc (see Gottfried for review [33]).

A key driver behind the research carried out in this thesis into phthalocyanines, was how iron phthalocyanine (FePc) can interact with and adsorb gases whilst supported on surfaces. The demonstration of the surface *trans*-effect with gases was a direct analogue to the chemistry solution-phase *trans*-effect [61]. In the traditional *trans*-effect, there is a “competition for the metal centre” as ligands coordinately bonded to the metal centre bond more or less strongly depending on the strength of the other ligands in the *trans* position, effectively changing the bonding length. The strength of the coordinate bond, and therefore the ligand’s *trans*-effect ability, is determined by it being either a strong σ-donor or π-acceptor [61]. The first direct evidence for the surface *trans*-effect was shown in the study by Deimel *et al.* [61]. FePc was deposited onto Ag(111), where it forms incommensurate close-packed structures. The sample was held at 60 K, whilst leaking either ammonia or water into the chamber, providing a Langmuir dose to the surface (pressure increases due to gas in the chamber and the sample is exposed to this for a period of time). Using normal incidence X-ray standing

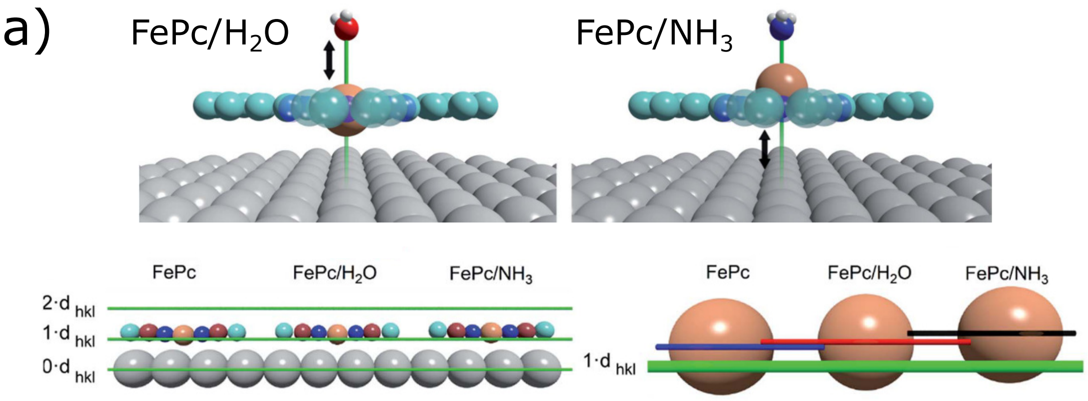

Figure 2.22: Top: Adsorption model of FePc with the surface, with either water or ammonia on top of the molecule in the *trans*-position to the surface. Bottom: How the adsorption height of the FePc changed depending upon the Fe with respect to the atomic planes of the surface lattice. Taken from Deimel *et al.* [61].

wave (NIXSW - see Section 3.2.4), it was determined that the height of the FePc depended on the adsorbed gaseous species (atop the FePc model in Figure 2.22). It was found that the addition of ammonia or water, increased the FePc-surface bond length compared to no adsorbed gas. The displacement of the Fe core was found to be 0.019±0.007 nm higher for ammonia and 0.017±0.004 nm higher for water. NIXSW is a powerful technique for determining specific atomic positions relative to the surface, which would provide insight into the reaction pathways that occur on the surface.

In contrast, the system of FePc on Ag(110) provides a different interaction with gas. In the experiment reported by Sedona *et al.*, iron phthalocyanine is deposited on to Ag(110), and depending upon the density, forms three self-assembled structures. These structures are shown in Figure 2.23a-c, in increasing density from R1, R2 and to OB1. The 'R' structures have a rectangular unit cell symmetry, compared to the oblique structure in OB1. The density of structures is reported to change the available reactivity of the FePc with O_2. Prior to gas dosing, the recognisable '+' shape of the phthalocyanine with the bright Fe core is visible in STM (at room temperature - see Figure 2.23d). Upon O_2 dosing either the R1 or R2 phase, the bright Fe core becomes dimmed (see Figure 2.23e). At this point, the oxygen is directly interacting with Fe core and DFT analysis suggests that the oxygen is adsorbed between the FePc and Ag surface (see Figure

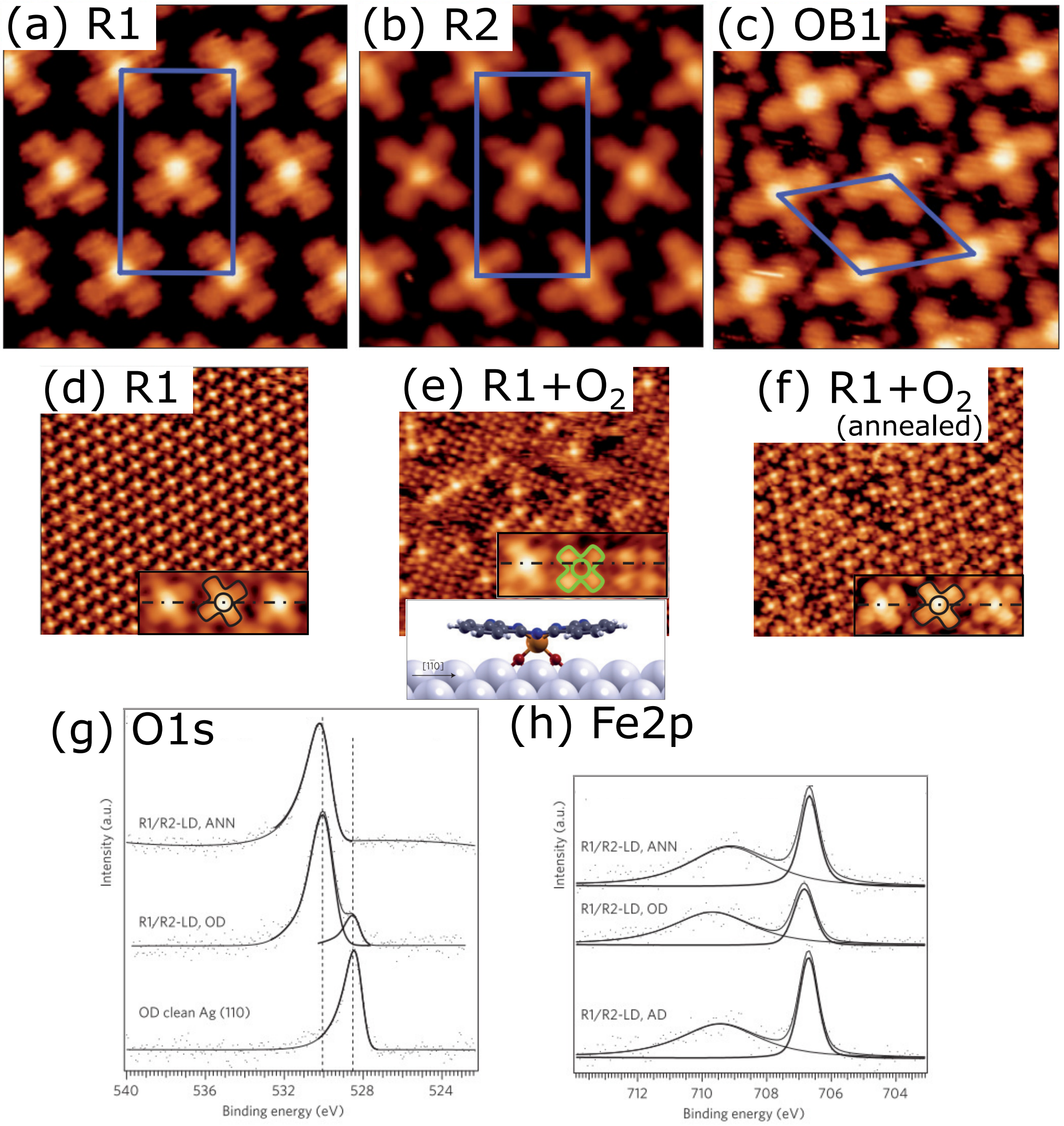

Figure 2.23: (a-c) Shows the three close-packed structures that assemble on the surface, increasing in surface density for (a) R1, (b) R2 and (c) OB1. (d) Shows an R1 surface prior to O_2. Inset shows the characteristic '+' of the phthalocyanine, with the bright Fe core. (e) Shows the R1 surface once exposed to 1500 L of gas, the bright Fe core is now dimmed (see inset). The DFT model for reported position of the oxygen between the FePc and Ag(110) surface. (f) The bright Fe core is returned when the surface is heated to 370 K. Inset shows the return of the bright core. (g) O 1*s* XP spectra for oxygen dosing (OD) on clean Ag(110), OD on the R1/R2 phase and the subsequent anneal of the oxygen dosed R1/R2 phase. (h) Similarly shows the Fe 2*p* spectra for OD on clean Ag(110), OD on the R1/R2 phase and the subsequent anneal of the oxygen dosed R1/R2 phase. Taken from Sedona *et al.* [62].

2.23e DFT inset). Heating of the surface to 370 K then returns the Fe core back to a bright feature in STM, implying that the oxygen is no longer interacting with the Fe core (see Figure 2.23f). The interaction with the iron core can be seen in the O 1*s* XP spectra shown in Figure 2.23g. The O 1*s* spectra of O_2 on clean Ag(110) shows a peak at 528.4 eV (attributable to molecular oxygen), on a R1/R2 FePc overlayer, the same dosing shows O 1*s* peaks at 285.5 eV and 530.1 eV. Upon heating the surface, the higher binding energy (BE) component is the only feature left at 530.2 eV. In the Fe 2*p* peaks (Figures 2.23h), there is little difference between the position of the peak at each of the described stages of the reaction, however, the intensity of the Fe 2*p* peak was reduced in the oxygen-dosed stage.

2.4 Overview of the literature

In summary, numerous factors affect a molecule's ability to interact with the surface, with other molecules, or with gases. A thorough understanding of the interactions presented in this chapter would enable one to design and build molecular structures on surfaces, and produce a functionalised surface that positively interacts with the environment. In the remainder of this thesis, I will build upon the current literature and present original research exploring the interaction of tetraphenylporphyrin and iron phthalocyanine in a variety of settings. Using numerous surface-sensitive characterisation techniques, as introduced in this chapter, we can make chemically sensitive and structural inferences about the molecules following surface treatments. The self-assembly of TPP within specific topography sites on Au(111) is explored using Arrhenius analysis in Chapter 4. We build on this fundamental interaction by investigating, in Chapter 6, the reaction of TPP when heated causing ring-closing reactions to occur within the molecule resulting in a change of self-assembly characteristics. Further heating causes self-metalation of the molecule. The TPP is functionalised with bromine atoms in Chapter 5, which causes changes to the molecular states of the molecule. The reaction of brominated TPP in an Ullmann-type coupling reaction causes long chains of TPP to be formed. Finally, in Chapter 7 we explore the interaction of FePc with near-ambient pressure gases.

Chapter 3

Experimental techniques, methods and materials

3.1 Scanning tunnelling microscopy

In 1981, the first successful vacuum tunnelling experiment was reported by G. Binnig and H. Rohrer *et al.* [63] and this has resulted in a plethora of surface characterisation methods at the atomic scale [64]. In their work they proposed ways of dealing with vibrational noise by mechanically decoupling the probe and sample from the environment, allowing stable tunnelling to occur. Theoretical work by Tersoff, Hamann and Baratoff provided a basis to understand the tunnelling effects observed in the experiment [65, 66]. Further developments allowed the surface to be scanned spatially by a probe and that enabled topographic features of the surface to be viewed. Such topographic features can be intrinsic features of a surface (e.g the silicon surface reconstruction, Au(111) herringbone etc.), or as a result of sample treatments (molecule deposition, passivisation, sputtering etc.).

The underlying principle of vacuum tunnelling can be described as a flow of electrons (due to quantum tunnelling) to the tip from the surface (or vice versa) when they are brought sufficiently close together. The applied bias between the two conductors (or indeed semiconductors), can determine the availability of filled (or unfilled) electronic states for tunnelling which in turn determines the current flow. In the most commonly used feedback mode (constant current), the tip height is controlled using feedback mechanisms to keep the current constant whilst the tip is scanned across a grid of spatially distributed points on the surface [67]. The grid, in combination with the recorded tip height required to keep the current constant at each point, allows a topographic image of the surface to be recorded. Importantly, STM is primarily a measure of the local density of electronic states (LDOS) present at the surface-tip junction, which varies between materials and molecules and is dependent upon the applied bias, hence the topography cannot be seen as a simple ‘height map’ of the surface and great care should be taken when interpreting STM ‘images’.

3.1.1 Quantum mechanical tunnelling

For current to flow between the tip and surface, through a vacuum barrier, electrons must overcome an energy barrier. The energy barrier is given by the work function within each region. In classical physics, the electron would not have sufficient energy to get to the other side of the barrier (by having sufficient energy to go ‘over’ the barrier), however, the electron can tunnel through the barrier by mechanisms described in quantum mechanical tunnelling. To model this tip → vacuum-gap → sample energy landscape, a one-dimensional rectangular potential barrier is used (see Figure 3.1), which is valid when the work function of the tip

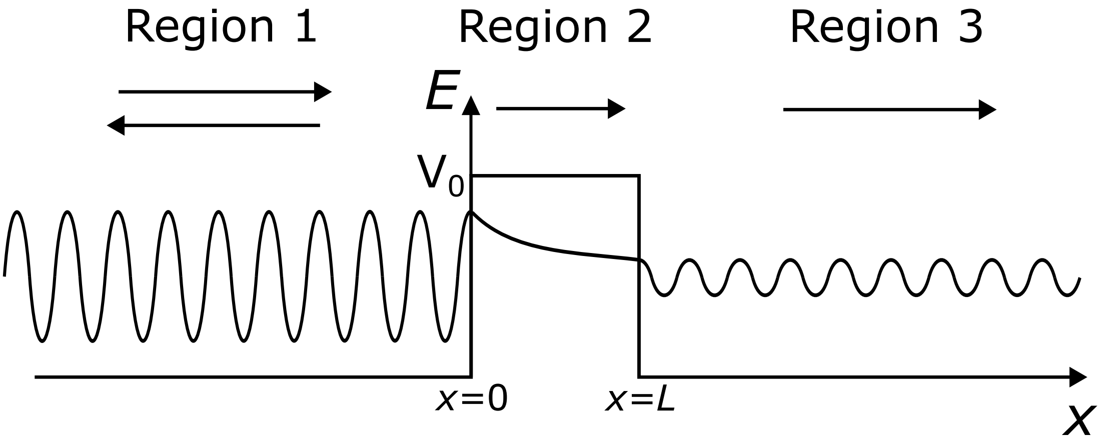

Figure 3.1: The one-dimensional barrier (of length L and height V_0) that represents the vacuum barrier between tip/sample. In region 1, some of the incoming electron wavefunction reflects from the barrier, however, some of the wave is transmitted into region 2 where it tunnels through and exponentially decays. Finally, the transmitted wave in region 3 shows that some of the wavefunction has passed through the barrier.

and sample are the same.

As a consequence of the wave nature of matter, the electron (of mass m and energy E) can be described as a wavefunction Ψ within each of the three regions (see Figure 3.1). At each boundary, the wavefunction may be reflected back [68], and so for each region the wavefunctions are described by:

$$\Psi_1 = A_0 e^{ikx} + Ae^{-ikx} \tag{3.1}$$

$$\Psi_2 = Be^{\alpha x} + Ce^{-\alpha x} \tag{3.2}$$

$$\Psi_3 = De^{ikx} \tag{3.3}$$

where $k = \frac{\sqrt{2mE}}{\hbar}$ and $\alpha = \frac{\sqrt{2m(V_0 - E)}}{\hbar}$. At each boundary ($x$=0 and $x = L$) the values of Ψ and $d\Psi/dx$ for the wavefunction should match. This leads to the two pairs of equations:

$$\left.\begin{aligned} A_0 + A &= B + C \\ ikA_0 - ikA &= -\alpha B + \alpha C \end{aligned}\right\} \text{Condition: } x = 0 \tag{3.4}$$

$$\left.\begin{aligned} De^{ikL} &= Be^{-\alpha L} + Ce^{\alpha L} \\ ikDe^{ikL} &= -\alpha Be^{-\alpha L} + \alpha Ce^{\alpha L} \end{aligned}\right\} \text{Condition: } x = L \tag{3.5}$$

By rearranging the equations at the $x = L$ condition and subsequent substitution of terms into each other, the equations become,

$$4ik\alpha A_0 = \left[(\alpha + ik)^2 e^{-\alpha L} - (\alpha - ik)^2 e^{\alpha L}\right] De^{ikL}. \tag{3.6}$$

To further simplify this, an approximation of a thick barrier where L is large enough such that $\alpha L >> 1$. This makes the first term in the square brackets very small compared to the second term. This leads to the equation,

$$\frac{D}{A_0} = -\frac{4ik\alpha e^{-(\alpha + ik)L}}{(\alpha - ik)^2} \qquad \text{(when } \alpha L >> 1\text{)}. \tag{3.7}$$

It is then possible to calculate the transmission probability T of the electron tunnelling through the barrier:

$$T = \left|\frac{D}{A_0}\right|^2 \approx 16\left(\frac{E}{V_0}\right)\left(1 - \frac{E}{V_0}\right) e^{-2\alpha L}. \tag{3.8}$$

As the tunnelling probability and the tunnel current are intrinsically linked, the current is therefore proportional to the length of the barrier by $I \propto e^{-L}$. This has the effect that changes to the barrier width exponentially change the measured current. The exponential dependence on barrier width provides clear changes in detected current, allowing for picometer scale vertical resolution [69]. Furthermore, this formulation also includes the dependence of the bias within the variable α.

3.1.2 Tersoff-Hamann theory

Albeit effective in one dimension, the wavefunction model of tunnelling as described above between the tip and surface in an STM is too simplistic. A general theory of tunnelling between two metal plates was developed by Bardeen [70] in 1961, many years before the first STM was produced. Bardeen's theory was further developed by Tersoff and Hamann [65]. Here, the tunnelling was assumed to occur between an atomically sharp tip and a metal plate. The tunnelling current for this system has been shown to be given by,

$$I = \frac{2\pi e}{\hbar} \sum_{\mu,\nu} f(E_\mu)\,[1 - f(E_\nu + eV)]\,|M_{\mu\nu}|^2 \delta(E_\mu - E_\nu), \tag{3.9}$$

where $f(E)$ is the Fermi function, V is the applied voltage, $|M_{\mu\nu}|$ is the tunnelling matrix element for transitions between the state in the tip ψ_μ and the surface state ψ_ν, and E_μ is the energy of an electron in the tip state ψ_μ in the absence of the surface.

Equation 3.9 may be explained by three distinct parts. The first part, $f(E_\mu)\,[1 - f(E_\nu + eV)]$, ensures that tunnelling only occurs from filled to empty states. It is formalised by the probability of an electron occupying a filled tip state ψ_μ, and the probability of an empty surface state ψ_ν of the same energy being in existence for the tunnelling of an electron to occur. This treatment is only valid for positive voltages as negative voltages have an alternative equation that considers empty states in the tip and filled states in the surface. The tunnelling matrix $M_{\mu\nu}$ represents the surface integral of the wavefunctions and their gradients, relevant for the tunnelling event, within the tip and surface. This matrix encodes the exponential dependence of current with the tip/surface separation, furthermore, it also includes the dependence from the effect of bias on the electron tunnel probability. Finally, $\delta(E_\mu - E_\nu)$, ensures that in the case of elastic tunnelling ($E_\mu = E_\nu$) energy is conserved, such that $I = 0$ if $E_\mu \neq E_\nu$. When applying the conditions of a small bias and the limit of low temperatures, Equation 3.9 may be further simplified to,

$$I = \frac{2\pi e^2 V}{\hbar} \sum_{\mu,\nu} |M_{\mu\nu}|^2 \delta(E_\mu - E_\mathrm{F}) \delta(E_\nu - E_\mathrm{F}), \tag{3.10}$$

where E_F is defined as the Fermi energy. Further simplification of the equation can be done when the tip is replaced by a point probe at $\mathbf{r}_0$ with a radius of R. This assumes a spherical point tip where the tip wave function can be approximated as an s-wave. The tunnel current then becomes,

$$I \propto \sum_{\nu} |\psi_\nu(\mathbf{r}_0)|^2 \delta(E_\nu - E_\mathrm{F}), \tag{3.11}$$

where $|\psi_\nu(\mathbf{r}_0)|^2$ is the probability density of the surface state wavefunction when evaluated at the probe $\mathbf{r}_0$ position. Therefore, the tunnel current is proportional to the LDOS of the surface at $\mathbf{r}_0$,

$$I \propto \rho(\mathbf{r}_0, E_\mathrm{F}). \tag{3.12}$$

The tip so far has been approximated as a point spherical s-wave probe. There are some general problems with this approach, as it limits the lateral resolution (due to the radius R of the spherical potential well) to around 0.6-0.9 nm, which is too large for the atomic resolution that is seen within STM images (~0.2-0.3 nm). Such problems may be resolved by considering that other tip states (such as p or d orbitals) may provide this resolution if they are involved in tunnelling [71]. The requirement of p or d orbitals within the tip for better lateral resolution provides a key requirement of the material of the tip, for example, metals that have d orbitals accessible for tunnelling (such as PtIr or W tips). Semiconductors (such as Si) can also act as tips with good lateral resolution due to p orbitals.

In Figure 3.2, an energy level diagram of the tip is shown. The density of states of the tip is often treated as constant across all of the energy levels. In practice, however, this is not always true and tip states should be considered when viewing STM images and dI/dV spectra, as observed features may be the result of tip states and not a true representation of the surface states. The value of ϕ_t indicates the workfunction of the tip (i.e the energy required to remove

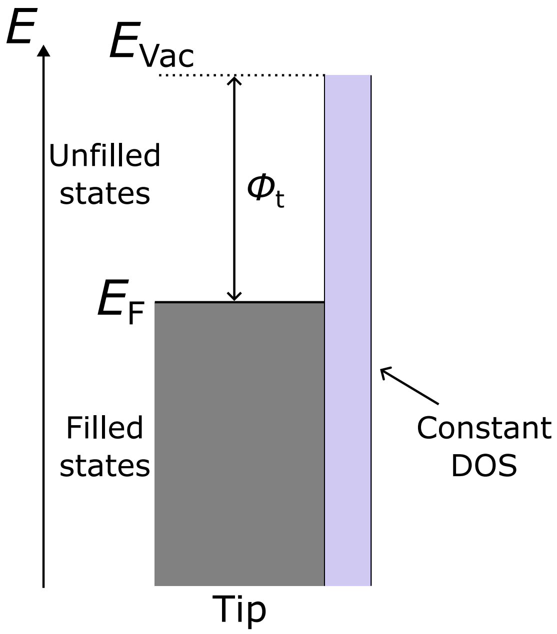

Figure 3.2: Energy level diagram of the tip. The LDOS of the tip is assumed to be constant, however in practice, this is not true and will alter the number of states available for tunnelling. The states below the Fermi level are filled and those above the Fermi level are empty.

one electron from the tip at the Fermi level E_{F} to the E_{Vac} level where it would have no kinetic energy). The Fermi level E_{F} of the tip is the point at which the probability of finding the state occupied with an electron is 50%.

A similar energy level diagram can be set up for the interaction between the tip and surface (see Figure 3.3). The energy level diagram of the surface shows a smaller work function ϕ_s than the tip (although this depends on the material that constitutes the surface), and varying DOS values. Initially, the Fermi levels are aligned (zero applied bias - see Figure 3.3a); the Fermi levels of the tip and surface are in equilibrium. No tunnelling occurs as there is no energetic overlap between filled states and empty states of the tip and the surface. Bias in an STM is applied, by convention, to the sample (this is done to reduce cross-talk with other measurements at the tip side, such as qPlus signals, although early STM setups biased the tip). A negative applied bias to the sample (in Figure 3.3b) moves all of the surface energy levels up. The position of the Fermi level within the sample stays constant with respect to the LDOS and the work function of the sample, but shifts with respect to the Fermi level of the tip. There are now

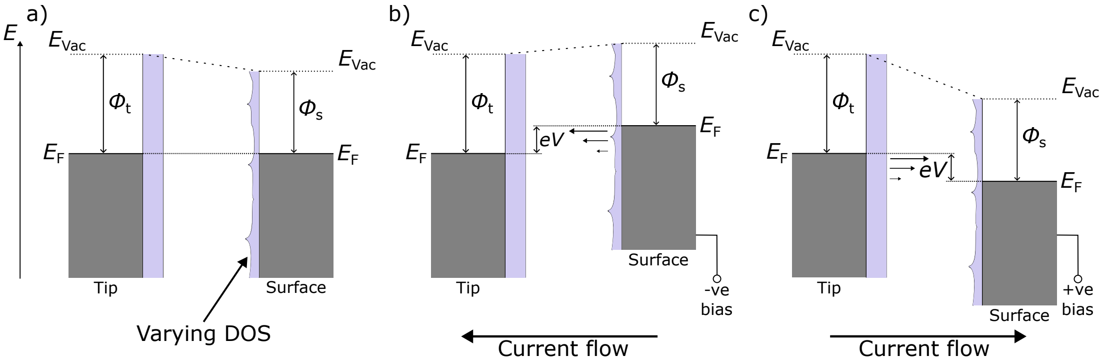

Figure 3.3: Energy level diagrams show the interaction between the tip and the surface for three situations. The surface is shown with a varying LDOS. (a) No applied bias between the tip and surface. Fermi levels match and there is no overlap between empty and filled states, resulting in no current flow. (b) A negative applied bias to the sample moves all of the energy levels within the sample up, resulting in filled states from the surface tunnelling into the empty states of the tip. (c) Positive applied bias to the sample moves all of the energy levels within the sample down, resulting in filled states from the tip tunnelling into the empty states of the surface.

energetically overlapping states between the tip and surface where filled states from within the sample are able to tunnel through the barrier (vacuum) into the empty tip states at the same energy. Since the energy of the tunnelling electrons is conserved, this is elastic tunnelling. A higher proportion of tunnelling will occur at energy levels close to the Fermi level (at the highest energy) since these have the longest decay lengths in vacuum. As the tip LDOS is assumed to be constant, this provides information on the filled states within the sample. As the negative bias is increased (more negative) there are more filled states in the sample that overlap with empty states in the tip, and therefore, will provide more current flow. Conversely, in Figure 3.3c, when a positive bias is applied to the sample, this has the effect of lowering the sample's energy states with respect to the tip. Now, the Fermi level of the sample is below the Fermi level of the tip so the electrons occupying the filled states of the tip will now tunnel into the empty states of the sample. This provides information on the empty states within the sample.

The addition of molecular species within the tip-sample junction provides additional complexity to the LDOS observed. For adsorbed molecules close to the surface, coupling between surface and molecular electronic states could be expected. The interaction will differ depending on the surface and adsorbed molecular species. Molecules have discrete energy states around the Fermi level. The highest occupied molecular orbital (HOMO) and lowest unoccupied molecular orbital (LUMO) states are present on either side of the Fermi level. The HOMO/LUMO states can be viewed as pinned relative to the Fermi level of the surface. These molecular states (see Figure 3.4) can be seen within the STM in a similar way as surface states were able to be explored in Figure 3.3. Shown in Figure 3.4 are the HOMO and LUMO states for an adsorbed molecular species on a surface. In (a), a negative surface bias allows for the HOMO state within the molecule to tunnel into the empty states within the tip. In (b), a positive surface bias allows for the LUMO state within the molecule to tunnel into the filled states within the tip. There are additional filled states at lower energies than the HOMO state and these are denoted as HOMO−1, HOMO−2 etc. Furthermore, empty states above the LUMO state are denoted as LUMO+1, LUMO+2 etc.

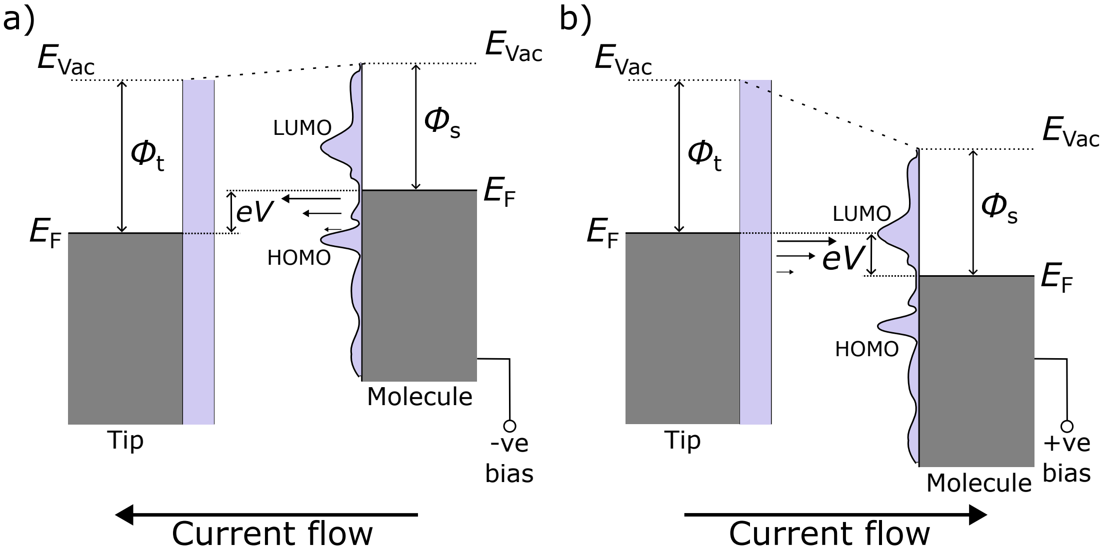

Figure 3.4: Energy level diagrams show the interaction between the tip and a molecule. (a) A negative applied bias to the sample shifts all of the states within the sample up, which results in filled states from the HOMO of the molecule tunnelling into the empty states of the tip. (b) A positive applied bias to the sample shifts all of the states within the sample down, which results in filled states from the tip tunnelling into the empty states of the LUMO in the molecule.

3.1.3 dI/dV spectroscopy

dI/dV spectroscopy is used to understand the local density of states of the sample as a function of their energy. As shown in Figure 3.3, when the bias is increased, the Fermi levels between the tip and surface separate by eV, providing more states for tunnelling to occur. This causes more current flow between the tip and the surface. This can be seen by taking the differential from equation 3.11 to give,

$$\frac{dI(V)}{dV} \propto \rho_s(E_{\mathrm{F}}{-}eV), \tag{3.13}$$

where ρ_s is the density of states of the surface.

The current can be measured whilst varying the bias applied to obtain an $I(V)$ data set. The greater the rate of change of the current, the more tunnelling states are available at that bias value. Conversely, a lower rate of change of the current indicates fewer tunnelling states are available at that bias value. To perform this measurement in the context of STM, the tip is initially held above the surface at a relatively high current (to increase signal/noise ratio and provide sufficient tunnelling to detect states at close to zero bias, currents $>$ 100 pA are typically used) with a suitable bias value. Once the piezoelectric creep/drift has been minimised, Z feedback is turned off and the bias is swept between two values in small bias steps to produce an $I(V)$ graph. Taking the numerical gradient of $I(V)$ data set will yield a quantity that describes the increase (or decrease) in the LDOS present in the surface/tip over a bias range. This approach produces noisy results due to the sensitivity of noise within the current signal.

To reduce the noise in the dI/dV signal, a lock-in amplifier may be used. The dI/dV signal at each bias value will be directly available from the lock-in as the bias is swept over a selection of values. A reference sine wave is added to each bias value, which has the effect of returning an oscillating current (see Figure 3.5). The magnitude of the oscillating current is proportional to the change of the current over the range of the reference sine wave that is added to the bias (compare Figure 3.5a-b).

In a similar way to the numerical differentiation of the $I(V)$ data, at each bias value within the bias sweep the lock-in would produce a dI/dV value. To extract

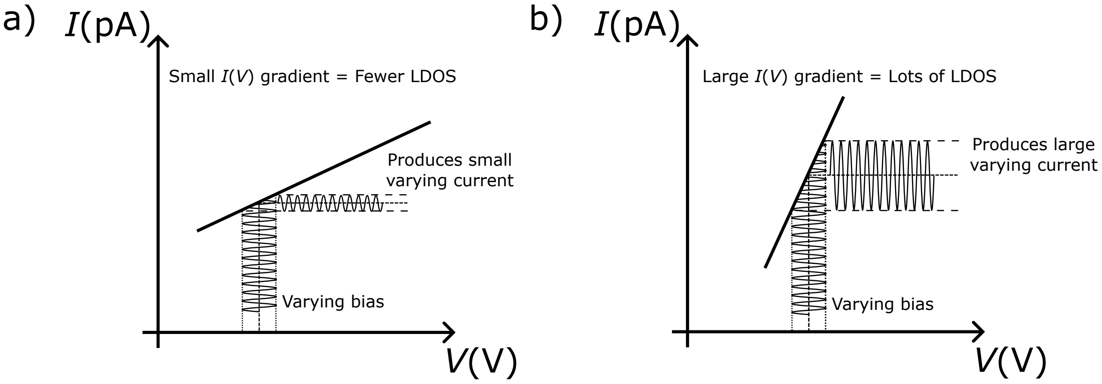

Figure 3.5: The effect of applying an oscillation to an applied bias to the output current detected. (a) The oscillating bias on a small $I(V)$ gradient, only produces a small oscillation within the current. (b) The oscillating bias on a large $I(V)$ gradient, produces a large oscillation within the current. This shows that the amplitude of the oscillation detected within the current at each bias step is directly related to the LDOS of the surface/tip.

this dI/dV value, the lock-in achieves this from the current channel by amplifying the current from pA-nA to a voltage V_I between −10 V to 10 V (dependent upon gain setting). The lock-in amplifier will multiply the V_I signal by a reference oscillation V_{ref}, with a maximum amplitude of $V_{\mathrm{ref_m}}$. This multiplication of the two signals forms a 'heterodyne' given by,

$$V_{\mathrm{hdyne}} = V_I \cdot V_{\mathrm{ref}}. \tag{3.14}$$

Each of the oscillating signals (V_I and V_{ref}) can be written as sine waves with a frequency of ω and a phase shift of θ. This gives,

$$V_{\mathrm{hdyne}} = V_{I_{\mathrm{m}}} V_{\mathrm{ref_m}} \sin(\omega_I t + \theta_I) \sin(\omega_{\mathrm{ref}} t + \theta_{\mathrm{ref}}), \tag{3.15}$$

where t describes the time. Using trigonometric identities, the equation can be expanded to,

$$V_{\mathrm{hdyne}} = \frac{1}{2} V_{I_{\mathrm{m}}} V_{\mathrm{ref_m}} \Big(\cos([\omega_I - \omega_{\mathrm{ref}}]t + \theta_I - \theta_{\mathrm{ref}}) - \cos([\omega_I + \omega_{\mathrm{ref}}]t + \theta_I + \theta_{\mathrm{ref}}) \Big). \tag{3.16}$$

This equation can be simplified by considering the case when the frequency of the reference and current signal are equal ($\omega_I = \omega_{\mathrm{ref}}$). The heterodyne equation then becomes,

$$V_{\mathrm{hdyne}} = \frac{1}{2} V_{I_{\mathrm{m}}} V_{\mathrm{ref_m}} \Big(\cos(\theta_I - \theta_{\mathrm{ref}}) - \cos([\omega_I + \omega_{\mathrm{ref}}]t + \theta_I + \theta_{\mathrm{ref}}) \Big). \tag{3.17}$$

Two cosine terms remain in this equation. The first cosine no longer provides an oscillation to the voltage as it does not depend upon time, but rather the phase difference between the current oscillation and the reference oscillation. If this phase difference equals 0 ($\theta_I = \theta_{\text{ref}}$), the first cosine term equals 1. The second cosine term provides an oscillation, but at twice the frequency of the initial oscillation. The lock-in amplifier will remove this oscillation using a low-pass filter, therefore removing the second cosine term from the above equation. The equation then becomes,

$$V_{\text{hdyne}} = \frac{1}{2} V_{I_{\text{m}}} V_{\text{ref}_{\text{m}}}. \tag{3.18}$$

This shows a clear dependence of the output of the lock-in amplifier (V_{hdyne}) on the maximum amplitude of the current oscillation $V_{I_{\text{m}}}$ (since the reference maximum amplitude stays constant). Any additional signal not in phase with the lock-in amplifier's reference signal will not appear in the data (for example capacitive coupling within the STM).

3.1.3.1 Energy resolution of states due to Fermi level

The energy of the Fermi level within either the tip or surface does not describe a sharp transition from filled to unfilled states at higher temperatures. Thermal energy, due to the temperature of the system, excites electrons from filled states to unfilled states. This leaves some normally filled states unoccupied until electrons from higher energy states relax to lower energies. The Fermi-Dirac distribution shown in Figure 3.6 describes the occupation probability of the states around the Fermi level for various temperatures. In this Figure, the Fermi level is set to 0.5 eV. As the temperature decreases, the probability function tends to a step function. Sharper dI/dV spectra can therefore be obtained whilst using lower temperatures due to a better-defined, filled-to-unfilled states transition around the Fermi level.

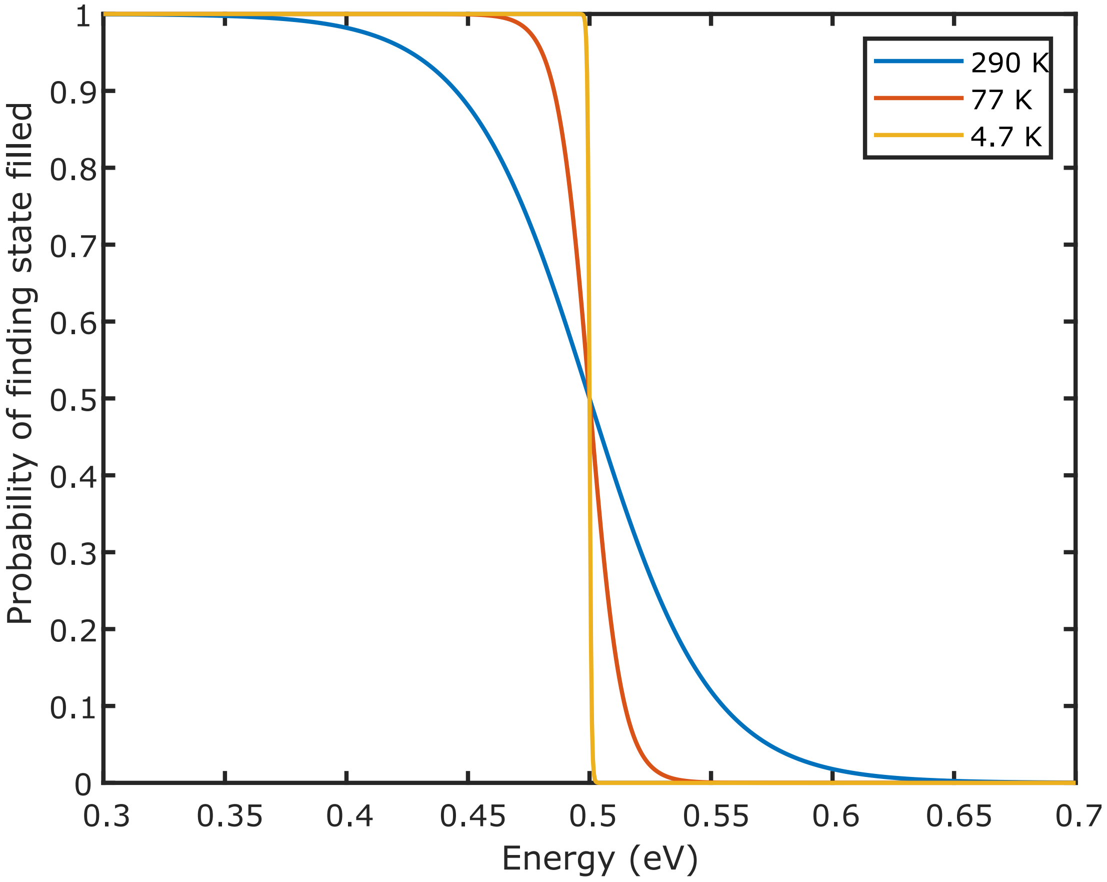

Figure 3.6: The Fermi-Dirac distribution for three temperatures: 290 K, 77 K and 4.7 K (the three temperatures easily accessible by low temperature (LT)-STM - ambient, liquid nitrogen and liquid helium). The probability of finding a state filled with an electron at energy E, above and below the Fermi level E_{F}. This shows that states will be more well-defined within dI/dV measurements when using lower temperatures.

3.1.4 STM feedback modes

As the current is exponentially dependent upon the gap between the tip and surface, the electronic topography of the surface can be determined accurately. Within the STM, the axis directions parallel to the surface are defined as X and Y, with the perpendicular axis out of the surface as Z. The Z position of the tip will depend upon the mode of scanning. In constant height mode (see Figure 3.7), the Z height of the tip will remain constant and the tunnel current will vary as the surface topography varies. In each tip position, the current value will be recorded. In constant current mode, a target current value is set and a feedback loop is used to move the tip in Z to maintain the set current value. At each

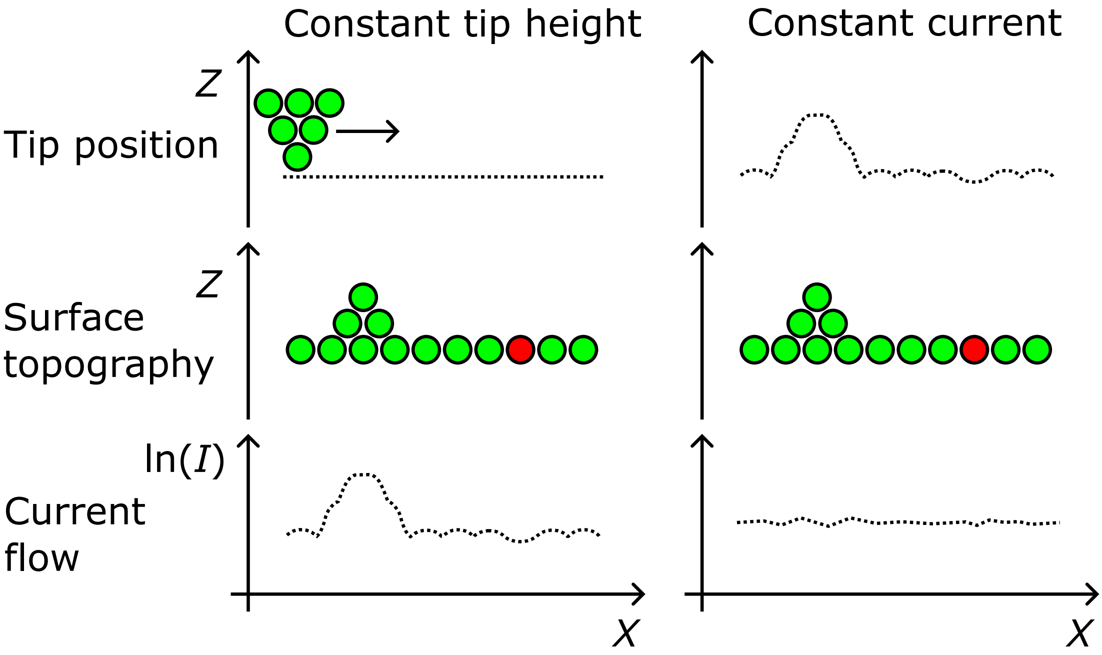

Figure 3.7: In constant tip height mode, the tip is kept at a constant Z as it is raster scanned across the surface. The changes in surface height are reflected in the current detected. Where the LDOS are reduced (in the case of the red atom - representing a hetero atom), current flow is reduced. In constant current mode, as the tip is raster scanned across the surface, the Z height of the tip is altered to keep the current constant. Where the LDOS are reduced (see red atom), the tip moves closer to the surface to keep the current constant.

position in X and Y, the Z height is recorded. An image of the surface could be produced by moving the tip in a discrete grid of positions (acting as pixels in an image) taking either the Z height or current for each pixel and therefore, forming an image of the surface. The tip is raster scanned over the surface to each of those pixel positions.

Constant height mode is a superior imaging mode in so far that the topography recorded is not subject to artefacts induced by the feedback loop. However, due to the lack of feedback, it is possible to crash into surface features. Thermal drift or piezoelectric creep changes may also occur over time and change the true Z height of the tip with respect to the surface. For this reason, the majority of STM images are acquired using constant current mode. Thermal drift and piezoelectric creep can be reduced by cooling the STM and sample with cryogens (typically LN_2 or LHe).

Even though the tunnel current (and therefore the apparent Z height of the surface) depends upon the gap between the tip and surface, the LDOS also plays a role in the tunnel current. Since the LDOS varies between parts of the surface (and also within the same molecule), the topography of the surface features viewed by either constant current or height mode cannot be truly defined as the topographical surface structure. This is shown within Figure 3.7, where the tip appears to follow the surface features, however, upon reaching the red atom the current reduces (in constant height mode) or the tip height goes closer to the surface (in constant current mode). This is due to the red atom having a reduced LDOS compared to the other atoms, such that for the same bias, the tip needs to be closer to the red atom to have the same tunnel current, therefore, appearing as a depression in the surface. Furthermore, as the tip is scanned over the surface protrusion, tunnelling will start to occur between the side of the tip and the side of the protrusion which reduces the resolution possible on vertical steps of on-surface features. Peak STM performance is therefore achieved on flat topographies, and the impact of studying 'non-planar' systems should be carefully considered.

3.1.5 STM movement

A fundamental part of the STM operation is to bring the tip and surface into close proximity such that when a bias is applied between them, a current will flow. The STM must also be able to control the Z height (separation between the tip and surface) as well as the X and Y directions of the tip scan plane in fine enough granularity to increase or decrease current flow and to resolve atomic-scale features often with picometer precision. This puts stringent conditions on the types of apparatus available for use within STM constructions. Typically, piezoelectric material supports the tip. When a voltage is applied to the piezo crystal, the lattice expands or contracts. The lattice displacement is proportional to the bias applied. The displacement can be made sufficiently small for STM applications.

To get the tip close enough to the surface for a current to flow, the tip (or surface) may need to travel distances of the order 1-10 mm. To achieve this with

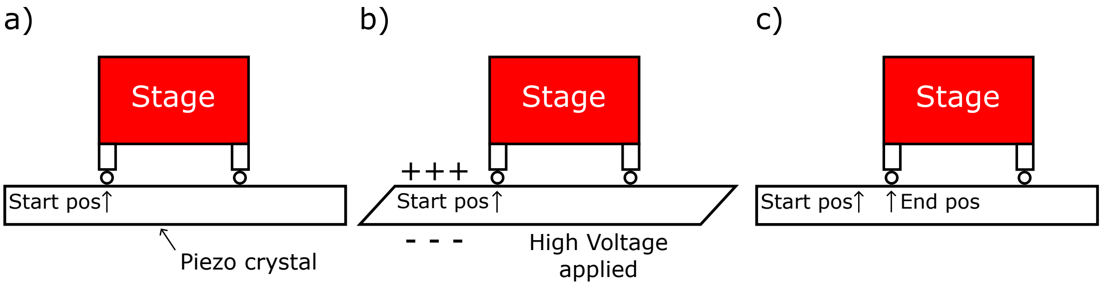

Figure 3.8: In (a) the stage is resting on the piezo crystal, held in place by friction. When a voltage is applied (b), the crystal is extended in one direction (sheer displacement), causing the stage to move over but still be in the same place relative to its position on the extended crystal. As the voltage is removed rapidly (c), the friction effect is lost until the piezo crystal is relaxed. The stage has now shifted over in real space and relative to the crystal.

a piezoelectric material, a slip-stick motor is used (see Figure 3.8). The stage (object to move) is positioned on some piezo crystal that is relaxed (no applied voltage). The stage is held in place by friction between the base of the stage and the crystal (shown in Figure 3.8a). A large voltage is applied to the crystal slowly, this has the effect of shearing the piezo crystal and therefore shifting the stage over (shown in Figure 3.8b). Then, the applied voltage is suddenly switched off, such that the piezo crystal returns to its original extension (see Figure 3.8c). As the returning force is greater than the friction effect holding the stage to the crystal, the stage *slips* on the crystal and then *sticks* due to friction when the piezo crystal has returned to normal. This has the effect of moving the stage along the crystal in a series of small steps. This can be used for coarse (large steps) in X, Y and Z. To avoid scratching the crystal, it is generally protected by a layer of metal. This process is repeated many times to move the stage large distances.

For fine motion, on the scale of picometers of displacement, only the extension of the piezo crystal itself is required. There are many different constructions of a piezo crystal setup for a scanner, however, one of the best (due to a high resonant frequency) is the tube scanner shown in Figure 3.9a. On each side of the tube is an electrode for the application of voltage to expand or contract the crystal. The crystal expands as shown in Figure 3.9b, in order to move the tip (which would be attached to the end of the tube) in X and Y directions. The Z extension of the tube is managed by a central electrode.

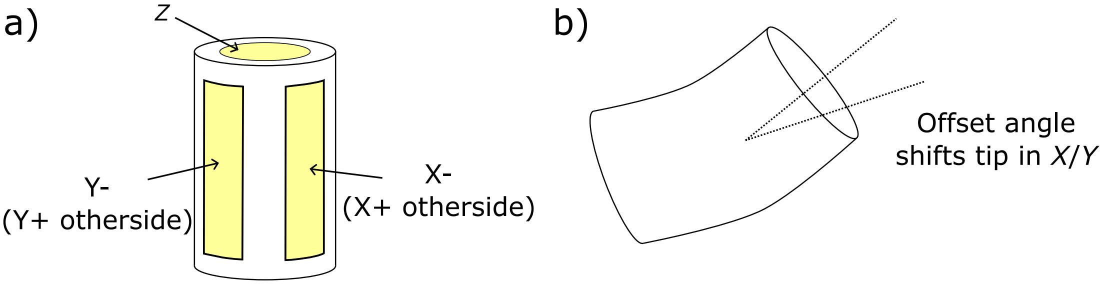

Figure 3.9: (a) Piezoelectric scanner tube with electrodes shown where voltage is applied to extend/contract the tube. (b) Shows how the extension/contraction of the tube leads to the tip moving in X and Y.

3.1.6 STM Tips

Atomically sharp tips are required to obtain atomic resolution with an STM. Electrochemical etching can produce tips of a high quality (see Figure 3.10a). Tips are commonly etched from a short length of tungsten wire (we use 0.5 mm diameter wire), that is held in a tip holder, and dipped into the centre of a ring electrode in 2 Mol/L NaOH solution. The ring electrode acts as a cathode when a

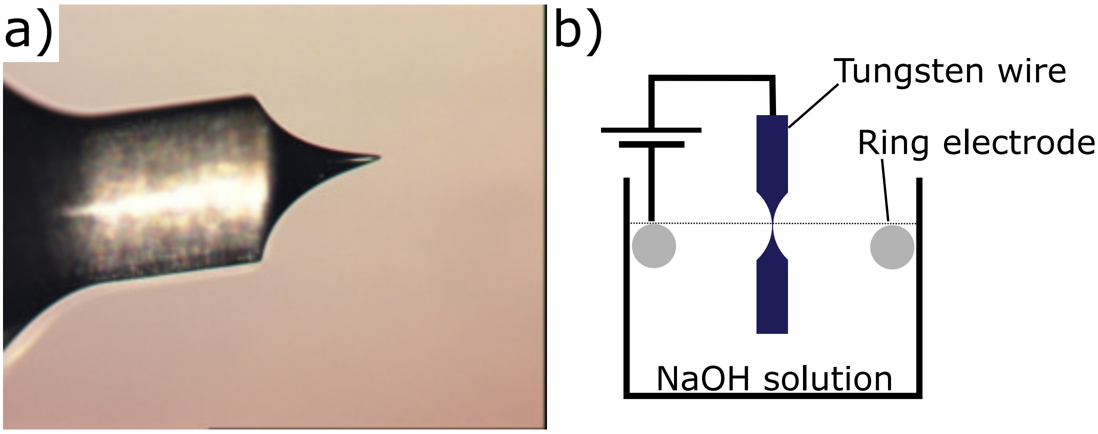

Figure 3.10: The STM tips used in this thesis were created using tungsten wire that was electrochemically etched to form a sharp apex. (a) One of the electrochemically etched tungsten wire tips produced with a sharp apex that was used on the Omicron UHV STM-1 system. (b) Schematic drawing of the setup used to electrochemically etch tips.

voltage is applied, whilst the wire acts as the anode. The majority of the etching occurs at the meniscus until a sharp apex is formed and the submerged wire falls away, leaving a sharp tip. This setup can be seen in Figure 3.10b. To prevent further etching, the tip should be removed from the NaOH solution and placed in deionised water. Other methods for creating an atomically sharp tip exist, but this is the method that we use to create the tips used in this thesis.

Despite electrochemical etching removing material and therefore exposing new tungsten at the apex of the tip, an oxide layer will still form on the surface of the tip. Depending on the thickness of this oxide layer (which can also vary if a tip was stored out of vacuum for long periods) this may need to be removed in ultra-high vacuum (UHV). Controlled indenting of the tip into the surface may remove the oxide and provide atomically 'sharp' new tungsten areas or areas of the surface's material on the apex of the tip which can act as the atomically 'sharp' tip. Thicker oxides or other contamination from dirty samples (lots of mobile molecules, non-conductive materials etc.) may need to be removed by other methods. Within our UHV chamber, two methods exist to further clean tips: annealing and sputtering. When annealing a tip, the tip is heated (by passing a current through the tip to heat the tip) to a sufficiently high temperature to desorb contamination without

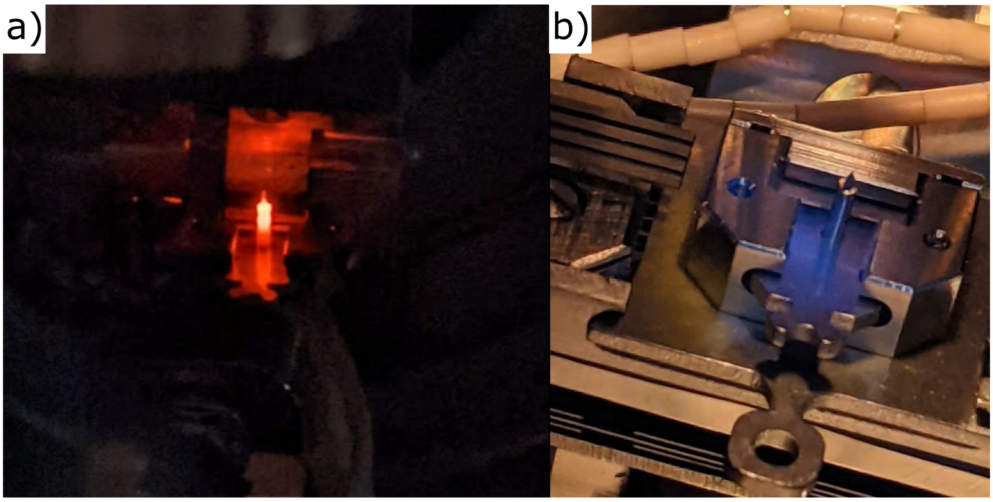

Figure 3.11: (a) Photograph showing the anneal of an STM tip to remove contaminants from the apex of the tip. This image is taken whilst ramping up to the maximum current. The tip should glow white hot for 5 seconds, then be allowed to cool. (b) Sputtering of an STM tip using argon ions. The blue glow is the result of a sufficiently high current passing through the argon gas (glow discharge).

melting the tungsten metal (shown in Figure 3.11a). Sputtering can also remove many layers of the top of the surface by providing charged, high-energy argon atoms impacting the surface of the tip (shown in Figure 3.11b, larger sputtering drain currents produce blue/violet light). Both of these methods can clean a tip, but may blunt the tip and make it less useful for STM by reducing lateral resolution.

Other types of tips, such as qPlus [72] used on the POLAR low-temperature STM/AFM system, can be used as both STM or AFM tips due to the cantilever upon which the tip is attached. These sensors, due to their fragility and custom design are usually purchased commercially, although the tip section can be replaced by removing the old tip and replacing it with new conductive epoxy. Shown in Figure 3.12 are scanning electron microscope images of a qPlus tip.

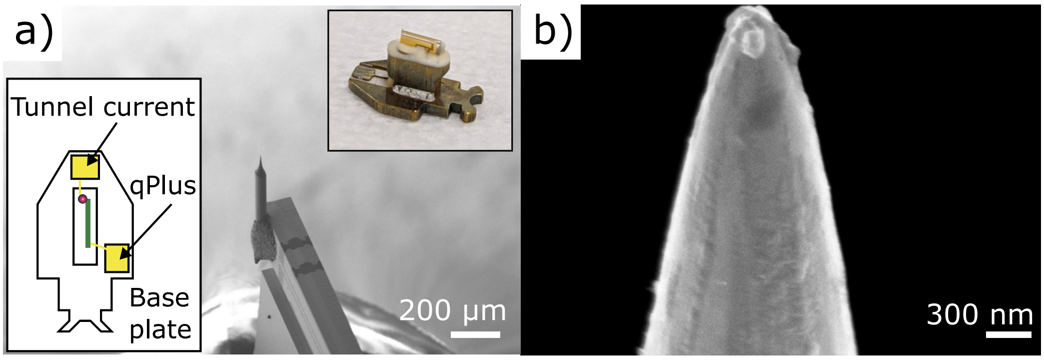

Figure 3.12: Scanning electron microscope images of a qPlus sensor from the POLAR system. (a) The tip is attached using conductive epoxy to the cantilever. To provide a contact for the tunnelling current, gold is evaporated onto the cantilever. Inset left shows the electrical contacts, for each connection allowing isolated tunnel current and qPlus signals. The inset right shows the full qPlus sensor. (b) Zoomed-in image of the tip (near the apex). The diameter is ∼300 nm at the end tip and this further reduces to form an atomically sharp area.

3.1.7 Sources of noise within SPM

The exponential dependence of the current on the tip-sample separation yields some important challenges. Firstly, mechanical noise in the form of vibrations will be coupled to the current (by the tip-sample separation variation) and therefore induce noise in the STM measurements. Vibrational noises can be present from a variety of sources: pumps, building vibrations and public infrastructure. The sources of noise can also vary by time of day. Shown in Figure 3.13, is a Fourier transform of the noise present on the floor in the vertical axis (normal to the floor) over Christmas 2021 in room B288 in the Physics building (where the POLAR SPM is housed). Between the hours of ∼8am-5pm, there are significant levels of noise (4 Hz, 8 Hz and 16 Hz), likely due to activities carried out during the day by others in the building. These vibrations are reduced during the nighttime, however, some vibrations continue regardless (20 Hz, 28 Hz, 35 Hz and 48 Hz). These noises are likely to transfer to the vacuum STM system. Further noises may also be present on the vacuum system itself, such as vibration from the turbo molecular and backing pumps. It is important to design STM systems with many methods to counter these environmental noises [67].

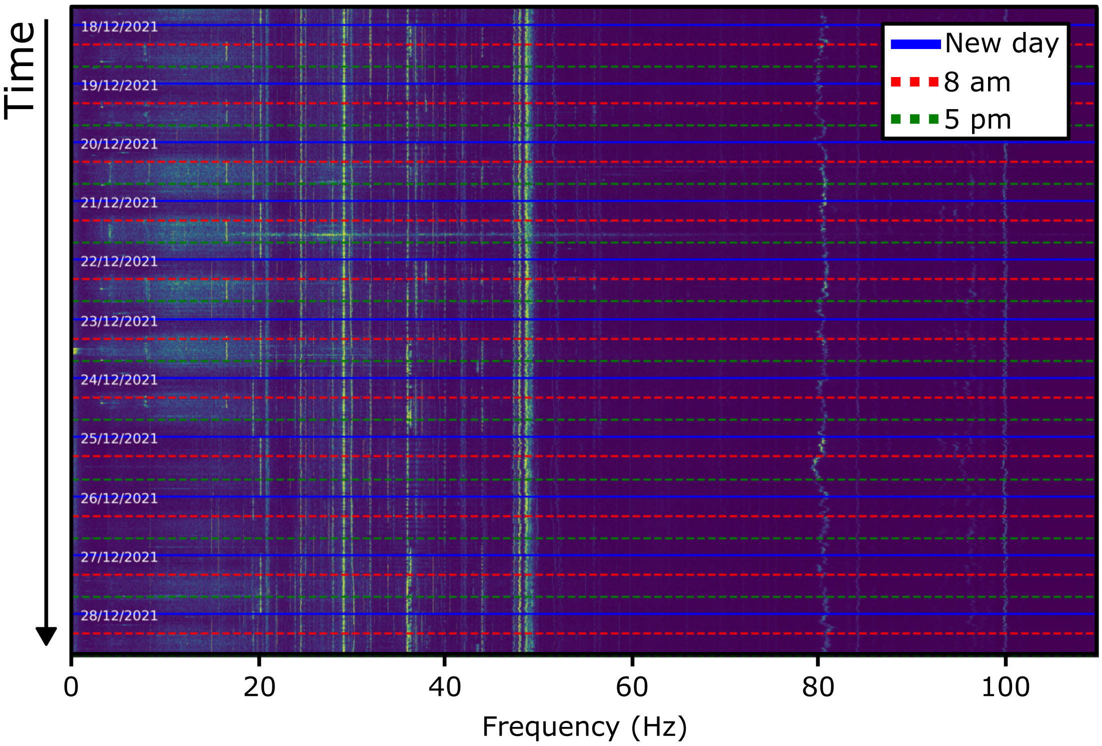

Figure 3.13: The Fourier transformed data collected of the vertical floor noise from an accelerometer in the University of Nottingham's Physics building over Christmas 2021. Brighter pixels indicate higher noise present at that frequency during that time of the day. Blue lines indicate new days, with the red dashed line showing 8 am and a green dashed line showing 5 pm. Outside of those hours, there is a reduction in general noise seen between 0-20 Hz.

Within STM designs there are many ways to ameliorate mechanical noises from the environment. The first is the use of dampening ‘air legs’, these are excellent at removing higher-frequency noises and provide a stable platform for the STM system to rest upon [73]. The STM is typically on a stage that is suspended by springs that attenuate oscillations. The stage may incorporate a ring of copper fins that are placed within a static magnetic field, which has the effect of inducing eddy currents within the copper fins which act with the magnetic field to reduce vibrations of the stage (see Figure 3.14). The design of the STM itself is to be highly rigid; this raises the resonant frequency of the stage vibrations relative to those present in the environment so that oscillations are not readily induced.

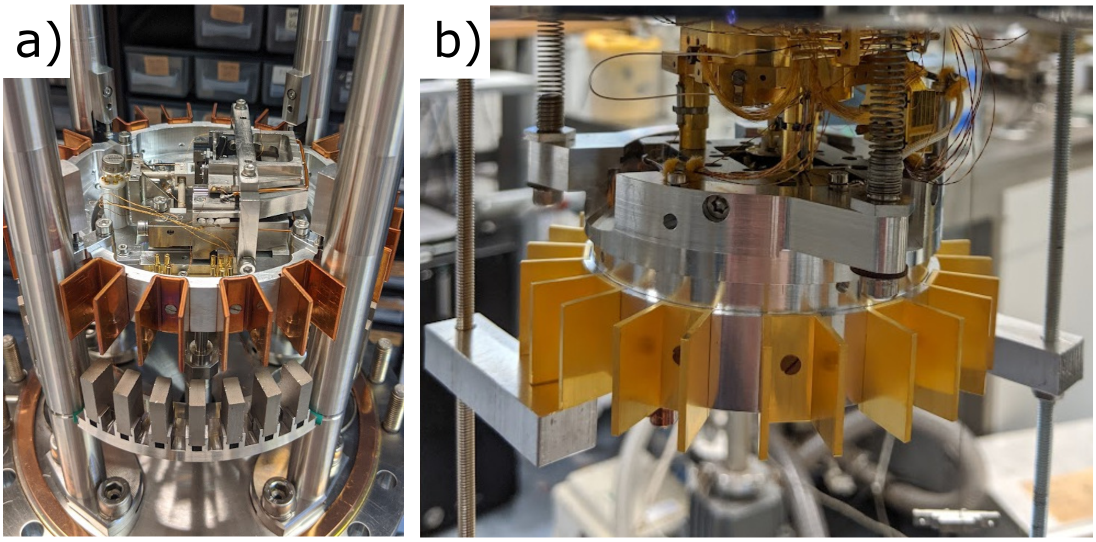

Figure 3.14: STM stages of: (a) the STM-1, copper fins provide eddy current dampening when the stage is lowered into the magnets (below the fins). Springs hidden by metal pillars. (b) LT-STM, similar fin design shown. Springs are visible and the stage is shown to be very rigid.

3.1.8 STM summary

Scanning tunnelling microscopy is a powerful technique that provides a spatial electronic topography of the surface. The resolution can be fantastic, such that atomic resolution of the surface can be obtained (see Figure 3.15a for atomic resolution of the Au(111) herringbone reconstruction). Furthermore, the use of scanning tunnelling spectroscopy (dI/dV spectra) can provide a detailed understanding of the electronic states above and below the Fermi level, that when compared to an analysis by density functional theory, can provide insights into the chemical state of the on-surface feature. Importantly, high-resolution images can be obtained with specific tip structures (an atomically sharp tip) and when this is not the case various anomalous readings would be given in an image. An example of a poor tip is shown in Figure 3.15b, where a double tip (significant tunnelling occurs in multiple points on a tip) makes it appear as if there are multiple chains of differing heights.

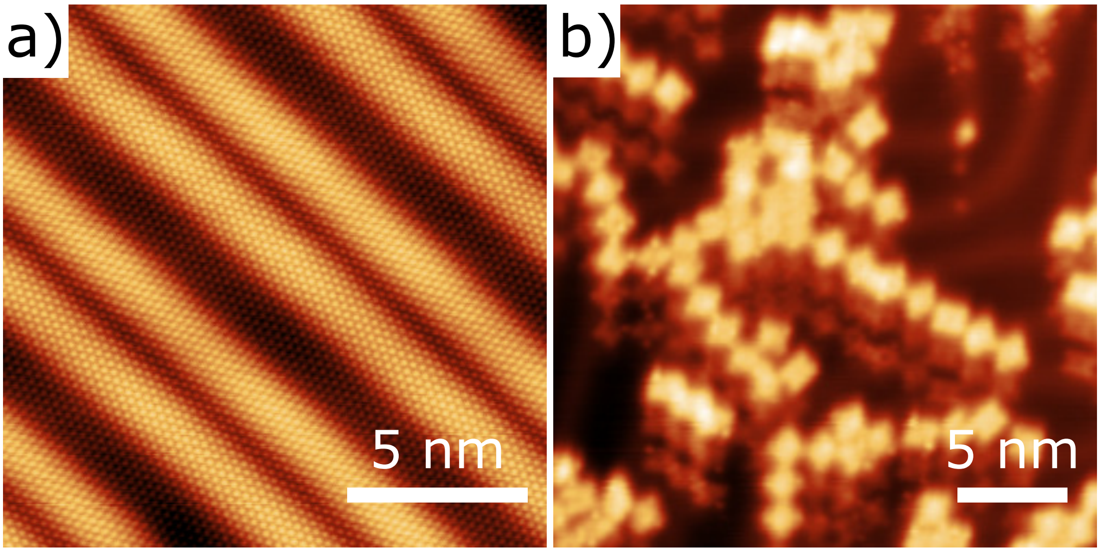

Figure 3.15: (a) Atomic resolution image of the Au(111) herringbone reconstruction. (b) An example of an image obtained with a bad tip, where the tunnelling is occurring in multiple places on the tip. This image makes it appear as if there are multiple chains of differing heights when this is not the case. Tip preparation in the form of bias pulses, or indentation into the surface is required to get the ideal atomically sharp tip. Image settings: (a) $V_{\text{sample}} = -1.0$ V, $I_{\text{set}} = 400$ pA and $T_{\text{sample}} = 4.7$ K. (b) $V_{\text{sample}} = -0.5$ V, $I_{\text{set}} = 300$ pA and $T_{\text{sample}} = 4.7$ K.

3.2 Photoelectron spectroscopy

Photoelectron spectroscopy encompasses a variety of techniques often used to determine the elemental composition, including the stoichiometry of a sample, and can provide information on the chemical state of specific elements. Some of these measurements rely on direct probing of the core atomic states, or the relaxation of electrons from excited to ground states. Photoelectron spectroscopy uses the principle of the photoelectric effect. In 1887, the photoelectric effect was discovered by Hertz, and the theory was later formalised by Einstein in 1905 [74,75]. The photoelectric effect can be described as the emission of electrons from a surface (called photoelectrons) after being irradiated by light. The kinetic energy of the photoelectrons from the surface is dependent upon their origin within the sample and the energy of the incoming photons. The maximum kinetic energy ($E_{\mathrm{KE_{max}}}$) of an emitted electron from the surface of a metal is given by,

$$E_{\mathrm{KE_{max}}} = h\nu\text{–}\phi_{\mathrm{s}}, \tag{3.19}$$

where h is Planck's constant, ν is the frequency of the light and ϕ_{s} is the work function of the metal. This equation is only valid as long as the energy of the photon is larger than the work function of the metal ($h\nu > \Phi$).

3.2.1 XPS

X-ray photoelectron spectroscopy (XPS) is one of the most commonly used photoelectron based surface characterisation tools. A quantitative analysis of the composition of the surface elements is possible, as this technique specifically probes the core levels of the electronic structure of atoms [76]. The core levels provide insight into the bonding of the elements on the surface [77, 78]. An energy level diagram for an atomic environment is shown in Figure 3.16. The energy levels show occupied levels below the Fermi level, containing the core energy levels (such as 1s, 2s, 2p etc. defined by quantum numbers to describe the orbitals) and occupied valence energy levels which are involved in the bonding of molecular species. The core levels are specific to the atom, however, the valence orbitals of each atom in a chemical bond overlap. These new molecular valence orbitals may

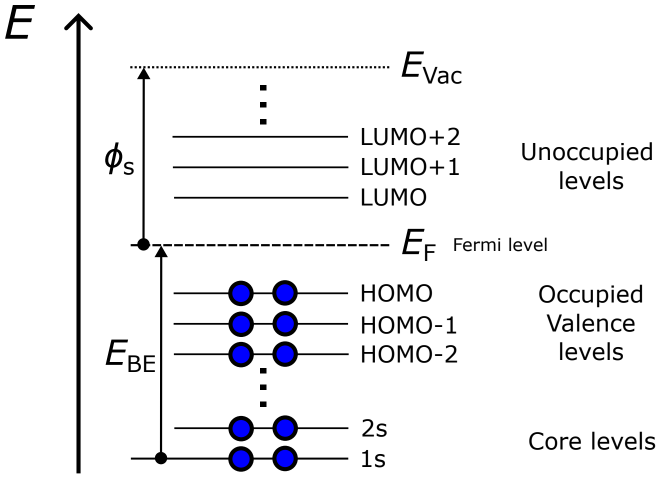

Figure 3.16: Energy level diagram of an atom within a molecule. The binding energy E_{BE} of an electron is defined as the energy required to excite an electron from a core level to the Fermi level. Below the Fermi level, are filled valence levels with the closest state to the Fermi level called the highest occupied molecular orbital (HOMO). Above the Fermi levels, the states are unfilled levels, with the closest state to the Fermi level called the lowest unoccupied molecular orbital (LUMO). The work function of a metal ϕ_s is defined as the energy required to liberate an electron from the Fermi level.

be described in terms of a linear combination of atomic orbitals (LCAO). The valence states are the HOMO, HOMO–1, HOMO–2, etc. states of the molecule. Above the Fermi levels exist the LUMO, LUMO+1, LUMO+2, etc. states which are similarly formed due to the LCAO.

3.2.1.1 From kinetic energy to binding energy

In practice, the kinetic energy of the photoelectrons that are emitted from the core levels are recorded using a hemispherical analyser (using an electric field to record only specific kinetic energy electrons), however, the measurement adds additional energy cost that is lost by the kinetic energy of the electron (work function of the analyser ϕ_{a}) in the determination of the kinetic energy E_{KE} as shown from Equation 3.19. The kinetic energy recorded of a photoelectron recorded by a hemispherical analyser can therefore be described by,

$$E_{\mathrm{KE}} = h\nu - E_{\mathrm{BE}} - \phi_{s+a}, \tag{3.20}$$

where E_{BE} is the binding energy of the core-level electron being emitted, and ϕ_{s+a} is the combination of the workfunctions from the surface and analyser which is surface specific (for further reading see [79] for a discussion of the analyser contact potential - which is the difference between the E_{vac} level between surface, analyser and Fermi level).

Calibration of the workfunction must be done to ensure that the binding energy reported is correctly offset by the workfunction of the system. This can be done in two ways: (1) the Fermi level can be measured using XPS and then this point is shifted (energy shift acts as a calibration to other spectra) to have a binding energy of 0 eV. (2) In the case where lab-based X-ray sources are used, the resolution of the Fermi level is generally poor. Using a well-known peak, such as a feature corresponding to the substrate, should be sufficient as a calibration.

3.2.1.2 Chemical sensitivity

Since the LCAO differs between bonding environments within a molecule for each atom, this causes the valence levels for each bonding environment to be different. Valence levels can perturb the atomic core levels by small energy values due to differing levels of interaction with the core levels. An example of the shift in the binding energy of core levels due to chemical bonding can be seen in Figure 3.17. Within the ethyl trifluoroacetate molecule, each carbon has a different combination of covalently bonded atoms, which leads to chemical shifts of the C 1*s* core level. This effect can be used to identify different chemical environments for each element present and can be used to determine changes to the environments following treatments to the surface (due to shifts in the peaks).

3.2.1.3 Surface sensitivity

The X-ray photons required for XPS are of sufficiently high energy to penetrate at least a few micrometres into the substrate [81]. This allows photoelectrons to be generated deeper within the material than just the surface. The penetration depth of X-rays increases as the photon energy is increased [81]. Despite this, photoelectron spectroscopy techniques are inherently surface-sensitive due to the inelastic scattering of electrons that occurs within the surface. The further an

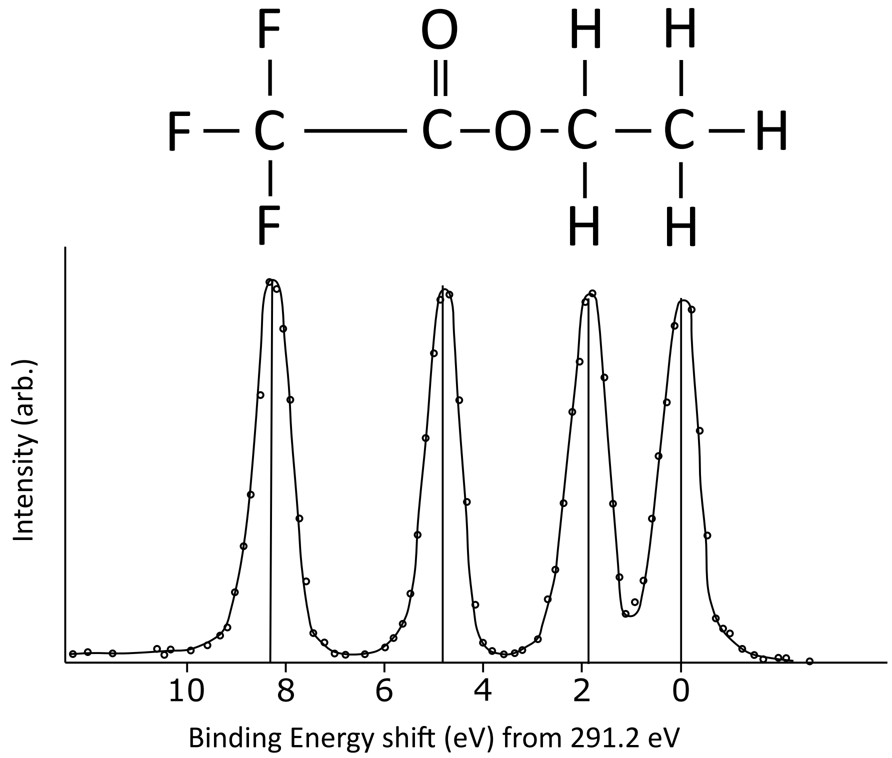

Figure 3.17: XP spectra from an ethyl trifluoroacetate molecule, showing how shifts in the C 1s peaks are due to the environment that the carbon atoms are in. Figure from [80].

electron needs to travel within the bulk (before it leaves and can be detected) means that there is an increased probability the electron will lose kinetic energy to inelastic scattering events. The effect of energy losses causes the apparent binding energy of the core level to appear to be higher than the true value. As electrons will lose different quantities of energy, this will produce a broad background of photoelectrons that have been subjected to a range of inelastic scattering events. These events include the production of phonons (lattice scale vibrations) and/or plasmons (free electron gas density vibrations). The initial intensity of an electron beam I_0 after it has travelled a distance d through the bulk will be attenuated to have the intensity,

$$I(d) = I_0 \exp\left(-\frac{d}{\lambda(E)}\right), \tag{3.21}$$

where $\lambda(E)$ is the inelastic mean free path that is dependent upon the surface and also the energy of the incoming photon. The inelastic mean free path is defined as the distance travelled by the electron beam when the intensity reaches

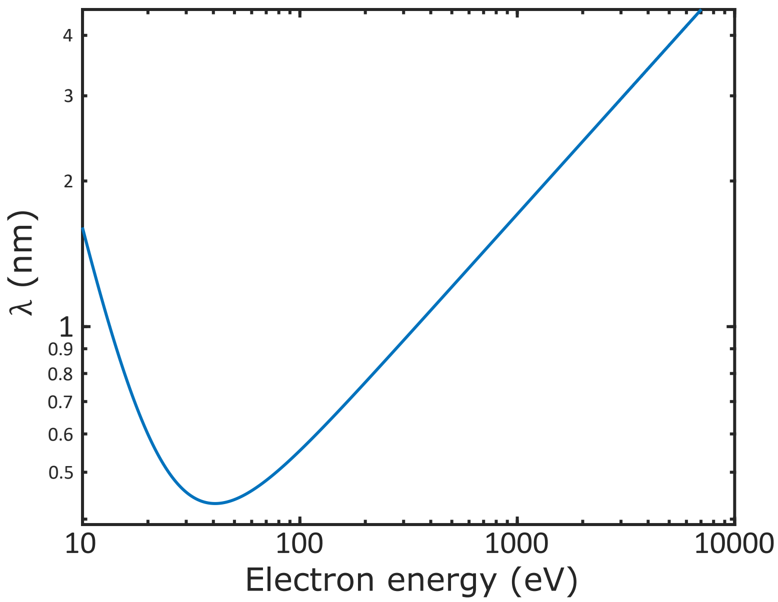

Figure 3.18: A characteristic universal curve for the mean free path of an electron travelling through a solid. This can be calculated using $\lambda = \frac{143}{E^2} + 0.054\sqrt{E}$ where E is electron energy.

$1/e$ of its initial intensity. The mean path length of the photoelectrons within the bulk can be seen in Figure 3.18. To reduce the number of photoelectrons which are able to escape from within the bulk, the appropriate choice of photon energy could be chosen to keep the mean path length to a minimum (assuming variable photon energy is possible by using synchrotron light).

3.2.1.4 Shake-up and shake-off features

When viewing XPS spectra, it is important to recognise that not all peak features observed can be attributed solely to the emission of an electron from a core level as a result of the photoelectric effect. An example of this is defined by Koopmans' theory, which states that electron energy levels are unperturbed by the removal of an electron, however, in practice, this is not true since the formation of a core-hole leaves the atom overall charged and therefore unstable. This can produce differing energy levels between the initial and final state of the atom and therefore lower the apparent kinetic energy of the electron (which makes the binding energy appear higher). Two specific transitions as a result of the difference between the initial and final states of the atom are shake-up and shake-off electron emissions

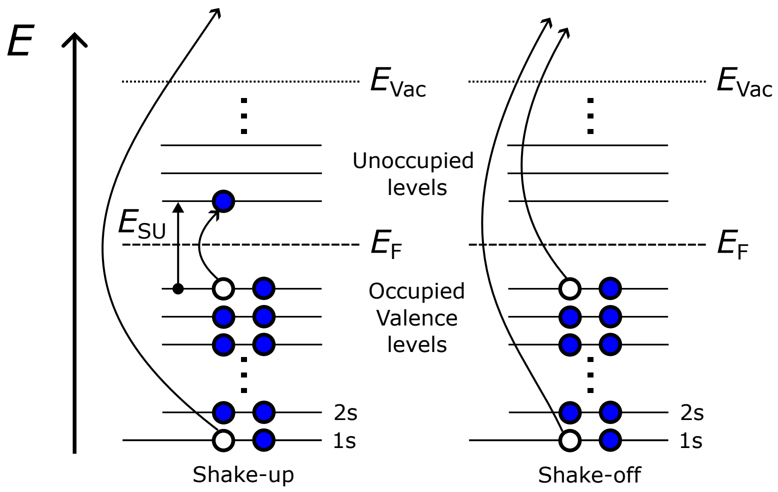

Figure 3.19: Energy level diagram showing the photoelectric process related to shake-up and shake-off processes.

(energy transitions shown in Figure 3.19). Within shake-up features, the initial photon liberates one electron from a core-level, however, this induces an electron to transition from an occupied valence state to an unoccupied state which has an energy requirement of E_{su}. This means that the photoelectron loses kinetic energy of E_{su}, so this electron appears to have a higher binding energy. Within shake-off features, the initial photon liberates one electron from a core-level, however, it also induces another electron in the occupied valence states to also be liberated from the atom. The initial photoelectron has lost kinetic energy related to the total energy required to liberate the occupied valence electron.

Despite XPS results being relatively repeatable (multiple spectra would likely look the same within the noise floor of the analyser and assuming that the X-ray intensity remained constant), beam-related surface changes (beam damage) can occur that affect chemical bonds and therefore the observed binding energies of on-surface structures. X-ray beams provide energy that liberate electrons from atoms that may be part of chemical bonds, and it is conceivable that charging could cause the breaking of those bonds. This yields a different LCAO which would produce different perturbations of the core levels and therefore differing surface binding energies.

3.2.1.5 Peak fitting

The peak shapes produced are frequently modelled as a combination of Lorentzian and Gaussian broadening of a specific binding energy. Lorentzian broadening can be explained due to a finite lifetime of a core hole formed when an electron is emitted and subsequently when electrons in the atom relax to fill the empty state. Gaussian broadening of the peak can be attributed to the experimental uncertainty in the kinetic energy of the electron as detected by the hemispherical analyser and by the natural uncertainty in the line width of the incident X-ray. This means that peaks can be fitted using a combination of Gaussian and Lorentzian line shapes, however, certain elements have additional interactions that could also be taken into account with more complex line shapes [82].

3.2.2 NAP-XPS

Near ambient pressure X-ray photoelectron spectroscopy (NAP-XPS) allows for the XPS measurement of a sample whilst the sample is subjected to ambient levels (<25 mbar) of specific gases [83]. This is useful for studying the gas-solid interface. Although not truly ambient, in that the applied pressure is <<1000 mbar (equivalent to ambient pressure), the partial pressure applied to the sample within a NAP system (the pressure exerted by an individual gas in a mixture) is the same (or similar) as experienced at ambient pressure levels. An example of this is CO_2, which has a partial pressure of 0.4 mbar at sea level, so samples exposed to this pressure can interact with ambient pressures of CO_2 mimicking real-world conditions. This technique requires specific apparatus within the UHV chamber. The NAP-cell (see Figure 3.20a) is a chamber within the UHV chamber in which the sample is placed, and gas is leaked into the cell via a mass flow device to carefully regulate the pressure within the cell. X-rays can enter the cell via a silicon nitride window on the side, where they are incident upon the sample. A cone with a hole at the end provides a route from the cell to the UHV chamber and the hemispherical analyser; allowing the egress of photoelectrons and gas from within the cell. As previously discussed, when liberated electrons travel through solid materials there are inelastic interactions with the bulk that reduce the kinetic

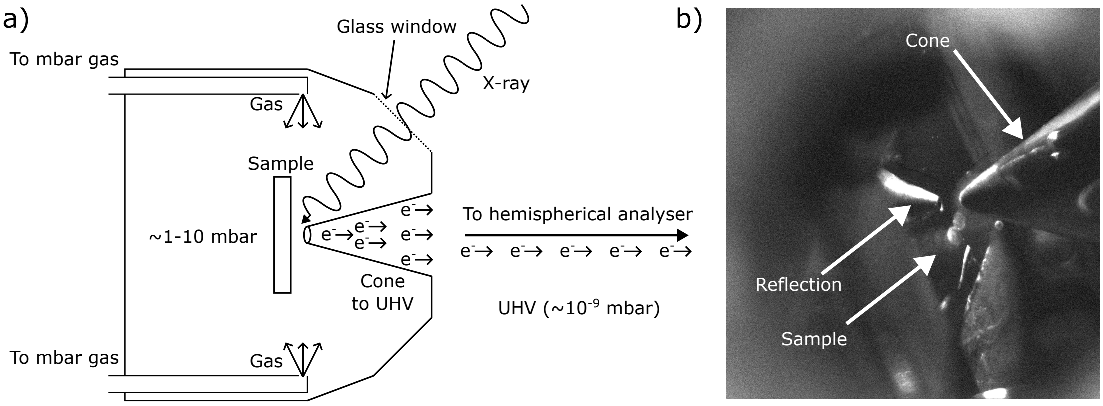

Figure 3.20: (a) Schematic diagram of a NAP-cell within a UHV chamber. Gas is leaked into the chamber and carefully controlled to keep the pressure inside the cell constant. The sample is placed inside the cell. The X-rays can enter the cell via a glass window, and cause photoelectrons to be released from the surface. The cone is brought close to the sample so that sufficient signal is received by the analyser. (b) Shows an image from within the NAP-cell where the relative positions of the sample and cone can be seen.

energy of some electrons, therefore, reducing the number of electrons detected at the analyser with the expected core-level binding energy. The gas acts as a less dense ‘solid material’, with which electrons inelastically interact and so fewer electrons exit through the cone to the analyser. The cone is brought close enough to the surface, typically less than 0.45 mm (see Figure 3.20b), to allow sufficient electrons to reach the hemispherical analyser. Positioning the cone closer to the surface results in an increased signal, but a lower partial pressure of the gas at the surface from which XPS measurements are being taken.

3.2.3 NEXAFS

The use of XPS allows for the inspection of core-level electrons, however, near-edge X-ray absorption fine structure (NEXAFS) spectroscopy allows for unoccupied states to be observed. In the case of molecular systems, this provides information on the LUMO and unoccupied states. Instead of using a fixed photon energy, the photon energy of the incident X-ray is swept over a range of values that matches the adsorption edge of a sample. Energies are chosen to match the difference between an occupied core level and the unoccupied levels (UL) ie. $h\nu = E_{\mathrm{BE}} + E_{\mathrm{UL}}$ where E_{UL} is a range of values and E_{BE} is the binding energy for one of the core electrons. The unoccupied region can provide more detailed information on the chemical state of an atom (since shifts here are more sensitive to changes in the LCAO) and sometimes provide larger shifts than those that are discernible with the resolution provided by XPS [84].

For molecular species formed from light elements, like nitrogen, the molecular valence states are described by π and σ bonding orbitals, which are typically filled orbitals, with π orbitals being closer to the Fermi level. The unoccupied states can be seen as mirroring the occupied states, with unoccupied π^* orbitals closest to the Fermi level and then σ^* orbitals at slightly higher energy levels. At higher energy levels, there is a transition to the continuum, where the states are sufficiently close together that the states appear to be continuous. Within the NEXAFS spectra, peaks occur at specific energies where the photon energy matches the energy required to elevate the core electron to an unoccupied level. A schematic of a spectra is shown in Figure 3.21.

To determine the unoccupied states using NEXAFS an incident photon on the sample excites a core-level electron (e.g $1s$) into the unoccupied states of the atom (see Figure 3.22a). Over all of the measurements, the photon energy is changed over a range of photon energies, and therefore, the electrons will be

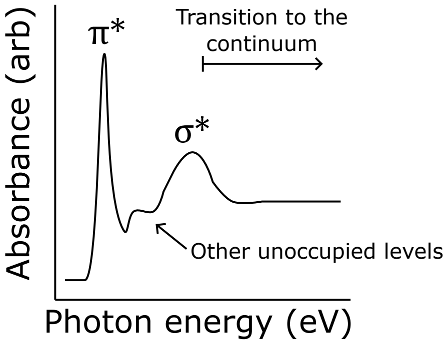

Figure 3.21: A schematic drawing of a NEXAFS spectrum for a nitrogen molecular species. As the photon energy is swept, more absorption of the photons (and therefore more photoemission) occurs when the photon energy matches the required energy to excite a core-level electron to one of the unoccuiped states. The unoccupied π^* orbitals are closest to the Fermi level.

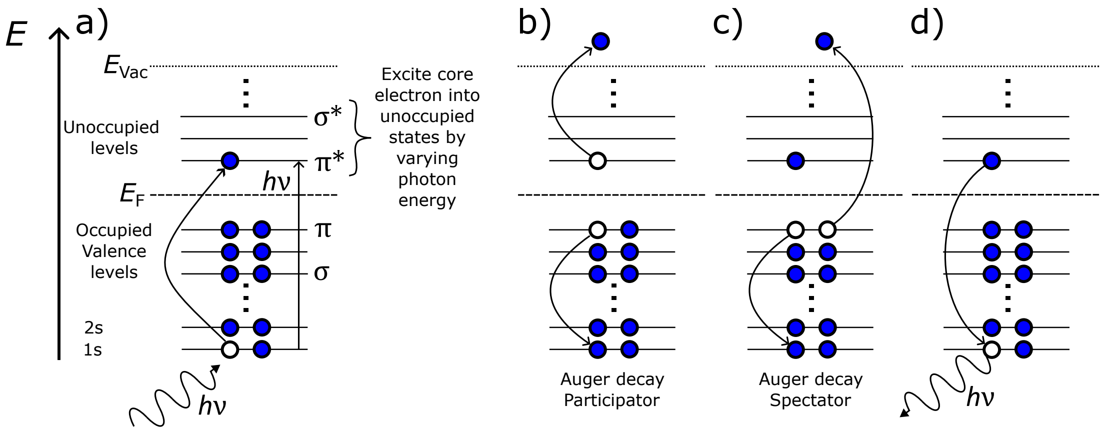

Figure 3.22: (a) An absorption of an incident photon, such that a core level electron is excited into an unoccupied state. In this case, a molecular system with π, σ, π^* and σ^* states. (b) Electrons in the occupied states recombine with the core hole, releasing the unoccupied state electron from the atom; Auger decay (participator). (c) Electrons in the occupied states recombine with the core hole, releasing another occupied state electron from the atom as an Auger decay (spectator). (d) Recombination of the excited electron in the unoccupied state to the core hole releases energy as a photon.

excited into various unoccupied states (in this case π^* and σ^* orbitals for this molecular species). The atom will return to the ground state by various methods, some of these produce a photoelectron by Auger decay which can be measured to determine the absorption of the sample at that photon energy. For example in Figure 3.22b, one of the occupied level electrons recombines with the core hole, causing energy to be released such that the electron in the unoccupied state is ejected as an Auger electron (participator decay). Or in Figure 3.22c, one of the occupied level electrons recombines with the core hole, but this causes another occupied level electron to be emitted as an Auger electron (spectator decay). And finally, in Figure 3.22d the excited electron just recombines with the core hole and emits the energy as a photon. The Auger decay electrons are measured as a proxy for X-ray adsorption. The Auger electrons can be measured using a detector (typically a metal mesh) within the UHV chamber or, in the case of low absorption of photons, by the hemispherical analyser by looking at electrons with the expected kinetic energy for the Auger transition.

3.2.4 NIXSW

With XPS, the resultant spectra provide insight into the chemical state of the elements, however, it does not provide any information on the spatial location of the absorbed species. Normal incidence X-ray standing wave (NIXSW) provides information on the chemical state of the core levels of the atoms whilst providing a signal which varies in intensity depending on where the atomic environment is spatially located. This is achieved by forming an X-ray standing wave at the surface, and then by varying the photon energy, the maximum intensity position of the standing wave moves so that species experience a different intensity of X-ray depending upon their position within the standing wave [85,86]. The standing wave is formed relative to the crystallographic planes that the incident X-ray is normal to, for example, if the X-ray is incident on the (111) plane the standing wave is formed with nodes (initially) at the (111) crystallographic planes. This can be extended such that if the X-ray is incident on the (220) plane of a (111) surface cut crystal, the standing wave will be formed with nodes (initially) at the (220) crystallographic planes. As the intensity of the standing wave between the nodes at the crystallographic planes varies, the quantity of photoelectrons produced by that species also varies depending on its position relative to the crystallographic planes. Using theoretical models, the position of the species can be determined.

The formation of X-ray standing waves can be simplified by considering the physics of the Bragg condition. An incident X-ray with a wavelength λ, meets the Bragg condition when,

$$n\lambda = 2d_{hkl}\,\sin\theta, \tag{3.22}$$

where n is the diffraction order, d_{hkl} is the vertical atomic spacing between crystallographic planes and θ is the angle of incidence for the X-ray. At wavelengths similar to the surface crystallographic planes spacing ($\lambda/2 = d_{hkl}$), the maximum intensity of the reflected X-ray would be at $\theta = 90°$. When considering the interference between the incoming wave and the reflected wave, a standing wave would be set up at the surface of the crystal. This is a simplification of the X-ray standing wave formation since the Bragg condition does not account for multiple scattering events within the crystal, where the intensity of the reflected X-ray is attenuated, or the fact that the X-ray can only travel a finite depth into the surface. This means that a standing wave is set up over a finite range of wavelengths around the Bragg condition, which means that we can change the wavelength of the incident X-ray to change the position of the nodes for the standing wave.

Shown in Figure 3.23 is a schematic of the experimental setup for NIXSW. An X-ray wave with a wavelength close to half the vertical crystallographic plane that is under inspection is incident on the surface, and the reflected wave produces interference between the incident and reflected X-rays, forming a standing wave at normal incidence to the crystallographic plane. The intensity of the reflected X-ray wave can be recorded by measuring the fluorescence on a screen with a camera, this allows for the position and intensity of the standing wave to be estimated (as discussed below).

The standing wave can be exploited to determine absorption positions. Shown

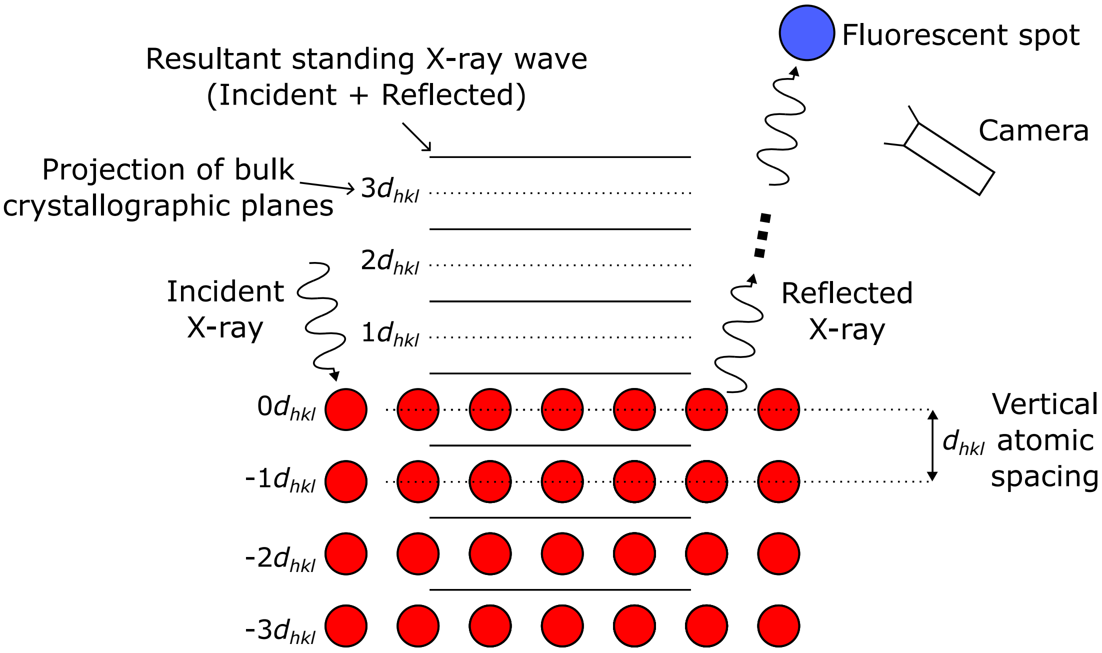

Figure 3.23: A schematic diagram of the NIXSW experimental setup. X-rays are incident on the surface, which causes an X-ray to be reflected. Interference between the incident and reflected X-rays causes a standing wave to form with maximum intensity between the vertical atomic spacing. The reflected X-ray causes a fluorescent spot which can be used to determine the details about the standing wave.

in Figure 3.24a are two atoms (blue and green), at two different positions within the vertical atomic spacing (red atoms interplane separation d_{hkl}). The positions of the atoms can be referenced with respect to the position within the crystallographic plane, with positions 0.0 to 1.0 referencing a position between the crystallographic planes. As the photon energy is increased (see Figure 3.24b), the reflection of the X-ray is increased to a point where it reaches the maximum reflection (see the plateau in the reflectivity in Figure 3.24b at the lowest photon energy). At this point, there is a phase difference of π between the incident and reflected X-rays, which sets up anti-nodes between the vertical atomic spacing lines (position 0.5) and nodes at the vertical atomic spacing lines (positions 0.0 and 1.0 - see Figure 3.24c for π phase difference photon intensity). Here, the absorption of the standing wave by the green atom is at the maximum, so the

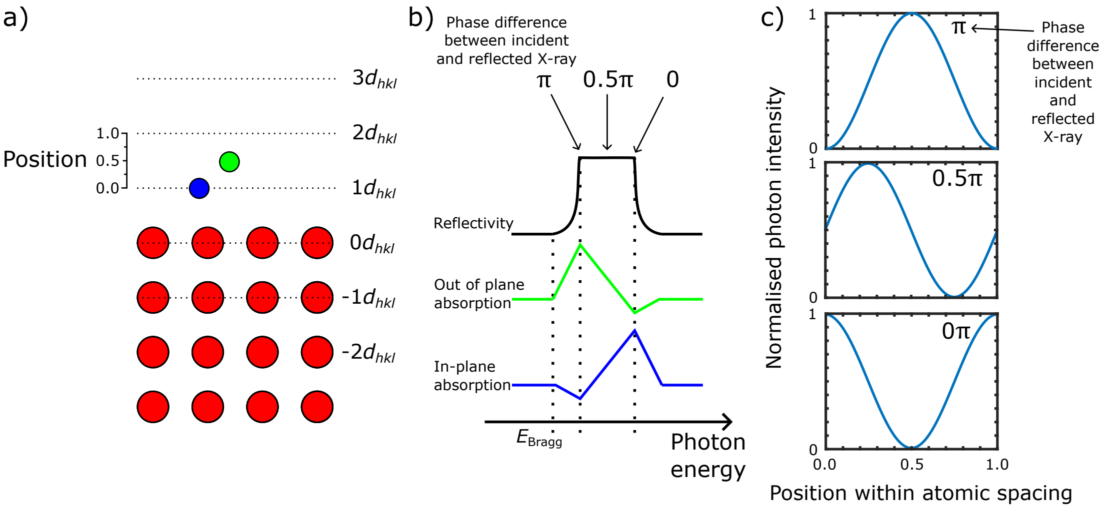

Figure 3.24: Illustration of the principles of NIXSW. (a) Two atoms are absorbed at different heights above the surface relative to the vertical atomic separation (dotted lines). The blue atom is in the 0.0 position and the green atom is in the 0.5 position. (b) As the photon energy of the incident X-ray is increased, at the Bragg condition an X-ray starts to be reflected, up to the point where maximum reflectivity is achieved where the phase difference between the incident and reflected X-ray is π. As the photon energy is increased the phase difference between incident and reflected reduces to 0. (c) For a phase difference of π, the photon intensity is highest at position 0.5. The green atom absorbs more photons than the blue atom. Reducing the phase difference shifts the position of the maximum intensity. Modelled from the cosine within Equation 3.26.

photoelectron yield from this state will be at a maximum. However, for the blue atom, the photon intensity is at the minimum, so the photoelectron yield from this state is at the minimum value. As the photon energy is increased, the phase difference between the incident and reflected X-ray is reduced (see Figure 3.24c 0.5π) this leads to the peak intensity of the standing wave shifting. As the phase difference is reduced to zero (see Figure 3.24c), the anti-nodes of the standing wave become aligned with the crystallographic plane, which results in the blue atom exhibiting the maximum photoelectron yield and the green atom exhibiting minimum photoelectron yield. At each photon energy the photoelectron yield is determined. An XP spectra is recorded, corresponding to the kinetic energy of photoelectrons for each atomic environment. The XPS peaks are fitted (similar to the fitting in Figure 3.17), which allows values for the photoelectron yield to be defined as the total area of that environment for a given photon energy. This process is performed over a range of photon energies which would, in principle, give rise to the form shown in Figure 3.24b for an ideal system.

In order to use the photoelectron yield from each environment to determine its position, the intensity of the standing wave at each position above the surface needs to be determined. A theoretical intensity I of the standing wave at position z above the surface can be defined as,

$$I = \left| 1 + \frac{E_\mathrm{r}}{E_0} \exp\left(-\frac{2\pi i z}{d} \right) \right|^2 , \tag{3.23}$$

where E_r and E_0 are defined as the reflected and incident wave amplitudes respectively and, the interatomic plane spacing is given by d. In the above equation, for simplicity, the initial incident amplitude (first term) is defined as unity. This approach is not taken for the reflected term (second term) as there is a phase dependence between the reflected and incident X-ray that will alter the intensity of the standing wave. By recognising this phase dependence, the reflectivity R can be written as,

$$\frac{E_\mathrm{r}}{E_0} = \sqrt{R} \exp\left(i\phi \right) , \tag{3.24}$$

where ϕ represents the phase between the incident and reflected X-rays and this varies by π across the whole reflectivity range. By substituting into Equation

3.23, this equation becomes,

$$I = \left| 1 + \sqrt{R}\, \exp\left(i\phi - \frac{2\pi i z}{d} \right) \right|^2 . \tag{3.25}$$

This can be further simplified to,

$$I = 1 + R + 2\sqrt{R}\, \cos\left(\phi - \frac{2\pi z}{d} \right) . \tag{3.26}$$

Unfortunately, in most real-world situations, the adsorption of atomic/molecular species does not occur in a singular position. There may be two or more positions for each atomic environment which is not currently considered by Equation 3.26. Thermal fluctuations in the absorption position may also introduce some small uncertainty in the position of the environment. To include multiple positions, the sum of all the contributions defined as fractions of atoms at each position z within the standing wave should equal 1, as shown by,

$$\int_0^d f(z) dx = 1. \tag{3.27}$$

This gives the standing wave intensity as,

$$I = 1 + R + 2\sqrt{R} \int_0^d f(z) \cos\left(\phi - \frac{2\pi z}{d} \right) dz. \tag{3.28}$$

This can be simplified to,

$$I = 1 + R + 2C_f\sqrt{R}\, \cos\left(\phi - 2\pi C_p \right) . \tag{3.29}$$

The coherent fraction (C_f) and coherent position (C_p) shown in Equation 3.29 describe the sum of all the fractions at each environment's position within the atomic planes. These coherent fractions and coherent positions can be best shown in an argand diagram, where C_f and C_p describe the r and θ values of the vectors in polar coordinates. To find the possible individual positions and fractions of the environments, vectors on the argand diagram can be used for each environment's position and fraction,

$$C_f \exp(2\pi i C_p) = \sum_v C_{f_v} \exp(2\pi i C_{p_v}), \tag{3.30}$$

where $C_{p_1} = z_1/d$ showing that the position of the state within the atomic spacing is clearly given by the coherent position.

3.2.5 Sources of photons

The source of photons that are incident on the sample is an important consideration for photoelectron spectroscopies as this determines the accessible surface states and/or the techniques that are available to characterise the sample. Within many research laboratories, anode-based X-ray lab sources are employed as they provide photon generation in a smaller space often at a relatively lower cost, however, these lab sources have restrictions to their usefulness. Synchrotrons are able to produce a large range of photon energies with higher intensities than lab-based sources. The pros and cons of these photon sources are discussed below.

3.2.5.1 Lab based sources

X-rays in lab-based sources are generated when electrons with sufficient kinetic energy (keV range) are incident on an anode material. The selection of the electron source can impact the output brightness of the X-rays, due to limitations in the thermionic emission of each material. The choice of the anode determines the X-ray photon energy, due to the material's characteristic excitation lines. For example, an aluminium anode emits X-rays from the Al$K\alpha$ line at 1486.6 eV with a full-width half maximum (FWHM) of 0.9 eV, whereas a magnesium anode emits X-rays from the Mg$K\alpha$ line at 1253.6 eV with a FWHM of 0.7 eV. The FWHM value influences the energetic resolution of the photoelectron peaks that will appear during photoelectron spectroscopy. The different photon energies will not change the observed binding energies of core level electrons (as the effect of $h\nu$ on kinetic energy is accounted for in Equation 3.20), but Auger electrons will have a reduced *apparent* binding energy by $1486.6-1253.6 = 233$ eV for the Al$K\alpha$ and Mg$K\alpha$ sources described above (due to the reduced kinetic energy of the Auger electrons). Changing the photon energy does not have an effect on the binding energy of the photoelectron peak, but will affect the position of the Auger peaks.

3.2.5.2 Synchrotron source

Within a synchrotron, light is generated by a magnetically forced ‘wiggle’ of electrons moving close to the speed of light, such that the electrons lose kinetic energy in the form of electromagnetic radiation. Synchrotrons are generally national (or international) experimental facilities. Examples of synchrotrons are MAX-IV, European Synchrotron Radiation Facility and Diamond Light Source. At Diamond, electrons are initially generated by an electron gun and are accelerated by a linear accelerator to energies of 100 MeV. The electrons are further accelerated by a booster synchrotron up to energies of 3 GeV, at which point the electrons enter the storage ring. The storage ring consists of 24 straight sections forming a closed loop, with bending magnets to shift the electron beam direction at each vertex (see Figure 3.25). The electrons travel around a storage ring and through insertion devices that cause a magnetic fluctuation to precisely tune the output photon energy to the required value. This light is then transmitted to the sample by various mirrors. Insertion devices allow for polarised light to be generated.

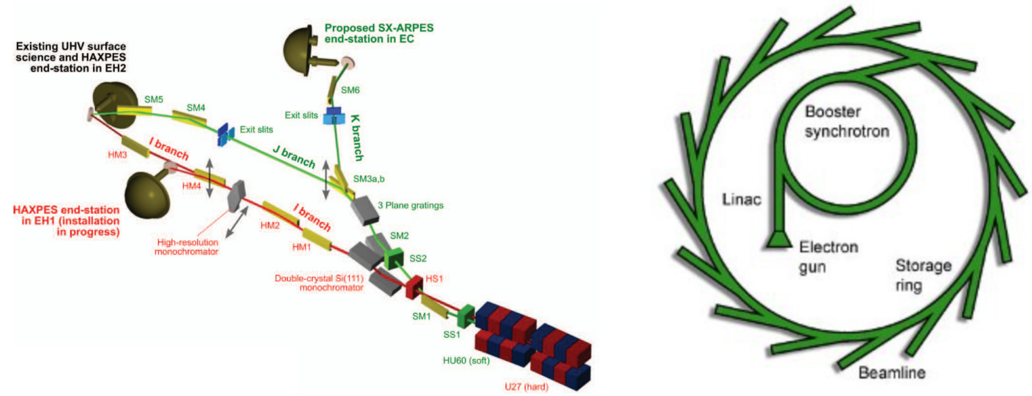

Figure 3.25: Left: Shows from the insertion device how photons reach the sample in i09 at Diamond Light Source. Right: Overview of Diamond Light Source ring layout. Taken from [87](left) and [88](right).

3.3 LEED

Low energy electron diffraction (LEED) allows for the determination of surface structure using low energy electrons (10-200 eV) that are incident on a sample and diffract back to form a characteristic pattern on a screen. A schematic diagram of LEED is shown in Figure 3.26a. LEED is inherently a surface-sensitive technique since electrons will undergo significant interaction with the surface atoms as the mean free path is short for electrons at these energies (see Figure 3.18).

The diffraction of electrons, as the result of interaction with a surface, can be described by the Bragg equation,

$$n\lambda = a\ \sin\theta, \tag{3.31}$$

where n is the diffraction order, λ is the wavelength of the incident electrons, a is the scatterer spacing (in this case atoms, but it may be overlayer molecules) and θ is the angle between the incident and reflected beam. The interaction between the electrons and the surface atoms is shown in Figure 3.26b. The reflected beams are incident on a fluorescent screen, appearing as bright spots

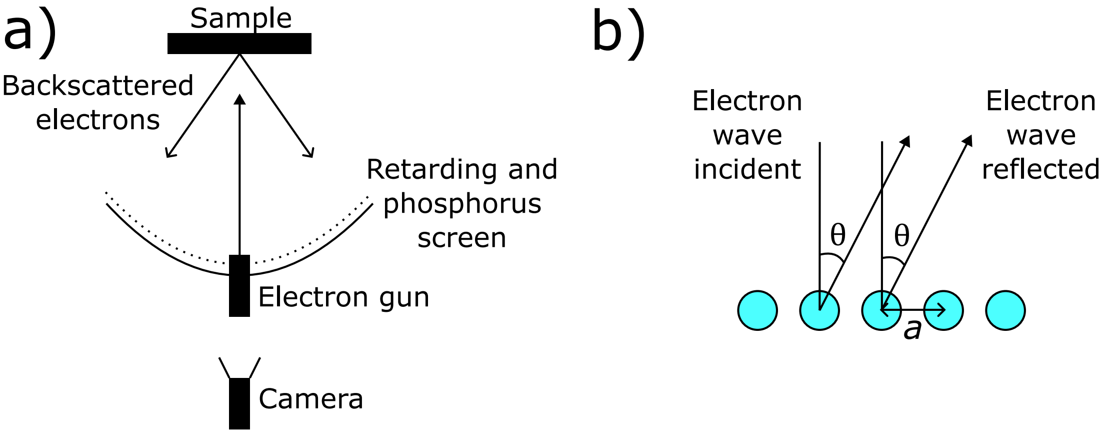

Figure 3.26: (a) Schematic diagram of a low energy electron diffraction experimental setup. Electrons incident on the sample are reflected back and constructively interfere on the phosphorus screen to create a diffraction pattern related to the surface structure. A retarding grid is used to only allow elastically scattered electrons to reach the screen. (b) Bragg diffraction of electrons. Electrons incident on the sample will be scattered back at various angles, and constructive interference of the electrons will only occur at angles that satisfy the Bragg equation.

where constructive interference occurs as described by the Bragg condition. By varying the wavelength of the incident electrons, the angle at which constructive interference occurs will vary, moving the spots on the screen; this allows for various scatterer spacings to be characterised.

LEED is based upon the elastic scattering of a beam of monoenergetic electrons from a crystal/periodic surface; the observed diffraction pattern does not provide the real space positions of the scatterer. It can be shown that the pattern is that of the reciprocal lattice of the ordered on-surface structures. The electron beam can be described by a wave vector $\mathbf{k}_{\mathrm{i}}$, that is incident on a planar array of scatterers. The scattered wave vector can be described as $\mathbf{k}_{\mathrm{f}}$. In three dimensions these wave vectors satisfy the Laue condition,

$$\mathbf{G}_{hkl} = \mathbf{k}_{\mathrm{f}} - \mathbf{k}_{\mathrm{i}}, \tag{3.32}$$

where (h, k, l) are a set of integers and $\mathbf{G}_{hkl}$ is a vector of the reciprocal lattice,

$$\mathbf{G}_{hkl} = h\mathbf{a}^* + k\mathbf{b}^* + l\mathbf{c}^*. \tag{3.33}$$

The reciprocal lattice is a way of describing the real lattice (described by $\mathbf{a}, \mathbf{b}, \mathbf{c}$) in Fourier space. Due to the requirement that the scattering is elastic, the magnitudes of the incident and reflected wave vectors are the same ($|\mathbf{k}_{\mathrm{i}}| = |\mathbf{k}_{\mathrm{f}}|$). Since only the top few layers of the surface contribute to the scattering of electrons, there are no diffraction conditions perpendicular to the surface direction, only in the parallel direction (conservation of total momentum). This narrows the Laue condition to the 2D form,

$$\mathbf{G}_{hk} = \mathbf{k}_{\mathrm{f}}^{||} - \mathbf{k}_{\mathrm{i}}^{||} = h\mathbf{a}^* + k\mathbf{b}^*. \tag{3.34}$$

This result means that the diffraction pattern returned is a series of beams whose pattern satisfies the above equation.

3.4 UHV experimental setup

Ultra-high vacuum (UHV) is defined as a pressure lower than 10^{-7} mbar [89]. It is fundamental to the research carried out within this thesis as it allows for high-purity sample preparation (low environmental contamination). The reduced gas-sample interaction means that the sample stays clean for longer. UHV is obtained by: 1) the careful consideration of materials for use within the vacuum, since outgassing (the process of releasing gas into the vacuum) from materials reduces the vacuum quality. The walls of the chambers are made from stainless steel and are generally treated to reduce outgassing. 2) An appropriate choice of pumps covering the lower vacuum and higher vacuum requirements. Pumping at lower vacuum levels is achieved by backing pumps, to reach higher vacuum levels turbo molecular pumps are used. Once at high/ultra-high vacuum, pumps such as ion-getter pumps may be used to maintain the vacuum with low vibrational noise. 3) Heating of the vacuum chambers to reduce water vapour in the vacuum allows for the vacuum to reach ultra-high levels. 4) An appropriate choice of connector for additions to the chamber. The ConFlat (CF) flange crushes a metal gasket between two sharp edges to prevent the ingress of gas molecules into the chamber. See [90] for more details.

3.4.0.1 Omicron UHV STM-1 system

The ambient temperature STM experiments discussed in this thesis were carried out using the Omicron STM-1 UHV system pictured in Figure 3.27, and was used in conjunction with Nanonis SPM control electronics. The SPM chamber was separated from the rest of the system by a gate valve and was pumped by an ion-getter pump. Two connected preparation chambers had direct heating stages (allowing current to be passed through a silicon heating element on the sample plate). Sputter and annealing cycles for sample cleaning and depositions were performed in one of these chambers. Each of the preparation chambers was pumped by an ion-getter pump. A fast-entry load lock allowed for the quick introduction and removal of samples and tips from the system (the turbo molecular pump was situated here). For the transfer of prepared samples to other systems,

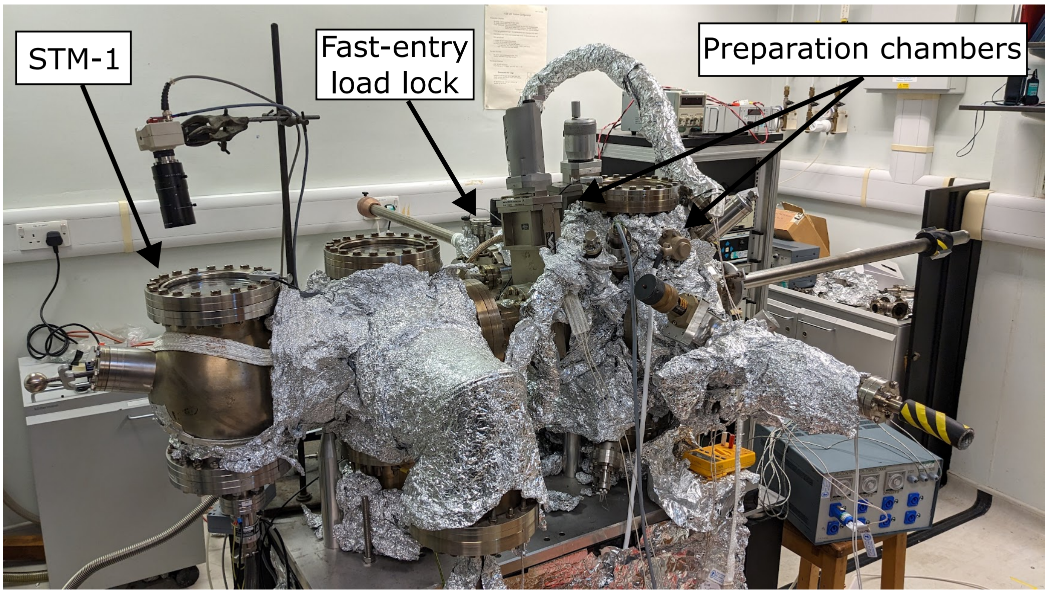

Figure 3.27: The Omicron UHV STM-1 system. The STM is located (on the left side) in the same chamber as the wobble stick. The wobble stick is used to transfer samples to the STM and between the transfer arms and carousel. Other parts of the system (right) are used for sample preparation.

a vacuum suitcase was also available for use, pumped by non-evaporative getter and ion-getter pumps. Base pressures of the system were between 2x10^{-10} - 3x10^{-9} mbar, depending upon the chamber and pumping speed of the pumps.

3.4.0.2 Scienta Omicron POLAR STM/AFM low-temperature system

The low-temperature bath cryostat AFM/STM system, pictured in Figure 3.28, was used for low and variable temperature SPM measurements. The SPM is controlled by an ‘SXM controller’. The system allows the use of sample plates with the capability to heat the sample in the SPM head whilst acquiring SPM measurements between 5-420 K. The main SPM chamber is pumped by both an ion-getter pump and titanium sublimation pump, producing a base pressure of 6.5x10^{-11} mbar and a lower pressure is possible when the cryostats are cooled with cryogens. An attached preparation chamber and load lock, pumped by a turbo molecular pump, is used for sputtering and annealing samples. The heating stage is also used for depositions via thermal sublimation. It is also possible to prepare tips by annealing and/or sputtering.

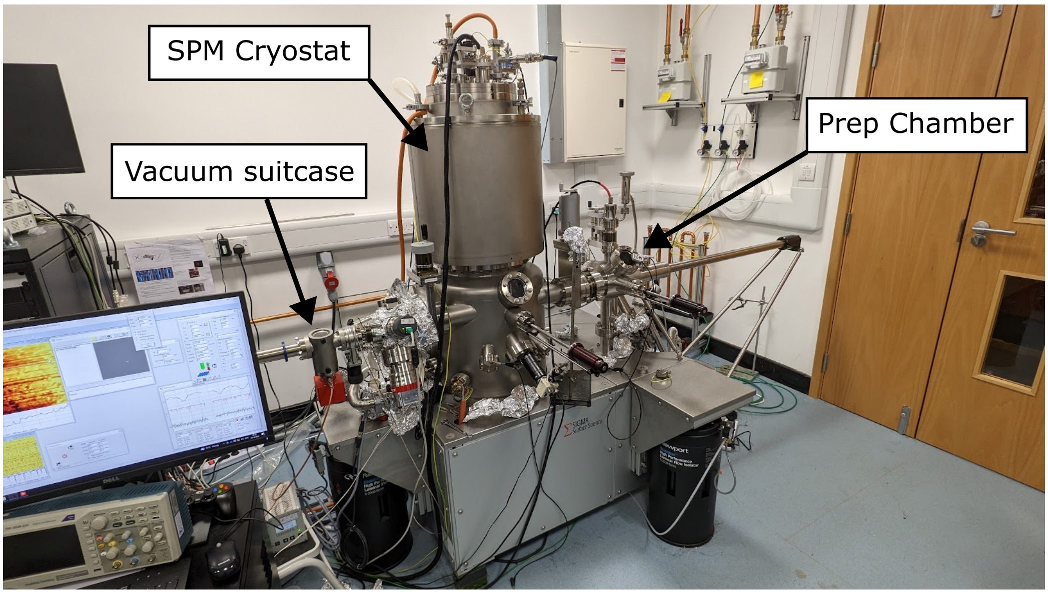

Figure 3.28: The Scienta Omicron POLAR low-temperature STM/nc-AFM system.

3.5 Surfaces

Within this thesis, the surfaces employed were crystalline metals possessing well-defined structures that can be described by a repeating unit cell. In the case of Ag and Au, used in this thesis, the metals are examples of face-centred cubic (*fcc*) metals (the unit cell is shown in Figure 3.29). Metals can be cut at a specific angle relative to the unit cell to create surfaces with a specific surface arrangement. Planes within the crystal can be described by Miller indices, which are three integer values (hkl), and the planes are therefore orthogonal to the vector described by $h\mathbf{x} + k\mathbf{y} + l\mathbf{z}$ where $\mathbf{x}, \mathbf{y}, \mathbf{z}$ are vectors of the unit cell. The plane (111) is shown in Figure 3.29 (green plane) for an *fcc* bulk crystal; it creates a surface with a hexagonal structure, whereas, for the (110) plane the surface structure appears as a rectangular arrangement of atoms.

3.5.1 Surface reconstruction of Au(111)

For Ag(111) and Cu(111), the experimentally observed surface shows the expected close-packed hexagonal structure, however, the Au(111) plane does not exhibit the same surface packing shown in Figure 3.29. Instead, the surface exhibits a $22\times\sqrt{3}$ surface reconstruction [91]. The top layer of surface atoms compresses to

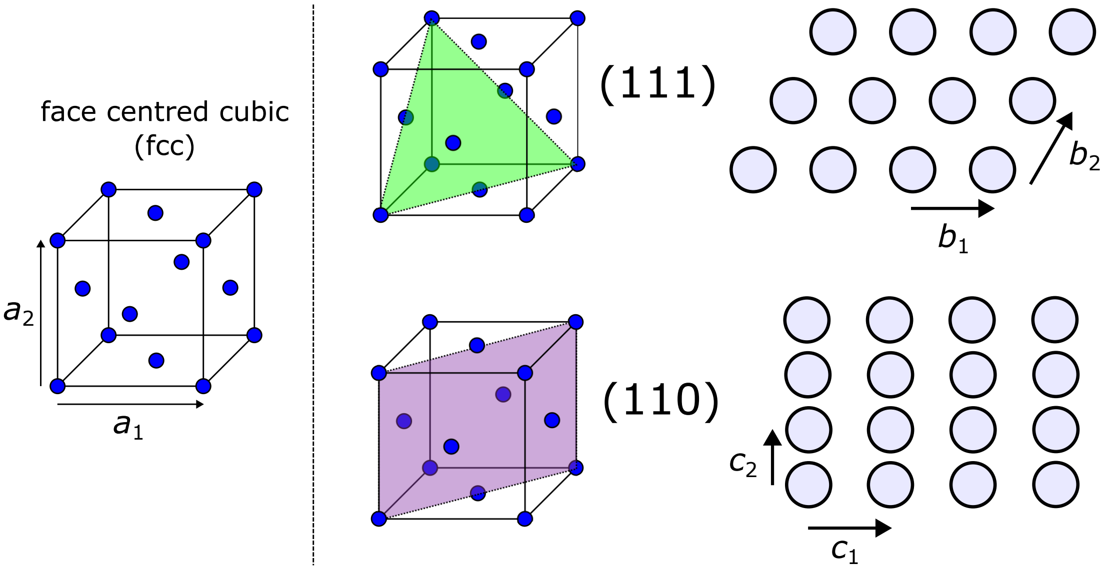

Figure 3.29: *fcc* unit cell, with lattice constants of a_1 and a_2. The (111) plane is shown as the green plane within the *fcc* unit cell, the surface plane gives hexagonal geometry with unit cell vectors of b_1 and b_2 (where $b_1 = b_2 = \frac{\sqrt{2}}{2}a$). The (110) plane is shown as the purple plane within the *fcc* unit cell, the surface plane gives rectangle geometry with unit cell vectors of c_1 and c_2 (where $c_1 = a_2$ and $c_2 = \frac{\sqrt{2}}{2}a$).

fit 23 atoms into the space of 22 along one of the $\langle 111 \rangle$ surface directions (see Figure 3.30a). This has the effect of causing a buckling of the surface, forming solitons (seen in Figure 3.30b). The surface atoms are laterally displaced from their bulk positions, resulting in *fcc* and hexagonally close-packed (*hcp*) vertical arrangements. This can be explained by the relationship between the surface atoms and the underlying substrate atoms. In Figure 3.30c, the *fcc* packing shows an "ABC" mode where the surface atoms line up with the substrate atoms after three atomic plane spacings ("ABAB"). The *hcp* packing shows that the surface atoms line up with the substrate atoms after only two atomic plane spacings. This small, but significant, registry change by surface atoms can lead to certain sites on the surface being more interacting than others [91].

At larger scales, the solitons form the herringbone reconstruction (see Figure 3.31a) and are observed to change direction on the surface (giving rise to the 'elbows' of the reconstruction). The solitons can be defined as either type x or type y. On type x solitons, point dislocations form due to the end point of atomic rows being incorporated into the surface layer as part of the reconstruction,

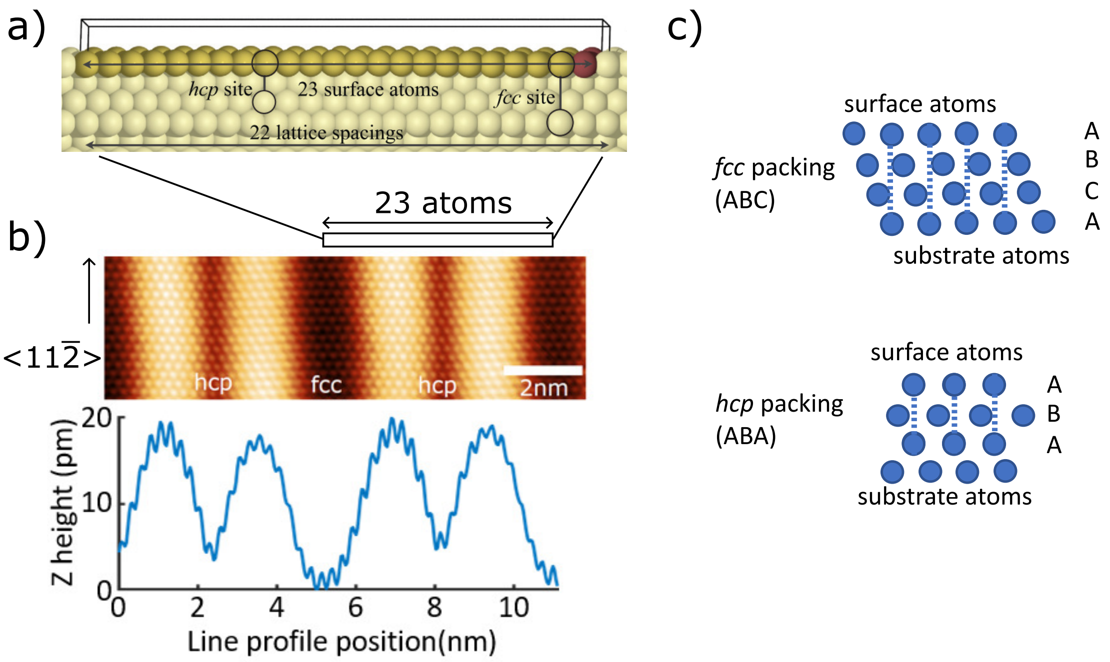

Figure 3.30: (a) Side view of Au(111) with the $22 \times \sqrt{3}$ herringbone surface recontruction [91]. (b) Shows the atomically resolved solitons in STM from the POLAR system. A line profile from the image shows the variation in height along the reconstruction. (c) Shows the difference in the registry for the *fcc* (AB packing) and *hcp* (ABC packing) surface atoms with the substrate. Further details: (a) Taken from F. Hanke *et al.* [91] (b) STM image parameters $V_{\text{sample}} = -1.0$ V, $I_{\text{set}} = 400$ pA, $T_{\text{sample}} = 4.7$ K.

leading to Burgers circuits with nonzero Burgers vectors (see Figure 3.31b iii, iv) [92]. Type x solitons do not form point dislocations due to a zero Burgers vector. Point dislocations are commonly adsorption and nucleation sites for atomic and molecular species [92]. In Figure 3.31a, we define *fcc* elbows as elbows with the majority of surface area being *fcc* sites, conversely, *hcp* elbows appear to have a larger surface area for *hcp* sites.

3.5.2 Surface preparation

To clean Ag and Au metallic surfaces in UHV, cycles of sputtering and annealing are performed on the surface to remove contaminants and then produce ordered structures by providing thermal energy for surface reconstruction. Sputtering is performed by leaking noble gases (typically high-purity Argon) into the system via a leak valve, and ionising the gas to Ar^+ ions using a sputtering gun. These

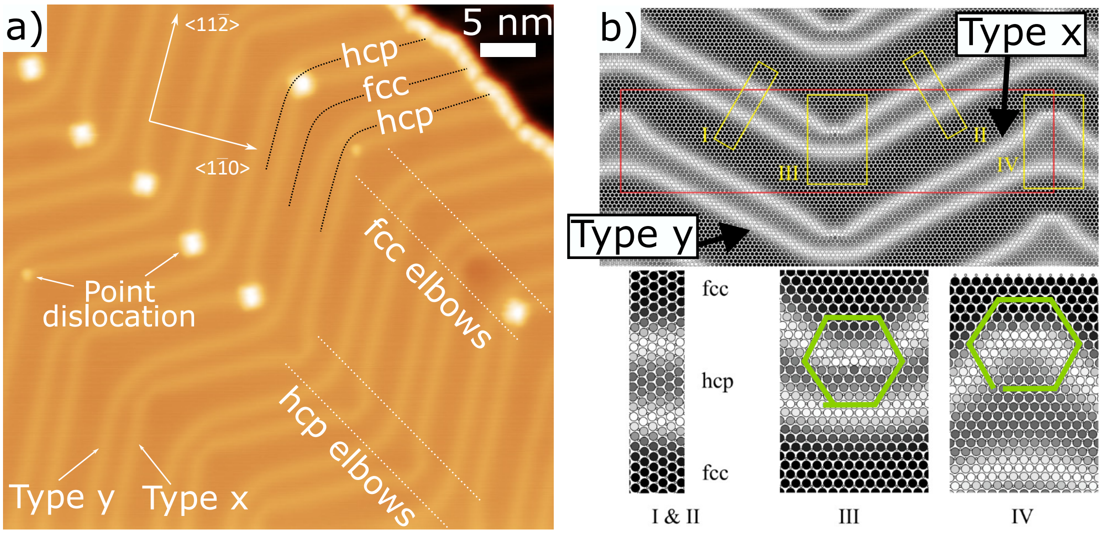

Figure 3.31: (a) Overview of the herringbone reconstruction formed on a Au(111) surface. The solitons form elbows on the surface and can be defined as either type x (forming point dislocations due to non-zero Burgers circuits where atomic or molecular species commonly adsorb, as shown by the bright features) or type y. *Fcc* elbows have the majority of the elbow as *fcc* sites, compared to *hcp* elbows that have the majority of the sites as *hcp* sites. (b) Shows the atomic resolution of the herringbone elbows, and shows the nonzero Burgers circuits formed at the type x point dislocations. Image settings: (a) $V_{\text{bias}} = 2.0$ V, $I_{\text{set}} = 20$ pA. Adapted (b) from Bartelt *et al.* [92].

ions are accelerated towards the surface by an electric field, where their impact on the surface causes the surface material to be removed. This treatment can be continued until all surface contaminants are removed (typically performed for 30 minutes in this work). The surface is then annealed to ~500°C. The annealing can be performed by a Pyrolytic Boron Nitride (PBN) heater in the case of a single crystal, or where Au or Ag on mica is used, current can be passed through a doped Si backing filament.

3.5.3 Surface summary

Within this thesis, the Au(111) and Ag(111) surfaces are employed to support on-surface processes, due to their inherent chemical inertness, allowing intermolecular interaction to take precedence. The metals produce large flat terraces and are relatively easy to prepare and keep clean within the ultra-high vacuum.

Furthermore, in the case of Au(111), the herringbone reconstruction provides an additional opportunity to study the effects of an anisotropic surface structure on molecular systems.

3.5.4 Molecular deposition

Within this thesis, molecular deposition was achieved by thermal sublimation of the molecules from a source onto a surface (see Figure 3.32). In the process of sublimation, molecules are heated to a specific temperature to achieve sublimation (phase change into a gas). The molecular gas is incident upon the surface held under UHV and adsorbs. The temperature used for deposition can be carefully controlled, and replicated, using thermocouples.

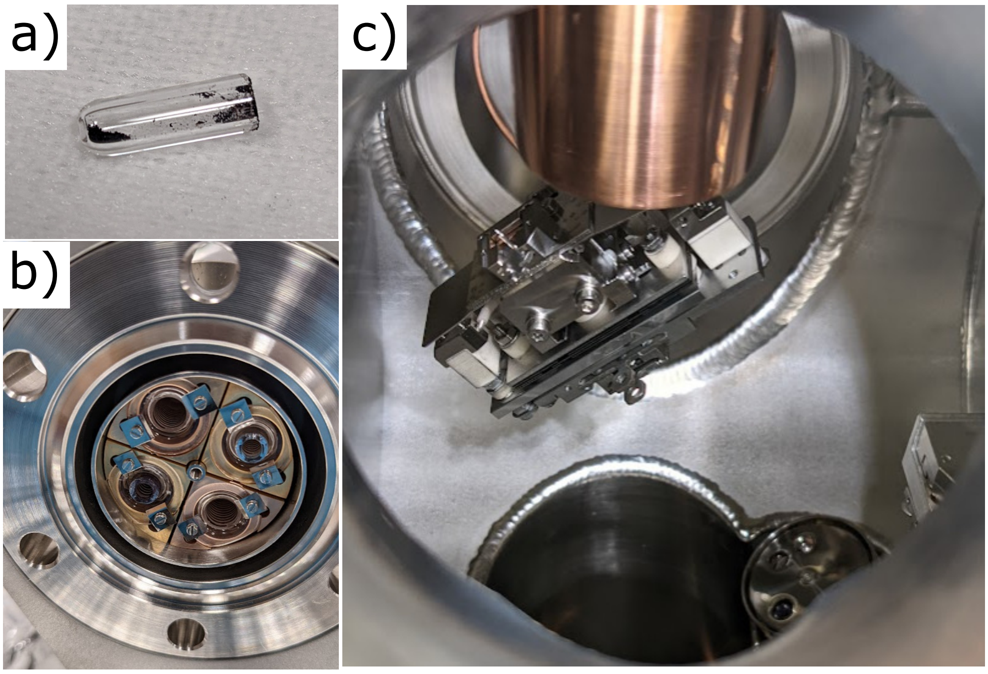

Figure 3.32: (a) Quartz crucible with tetraphenylporphyrin molecule inside. (b) The heating stage for the crucible. (c) Deposition of molecule from the crucible onto the sample.

3.6 Summary

In this chapter, the experimental techniques STM, XPS, NAP-XPS, NEXAFS, NIXSW and LEED used to characterise the structural, chemical and electronic properties of molecules, and on-surface processes were introduced. These techniques require ultra-high vacuum for optimal function and sample cleanliness.

Chapter 4

Self-assembly and diffusion of tetraphenylporphyrin on Au(111)

In this chapter, the preferential formation of close-packed islands of tetraphenylporphyrin within the fcc *regions of the Au(111) surface is explored. Submonolayer coverages of tetraphenylporphyrin were deposited onto Au(111), and upon cooling the surface to 4.7 K, small islands (2-3 TPP wide) formed within the* fcc *regions of the herringbone reconstruction. The close-packed islands have a specific orientation (15±3°) with respect to the herringbone soliton direction* ($\langle 11\bar{2} \rangle$)*. Variable temperature STM is used to observe island formation of the TPP by a series of consecutive STM images providing temporal resolution. Arrhenius analysis was employed to determine the barrier to diffusion within the* fcc *and* hcp *regions of the surface. This work formed part of a publication in Nano Letters.*

4.1 Self-assembly on Au(111)

An understanding of self-assembly and on-surface reactivity of molecular species is fundamental to the fabrication of devices which incorporate the functionality of molecular components [35]. Materials with specific catalytic, electronic, optical, and/or magnetic properties can, in principle, be realised by an appropriate choice of molecule-substrate systems [33]. The preparation of such materials, however, requires an understanding of the processes which give rise to ordered molecular arrays and, in the case of covalent organic frameworks (COFs), the mechanisms underlying the observed on-surface chemistry [93]. Scanning probe microscopy (SPM) approaches allow on-surface processes to be studied on the single-molecule and single atom level [94], and studies utilising non-contact atomic force microscopy have provided chemical-bond level resolution of these processes [95]. In addition, SPM techniques combined with photoelectron spectroscopies can provide detailed structural and chemical characterisation of on-surface processes [96–98].

The temporal evolution of on-surface diffusion has been studied *via* a variety of techniques [99], with Arrhenius-based analysis of sequential SPM 'images' providing the temperature-dependant rates of on-surface processes from which activation barriers and thermodynamic quantities may be obtained under UHV STM [42] and liquid STM [100] conditions. Examples of such quantities include the energy barriers for molecular diffusion [41, 101] and rotation [102].

Substrate topography plays a crucial role in on-surface processes, with SPM techniques facilitating the characterisation of both molecular species and surface features. Specifically, SPM studies have demonstrated that step-edges and surface reconstructions affect molecular diffusion [42], orientation [103, 104], and reactivity [42,105,106]. Molecular templates have also been employed to influence on-surface diffusion and reactivity [10,105]. Understanding the interplay between topography and surface-confined processes is a key prerequisite to influencing and controlling molecular structure formation and on-surface chemistry.

The Au(111) surface is frequently used to support molecular self-assembly and on-surface reactions. The shorter surface Au-Au bond length compared to that within the bulk, and the reduction in surface free energy provided by the AB/ABC packing of atomic layers parallel to the surface plane, results in atomic reconstruction where surface atoms buckle to form the characteristic $22\times\sqrt{3}$ herringbone structure [107, 108]. Nucleation of atomic [109, 110] and molecular [111–113] species within the *fcc* and *hcp* regions of the reconstruction have previously been observed, and the surface itself can initiate reactions. Interestingly, differences in the reactivity and surface interaction energies at the *fcc* and *hcp* sites, as calculated by DFT [91], may lead to preferred nucleation/reaction sites [114] (similar to the observation that Cu adatoms, and larger clusters, prefer *fcc* over *hcp* sites on Cu(111) [115]). The reaction products of on-surface synthesis have also been reported to be ordered by the Au reconstruction [27, 116, 117].

This leads to our study of TPP on Au(111). TPP is a well-studied molecule and is known to form close-packed structures on surfaces at LHe temperatures. We aim to characterise the self-assembly of these molecules on the Au(111) surface, whilst taking account of the additional effects of the anisotropic surface structure. Using STM and Arrhenius analysis to obtain a barrier to diffusion, we can try to understand the preferential *fcc* adsorption sites for TPP on Au(111).

4.2 Experimental methods

2H-TPP was purchased from Merck with a quoted purity of 99.8%. Molecules were thermally purified by degassing at 200°C for several hours prior to deposition. The molecules were deposited (using a Kentax UHV Evaporator heated to 225°C) onto a Au(111) single crystal (Surface Preparation Laboratory) held at room temperature. Coverage of 2H-TPP was altered by increasing/decreasing deposition time following surface cleaning. Surfaces were cooled (unless otherwise stated) to ∼4.7 K by inserting them into the STM head of the POLAR system and characterised using constant current scanning mode at that sample temperature.

4.2.1 Performance of STM under elevated sample temperatures

Later on in this chapter, Arrhenius analysis is performed to determine energy barriers to the motion of the TPP molecules. A main requirement to perform this is the ability to vary sample temperature and for the temperature to be stable over time. The POLAR low-temperature scanning probe microscope has the ability to have variable sample temperature while being cooled using LHe. The POLAR achieves variable sample temperatures on a small ‘flag-style’ plate (which the sample is attached to) and that is inserted into a normal sized flag-style heating plate containing a heating element and temperature diode (small sample plate shown in Figure 4.1a inset and heater plate Figure 4.1b inset). The heater element and temperature probe on the STM sample holder are connected via a feedthrough to a Lake Shore temperature proportional–integral–derivative (PID) controller.

The heating of the sample requires a feedback mechanism due to the thermal mass of the metal sample, holder and the changing cooling power of the system as the system heats up. The feedback mechanism, a PID controller, provides power (P) to heat the sample depending upon the set feedback PID constants ($K_\mathrm{P}, K_\mathrm{I}$ and K_D respectively) and the difference between the set temperature (T_set) and current temperature (T_cur). This feedback relationship is given by,

$$P(t) = K_\mathrm{P} T_\mathrm{d}(t) + K_\mathrm{I} \int_0^t T_\mathrm{d}(\tau)\, d\tau + K_\mathrm{D} \frac{dT_\mathrm{d}(t)}{dt}, \tag{4.1}$$

where $T_\mathrm{d} = T_\mathrm{cur} - T_\mathrm{set}$. The first term provides proportional control depending upon the magnitude between the set and current temperature. The second term accounts for the past values of the temperature difference and the third term acts to reduce the overshoot of the system by providing a damping response. In Figure 4.1, an example of changing temperatures to new set points is shown for both increasing (to 30 K) and decreasing (to 165 K) sample temperatures. In both of

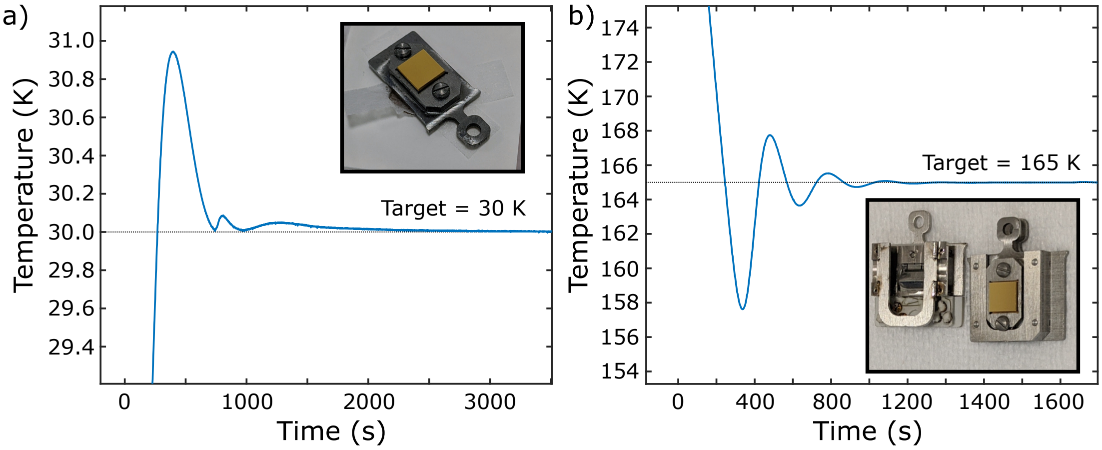

Figure 4.1: Temperature-time response for a resistively heated sample plate in the SPM stage of the POLAR system. The response is shown for a target temperature of (a) 30 K (heating from 20 K) and (b) 165 K (cooling from 205 K). Inset (a) shows the smaller 'flag-style' plate with the metal crystal attached. Inset (b) shows an empty sample heater plate (left) and the smaller sample plate inserted into the carrier plate (right).

these examples, the sample temperature overshot the target temperature before settling to the target. More careful calibration of the PID values could reduce the overshoot and improve the time taken to reach a stable temperature. However, as we look at a range of temperatures and care about the stability at lower temperatures, we settle for allowing the sample to thermalise over 1 hour. Feedback was optimised for the 20-30 K range where stable temperatures were reached after ∼30 minutes with less than 0.01 K of temperature variation detected.

4.2.2 Drift over time at elevated temperatures

One common issue within SPM is drift; either from piezoelectric creep or the sample temperature thermalising with the environment. At elevated temperatures, to study the same area of the surface, we require drift to be minimised. To reduce piezoelectric creep, we scan in the same area for a short amount of time (∼30-60 minutes). For thermal drift, we need the sample temperature to be stable over long periods of time. To do this, before scanning, the sample is left at the target temperature for one hour prior to the commencement of scanning. Following this, 5-20 images are taken in approximately the same fine piezo position before the measurement of the data for Arrhenius analysis. Whilst sequential STM images were taken in the same place on the sample for Arrhenius analysis over ∼20 hours, the surface features within the image drifted slightly. Shown in Figure 4.2 is the root mean squared (RMS) displacement of a static feature of the surface for each elevated sample temperature as a function of time at that location. The displacement is measured for each image compared to the 'first' image in the series. The oscillation of the displacement is due to the change in scan direction between the up and down scan.

4.2.3 Comparison of cooldown rate of counter-heated and normal samples

As the sample plate is resistively heated (with the bath LHe cryostat counter cooling the sample), the surrounding area of the STM head is also heated until thermal equilibrium is reached between the cryostat and the heating stage. When

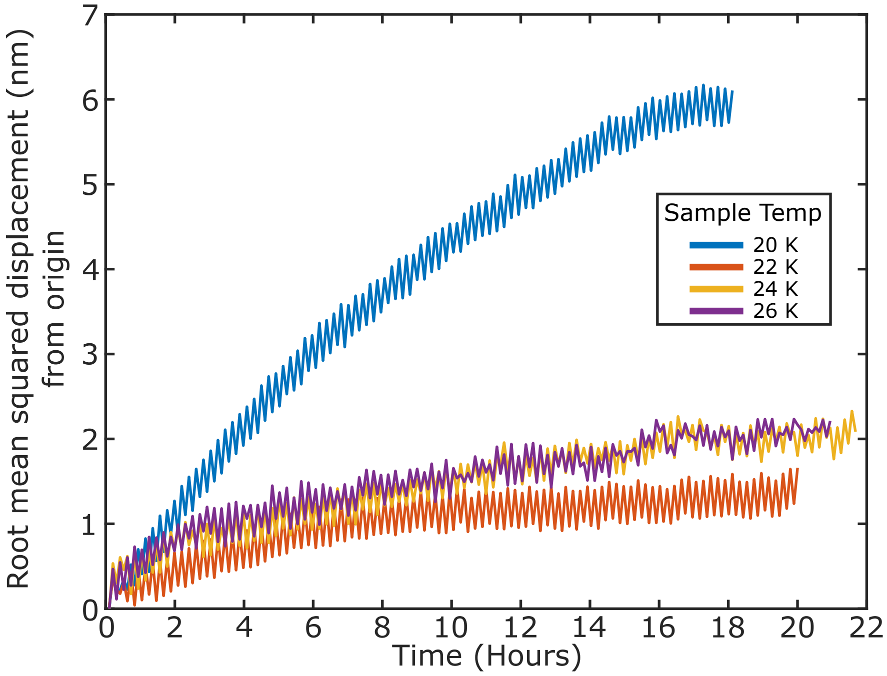

Figure 4.2: Root mean squared (RMS) displacement of a static feature on the surface, showing how that feature appears to move over time at elevated sample temperatures. Movements are attributed to thermal drift over time. The oscillation can be attributed to the changing of the slow axis scan direction. The 20 K temperature drifted more than the other temperatures, but this is likely due to it being the first temperature recorded in the sequence. Taken from images with dimensions of 100 × 100 nm (pixel count 500 × 500, the effective resolution is 0.2 nm).

sample heating is no longer required (and is turned off), effective cooling power on the sample is reduced (as the surrounding STM stage is warmer than 4.7 K). Therefore, the sample cools to 4.7 K more slowly, following heating the sample in-situ to 125 K taking ∼2.1 hours, compared to cooling immediately from 280 K to 4.7 K; taking ∼1.1 hours. The difference in cooling rates is shown in Figure 4.3. From experience, the Z axis STM drift is minimal ∼1 hour after reaching 4.7 K (indicating minimal further cooling).

4.3 Self-assembly for low coverages of TPP

At very low coverages (∼0.04 ML), TPP is shown in Figure 4.4a-b to absorb at step-edge sites and point dislocations on type x solitons [118]. Some of the additional features of the Au(111) surface highlighted in Figure 4.4a are described

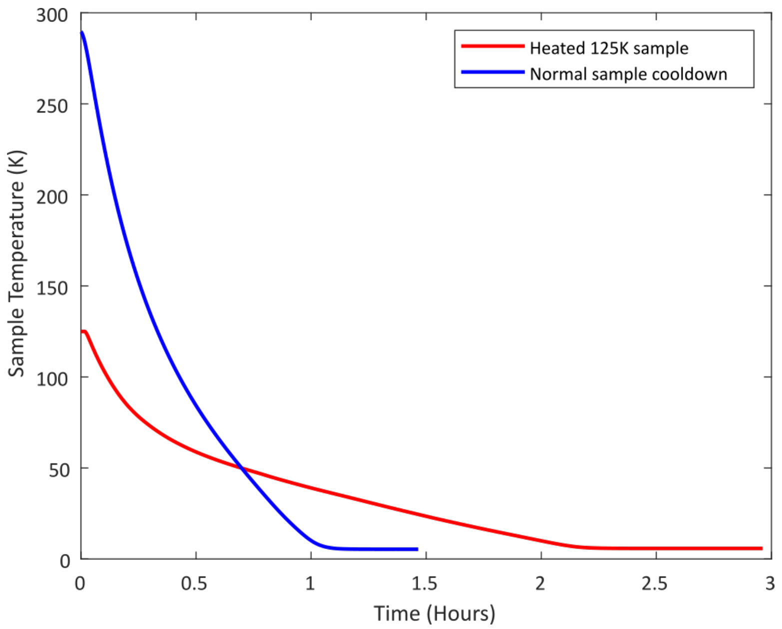

Figure 4.3: Temperature change as a function of time for a Au sample cooling to 4.7 K for; (i) a sample that has been counter-heated to maintain a sample temperature of 125 K (red), and (ii) the same sample that was at room temperature prior to being cooled to 4.7 K immediately upon insertion into the STM (blue).

in Section 3.5.1. At this coverage, no close-packed structures were observed and not all point dislocation sites are filled. We conclude that the step edge is the preferred adsorption site over point dislocations. Such behaviour is frequently observed with lower coverage meaning molecules may freely diffuse and be captured at favourable adsorption sites, such as step-edges and surface defects. The adsorption of TPP at the step-edge (Figure 4.4b) shows that the core of the TPP molecule is above the low-coordinated Au atoms within the terrace step-edge, leading to the phenyl 'legs' of the TPP being observed on both upper and lower terraces.

Increasing the coverage (see Figure 4.5) to ~ 0.2 ML results in the formation of close-packed islands of TPP (as previously reported [37, 38, 98] and discussed in Section 2.2.1). Individual TPP are now adsorbed at nearly all point dislocation elbow sites of the herringbone reconstruction (see labelled 'PD') and, infrequently, are found within the *fcc* or *hcp* regions of the herringbone reconstruction. The small close-packed islands of TPP display anisotropic growth, constrained within the *fcc* regions of the reconstruction. We identify two distinct

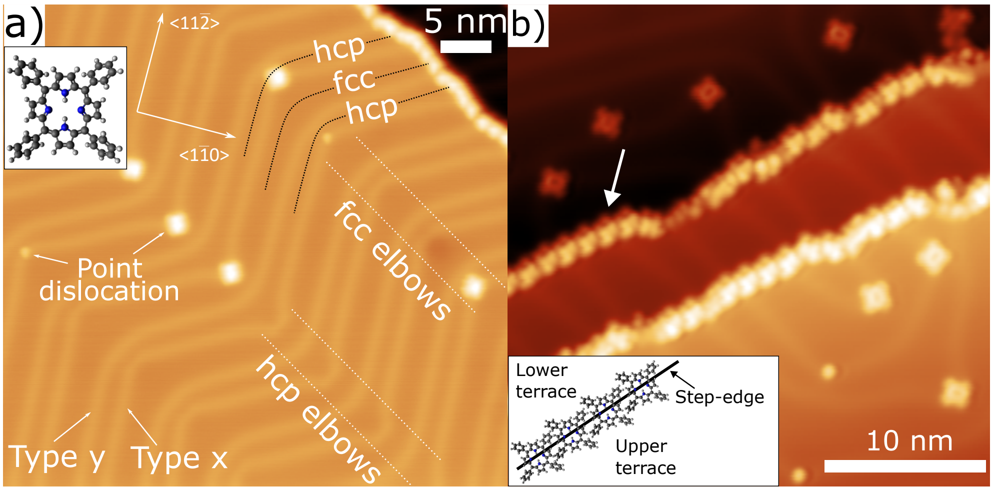

Figure 4.4: STM images showing very low coverages (∼ 0.04 ML) of TPP on Au(111). (a) The herringbone reconstruction is clearly visible; the bright lines (solitons) can be divided into type x (with point dislocations at elbows where TPP adsorb) or type y (with no dislocations). Solitons separate the *fcc* and *hcp* regions. We define *fcc* elbows as elbow regions with more *fcc* than *hcp* area and *vice versa*. (b) TPP is adsorbed at the point dislocation sites and the step-edges. The phenyl 'legs' appear on both the upper and lower terraces of the step-edge (see arrow and inset for schematic diagram). Image settings: (a) $V_{\mathrm{sample}} = -1.8$ V, $I_{\mathrm{set}} = 50$ pA. (b) $V_{\mathrm{sample}} = 1.0$ V, $I_{\mathrm{set}} = 50$ pA.

types of elbow regions, which we label as *fcc* elbows (B_{fcc}) and *hcp* elbows (B_{hcp}), (see Figure 4.4a and 4.5a) where a local distortion ('pinching' and/or 'bulging') of the solitons gives rise to an increase in the area covered by either the *fcc* or *hcp* regions respectively. Our STM data indicates the B_{fcc} has a 'growth region' (see Figure 4.5) that promotes the formation of TPP islands, something that is not typically seen in the B_{hcp} regions. This is consistent with a process where TPP islands nucleate at B_{fcc} and grow along *fcc* regions. The ordering of molecular species within the herringbone reconstruction has been observed frequently [27,111–113,116,117,119], but to the best of our knowledge the mechanisms driving the formation of anisotropic growth have not been characterised with respect to the energy barriers for diffusion. It is clear from Figure 4.5a that islands form preferentially in *fcc* regions (see dashed lines for highlighting some *fcc* regions), with the long axis of the islands orientated at 15±3° to the bright line of the herringbone reconstruction ($\langle 11\bar{2}\rangle$ directions). These rectangular islands typically contain 2-3 TPP species across the short axis; limited by the area

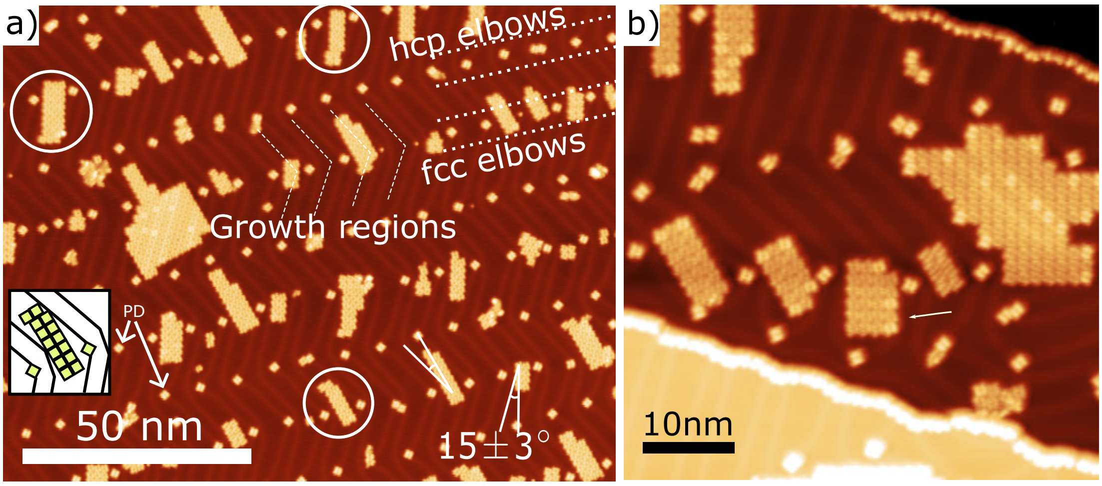

Figure 4.5: (a) STM image of a ~0.2 ML preparation of TPP ($V_{\text{bias}} = 2.0$ V, $I_{\text{set}} =$ 20 pA). Small close-packed islands form almost exclusively within *fcc* sites of the *fcc* elbows ('growth regions'). The ends of these islands can be seen to laterally shift to stay within the *fcc* regions of the surface (circled - inset shows a schematic diagram of this shift). Larger islands appear to grow out into the *hcp* regions of the surface. The islands are orientated approximately ±15° from the soliton direction. Point dislocation sites (labelled 'PD') are almost all exclusively filled with adsorbed TPP. A full sized version of this image can be found in Appendix A.2 (b) Similar packing as seen in (a), but disruptions in the herringbone allow for larger *fcc* regions. This larger *fcc* region (arrow) is filled with TPP islands. Showing a clear preference for *fcc* regions. In (a) and (b) bright TPP within islands could be attributed to TPP sitting atop an adatom [37]. Image settings: (a) $V_{\text{bias}} = 2.0$ V, $I_{\text{set}} = 20$ pA. (b) $V_{\text{bias}} = -1.8$ V, $I_{\text{set}} = 50$ pA

within the *fcc* regions (at B_{fcc}). TPP molecules can be observed to be laterally displaced to maintain island growth within the *fcc* area (see circled islands in Figure 4.5a and inset showing a schematic diagram of the TPP displacement). When the Au reconstruction is locally disrupted, such that the area of the *fcc* region is increased, TPP islands fill this *fcc* region and exhibit an island aspect ratio closer to 1 (see Figure 4.5b) whilst still avoiding *hcp* regions. Another example of a locally disrupted herringbone reconstruction is shown in Appendix A.1. Packing of TPP here shows that there is not an intrinsic requirement for islands to be 2-3 TPP wide, but rather growth laterally is not as energetically favourable into *hcp* regions.

Larger island growth is observed to extend into *hcp* regions (see Figure 4.5a-

b) where there is sufficient local availability of TPP molecules that results in the saturation of the growth region area. We postulate that angularly aligned islands in neighbouring *fcc* regions (the smaller 2-3 TPP wide islands) may stabilise growth in the interstitial *hcp* regions forming the larger islands. In all cases, it is clear that the structure of the herringbone reconstruction drives the alignment and distribution of the molecular islands. The internal structure of the larger close-packed islands (see Figure 4.6) are similar to that previously reported [98]. In this study, an overlayer was measured by STM to the unit cell dimensions of $a = 1.46 \pm 0.05$ nm, $b = 1.49 \pm 0.10$ nm and $90 \pm 3°$. This was the only packing motif found, compared to those previously reported which showed multiple packing modes [98].

The adsorbed TPP are assumed to all have the same chemical structure. However, TPP adsorbed at point dislocation sites have a different apparent to-

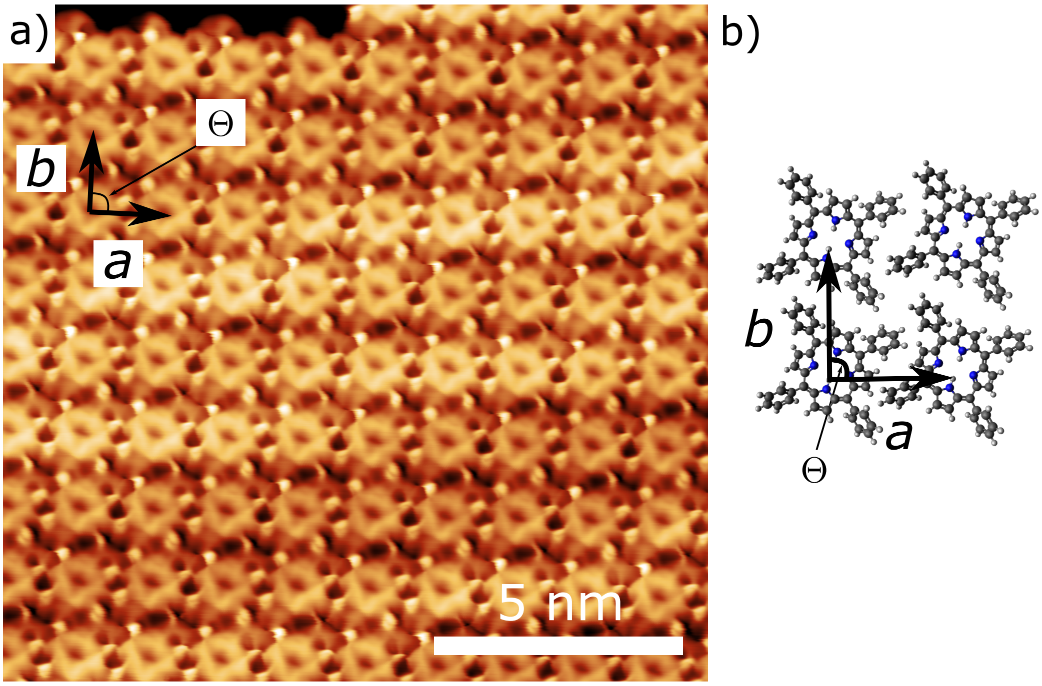

Figure 4.6: (a) Calibrated STM image (using Au(111) atomic resolution image) of a close-packed TPP island showing the vectors of the square unit cell. Within this image, it is assumed that the TPP is adsorbed in the ‘saddle’ confirmation. As seen later in this chapter, planar TPP species are reported to have a single central lobe topography [55]. (b) A ball-stick diagram of the TPP close-packed overlayer that forms the island. Image settings: (a) $V_{\text{bias}} = 0.45$ V, $I_{\text{set}} = 610$ pA.

pography compared to those within a close-packed island. This difference can be clearly seen in Figure 4.7a, where the TPP at a point dislocation site (i) has two opposite parts of the porphine ring raised (see line profiles in Figure 4.7b), in comparison to a TPP that appears to have a flatter structure (ii) and this topography structure makes up the majority of the adsorbed TPP. Although, some TPP are also observed to have a different topography (iii) where one side of the porphine ring appears to be raised. The question here is whether this is predominately an electronic or topographical feature, or a combination thereof.

As reported by Mielke *et al.* [37], TPP adsorbed atop adatoms on the surface can appear to have differing molecular topographies (see Mielke *et al.* data for DFT and simulated STM data in Figure 4.8a [37]) consistent with (i) adatom

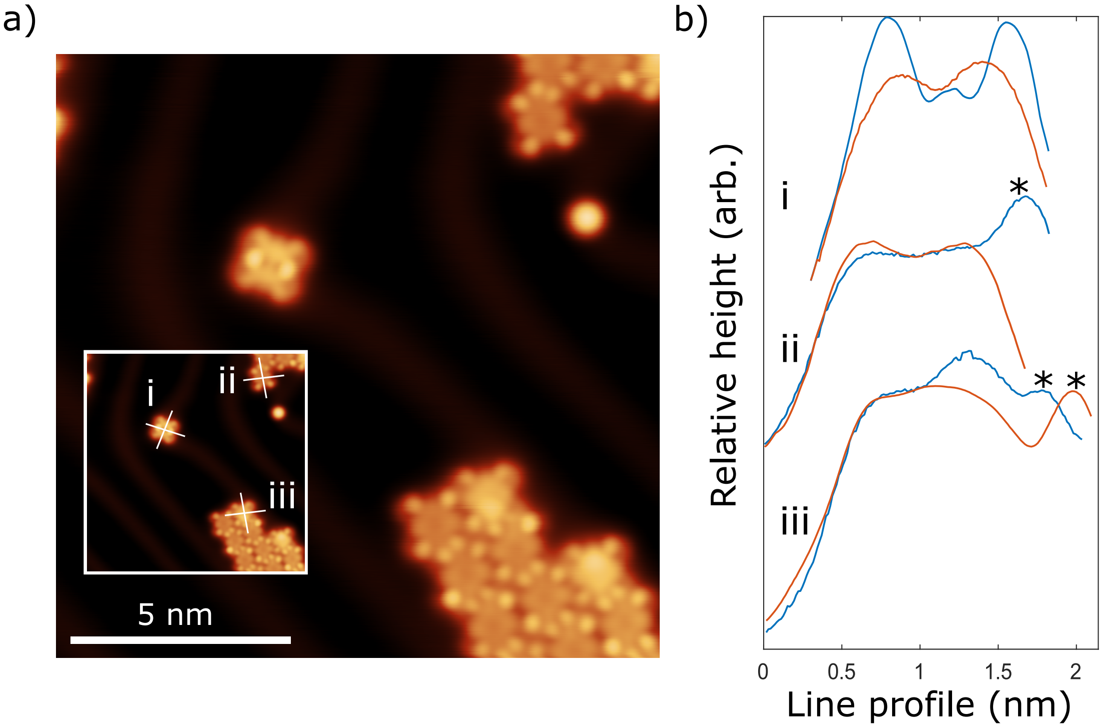

Figure 4.7: (a) Shows an STM image of TPP within an island and one TPP adsorbed at a point dislocation site. Inset shows the location of line profiles shown in (b). (b) Shows the line profiles of (i) a TPP adsorbed at a point dislocation site (shows topography indicative of adatom TPP), (ii) a TPP adsorbed within an island and (iii) a TPP with one side of the porphine higher. Lines clipped on the right hand side (RHS) when clear heading down. The blue line corresponds to the vertical line profile, and the red line corresponds to the horizontal line profile. Starred peaks indicated where these features are due to other TPP. STM image parameters $V_{sample} = -0.54$ V, $I_{set} = 510$ pA.

TPP and (ii) adsorbed TPP with no adatom (in Figure 4.7). The DFT structure within Figure 4.8a does not appear to show a clear structural difference between the saddle confirmation or the adatom TPP variation, however, the simulated STM images taken around the Fermi level show differing structural topographies. Mielke *et al.* show using DFT and dI/dV spectra (as shown in Figure 4.8b), that the differing surface topography in STM is likely due to electronic properties of the TPP differing between the adsorption types. In addition, Mielke *et al.* [37] noted that adatoms at point dislocation sites and within the bulk may also have different heights compared to the local surrounding area - potentially providing a reason for the difference in the topography between dislocation and other adatom TPPs (i vs iii topography). It is important to note, however, that due to STM limitations, we are observing the electronic properties (principally the LDOS) of the molecule rather than absolute height differences. We should consider that these anomalous TPP topographies may be the result of impurities in the source material, which may show alternative properties, however, the findings are consistent with Mielke *et al.* [37].

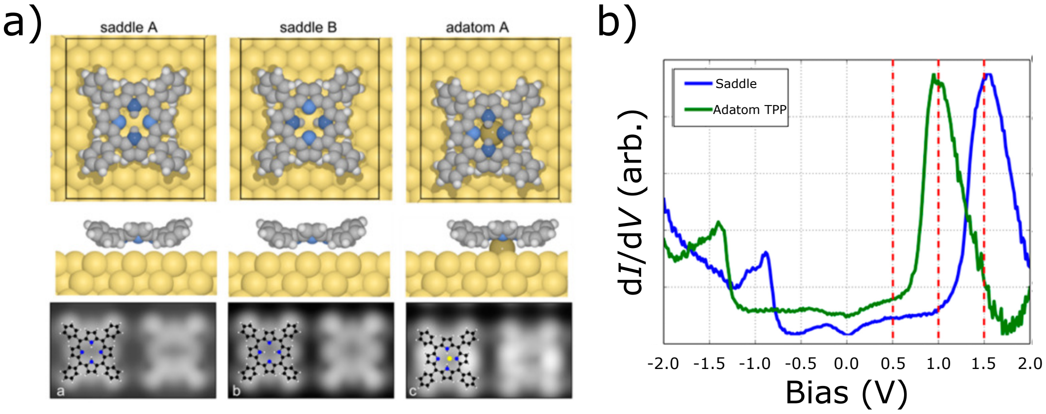

Figure 4.8: Data from Mielke *et al.* showing the variation in electronic states due to adsorption characteristics. (a) DFT structural adsorption conformations of two tautomers of saddle TPP, compared to an adatom TPP. The simulated STM image from the DFT model is shown, taken around the Fermi level. (b) Shows the difference in electronic states between saddle and adatom TPP as measured by STM. Taken from Mielke *et al.* [37].

4.4 Kinetic and thermal effects on the self-assembly of TPP on Au(111)

In the previous section, we observed the result of TPP self-assembling into close-packed islands on Au(111) following deposition onto a room temperature surface followed by cooling the substrate to 4.7 K. Under these conditions, the TPP preferentially formed islands within *fcc* growth regions of the herringbone reconstruction. To explore the dynamics of diffusion and island growth of a sub-monolayer TPP on Au(111), a series of STM measurements were performed with the sample held at temperatures in the range 4.7-285 K (achieved using a base plate containing an integrated heater and temperature diode). A preparation of ∼0.16 ML TPP on the Au(111) surface was thermally sublimated onto a surface at room temperature. The sample was then inserted into the STM head (at 4.3 K) and began counterheating the sample using the Lake Shore controller proportional–integral–derivative (PID) to maintain sample temperature at 285 K.

Figure 4.9 illustrates the temperature of the sample as a function of time, with the plateau regions indicating where the temperature was allowed to stabilise for image acquisition. For sample temperatures in the range 285-205 K (see insets in Figure 4.9), molecular diffusion is on a timescale faster than that of image acquisition and only surface features such as the herringbone reconstruction and step-edges are resolved; discontinuities and 'noise' in the images are indicative of molecular diffusion. At T_{sample} = 165 K, TPP islands are visible which exhibit a close-packed structure with a square lattice. The diffuse appearance at the edges of the island suggests that continuous diffusion is occurring to and from the island (discussed in detail in Section 4.5). Features are also observed at the point dislocation sites of the herringbone reconstruction, where individual TPP species are absorbed. Reducing the temperature to 125 K confirms the presence of TPP at point dislocation sites, due to the improved tip condition. Smaller islands (relative to those present at 165 K) are now observed, in line with the expected dependence of critical island size on temperature [43,120]. The expected critical island size decreases with temperature, due to reduced diffusion from the island, meaning that smaller islands will be visible [43, 120]. Upon cooling down

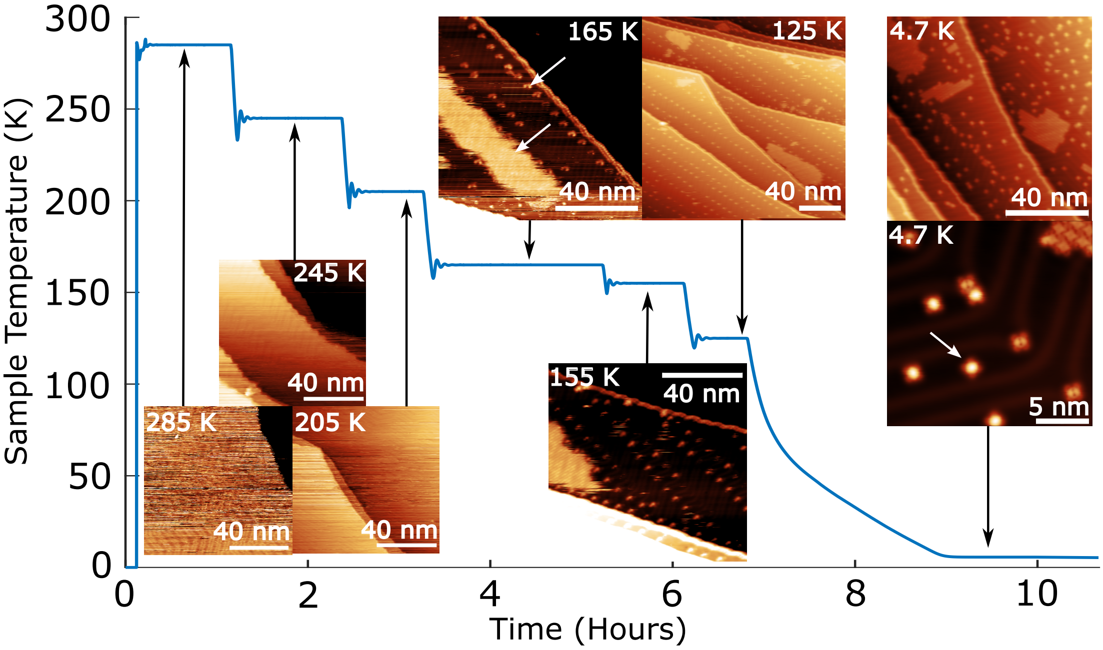

Figure 4.9: Sample temperature, with corresponding STM data, as a function of time (sample initially at room temperature, with discontinuity indicating sensor being connected). STM images show freely diffusing TPP at 285-205 K; mobile islands at 165-155 K with TPP adsorbed at point dislocation sites on herringbone; stable islands and TPP at point dislocations at 125 K; and coexisting stable islands and individual TPP within both *fcc* and *hcp* regions at 4.7 K. All images (except close-up image) scan settings were $V_{\text{bias}} = 0.5$ V, $I_{\text{set}} = 10$ pA, close-up 4.7 K (bottom right) image settings were $V_{\text{bias}} = 0.4$ V, $I_{\text{set}} = 630$ pA. See Appendix A.3 for larger versions of these images.

the samples to 4.7 K, stable islands are observed (compared to the diffuse islands seen at higher temperatures), with a significant number of isolated TPP species adsorbed within the *fcc* (~80-90% of individual TPP) and *hcp* regions. The slower cooling rate for a sample imaged at several temperatures in the range 285-4.7 K (due to counter heating of the sample and by extension parts of the cryostat), as compared to one cooled directly from room temperature to 4.7 K, may underlie the observed prevalence for isolated TPP species.

The isolated TPP species that were formed due to the slower cooldown of the sample appear to have a different topography compared to normal TPP (compare to ‘normal’ TPP Figure 4.7 to isolated TPP Figure 4.10a). Line profiles of the TPP shown in the inset of Figure 4.10a are in Figure 4.10b. Within the individual TPP (Figure 4.10 i), there is little to no definition within the porphine centre, displaying only a bright central lobe. A similar topography profile was previously reported by L. Grill *et al.* (see Figure 4.11a, compared to our results in Figure 4.11b) [55]. There is a similar central 'intense lobe', that they attribute to a planar TPP (note, when comparing to later sections of this thesis, the planar TPP here is the result of the non saddle-shaped confirmation of the TPP, not the result of a ring-closing reaction) [55, 121]. These planar TPP may not be able to participate within the structure of the close-packed islands since the CH-π bond is one of the main interactions between TPP to form islands, and the π interaction is strengthened by the saddle-shape, which may not occur in these planar TPP species. The point dislocation TPP (ii) and within the island TPP

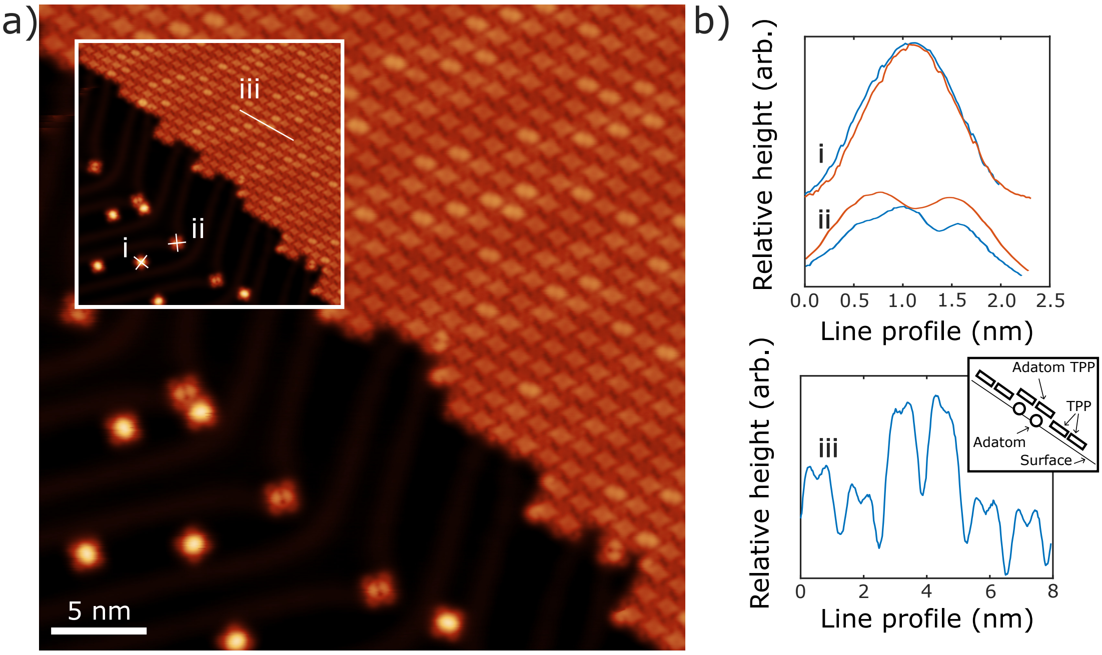

Figure 4.10: (a) Shows the edge of a close-packed island of TPP, with some TPP adsorbed at point dislocation sites. Due to the slower cooldown, isolated kinetically trapped TPP are also present in the image. These isolated TPP have a different topography structure from the other TPP. In the inset, line profiles of the topography of (bi) isolated TPP (broad centre peak), (bii) point dislocation TPP (similar structure to Figure 4.7) and (biii) multiple TPP showing height variation within the island (indicative of adatom TPP). Inset in (biii) shows a model of adsorption of the TPP in that line spectra. The line spectra are shown in (b) and are offset in the y-axis for clarity. The blue line corresponds to the vertical line profile, and the red line corresponds to the horizontal line profile. Image settings: $V_{\text{bias}} = 0.4$ V, $I_{\text{set}} = 630$ pA.

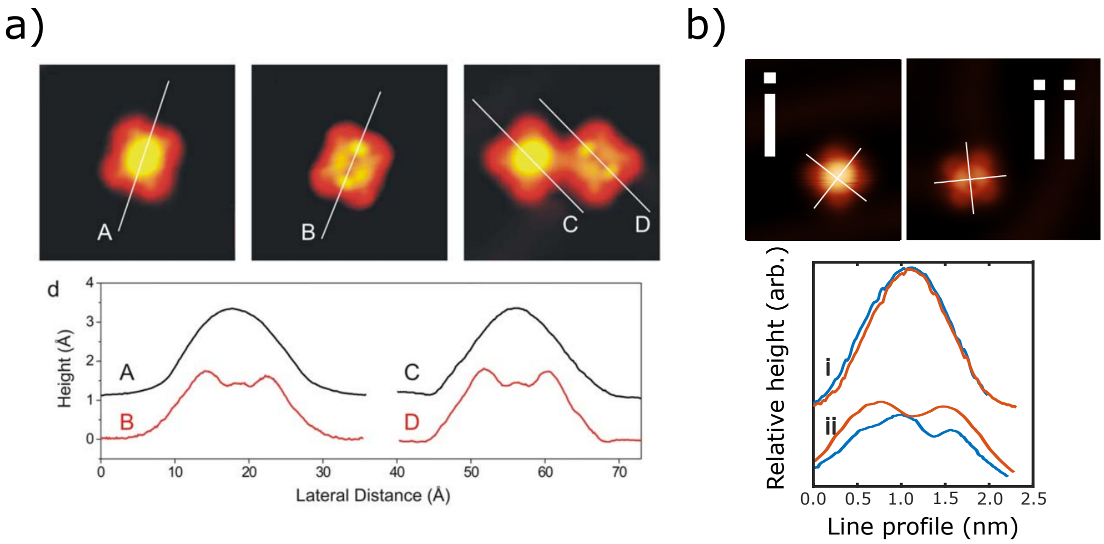

Figure 4.11: (a) Line profiles of the ‘planar’ and ‘saddle’ shaped adsorbed TPP as reported by L. Grill *et al.* [55], compared to the (b) TPP species observed in our experiments following slower cooldown. Comparing the line profiles of similar species. The blue line corresponds to the vertical line profile, and the red line corresponds to the horizontal line profile. Image settings: $V_{\text{bias}} = 0.4$ V, $I_{\text{set}} = 630$ pA. Taken (a) from L. Grill *et al.* [55].

(iii), however, appear to have a similar topography to those previously discussed in this chapter. The line profile within the island (iii) shows two elevated TPP with two ‘lower’ TPP on either side. This is indicative of the middle two TPP being adsorbed on an adatom (see model in Figure 4.10b iii inset) [37]. The herringbone reconstruction can be seen through the TPP island, but the height difference is not sufficient to be the cause of the two elevated TPP.

4.5 Island shape/formation at elevated temperatures

As part of this investigation, we view island formation ‘in real time’ to elucidate the mechanisms which result in the island formation observed at 4.7 K. Despite repeated efforts, we observed island formation at 165 K but were unable to view specifically individual TPP arriving to and diffusing from the island. As seen in Figure 4.9, the edges of islands are diffuse and appear to change readily between scans. This behaviour is attributed to TPP diffusing to and from the island. In

Figure 4.12, six consecutive images of a TPP island are shown at 130 K. The edges of the island vary significantly between the images, specifically at the top left corner, where throughout the images, the island is seen to grow to form a square-shaped corner. At this temperature, diffusion to and from the point dislocations can also be seen. There is also the spontaneous formation of an island (in Figure 4.12c) 2-3 TPP wide in *fcc* elbow region (growth region). This smaller island could be assumed to be below the critical island size for stability, as it was no longer present on the next image, where the diffusion quantity away from the island is greater than TPP joining the island [43]. We postulate that the energy barrier to diffusion is significantly lower than that for diffusion away from an island.

We took various STM measurements of islands over short periods of time at different temperatures. We wanted to determine if there was any dependency upon island changes per image as a function of temperature. Unfortunately,

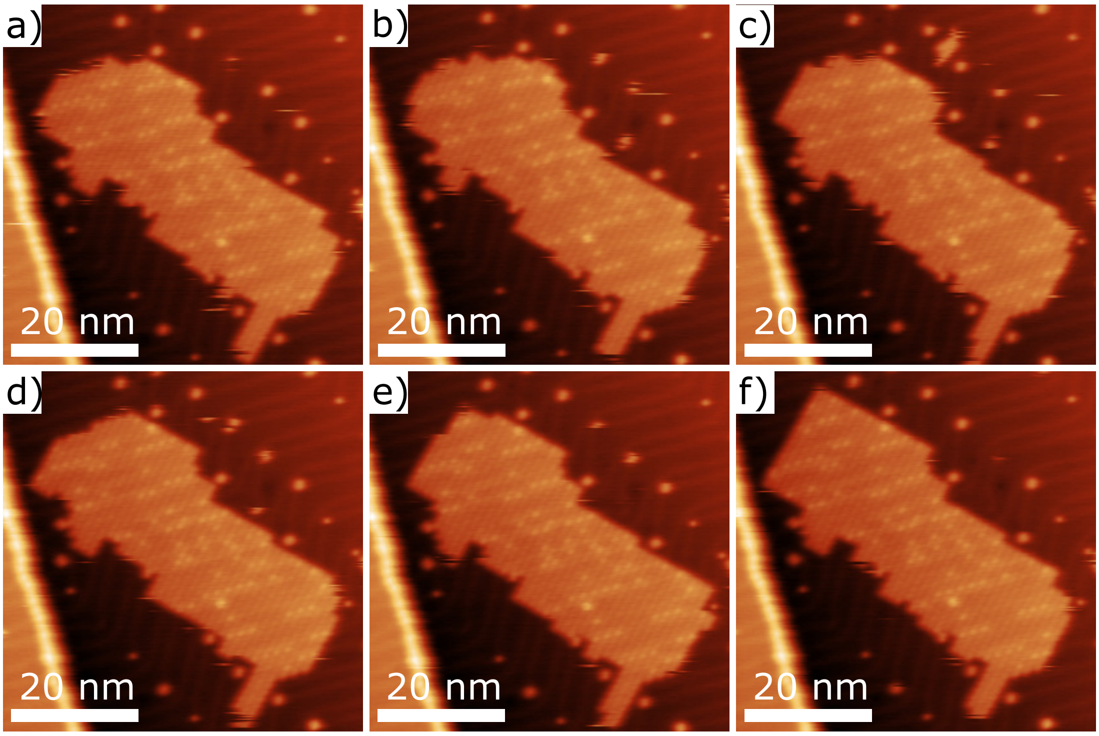

Figure 4.12: Sequential STM images of an island of TPP at 130 K. The edges of the islands differ from (a)-(f) showing significant nucleation and diffusion events. STM image parameters $V_{sample} = 0.5$ V, $I_{set} = 5$ pA (3 minutes per scan - image cropped from a larger image).

despite obtaining molecular resolution (similar to that in Figure 4.12) the quantitative determination of the island size over time was difficult. In summary, we could view the island growth of TPP that formed square shaped close-packed islands like those observed at lower temperatures. Now we move on to characterise the diffusion of individual TPP molecules.

4.6 Arrhenius analysis of individual TPP

To characterise the energy barrier to diffusion for individual TPP species within the *fcc* and *hcp* regions, a temperature-dependent rate of diffusion events was calculated. At $T_{sample} = 20$ K diffusion events were infrequently observed, while at 30 K the diffusion rate is faster than the image acquisition time. Upon reaching the target sample temperature, the sample was held at that temperature for 1 hour prior to data acquisition, this allowed for X, Y and Z thermal drift to be minimised. STM images were obtained for $T_{sample} = 20$, 22, 24 and 26 K (sequence of images numbering ∼180-210) over ∼20 hours from which the temperature-dependent rate could be obtained.

To extract the rate for the diffusion of TPP species on the surface of the Au(111) from a sequence of STM images, image processing was performed by MATLAB and Python code. A flow diagram showing the key parts of the processing is shown in Figure 4.13.

4.6.1 Image processing

The STM control software saves images of each recorded data channel as '.int' files, with a '.txt' parameter file containing the image parameters. Currently, these files are not able to be read using common scripting languages. Instead, approximately 850 images were opened, three-level planed and exported to .txt files containing pixel data using the 32-bit version of Gwyddion (image processing tool) powered by the inbuilt scripting Python code.

(i) Each .txt file contains one image and can be read by MATLAB. The file contains a grid 500 × 500 grid of pixels (=250000 total pixels per image). Each pixel contains one value (in nanometers) relating to the Z height of the tip (for that X/Y position). The pixels were normalised so that the lowest values equal 0, and the highest values equal 1 (shown in Figure 4.13(i) by the log-histogram of the pixel count vs. pixel height). By removing certain heights within the image (and setting those values to equal 0), parts of the image can be removed. For example, in Figure 4.13(i), when using all heights (red and blue values from the log-histogram), the full STM image is shown, however, when only the blue values are used (>0.23 normalised value), the herringbone is removed from the image and this only leaves surface features that are present on top of the surface.

(ii) Within MATLAB, a function called `regionprops` is used to determine connected features in a binarised image. The image generated by only using the blue values in part (i), can be binarised by setting all values to equal 1 unless they already equal 0. The function (`regionprops`) can then be used to detect surface features on the surface, as shown within Figure 4.13(ii). Appropriate thresholding of the image feature size removes too large or too small features.

Once the features over all images are identified, the position of one of those features can be tracked. A TPP adsorbed at an elbow site was generally chosen as it rarely changed position on the surface between images. This provides data on the drift of the scan window with respect to the surface. The image pixels were shifted to maintain the position of the fixed object in the same pixel location as shown in the schematic diagram in Figure 4.13(ii). This took a substantial effort to remove the drift/piezoelectric creep over approximately 20 hours. Furthermore, when there was a change in scan direction at the end of a scan, this caused a ‘wobble’ type effect in the Z position (where the image appears to move up and down between scan directions - we attribute this to the piezoelectric response in the slow scan axis) and this was seen to a lesser extent in the X and Y position of the images; this effect was mostly removed by this tracking treatment.

(iii) Once the drift between images was removed, the only change between subsequent images should be due to diffusion of the TPP species. The function `regionprops` was used to detect the TPP again in each drift removed image. The positions of the TPP were compared between subsequent images, to determine if the TPP had moved. To reduce false-positive readings, further checks were made with images two and three iterations along to ensure that movement had occurred (and was not an artefact of a single image). The position of the diffusion event was recorded.

The resolution of this diffusion detection was capped at 0.6 nm (or 3 pixels) due to a combination of the piezoelectric response of the SPM scan tube and thermal effects. This is a trade between statistics and resolution. A bigger image would capture more TPP diffusion events but would provide reduced resolution. It is therefore likely that diffusion events on the length scale of single atomic sites are not fully captured and that the diffusion events recorded are 'long' jumps over several atomic sites [101, 122].

(iv) To determine if the diffusion event occurred in the *fcc* or *hcp* regions of the surface, the *fcc* regions could be drawn on to the image. The diffusion event positions could then be compared to those regions and counted.

The diffusion events per image (and region) were converted into a rate by reading the acquisition time per image from the image metadata. This was then used in Arrhenius analysis to calculate an energy barrier for diffusion for each surface region for the TPP. We initially attempted to determine diffusion events manually, but this is not possible as there is too much data, and it is not possible to easily see movement between images on the scale of ~ 3 pixels.

Figure 4.14 shows an example of sequential STM images with the position of diffusing molecules highlighted. These images reveal two distinct molecular contrasts (bright/dark) which are assigned to TPP within *fcc*/*hcp* regions (bright) and TPP pinned at the point dislocation sites on the herringbone reconstruction (dark). Over the temperature range investigated, diffusion of the pinned TPP was not generally observed; likely due to enhanced adsorption energy at these sites. This bright/dark contrast is distinct from that previously reported and assigned to the presence of Au-adatoms below TPP [37] since the topography of these isolated TPP is a single peak (see Figure 4.10).

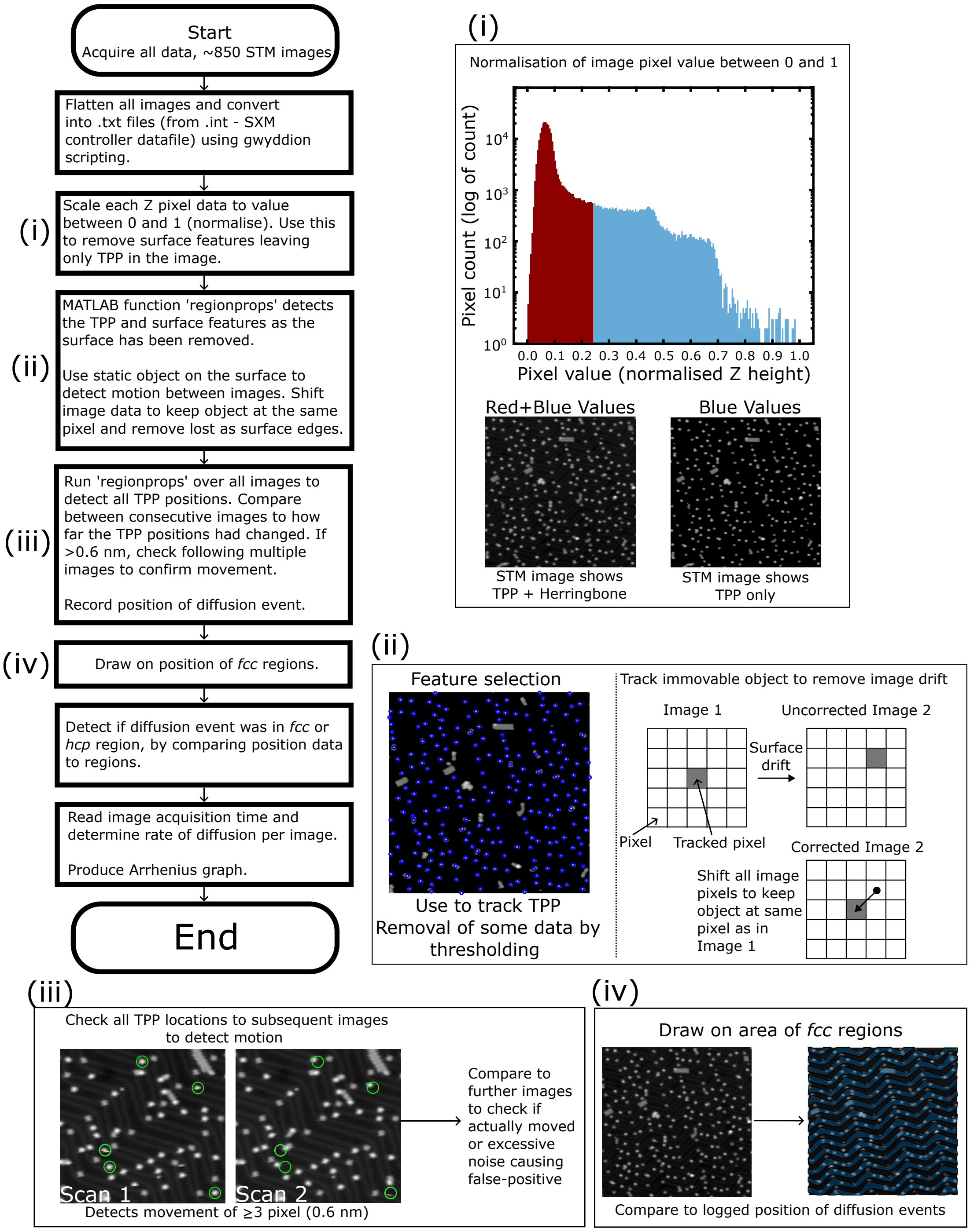

Figure 4.13: Flow diagram describing the main steps to the determination of the rate for TPP movement. Each stage is described in more detail in the main text.

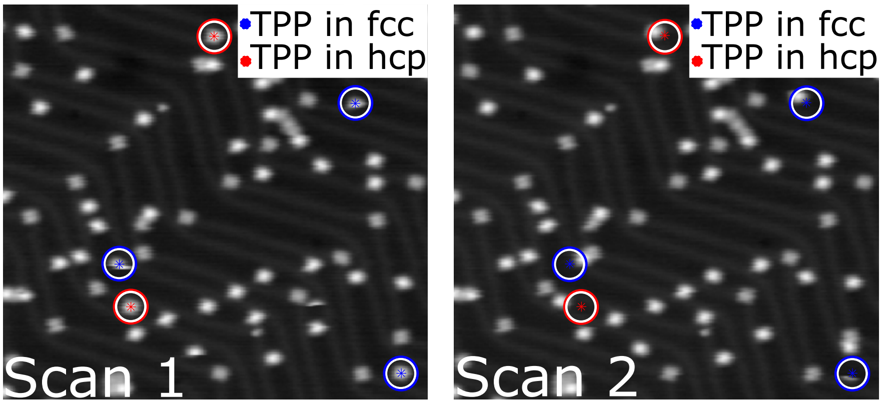

Figure 4.14: Sequential STM images showing the detected movements of molecules between images. The code detects if the molecule is in *fcc* or *hcp* regions. Both images: $V_{\text{sample}} = 0.5$ V, $I_{\text{set}} = 5$ pA.

To convert diffusion events per image to a molecular hopping rate, h, the total number of TPP features in an image, N, and the number of TPP features observed to be at the same location in the subsequent image (i.e. no diffusion occurs), n_0, were counted. Using the ratio of these observations we can obtain h,

$$\frac{n_0}{N} = \exp(h\Delta t), \tag{4.2}$$

where Δt is the time interval observed; the scan acquisition time (∼380s). The mean value of h, calculated at each temperature, is equated to the rate, k, in the Arrhenius equation,

$$k = A \exp\left(-\frac{E_D}{k_b T}\right), \tag{4.3}$$

where A is the exponential prefactor, commonly called the attempt frequency, and T is the substrate temperature. The experimentally determined energy barrier for diffusion, E_D, can be obtained by plotting $\ln(h)$ as a function of $1/T$ (Figure 4.15). By considering hopping rates for TPP within *fcc* and *hcp* regions of the surface, the energy barrier to diffusion for molecules in each specific region of the surface can be obtained. There is a significant difference between the diffusion barrier of TPP at *fcc* sites, $E_D = 29 \pm 5$ meV, and *hcp* sites, $E_D = 14 \pm 2$ meV. The diffusion barriers reported for porphyrin species on Cu(111) are significantly higher, e.g. 0.96 eV [123] and 0.71 eV [41]. Such a difference compared to the values reported here may be attributed to the increased reactivity of the Cu substrate as compared to Au. We propose that the difference in diffusion barrier

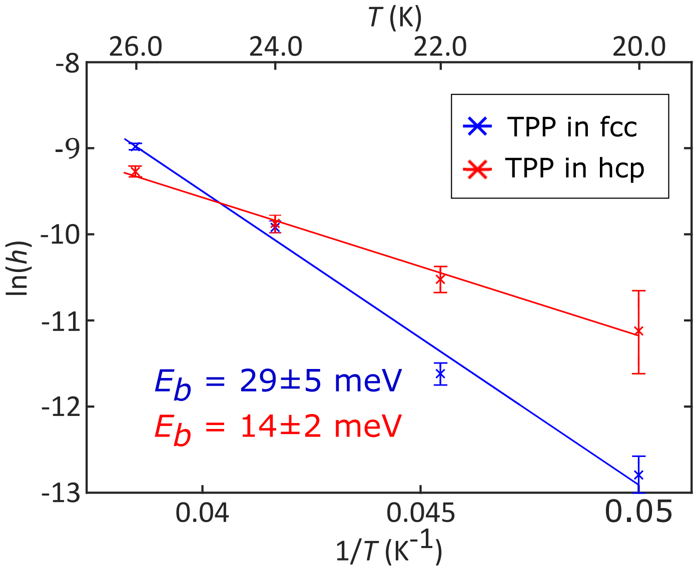

Figure 4.15: An Arrhenius plot of $\ln(h)$ as a function of $1/T$ for diffusion on both the *fcc* and *hcp* regions of the Au(111) herringbone reconstruction.

(between *fcc* and *hcp* regions) underlies the preferential formation of molecular islands within the *fcc* growth regions. As TPP molecules may diffuse between *fcc* and *hcp* regions, and as there is a higher barrier to diffusion for TPP at *fcc* sites (corresponding to a lower rate of diffusion), one would expect an increased residence time within the *fcc* regions resulting in an increased likelihood of island nucleation (similar to the lower 'diffusion potential' reported for benzene within *fcc* regions of Au(111)) [124]. Hence, we propose that the ordered self-assembly of molecular structures on Au(111) is driven by the local difference in diffusion barrier at the *fcc* and *hcp* regions of the surface.

Arrhenius analysis also yields values of the prefactor, A, which for TPP within the *fcc* and *hcp* regions is calculated to be 6x$10^{1\pm1}$ Hz and 4x$10^{-2\pm1}$ Hz, respectively. For simple (monatomic/diatomic) systems a value on the order of 10^{13} Hz is typically expected, and values of the order 10^9 to 10^{13} have been obtained for porphyrin species on Cu(111) [41, 123]. Interestingly, anomalously low values of A have been reported where diffusion barriers are below 100 meV [125], as is the case here, including 2x$10^{3\pm1}$ Hz for Al on Au(111) [126]. For smaller molecules (e.g. CO) quantum tunnelling processes have been suggested as an explanation for low frequency values [3], but are unlikely to contribute here due to the comparatively high molecular weight of TPP. The values reported here should be considered in light of; (i) the non-trivial assignment of an expected prefactor. As recently discussed [127], viewing A as simple 'attempt frequency' to the transition state is potentially an oversimplification for large/flexible molecules, and the change in partition function, with associated entropic considerations, is likely to be relevant. (ii) The diffusion lengths recorded here are greater than the lattice spacing of the substrate, suggesting that the transition state accessed here may not be directly comparable to systems where smaller displacements are observed.

4.6.2 Tip influence on the molecules

It should be noted that while STM offers single-molecule resolution and facilitates the measurement of individual diffusion events, there is potential for the STM tip to interact with molecular species and enhance or suppress diffusion. When taking STM measurements, the tip is raster scanned over a small area of the surface, and the tip will therefore pass over single molecules multiple times during an image. It is conceivable that not only direct tip-molecule interaction moves the molecule [2], but also that the applied bias can play a role in inducing motion [128]. Previous STM Arrhenius studies have quoted that tunnel resistances between 1-10 GΩ are sufficient to prevent tip interaction [41, 101], we employ a resistance of 100 GΩ (500 mV and 5 pA) to reduce the likelihood of tip-induced processes, providing a significant tunnelling resistance while limiting the magnitude of the electric field present in the tip-sample junction. We do not exclude the possibility of tip-induced processes, but the simultaneous measurement of diffusion barriers for *fcc* and *hcp* regions allows a direct comparison under the same tip conditions.

4.7 Conclusion

The high spatial resolution of the variable-temperature STM measurements allows the diffusion rates (and associated energy barriers) for site-specific diffusion over the Au(111) substrate to be characterised. Preferential formation of atomic and molecular islands within the *fcc* regions of the Au(111) herringbone reconstruction is ubiquitous, and the observed difference in a diffusion energy barrier between TPP molecules within *fcc* and *hcp* may offer an explanation for the underlying mechanism. Consideration of molecular diffusion barriers, driven by local substrate atomic order, offers a route to control the spatial distribution and orientation of on-surface self-assembled structures and reactions.

Further work on this system could explore the diffusion to and from larger islands at higher temperatures, with the scope for energy barriers of these diffusion events to be determined. Work by Venables *et al.* [43] looked at the determination of the critical island size of atomic species, which we may be able to develop for molecular systems.

Chapter 5

Ullmann coupling of Br_xTPP: characterisation via scanning tunnelling spectroscopy and differential conductance maps

Ullmann-type coupling reactions on surfaces give rise to covalently bonded structures formed from functionalised molecules. In this work, we deposit brominated tetraphenylporphyrin (Br_xTPP) onto Au(111) and cool the sample to 4.7 K for STM characterisation. The packing and electronic states of Br_xTPP and TPP are characterised and compared. We find that bromine functionalised TPP within close-packed islands exhibit a shift in the highest occupied molecular orbital electronic state to lower energy levels. Using differential conductance maps, we were able to determine the number of bromine atoms on a TPP species in a close-packed island due to the shift in HOMO state, providing a method for chemical characterisation (as visual identification using topography measurements alone is non-facile). Upon annealing the sample, a different packing of the adsorbed brominated and non-brominated tetraphenylporphyrin species is observed. Higher temperature annealing forms covalently bonded TPP chains. Further heating caused a secondary reaction to occur within the TPP sub-units within the polymer chains (see the ring-closing reaction in Chapter 6). Finally, evidence of the formation of the AuTPP species is presented with STM measurements (see Chapter 6 for further discussion on AuTPP formation).

5.1 Motivation

The synthesis of molecular wires on surfaces is a key requirement for molecular-scale electronics [52]. A route towards this goal is the 'bottom-up' synthesis of molecular wires through the self-assembly of molecular building blocks. Obviously, any nano-electronic device should be capable of effective charge transfer, with the supramolecular structures formed by intermolecular forces often displaying reduced charge transfer and thermal stability as compared to covalently bonded molecular structures [54, 129]. With the appropriate design of molecules, specific structures on surfaces can be produced. In the case of brominated TPP molecules, differing quantities of bromine atoms at specific locations on the molecule can produce different covalently coupled structures (dimer, chains or grids) [55, 119].

In order to produce structures with specific geometries, we need to understand the mechanisms by which the reaction proceeds. Normally, scanning tunnelling microscopy is used to provide a topographical characterisation of the system under study. This usually provides sufficient detail as the reactants and products of the reaction differ in their overall structure. STM operation relies on tunnelling to/from the local electronic states of the system under study. Instead of simply relying on the topographical detail of the surface, can we characterise the molecular states and chemistry using the electronic states of the system?

In this chapter, we study brominated TPP (Br_xTPP - where $x = 0 \rightarrow 4$) on Au(111). Br_xTPP forms close-packed molecular islands on the surface (similarly to TPP), however, the topographical difference between different quantities of bromine on the TPP molecules ($x = 0 \rightarrow 4$) is not apparent without detailed analysis. Using scanning tunnelling spectroscopy, differential conductance maps and topographical images, we identify differences between Br_xTPP species. The molecules are characterised at each stage of the Ullmann-type coupling reaction process.

5.2 Experimental methods

The *trans*-Br$_2$TPP molecules were synthesised within the group of Professor Neil R. Champness at the University of Birmingham. The material is a crystalline powder and is likely to contain non-brominated TPP and other Br$_x$TPP (x=1,2,3,4) due to the synthesis method used [130]. The chemical structure of TPP, and the various Br$_x$TPP versions present in this sample are shown in Figure 5.1.

Prior to deposition, the molecules were thermally purified in UHV for several hours at 200°C, and for one hour at the deposition temperature of 250°C. The molecules were deposited onto a clean Au(111) single crystal substrate, supplied by Surface Preparation Laboratory, held at room temperature. The surface was cleaned using Ar sputtering (1.0 kV, 10 mA and drain current 5 μA) and annealing (550°C) cycles. All temperatures were determined using K-type thermocouples close to the pyrolytic boron nitride (PBN) heating elements. Samples were cooled to 4.7 K in the STM stage and were characterised at this temperature. All dI/dV spectra, including conductance maps, were performed using the STM internal lock-in amplifier using an applied bias oscillation (2143 Hz at 20 mV RMS). The direction of dI/dV spectra bias sweep (negative to positive or vice versa) changed throughout the experiment due to an unstable tip at various bias values. The dI/dV conductance maps were performed in constant current mode (see discussion in Reecht *et al.* on conductance mapping modes [131]).

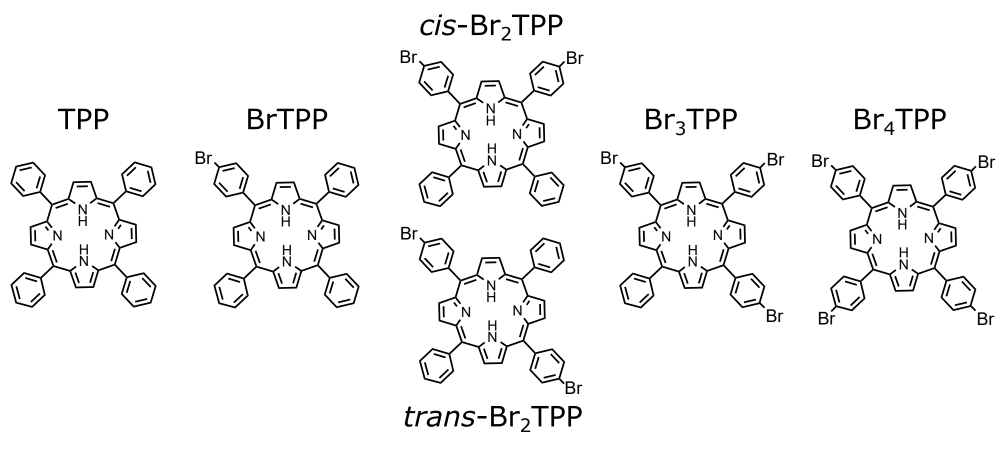

Figure 5.1: Skeletal drawings of the non-brominated and brominated TPP molecules present in the deposited crystalline powder.

5.2.1 dI/dV spectra of Au(111)

Throughout this chapter, differential conductance (dI/dV) spectra are acquired for molecular assemblies and the Au(111) surface. Initially, spectra of the clean Au(111) were recorded. Interestingly, the Au(111) spectra obtained did not appear to have the same structure in every spectrum recorded. The scanning tunnelling spectra (STS) of five positions on the surface are shown in Figure 5.2. The bottom three spectra show a clear peak at ~ -0.48 V, related to the surface state of gold, however, this peak and those around it differ between spectra in shape. Each of these three spectra were taken over *hcp* sites of the surface, but the difference in tip and/or surface state makes the spectra appear differently. The type and coordination of the atom on the end of the tip will change the LDOS of the tip and therefore the spectra of the gold obtained. Other on-surface, or sub-surface, species may also cause changes to the LDOS at the gold surface (that may or may not be resolved with the STM scanning modes). Furthermore, differences between surface states can be seen between the *fcc* and *hcp* regions of the surface (see Chapter 3.5.1 for a discussion of the surface reconstruction of Au(111)). The same tip state was used to acquire the top two spectra within Figure 5.2. On the *hcp* region, the peak at ~ -0.48 V was clearly visible, which is not true for the *fcc* region spectra. This was also reported by Andreev *et al.* [132] (see inset in Figure 5.2), which shows a reduction in the characteristic gold surface state in the *fcc* region.

In general, to determine if the tip was in a suitable state for spectroscopy, we ensured the characteristic surface state was visible, and there were no other major peaks within the regions of interest for the HOMO and LUMO of our molecules. The energy resolution of the states is affected by the bias oscillation used

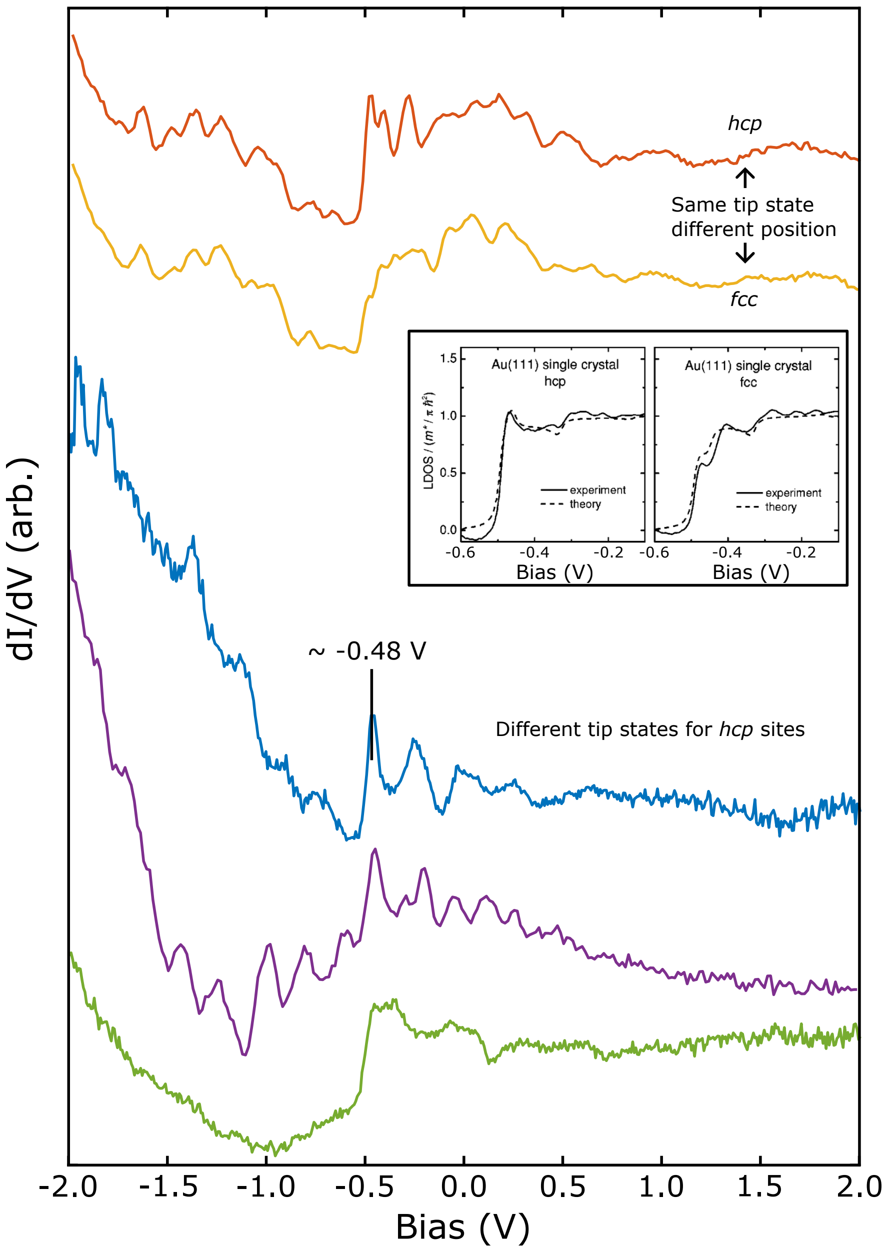

Figure 5.2: Five dI/dV spectra acquired on a Au(111) single crystal at 4.7 K. The characteristic surface state of gold (~ -0.48 V) is visible in spectra at *hcp* sites but is less visible in spectra at *fcc* sites. The top two spectra were taken with the same tip state with spectra at different regions on the surface (*hcp* or *fcc*). The bottom three spectra were all taken in *hcp* regions, but with different tip states. Inset shows the difference between the surface state of Au(111) by experiment and theory as reported by Andreev *et al.* [132].

5.2.2 Comparison of numerical differentiation to lock-in dI/dV

All spectra within this chapter were determined using a lock-in amplifier (see Section 3.1.3 for more details). We show in Figure 5.3 the difference in the lock-in derived dI/dV signal and a numerical differentiation of the current. It is clear that both the dI/dV spectra (lock-in and numerical differentiation) show similar features (surface state peak clear and shape of the spectra is roughly the same), however, the numerical differentiation spectra shows higher noise levels that may make it harder to detect smaller peaks within the spectra.

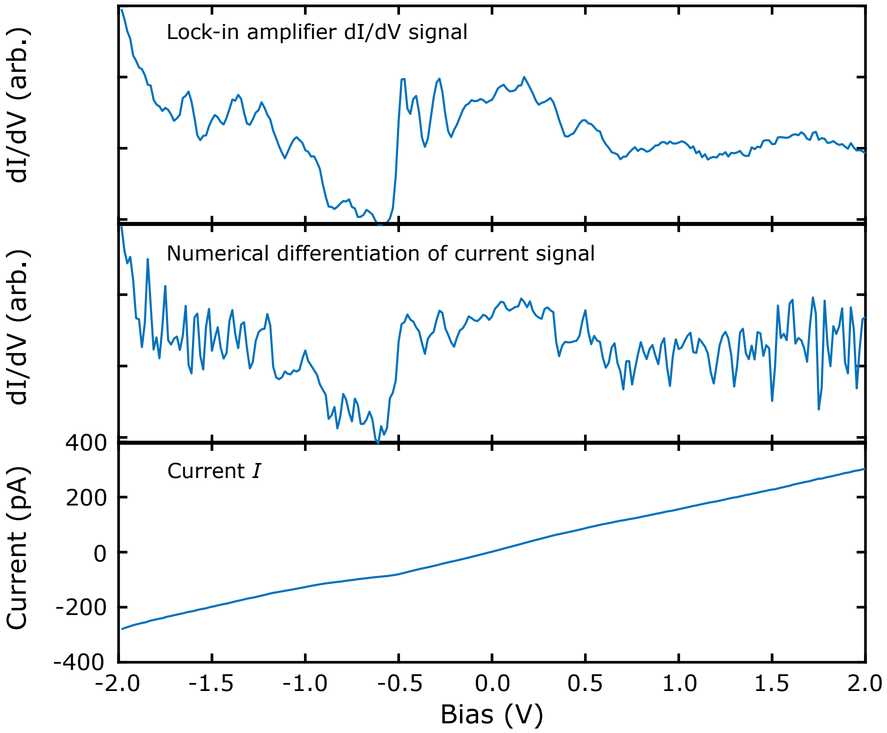

Figure 5.3: The comparison of the dI/dV signal as detected by the lock-in amplifier, and through numerical differentiation of the current channel. The numerically differentiated spectra shows more noise in the result.

5.3 TPP/Br_xTPP: Characterisation of molecular packing and structure, based on STM topography

5.3.1 Confirming the presence of Br_xTPP

Sub-monolayer coverages of Br_xTPP were deposited onto the Au(111) surface. The resultant surface was then characterised using STM at 4.7 K. Upon cooling, the molecules self-assemble into close-packed structures similar to TPP [98, 133]. Similar to TPP, individual Br_xTPP are scattered across the surface (mainly at point dislocation sites). We will focus on the individual Br_xTPP structure, before investigating molecular interaction motifs with reference to observed dimensions and common molecule-molecule interaction mechanisms.

By comparing the topography between individual Br_xTPP, the width of the molecules displays clear differences based on the number of bromine atoms in the molecule. This difference is explored in Figure 5.4. The inset of Figure 5.4a shows the location of molecules where line profiles are taken are: (i) TPP, (ii) BrTPP and (iii) Br_2TPP. The addition of the bromine to the phenyl ring has the effect of increasing the length of the TPP species along that axis, which can be seen visually, but also verified in line profiles of the species. The line profiles of these molecules along the axis of the phenyl rings are shown in Figure 5.4b, with inset images and models of the TPP shown. Taking the average of several brominated TPP species shows that the addition of a bromine atom increases the length of the TPP by 0.25±0.10 nm (measured between the half maximum of the line spectra on each side of the molecule). Br_xTPP species, where $x = 0 \rightarrow 4$, are observed following deposition.

5.3.2 Close-packed structures with halogen bonds

A close-up of a close-packed island is shown within Figure 5.5a, with a model of the TPP packing and estimated positions of bromine atoms indicated in Figure 5.5b-c. The C-Br bonds are situated at approximately 90° to each other, and

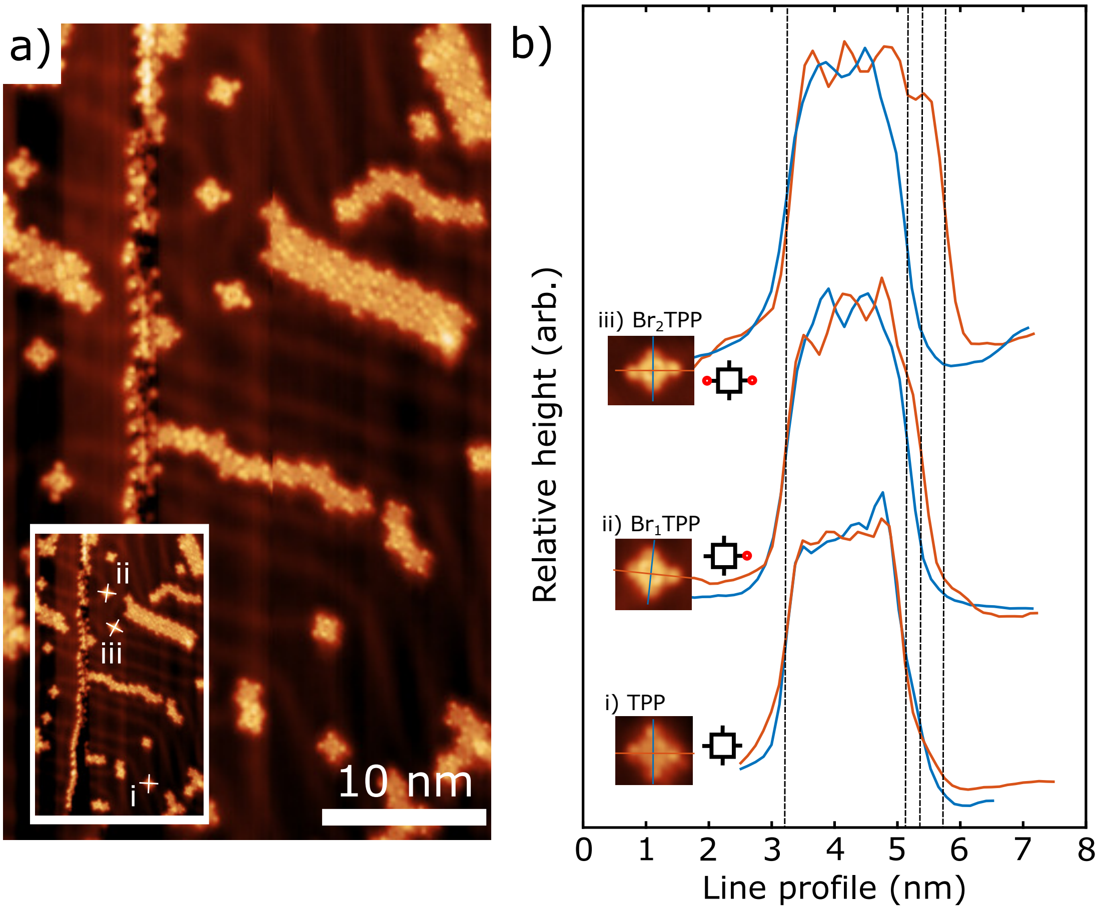

Figure 5.4: (a) STM image showing some individually adsorbed Br_xTPP. Inset shows the positions of TPP used for the line profiles. (b) Shows the line profiles of different TPP species: (i) TPP, (ii) BrTPP and (iii) Br_2TPP. The profile along each axis is compared and measured between the half maximum on each side of the TPP to compare widths. The insets show the molecules and models highlighting the position of the bromine on the molecule. The blue line corresponds to the vertical line profile, and the red line corresponds to the horizontal line profile. Image parameters: (a) $V_{\text{bias}} = 0.1$ V and $I_{\text{set}} = 100$ pA.

match the expected packing modes from halogen bonding on Au(111) (see inset) [14]. The close-packed structure is similar to other TPP structures. Here we observe a square unit cell ($\theta = 90 \pm 5°$) with unit vector lengths of $a = 1.5 \pm 0.1$ nm and $b = 1.5 \pm 0.1$ nm. From close visual inspection of the number of bromine atoms per Br_xTPP, not all are *trans*-Br_2TPP; some are *cis*-Br_2TPP or have different quantities of bromine atoms. However, it is non-trivial to determine the exact number of bromine atoms on each Br_xTPP molecule. This uncertainty is shown in Figure 5.5c as the blue dots. The red dots show clear bromine atom

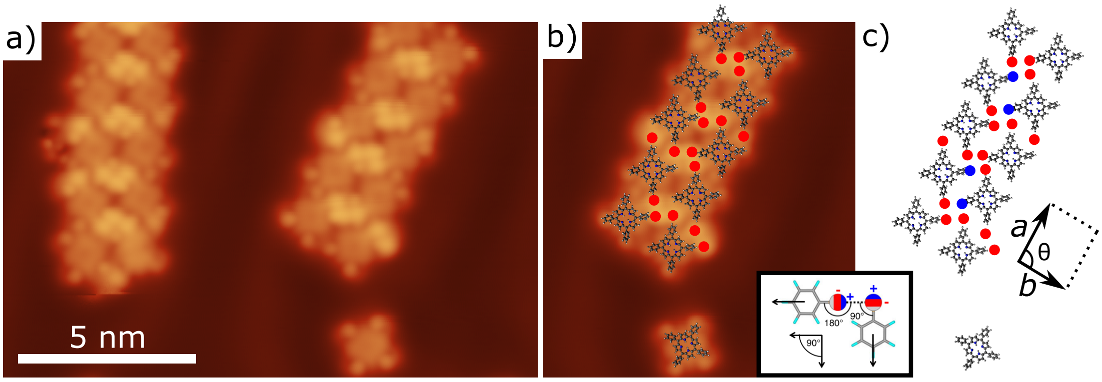

Figure 5.5: (a) Shows a close-up of two close-packed islands of Br$_x$TPP within the *fcc* regions of the surface. (b) the overlayer with indicated and scaled Br$_x$TPP are displayed on top of the right island from (a) with bromine atoms indicated as red dots. (c) shows the same overlayer structure as (b), and shows the uncertain position of bromine atoms as blue dots. Inset shows the interaction of halogen atoms on Au(111), indicating a 90° bonding angle that may drive molecular self-assembly (taken from Tschakert *et al.* [14]). Image parameters: (a-b) $V_{\text{bias}} = 0.3$ V and $I_{\text{set}} = 200$ pA.

locations, however, the blue dots indicate the possible location of bromine atoms. When comparing the blue locations to the red locations, it is clear that the blue 'bright' features appear less intense in the topography. In Section 5.4.3, the effect of bromine functionalisation on the HOMO and LUMO states of the molecule are explored via dI/dV spectra and differential conductance maps. These characterisations will allow us to accurately determine the number of Br atoms on the Br$_x$TPP molecule within an island.

An alternative hypothesis of the bright features (currently assigned to bromine atoms) could feasibly be the inclusion of Au adatoms within the close-packing of the Br$_x$TPP. When considering their role with Ullmann-type coupling reactions, the molecule forms an organometallic intermediate with a Au adatom (or surface atom). This usually requires elevated temperatures, in this case, to debrominate the TPP (∼550-590 K - see Ullmann coupling of brominated TPP as reported by Grill *et al.* [55]). Furthermore, the surface energetics of Au(111) do not readily allow the formation of a stable organometallic intermediate [27], and to form the organometallic intermediate bromine needs to dissociate from the TPP molecule. This can happen on the surface (requiring surface annealing) or within the evaporator requiring sublimation temperatures of ∼320°C [55]. In the case where the dissociation occurs within the evaporator, the TPP has been previously reported to form covalent bonds with other TPP directly on the surface [55] after deposition, rather than packing into close-packed islands or close-packed 'chains' as shown in Figure 5.6. There is no strong evidence for metal-organic frameworks or the inclusion of Au within these structures. It is more likely that in this case the halogen is driving order via halogen bonding.

5.3.3 Single-row structures

In general, the close-packed structure of the Br_xTPP islands shows similar behaviour to TPP (see the overview images in Figure 5.6). Br_xTPP forms close-packed islands within the *fcc* elbow regions (see Chapter 4), and decorates the step-edges of the Au(111) terraces.

As already noted above, the internal packing structure of the Br_xTPP islands

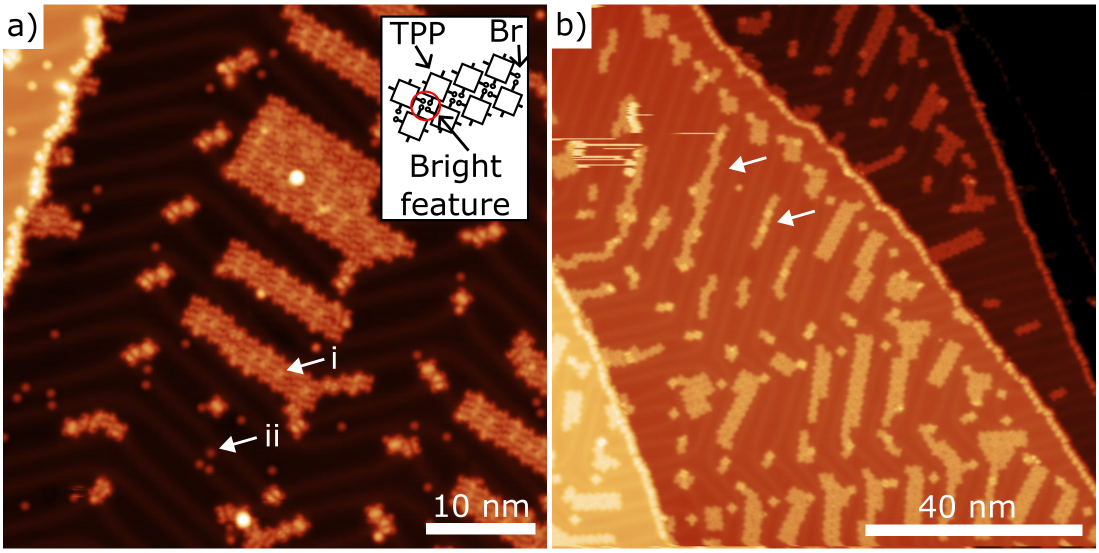

Figure 5.6: STM images showing close-packed Br_2TPP on Au(111). The islands are generally packed similarly to Chapter 4.3, as they are within the *fcc* regions of the herringbone. (a)i Shows brighter features within the close-packed islands attributed to bromine atoms attached to the phenyl rings of the TPP (inset shows a schematic diagram of the bright feature packing). (a)ii Shows excess Au surface adatoms. Within (b) shown with arrows, are unusual close-packed 'chain-like' structures (not observed for TPP). Image parameters: (a) $V_{\text{bias}} = -2.0$ V and $I_{\text{set}} = 300$ pA, (b) $V_{\text{bias}} = 1.0$ V and $I_{\text{set}} = 20$ pA.

differ due to the presence of bromine atoms. In Figure 5.6a(i), the bright features within the islands are attributed to the bromine atoms that contribute to the self-assembly order (see inset). There are lots of bright features (independent of the Br_xTPP molecule - see Figure 5.6a(ii)) on the surface, which we attribute to Au adatoms [37].

Interestingly, in Figure 5.6b as highlighted by arrows, 'chain-like' structures within the *fcc* regions of the surface are present. These structures do not appear to be Ullmann-type covalently coupled chains, but rather are close-packed in nature. It is likely that Br-Br bonds stabilise these 'chains', which is not possible for non-brominated TPP (double rows observed - in all cases see Chapter 4). Potential mechanisms that may facilitate this are, either the same halogen bonding that directly affects the close-packing structure within close-packed islands, or the strengthening of the CH-π bonding that usually drives self-assembly in TPP [134] by the strongly electronegative influence from the bromine atom.

Closer detail of these 'chains' was not obtained as the investigation was focused on spectroscopy. As shown in Figure 5.4, where similar chains are present, the topographic characterisation of the surface does not easily reveal the presence of Br_xTPP within the islands or chains.

5.3.4 How to distinguish between Br_xTPP species

Topographical features of the Br_xTPP can obviously provide evidence for the presence of brominated species on the surface. These features are easily distinguishable on individual Br_xTPP adsorbed at point dislocation sites, but attributing bromine atoms to each molecule becomes more difficult when the molecules have self-assembled to form an extended island. Using scanning tunnelling spectroscopy, we characterise the electronic differences between the Br_xTPP molecules for values of x ranging from $0 \rightarrow 4$. The spectroscopy data can then be used in conjunction with differential conductance mapping to spatially show the location of the electronic states within the molecule. The mapping can also be used to identify Br_xTPP molecules depending on the value of x. This approach is detailed in the following section.

5.4 Scanning tunnelling spectroscopy to identify Br$_x$TPP species

The dI/dV spectra of TPP has been previously reported, showing a HOMO state at −0.9 V (TPP) and −1.4 V (adatom TPP) and a LUMO state at 1.5 V (TPP) and 1.0 V (adatom TPP) [37]. As noted by Cirera *et al.*, the strong electronegativity of halogens bonded to molecules can be expected to shift the HOMO and LUMO states of the molecule [49].

5.4.1 STS characterisation of individual TPP

Individual TPP are frequently identified at point dislocation sites of the herringbone elbows. Shown in Figure 5.7 are the dI/dV spectra over the course of a few hours over the same TPP molecule following a surface anneal to 250°C. This example shows several different electronic states that can be identified. Initially (state 1), the TPP displays a HOMO state at −1.00 V and LUMO state at +1.30 V (gap = 2.30 eV). Within the forward and backward sweep of a spectrum (−ve to +ve and back again), the spectra obtained shifted to a new spectra type (see transition spectra containing both states 1, blue line forward spectra, and state 2, red line backward spectra). State 2 was determined to have a HOMO state at −0.9 V and LUMO at +1.53 V (gap = 2.43 eV). A further change to the obtained spectra happened spontaneously, giving state 3 with a HOMO state at −1.35 V and LUMO at +1.0 V (gap = 2.35 eV).

As expected, and previously reported by Mielke *et al.* [37], we obtain the ‘adatom adsorbed’ TPP spectra (state 3), as well as the ‘normally adsorbed’ TPP spectra (state 2). Interestingly, state 1 does not match previously reported values for TPP on Au(111). It has been reported that charging of the π-conjugated macrocycle may result in shifting of the electronic states of a TPP species [135]. In the case above, it appears that a ‘charged’ TPP transitions to the ‘normal’ states, and we then observe an ‘adatom TPP’ (likely due to the capture of an adatom species) [136].

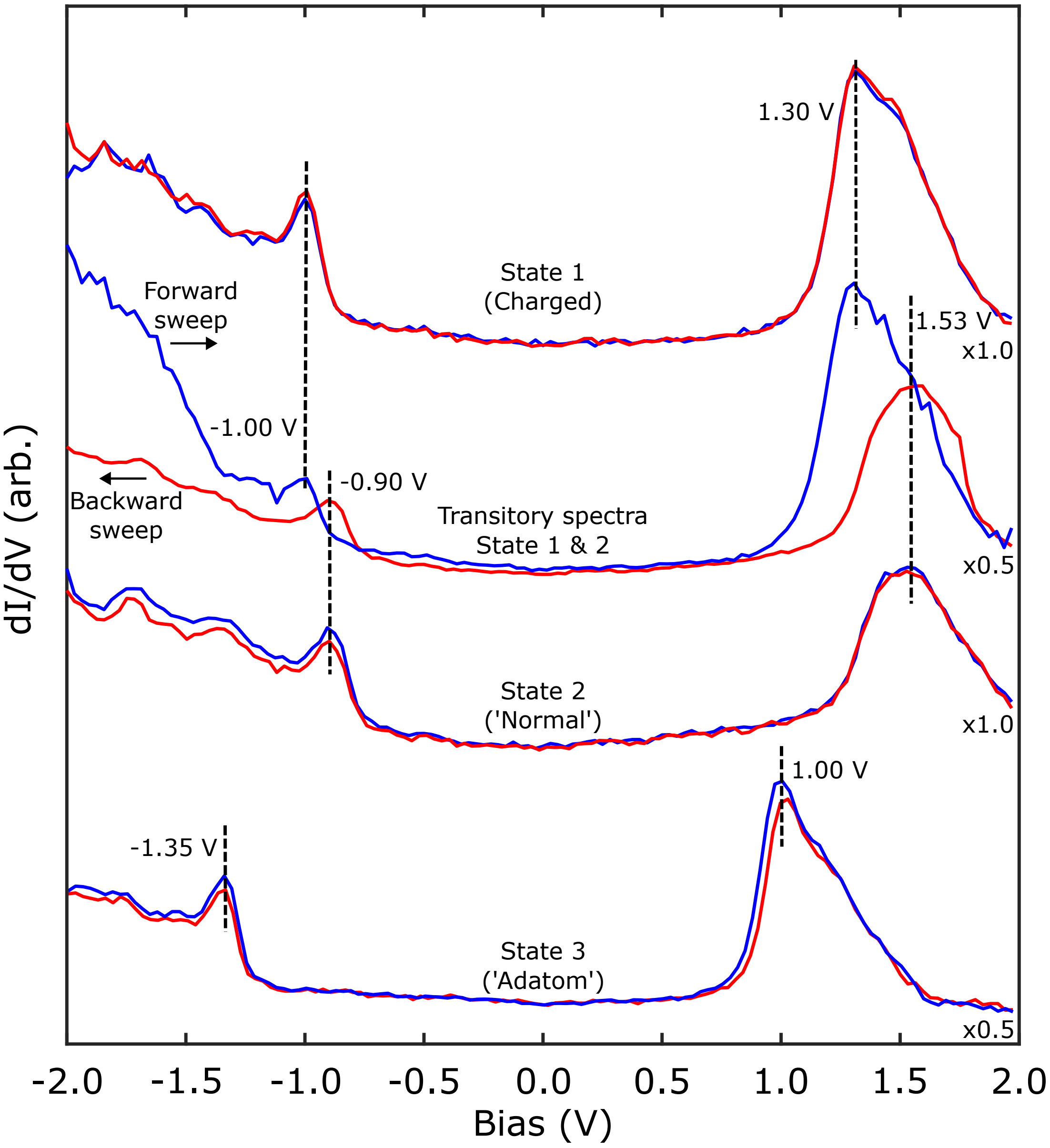

Figure 5.7: Spectra shown are taken over one TPP over the course of a couple of hours following an anneal of the surface to 250°C. State 1 has not been previously reported (but likely due to the charging of the macrocycle [135]). Then, whilst recording a spectra, the state of the TPP changed between the forward (blue, −ve to +ve bias) and backwards (red, +ve to −ve bias) spectra from state 1 to state 2. State 2 is similar to ‘normal’ TPP [37]. After scanning this surface region, the same TPP displayed a shift of ∼0.5 V previously assigned to adatom TPP [37]. Spectra parameters: −2.0 V to 2.0 V (forward sweep), at 250-300 pA starting current. Spectra are scaled by x0.5 or x1.0.

5.4.2 Individual Br_2 TPP

As expected by Cirera *et al.*, the halogenation of TPP may cause a shift in the electronic states of the molecule due to the electronegativity of the halogen [49]. Here, we investigate whether the presence of bromine influences the electronic states. Shown in Figure 5.8 are dI/dV spectra acquired over specific spatial locations within a Br_2TPP molecule adsorbed on a point dislocation site (indicating an adatom Br_2TPP species). The spectra were obtained for the same molecule, and are shown as a 'heat map'. Spectra were obtained at five positions on each axis of the Br_2TPP. The bright features in the heat map indicate the bias value of a peak in the STS. Each heat map row directly corresponds to a position circled on the Br_2TPP to the right.

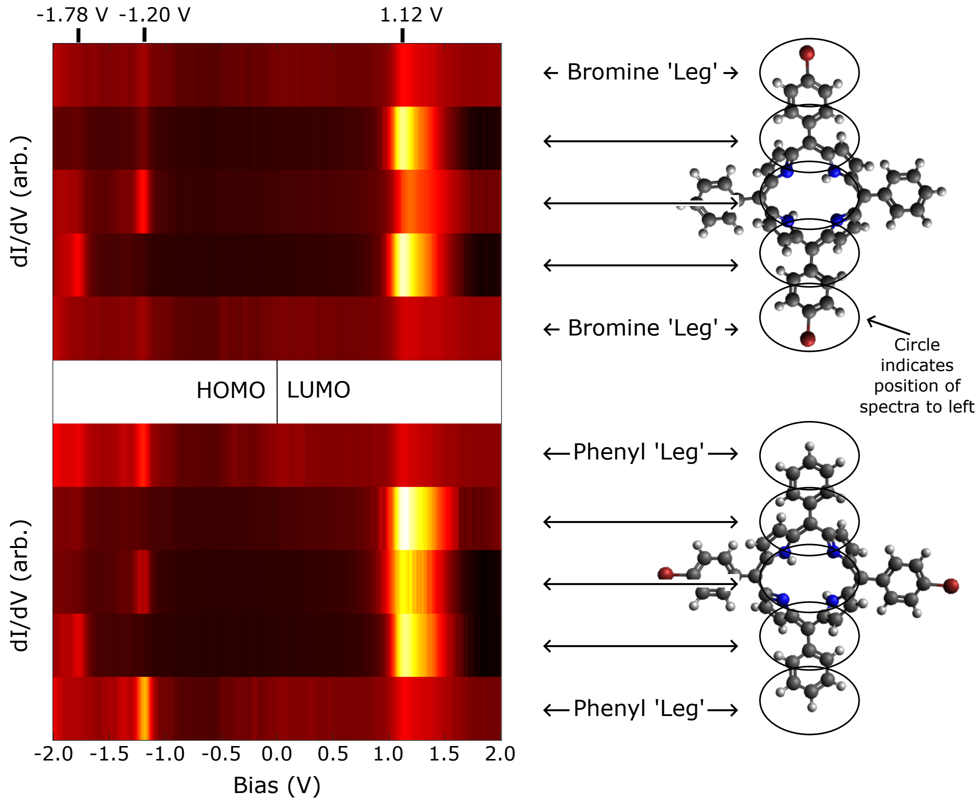

Figure 5.8: Heat map of the dI/dV states along each axis (top - brominated phenyl ring axis, bottom - phenyl ring axis) of the Br_2TPP. Bright features indicate more dI/dV states, whereas darker colours show fewer states. Each circle indicates the estimated position the spectra (to the left) was taken. The data was taken from line/grid spectra along each of the axis. Spectra parameters: −2.0 V to 2.0 V (forward sweep), at 300 pA starting current.

The macrocycle across each axis has common features; in general, it shows occupied orbital peaks at −1.20 V and −1.78 V and the LUMO at 1.12 V (gap = 2.32 eV). Specifically, the core of the Br_2TPP shows features at −1.20 V and 1.12 V. The porphine ring shows features at −1.78 V and 1.12 V. Peaks on the phenyl ring (including brominated versions) show at −1.20 V and 1.12 V. When comparing the 'bromine + phenyl legs' to the 'phenyl legs', it is clear that the peaks present at −1.12 V are attenuated on the bromine 'legs'. This effect might be expected as the charge density within a benzene ring is reduced due to the presence of bromine [14] (electronegativity of Br removes electron character from the ring). The HOMO peak of the molecule is broad and centred on the porphine ring.

These states, as characterised by individual point spectra, can be explored with differential conductance mapping that provides spatial information on the electronic states of the Br_2TPP molecule. The differential conductance maps of a Br_2TPP molecule are shown in Figure 5.9a. In these maps, bright features indicate a significant density of states present at that bias value. The HOMO state is highlighted at −1.2 V, with a further occupied state at −1.8 V, showing these states are generally localised in intensity at the porphine core. At −1.2 V, it is clear that the states present in the phenyl + bromine 'legs' are attenuated compared to the phenyl legs (see Figure 5.9b). This can be further compared to a differential conductance map of a TPP molecule (see Figure 5.9c) where each of the molecule's phenyl 'legs' are clear. Interestingly, the wide LUMO state is clear in the differential conductance mapping; the states are spread out over many bias values. In this dataset, between the HOMO/LUMO gap (±0.5 V), no bright molecular states are visible in the dI/dV conductance mapping as shown by the lack of bright features in Figure 5.9a at those bias values.

In this work, we were looking for specific features to identify Br_xTPP species. The presence of bromine appears to show a very distinct attenuation of states that would be present in the phenyl rings. Hence, we use the occupied states at ∼−1.2 V as a 'fingerprint' for bromination. In the next section, we take individual STS data points on multiple Br_xTPP within a close-packed island to determine the effect bromine has on the electronic states of the TPP molecule.

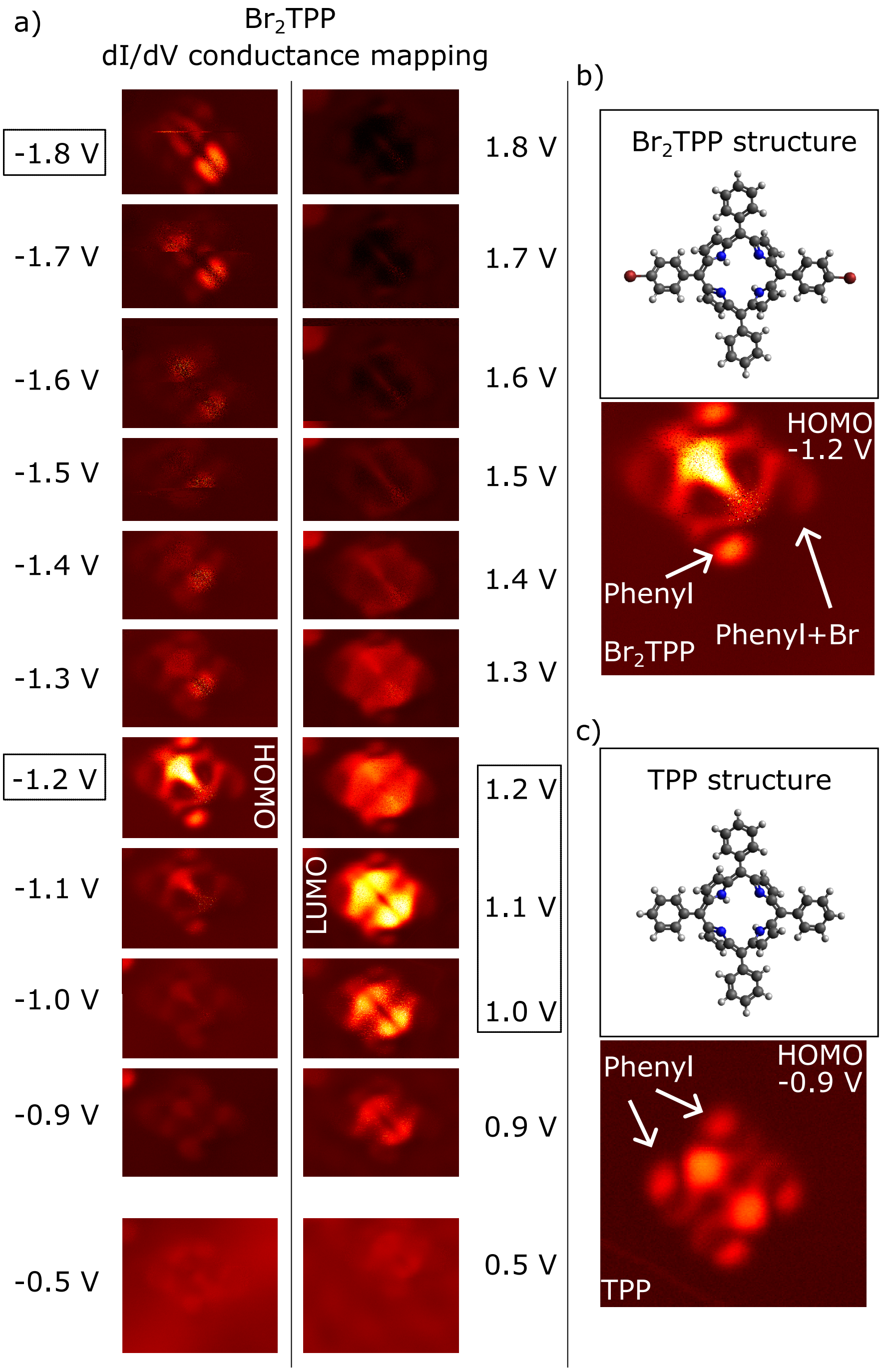

Figure 5.9: (a) Differential conductance maps of Br$_2$TPP over a range of bias values about the HOMO and LUMO states. The bright features show a greater local density of states. The HOMO and LUMO states appear highly localised to the porphine ring. The heat map parameters were fixed for all images, therefore the intensity is comparable between images. (b) The molecule model has the same alignment as the Br$_2$TPP conductance maps in (a-b). Note: we are unsure of the orientation of the porphine ring with respect to the hydrogen position. The dI/dV map shows clear attenuation of the states available in the bromine + phenyl rings compared to the phenyl rings alone. (c) TPP which shows no attenuation of the phenyl rings. Image parameters: (Br$_2$TPP) $I_{\text{set}} = 300$ pA, (TPP) $I_{\text{set}} = 120$ pA.

5.4.3 STS and differential conductance maps as a method of chemical identification

It is clear from the discussion above, that determining the number of bromine atoms attached to a single Br_xTPP species from a constant current Z topography image is difficult (see Figure 5.5 to see the difficulty in identifying species directly from topography alone). Within this work, we aim to determine if there is a 'signature' within the Br_xTPP spectra specific to the number of bromine atoms attached to the TPP.

Shown in Figure 5.10a is a close-packed island of Br_xTPP, containing TPP species with $x = 0 \rightarrow 4$. By visual inspection of the topography image, we can determine four distinct Br_xTPP with $x = 1 \rightarrow 4$ (see Figure 5.10b). These assignments are based on a reasonable interpretation of the topography of the close-packed island, as we do not currently have an independent method to identify the four distinct Br_xTPP molecules with $x = 1 \rightarrow 4$. STS data was obtained at the centre of each of these molecules and plotted in Figure 5.10c. Within these spectra, we see a shift of the HOMO peak from a non-brominated TPP at −0.90 V to −0.96 V for BrTPP. The HOMO state continues to shift to more negative values as more bromines are present in the molecule, Br_2TPP = −1.01 V, Br_3TPP = −1.09 V, and Br_4TPP = −1.12 V. The LUMO state is slightly more complex as one could fit multiple peaks within the feature at ∼1.3→1.6 V. For the LUMO feature, in general, there appears to be one peak at ∼1.5 V that seems to be fixed, whilst a peak at a slightly lower bias appears to shift closer to the Fermi level as more bromine atoms are present in the molecule (indicated on Figure 5.10c). We were unable to determine if there are any spectral differences between *trans* or *cis*-Br_2TPP molecules. The molecule considered here does not appear to be in an 'adatom' state.

We have previously shown that dI/dV conductance mapping can show the LDOS spatial distribution, and could be used to identify a specific number of bromine atoms attached to a TPP molecule. Shown in Figure 5.11 is the dI/dV map of a brominated TPP island recorded at a bias of −0.80 V. This is taken within the HOMO/LUMO 'gap' (at a bias lower than the HOMO of the molecule);

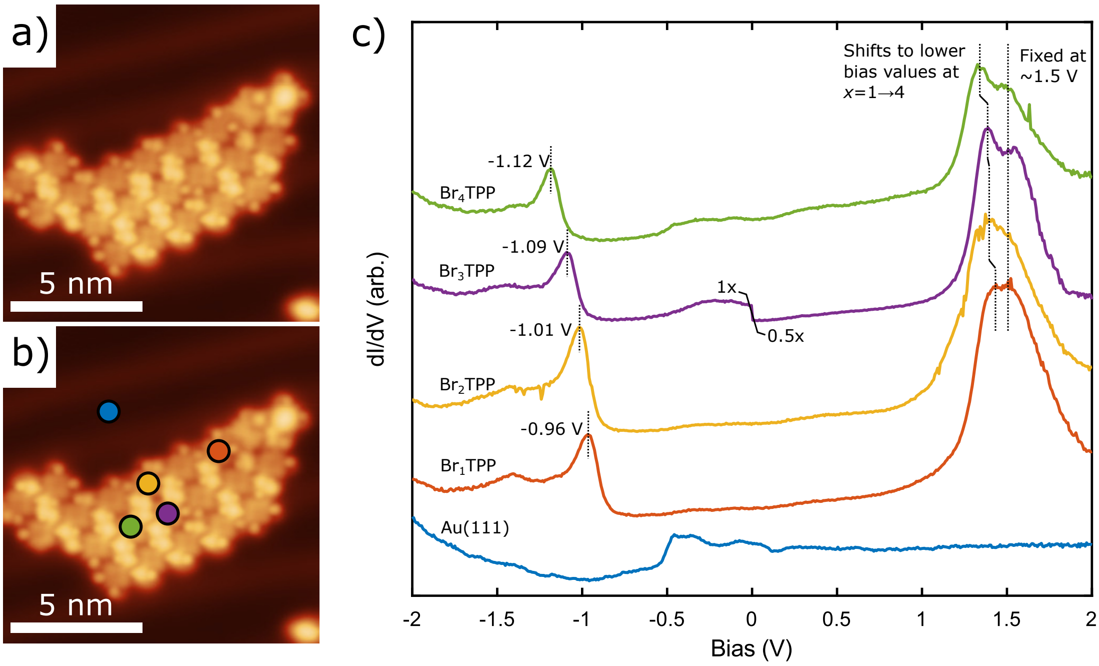

Figure 5.10: (a) STM image of a close-packed island with a mix of brominated TPP molecules with varying quantities of bromine attached. By visual inspection, four different quantities of bromine on brominated TPP molecule have been identified in (b). In (c), the dI/dV spectra from each of those brominated TPP molecules have been displayed. A shift to more negative values in the HOMO state can be seen as more bromine atoms are added. The LUMO state appears to be made of two features: 1) fixed at 1.5 V and 2) that shifts towards the Fermi level as more bromine atoms are on the TPP. Image parameters: (a-b) $V_{\text{bias}} = -0.5$ V and $I_{\text{set}} = 200$ pA. Spectra parameters: −2.0 V to 2.0 V (forward sweep), at 200 pA starting current.

resulting in a characteristic absence of states within in the image. Further images were taken at −0.94 V, −1.00 V, −1.08 V, −1.16 V which are chosen to align with the peak position $x = 1 \rightarrow 4$ as seen in Figure 5.10. Within each of the 'dI/dV maps' the bright features indicate the position of HOMO state for brominated TPP molecules. These are identified within the left images, and then mapped onto the topography image (right) to determine how many bromine atoms each TPP has attached. This method, if scaled up to a large area, could identify many molecular species of a particular type without the requirement for point spectra. In combination with automated methods, one would be able to find a particular species on the surface without manual searching involving topography or point spectroscopy methods.

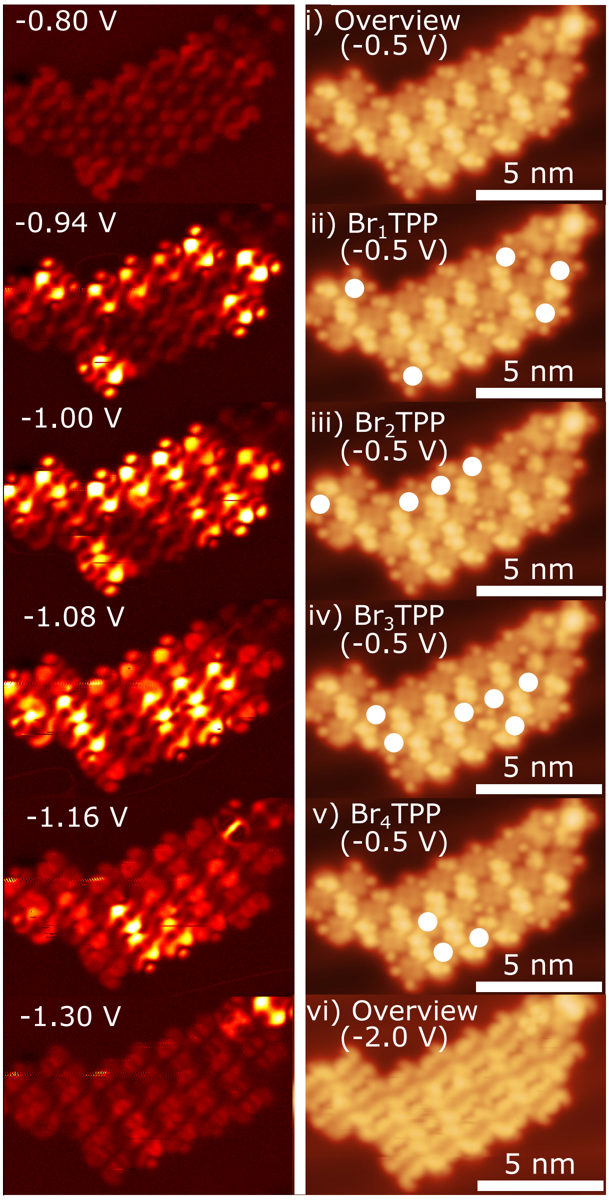

Figure 5.11: Left side: constant current dI/dV maps (differential conductance maps) showing bright features (electronic states within molecule accessed at that bias) of Br_xTPP molecules. The bias values used are −0.80 V (below the HOMO state), −0.94 V for BrTPP, −1.00 V for Br_2TPP, −1.08 V for Br_3TPP, −1.16 V for Br_4TPP, and −1.30 V for above the HOMO state. Right side: STM images of a close-packed island, with the same image shown in (i-v). The TPP that are bright on the left side are labelled with white dots on the right side, which indicates that these TPP have one, two, three or four bromine atoms. (vi) Shows the difference in topography of TPP species when the bias is changed to −2.0 V from −0.5 V. This makes it more difficult to see the bromine features. Image parameters: Left side $I_{\text{set}} = 200$ pA. Right side, (i-v) $V_{\text{bias}} = -0.5$ V and $I_{\text{set}} = 200$ pA (vi) $V_{\text{bias}} = -2.0$ V and $I_{\text{set}} = 200$ pA.

This method is not perfect as there is some overlap between the states we observe for BrTPP and Br_2TPP (and the same is true for Br_2 to Br_3 and Br_3 to Br_4). The resolution (energy) of the maps could potentially be increased by using a smaller bias dither (set at 20 mV RMS for the results as shown, whereas a smaller dither would result in a smaller bias range of states included in the maps). It is likely that states may vary by 10s of mV (likely due to the result of unresolved differences in adsorption sites - see DFT/experimental data from Mielke *et al.* [37]), making an absolute comparison somewhat difficult. However, this approach still provides important information; we can find the spatial position of specific chemical species.

5.5 Characterisation of Ullmann-type coupling

As reported by Grill *et al.*, upon heating the surface, an Ullmann-type coupling reaction will occur between the brominated TPP to form covalently coupled chains [55]. Here, a Au(111) surface (with sub-monolayer coverage of Br_xTPP) was annealed at 250°C, 300°C, 325°C and 450°C. The goal of this investigation is to obtain spectroscopic information from the Br_xTPP molecules involved in the on-surface reaction by sequentially heating the surface and characterising the structures formed for each step of the reaction.

5.5.1 250°C anneal

Following annealing to 250°C, Ullmann-type coupling has been initiated, as evidenced by coupling between brominated TPP species; chains of covalently bonded TPP are formed (some chains highlighted with arrows in Figure 5.12a). Following the coupling, we see changes to the herringbone reconstruction, potentially due to the Ullmann-type coupling reaction pathway requiring interaction with the substrate that may pull up and/or interact with a Au atom, and therefore induce changes to the herringbone reconstruction of the surface [27]. The movement of the solitons in the reconstruction results in significantly larger *fcc* and *hcp* regions (see Figure 5.12b). This can be seen by comparing the *fcc* regions in Figure 5.12b where the distance between point dislocation sites on the *fcc* elbows

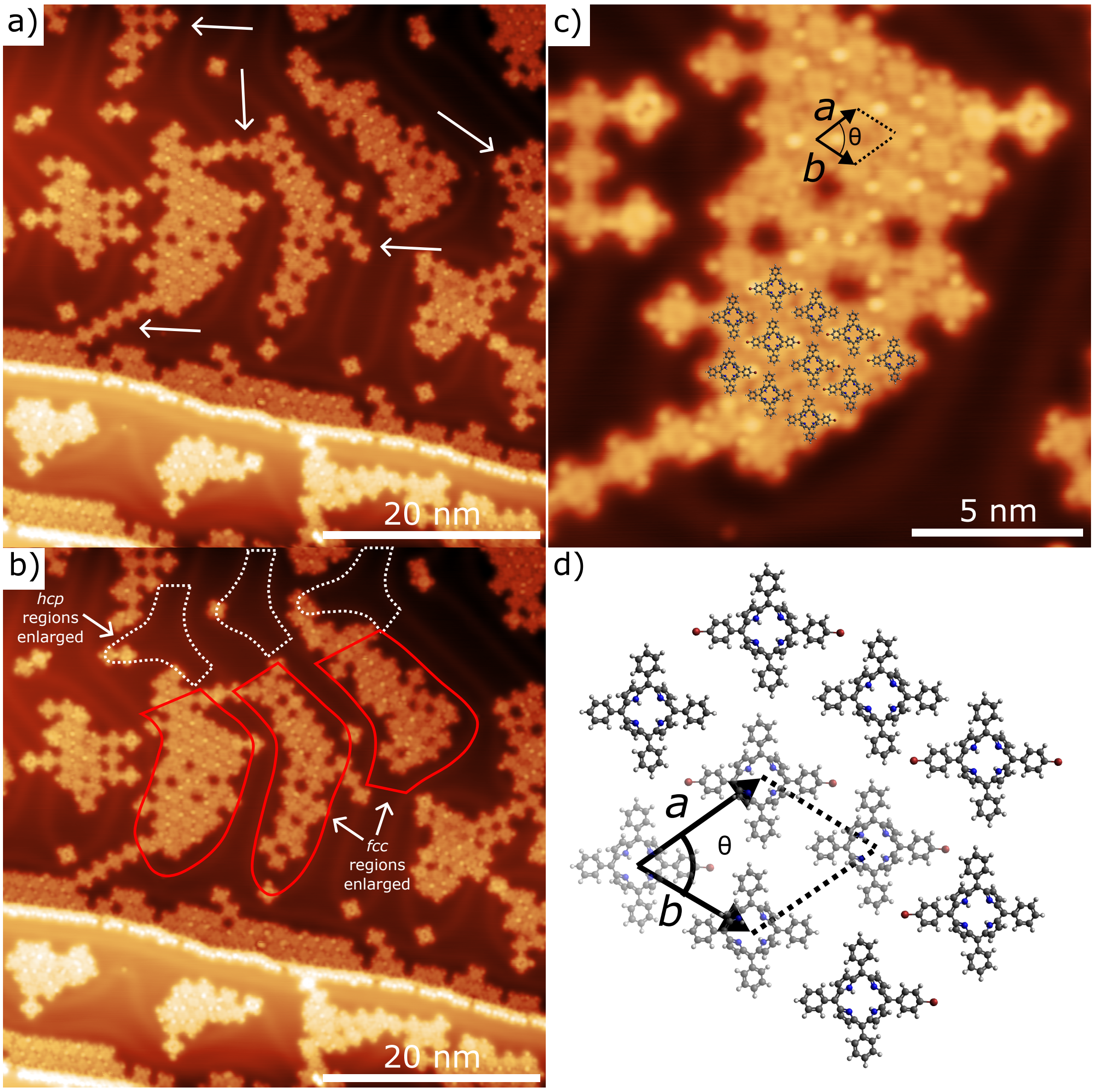

Figure 5.12: (a) Covalently coupled TPP chains formed following annealing to 250°C (highlighted with arrows). (b) Close-packed islands formed within the *fcc* regions of the surface. The *fcc* regions are enlarged compared to pre-anneal (see red areas), as have *hcp* regions (likely due to interaction between the surface and TPP causing disruption to the herringbone reconstruction). (c) The close-packed motif is different from previously seen, as the bromine features (bright phenyl ring parts) are no longer clumped together. The packing is no longer square (compared to previous TPP and brominated TPP results). (d) The overlayer unit cell is shown. Image parameters: (a-b) $V_{\text{bias}} = 0.5$ V and $I_{\text{set}} = 100$ pA.

are measured to 7.5-11.5 nm apart, compared to the distances seen previously in Figure 4.5a where the distance was measured to be 7.5-8.3 nm. As discussed in Chapter 4, the TPP species preferentially formed islands within *fcc* regions of the surface, this is similarly seen in this packing mode within Figure 5.12. Molecules can also be seen to be straddling the step-edge sites as previously described for TPP in Section 4.3.

The close-packed structure formed by the mixture of TPP and brominated TPP forms a new packing domain not previously seen in our studies. The overlayer structure shown in Figure 5.12c-d, has vector lengths of $a = 1.54 \pm 0.10$ nm and $b = 1.32 \pm 0.10$ nm with an angle of $66 \pm 5°$. Previously, the bromine atoms on the Br_xTPP molecules were seen to be driving order, by potentially facilitating halogen bonding.

Within the covalently coupled chain, see highlighted chains within Figure 5.12a, the location of covalent bonds between TPP are visible. A close-up of this chain is shown in Figure 5.13, which is a reaction product of the covalent coupling between *trans*-Br_2TPP. Interestingly, the phenyl rings on the top and bottom of the TPP chain appear to switch sides (brighter feature on the right or

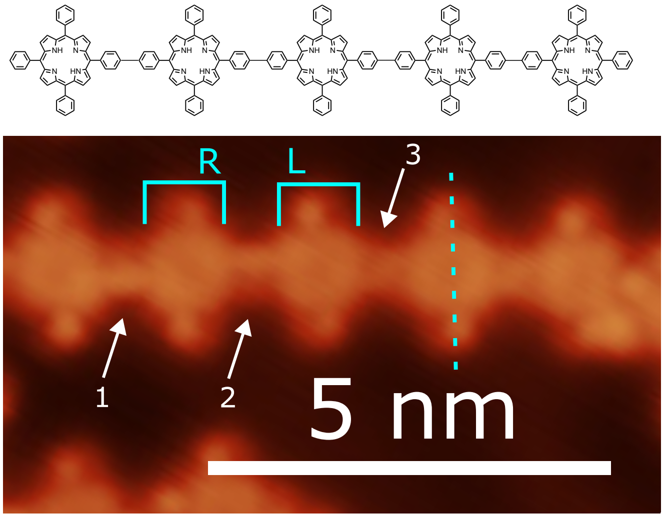

Figure 5.13: Close-up STM topograph of a coupled chain formed as the result of annealed surface-confined *trans*-Br_2TPP on Au(111). The bromine atoms on the phenyl rings dissociate and covalent bonds are formed with similarly debrominated phenyl rings on other TPP. The non-coupled phenyl rings above and below the chain appear to either be on the right (R) or left (L) side of the central axis of the TPP unit. Arrows highlight the differences between the phenyl ring involved in bonding between the TPP molecules, showing that for arrow 1 the phenyl ring is in a lower position, for arrow 2 it is in a higher position, and for arrow 3 the position is unclear. The skeletal drawing above the STM image shows the expected reacted products. Image parameters: $V_{\text{bias}} = 0.5$ V and $I_{\text{set}} = 100$ pA.

left side of the central vertical of the TPP molecule - see 'R' and 'L' markings in Figure 5.13) due to the twisting/rotation of the phenyl ring with respect to the surface. The distance between the core of each TPP molecule is measured to be 1.7±0.1 nm. As highlighted with arrows in Figure 5.13, the positions of the phenyl rings involved in the coupling between the TPP species may differ between a lower position (see arrow 1) or a higher position (see arrow 2), or indeed not be clear in the case of the third arrow. The bond formed via the Ullmann-type coupling reaction between the phenyl rings is typically seen as forming in the same position that the halide was bonded (between the para-para positions on the phenyl ring – see the model above the STM image), however, it is possible that the bond may form with meta or orth carbons [49]. The bond formation position may drive the differing relative positions of the phenyl rings.

5.5.1.1 Summary of 250°C anneal

Following the annealing to 250°C we observe two key points. 1) Partial coupling of the chains occurs, as some chains are formed, but a significant proportion of the non-coupled close-packed Br_xTPP remain. 2) The Ullmann-type coupling is linked to a change in the herringbone reconstruction.

5.5.2 300°C anneal

Annealing the surface to 300°C results in the coupling reaction progressing to completion with the majority of Br_xTPP now being covalently coupled. An overview of the surface is shown in Figure 5.14a. Chain lengths vary between 2-18 TPP units within that image. Chains (minimum two bonds per TPP) and branching chains (minimum three bonds per TPP) can be seen as a result of differing quantities of bromine atoms attached to the TPP prior to the anneal (as seen in Section 5.4.3 - Br_xTPP with $x = 0 \rightarrow 4$ are present). Not all of the Br_2TPP are of the *trans* type, as some of the chains have right-angled parts indicating *cis* isomers (although the *trans* isomer appear to be the majority type).

A close-up of one of the chains formed is shown in Figure 5.14b revealing several interesting features. Here, a chain containing mainly *trans*-bonded TPP with a right angle *cis*-bonded TPP is shown (*trans* and *cis* coupled TPP labelled in the Figure 5.14b). We identify several features, and discuss them in turn, individual porphyrin features are highlighted in Figure 5.14b (i→iv):

(i) We assign this molecule to a 'saddle' confirmation TPP macrocycle. As discussed above, the phenyl rings are clearly 'offset' from the central axis of the porphine, indicating that these rings are free to rotate.

(ii) TPP adsorbed atop an adatom at a point dislocation site (most similar to Figure 4.7i).

(iii) Topography matches that of a ring-closed TPP (see Chapter 6 for further analysis of the reaction from 'saddle' shaped TPP to ring-closed). The chemical structure is shown in Figure 5.14b inset. Phenyl rings dehydrogenate and form covalent bonds with the outer carbons atoms of the porphine core.

(iv) TPP attributed to an incomplete ring-closing reaction.

Of particular interest is the observation that some of the coupled TPP within the chains have become ring-closed [38, 98]. This reaction was not previously reported when annealing brominated TPP into covalently coupled chains, although

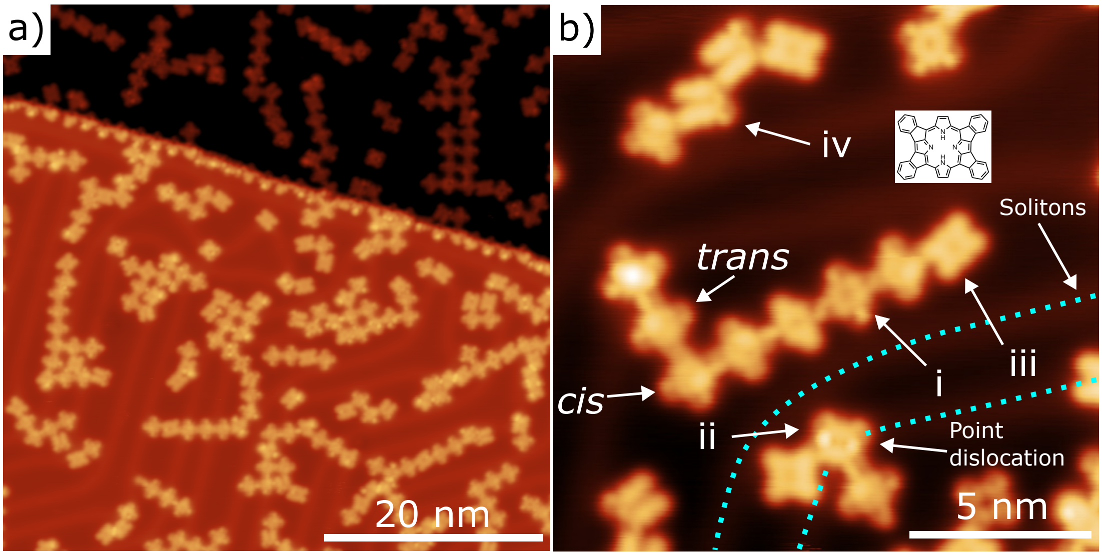

Figure 5.14: (a) Overview STM image of 300°C annealed brominated TPP on Au(111) which forms covalently coupled TPP chains. (b) Close-up STM image of a covalently coupled TPP chain, with various states of molecule pointed out. Image parameters: (a-b) $V_{\text{bias}} = -1.0$ V and $I_{\text{set}} = 100$ pA.

this effect can be seen within the coupled chain images in Grill *et al.* [55]. From our study, we see evidence for the sequential nature of this reaction (i.e coupling followed by ring-closing).

5.5.2.1 STS characterisation of the reaction products

Following the visual identification of reaction products, dI/dV spectra were obtained to determine any change in the energy of the HOMO and LUMO electronic states. In Figure 5.15, the spectra of four covalently coupled TPP species are shown (locations of spectra shown in the inset). In general, the spectra of TPP (i), (ii), (iii) and (iv) are similar to that of a 'saddle' adsorbed TPP species (see Figure 5.7 to compare). The LUMO state is broad, centred around 1.5 V (compared to the 'saddle' shape TPP at 1.5 V). Similarly, the HOMO state is well-defined, at −0.85 V (compared to the 'saddle' shape TPP at −0.90 V). As already discussed, the exact adsorption position of the TPP species on the surface can impact the HOMO and LUMO states as reported by DFT analysis by Mielke *et al.* [37]. It is likely that small differences in the energies of the HOMO and LUMO states are as the result of small differences in adsorption to the surface; covalently coupled TPP likely are not fully relaxed due to the reduced degrees of freedom by their incorporation within the chain.

Our goal here is to define a chemical signature via STS that would allow us to identify different TPP within the covalently coupled chains. The species i, ii, iii and iv show similar HOMO. There are small shifts in the HOMO state likely as a result of adsorption sites. However, the shifts in the HOMO−1 of the molecules (peak at −1.41 V for i and no additional feature for ii) that appear to be in the same state, make it difficult to distinguish if we are seeing useful information relating to a molecule or that we are too sensitive to any environmental changes (e.g. effects induced by nearest-neighbours).

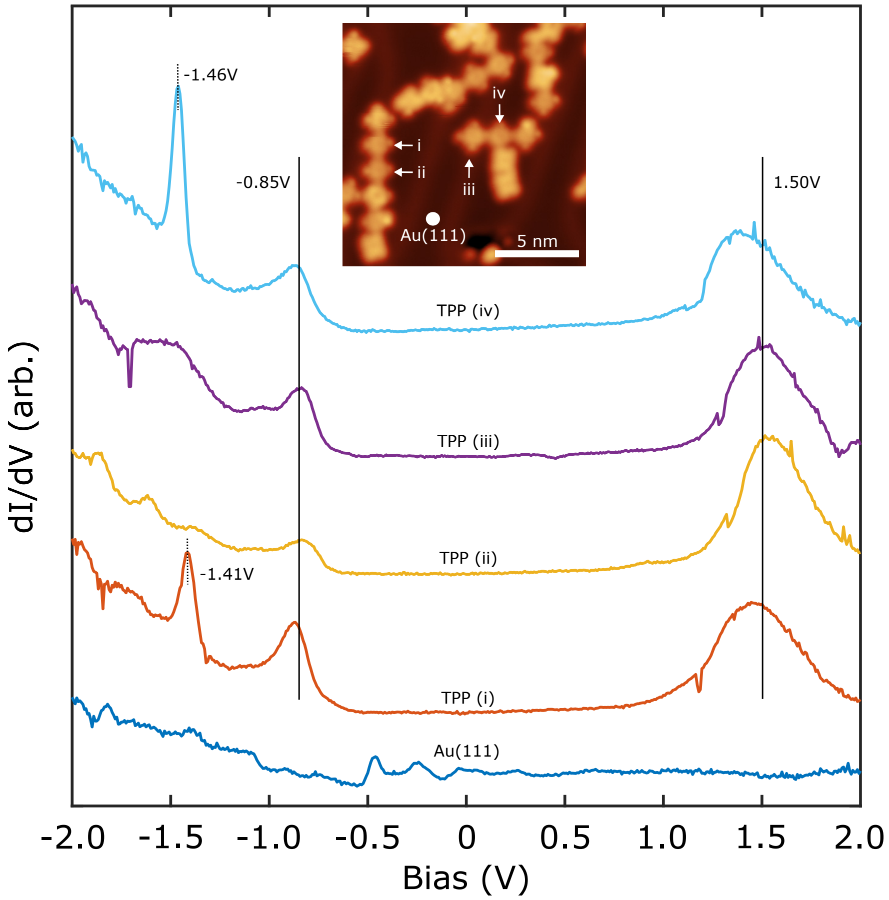

Figure 5.15: dI/dV spectra taken on specific locations within the inset image over covalently coupled TPP within chains. Spectra parameters: −2.0 V to 2.0 V (forward sweep), at 300 pA starting current. Image parameters: (inset) $V_{\text{bias}} = 0.8$ V and $I_{\text{set}} = 300$ pA.

5.5.3 325°C anneal

Following annealing to 325°C (STM overview shown in Figure 5.16a), the majority of the TPP within the chains have undergone ring-closing. The small number of TPP that have not undergone the ring-closing reaction are highlighted by arrows; these polymer chains have not been broken by the subsequent ring-closing process. As previously reported, various ring-closed TPP structures are formed as a result of how the phenyl rings have reacted with different parts of the porphine macrocycle [38,46]. The ring-closed structures are highlighted within Figure 5.16b i-iv (with the skeletal structures shown below the images).

It has previously been reported that the yield of each of these structures is (i) 57%, (ii) 17%, (iii) 21% and (iv) 5% yield [38]. In our work, we have not determined the yields of each of these products. As discussed by Lu *et al.* and Wiengarten *et al.*, structure (i) has been predicted via DFT to be the favoured product. The phenyl rings are expected to react with the iminic nitrogen (=N-) ring [38,46]. In Figure 5.16, we show the structure of (i) having reacted in line with the model proposed within the literature. TPP species ii and iv show variations where the phenyl ring bond formation with either the iminic or pyrrolic rings.

The ring-closing reaction breaks the linear symmetry of the TPP monomer units, resulting in two distinct types of chain shapes (see Figure 5.16b (v-vi) and in the skeletal form v and vi). The (v) chain, shows two orientations for the TPP, leading to the chain appearing as a 'bumpy road'(1.69±0.10 nm between TPP

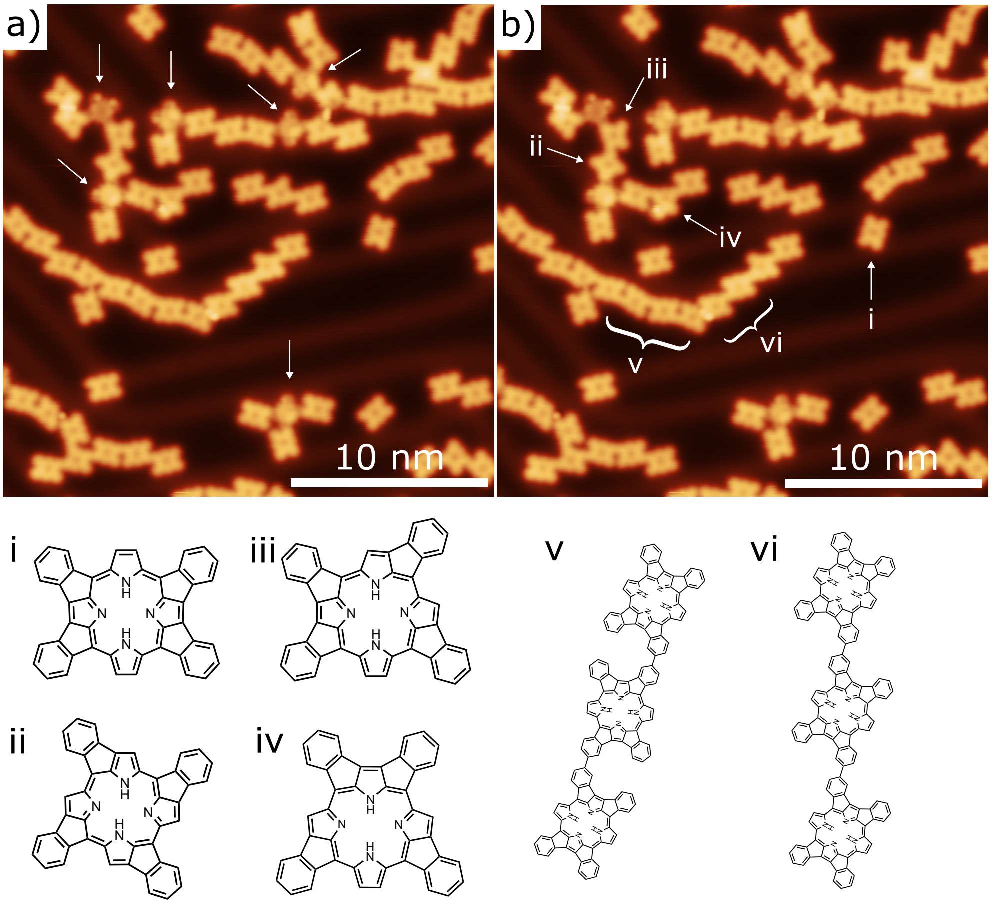

Figure 5.16: STM image showing the covalently coupled and ring-closed TPP on Au(111) following a surface anneal to 325°C. (a) Arrows show covalently coupled TPP that have not become ring-closed. (b) Shows the various shapes formed by ring-closed TPP (i-iv) and how (i) forms two distinct chain shapes (v-vi). The skeletal drawings of the ring-closed TPP are shown below (a-b). Image parameters: (a-b) $V_{\text{bias}} = -0.5$ V and $I_{\text{set}} = 300$ pA.

core). For the (vi) shape, the (i) TPP species are all orientated in one direction leading to a general chain shape resembling ‘stairs’ (1.64±0.10 nm between TPP core).

5.5.3.1 dI/dV of polymers

Within this section, we characterise the changes to the electronic structure which result from the ring-closing reaction and compare them to the dI/dV results obtained for non-covalently coupled TPP species as reported by Lu *et al.* [38].

5.5.3.1.1 dI/dV of ring-closed TPP species

The dI/dV spectra of four ring-closed covalently coupled TPP species (the structure was that of Figure 5.16i) were obtained, and are shown in Figure 5.17. A HOMO state was found at −0.88 V to −1.06 V. The LUMO state was found at either 0.85 V or 1.58 V. Compared to the previously reported values of HOMO = −1.2 V and LUMO = 0.6 V and 1.5 V (see Figure 5.17 inset [38]).

Our results somewhat differ from that previously reported, Lu *et al.* [38], we observe 0.14-0.32 V for the HOMO state and 0.08-0.15 V for the LUMO state. It is feasible that the difference in the electronic states we find are as a result of the TPP species being part of the covalently coupled chain. We find that the centre of the ring-closed TPP species within the chain did not produce any clear result in scanning tunnelling spectroscopy. The best results were obtained towards the periphery of the monomer, similar to that found by Lu *et al.* [38].

5.5.3.1.2 dI/dV of ‘saddle’ shaped TPP species

Shown in Figure 5.18 is the dI/dV spectra of ‘saddle’ shaped TPP species (see inset for TPP spectra positions). The HOMO state appears to range between −0.66 V to −0.90 V. The LUMO state ranges between 1.5-1.6 V. Comparing this to previous ‘saddle’ shaped TPP species in this chapter shows that the HOMO states have moved closer to the Fermi level (TPP HOMO state = −0.9 V, TPP chain 300°C anneal HOMO = −0.82 V). The energy level of the LUMO state are not similar to the previous values (TPP LUMO state = 1.53 V, TPP chain 300°C anneal LUMO = 1.40-1.62 V). Shifts from the previous values are likely due to

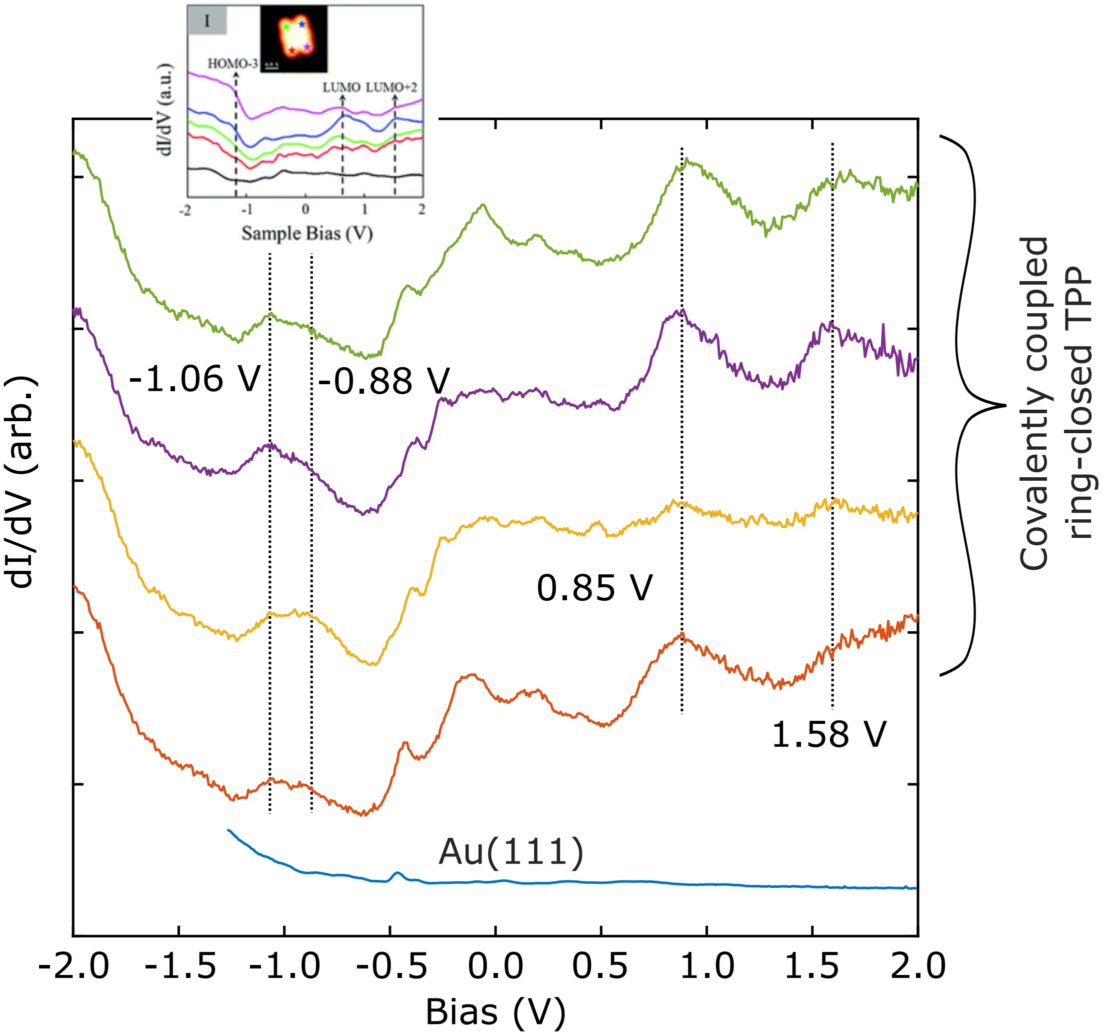

Figure 5.17: Scanning tunnelling spectroscopy of ring-closed covalently coupled TPP species taken over four different molecules within a chain. The Au(111) peak at ∼0.45 V is visible in the molecular spectra as the molecular states were only visible at the edge of the TPP. The LUMO state was found at 0.85 V and 1.58 V. HOMO state was found at −0.88 V to −1.06 V. The Au(111) spectra saturated the pre-amp at −1.3 V, so no data is shown past that point. Inset is from Lu *et al.* [38], showing the previously reported values.

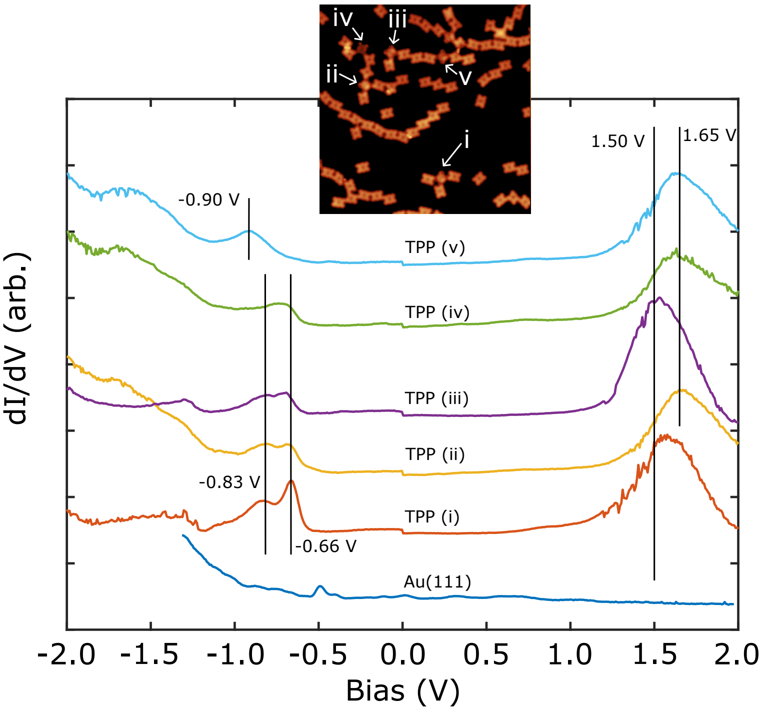

Figure 5.18: Scanning tunnelling spectroscopy of 'saddle' shaped covalently coupled TPP species. The inset shows the position of each of the spectra taken over the centre of the molecule. HOMO state is shown at −0.66 V to −0.90 V. The LUMO state is shown at 1.5-1.6 V. The Au(111) spectra saturated the pre-amp at −1.3 V, so no data is shown past that point. Spectra parameters: −2.0 V to 2.0 V (forward sweep), at 300 pA starting current.

either changes in conjugation or adsorption position on the surface.

The LUMO feature at 1.5 V is significantly large enough to be identified and is the most common electronic feature amongst the remaining TPP species. In Figure 5.19b, we show a differential conductance map that identifies (as bright features) the non-ring closed TPP species. Using this technique it may be possible to view larger areas to easily detect desired species quickly by looking for the specific electronic states.

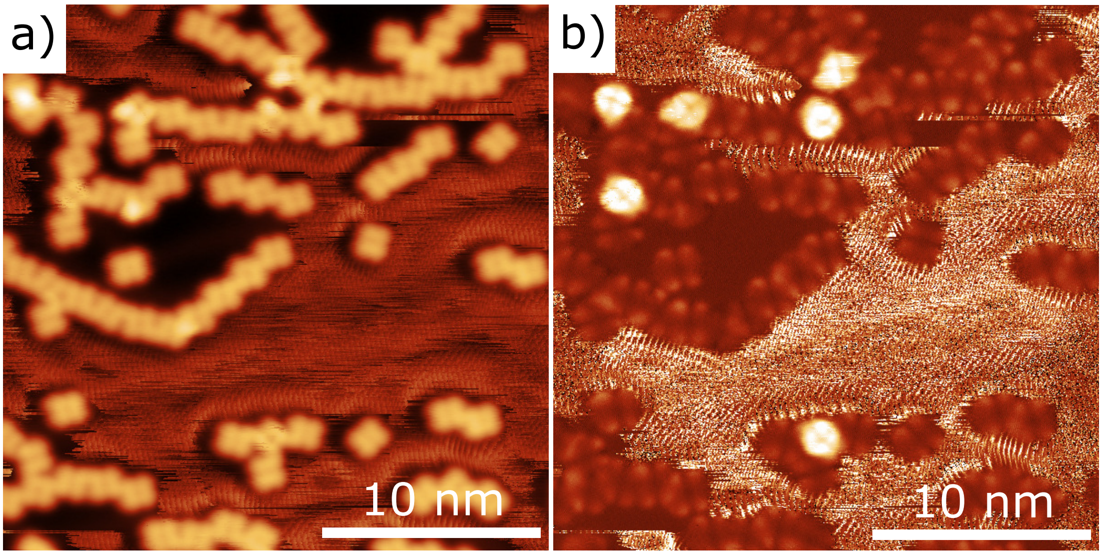

Figure 5.19: (a) STM image of the Br$_x$TPP/Au(111) surface showing the ring-closed covalently coupled chains. Tip/surface interactions caused intermittent atomic resolution of the surface. The resolution of molecular species appears reduced at higher bias values (due to tunnelling into the molecular states). In (b), we use differential conductance mapping to highlight the remaining 'saddle' shaped covalently coupled TPP species, with the 1.5 V LUMO state. Image parameters: $V_{\text{bias}} = 1.5$ V and $I_{\text{set}} = 300$ pA.

5.6 Self-metalation of TPP within covalently coupled chains

As reported by others [47, 49], the self-metalation (sequestration of Au from the surface into the empty TPP cavity) of TPP species is possible upon annealing the surface. We heat the sample to 450°C for 30 minutes to form metalated TPP species on the surface [98]. Shown in Figure 5.20a is an overview of the surface following annealing (in Figure 5.20b the contrast is changed to remove surface features and to show three variants of the TPP species formed). The species formed now differ by the central cavity within the porphine ring: (i) shows a bright feature, (ii) shows a flat feature and (iii) shows an empty feature. The non-metalated species is likely to be the molecule shown by (iii) as this matches the results shown in previous sections. Both (i) and (ii) are likely to be metalated species, with the difference in topography due to different charged states of the Au atom in the macrocycle [135].

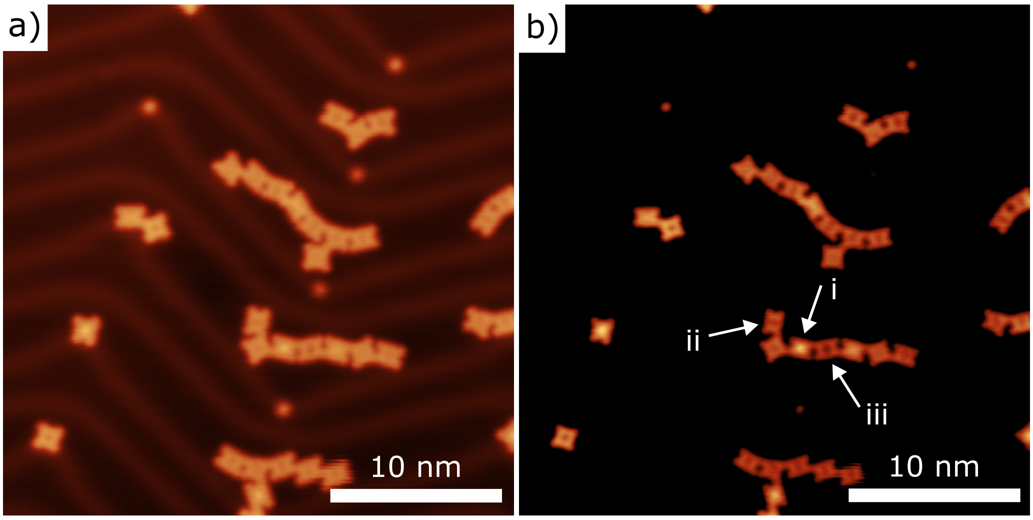

Figure 5.20: STM images of the covalently coupled chains following annealing to 450°C. (a) Overview of the surface, the central cavity of the TPP appears different for some TPP species. (b) Increased contrast of the molecules to show the cavity contrast. Three cavity contrasts are visible (i) bright feature, (ii) flat feature and (iii) empty feature. (i-ii) are most likely metalated TPP species, and (iii) is similar to previous results of ring-closed TPP with no metalation. Image parameters: $V_{\text{bias}} = -1.8$ V and $I_{\text{set}} = 100$ pA.

5.7 Conclusion

In this work, we show that as $x = 0 \rightarrow 4$ for Br_xTPP, the topography of the molecule changes due to the bromine atom attached to one of the phenyl rings of the TPP. The bromine atom drives order within self-assembled close-packed islands of Br_xTPP, forming a square lattice, with the bromine atoms interacting with each other (Br-Br bond at 90° angles to each other).

The presence of bromine within the molecule leads to changes in the electronic structure of the molecule. These changes are summarised in Figure 5.21, showing that we obtain a spectroscopic signature for these species. The most pronounced change is seen in the HOMO state as $x = 0 \rightarrow 4$ for Br_xTPP the HOMO state becomes more negative. This effect, in conjunction with differential conductance mapping, was used to spatially show the positions of Br_xTPP and identify the number of bromines associated with each TPP molecule.

The surface was heated, demonstrating that Ullmann-type covalent coupling of the Br_xTPP occurred on the surface, forming chains of covalently coupled TPP species. The type of molecule drove the structures formed, for example, with *trans*-Br_2TPP we obtained liner chains, whereas Br_3TPP formed branching chains. Further heating showed that ring-closing of the covalently coupled TPP species occurs, which converted the molecules from a 'saddle' shape conformation to a more 'planar' structure. This reaction did not appear to break the covalent chains, however, the symmetry of the ring-closed chains depended upon the ring-closing products within the chain. STS showed that the electronic states of 'saddle' shaped TPP were lost upon ring-closing and these states shifted to produce a smaller HOMO-LUMO energy gap. Finally, heating to 450°C induced self-metalation of the ring-closed TPP species within the chain. This was seen in the macrocycle cavity topography, as the empty feature became bright following self-metalation.

Further work employing bond-resolved nc-AFM would provide a further structural characterisation of the Ullmann-type coupling reaction at each stage of the reaction. The use of variable temperature STM to view these reactions as they occur may yield interesting insights into the reaction process of molecules of surfaces, although care must be taken to ensure the reaction occurs within the range of the variable temperature STM.

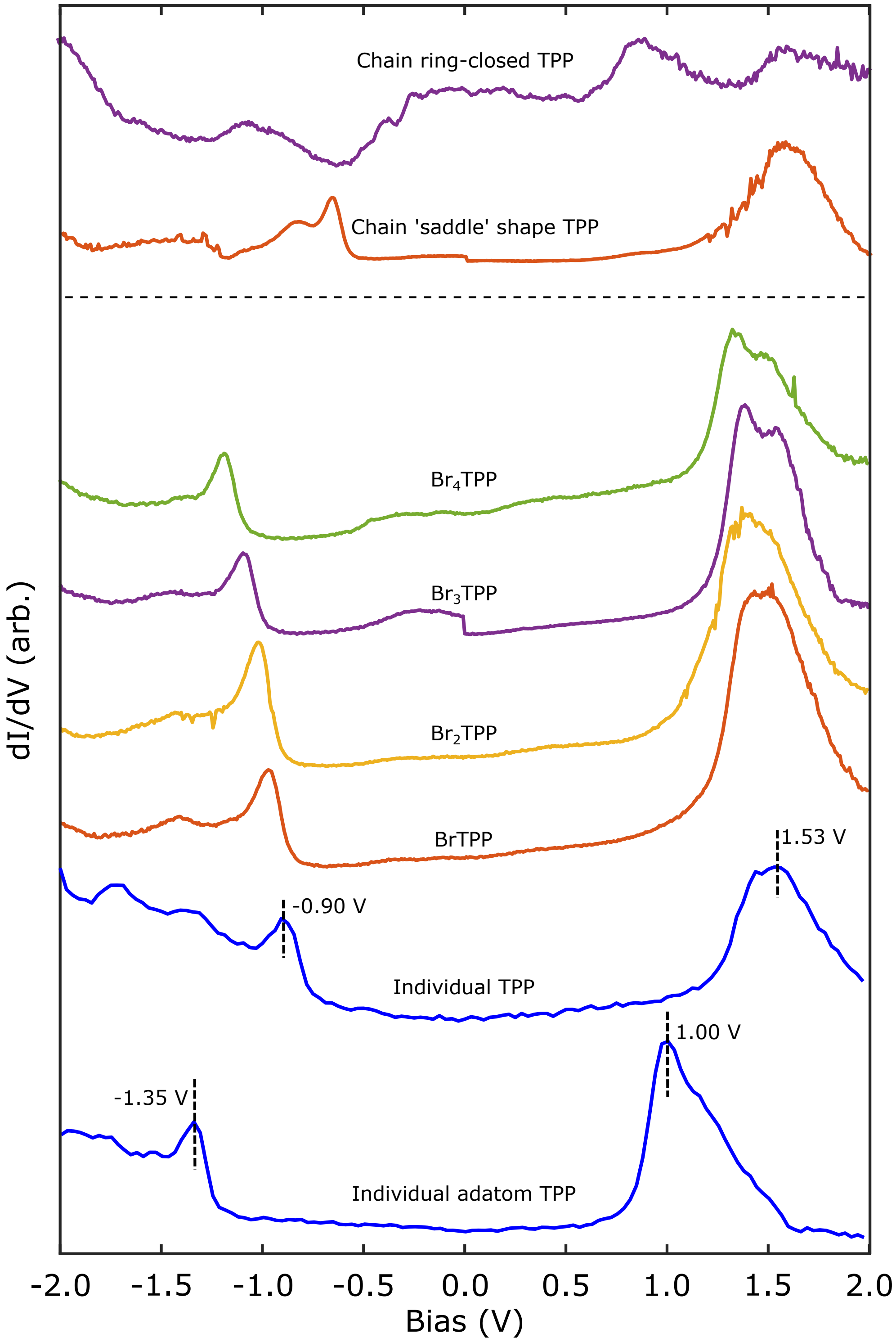

Figure 5.21: Scanning tunnelling spectra of the TPP species in each stage of the reaction. These spectra show a spectroscopic signature for these species, with shifts in the HOMO and LUMO states as a result of changes to the molecule.

Chapter 6

Order to disorder and self-metalation of tetraphenylporphyrin

This chapter initially details previous STM studies of tetraphenylporphyrin on Au(111) where TPP was found to form close-packed structures on Au(111) and then, following annealing to ∼580 K, the close-packed ordering is removed. To elucidate the observations in the previous work, low energy electron diffraction was used to demonstrate that the close-packed islands became diffuse following the annealing of the sample. X-ray photoelectron spectroscopy measurements show chemical changes within the carbon spectra following the anneal to the diffuse phase, however, no chemical shifts were seen in the nitrogen spectra. This indicated reactions involving the carbon periphery of the molecule. Following further annealing to higher temperatures, we found the formation of a single N 1s peak which is indicative of self-metalation whereby a metal atom from the surface is incorporated into the molecule. Experimental data from nitrogen near edge X-ray absorption fine structure spectroscopy data show that it is likely that a AuTPP species was formed (when compared to a similar system of TPP on a Cu surface). Normal incidence X-ray standing wave was also used to provide a structural characterisation of TPP at three distinct points within a thermally induced on-surface reaction.

6.1 Motivation

Porphyrins are π-conjugated macrocycles which may exhibit bespoke chemical functionality via the addition of specific chemical groups at the periphery of the molecule. Incorporation of a metal atom within the macrocycle cavity provides further functionality and access to applications based upon catalysis [30, 137, 138] and sensing [31]. Porphyrins, and associated derivatives, have been extensively studied by a range of surface-sensitive techniques [33], including scanning probe microscopies [139]. Of particular interest is the metalation of porphyrins, with various strategies being employed, including: solution phase synthesis [140], metal-uptake via co-deposition of metal and porphyrin species [141, 142], and self-metalation involving sequestration of metal atoms from a substrate [48–50, 143, 144].

The archetypal example of thermally activated self-metalation is the interaction of 2H-tetraphenylporphyrin (2H-TPP) with Cu(111) [47, 48]. During self-metalation of 2H-TPP, the two distinct nitrogen environments (iminic, =N-, and pyrrolic, -NH-) are replaced by a single environment with the loss of hydrogen atoms and all nitrogen atoms interacting with a central metal atom [47]. Other thermally activated reactions may occur that change the structure of the macrocycle, such as cyclodehydrogenation of the ring structure (removal of hydrogen and formation of C-C bonds between the porphine and phenyl groups which flattens the conformation of the porphyrin) [38, 46].

The self-metalation of 2H-TPP on Au(111) is less well studied, partly due to the perception that gold is a relatively inert substrate. However, the uptake of gold into porphyrin macrocycles, to form a AuTPP species, has recently been reported [49], and novel methods of gold porphyrin synthesis are relevant due to a possible role as a functional species within anticancer complexes [145].

6.1.1 Previous STM characterisation of TPP on Au(111): work by the Nottingham Nanoscience group

A thorough STM/STS investigation of TPP on Au(111) was carried out by Dr. Eleanor Frampton prior to photoelectron studies detailed in the rest of this chapter. The TPP material studied was synthesised by Dr. Frampton and deposited, via thermal sublimation, on to Au(111) and subsequent STM characterisation is detailed in reference [130].

To provide context to the work described below, the previous STM work is first described. The coverage of TPP on Au(111) was determined by the length of deposition time onto a clean substrate. Two surface preparations were studied, described here as monolayer and sub-monolayer coverages of TPP (Figure 6.1a-b respectively). The preparations once cooled to cryogenic temperatures, exhibited close-packed structures of TPP that were observed using STM (see Figure 6.1). Following the surface anneal to 580±50 K, the close-packed structures in both the monolayer and sub-monolayer coverages were disrupted, giving rise to molecules with a 'flatter' appearance within STM images, and now appear disordered with the removal of close-packed structures (see Figure 6.1c-d). The 'flattening' process of the TPP results in similar features to those reported by Wiengarten *et al.*, where the removal of hydrogen and formation of C-C bonds between the porphine and phenyl groups flattens the conformation of the porphyrin [46]. Compare (a) and (c) in Figure 6.1: (a) shows bright features assigned to non-planar phenyl rings, (c) shows that the majority of the 'bright' features (highlighted with arrows) attributed to incomplete ring-closing reactions (see Figure 2.17).

Within the new work presented in this chapter, the on-surface reactions of TPP will be characterised by various techniques to further characterise molecular changes shown via SPM. Using XPS, we can determine chemical changes to the molecule and relate this to the TPP structures observed in STM following annealing. NEXAFS provide a 'fingerprint' for the local chemical environment (specifically metalation). Finally, NIXSW should show a change in the adsorption of TPP relative to the surface for each surface annealed state. The use of synchrotron light is essential for these techniques since it provides a tunable photon energy and high X-ray brightness (an essential requirement for NEXAFS and NIXSW).

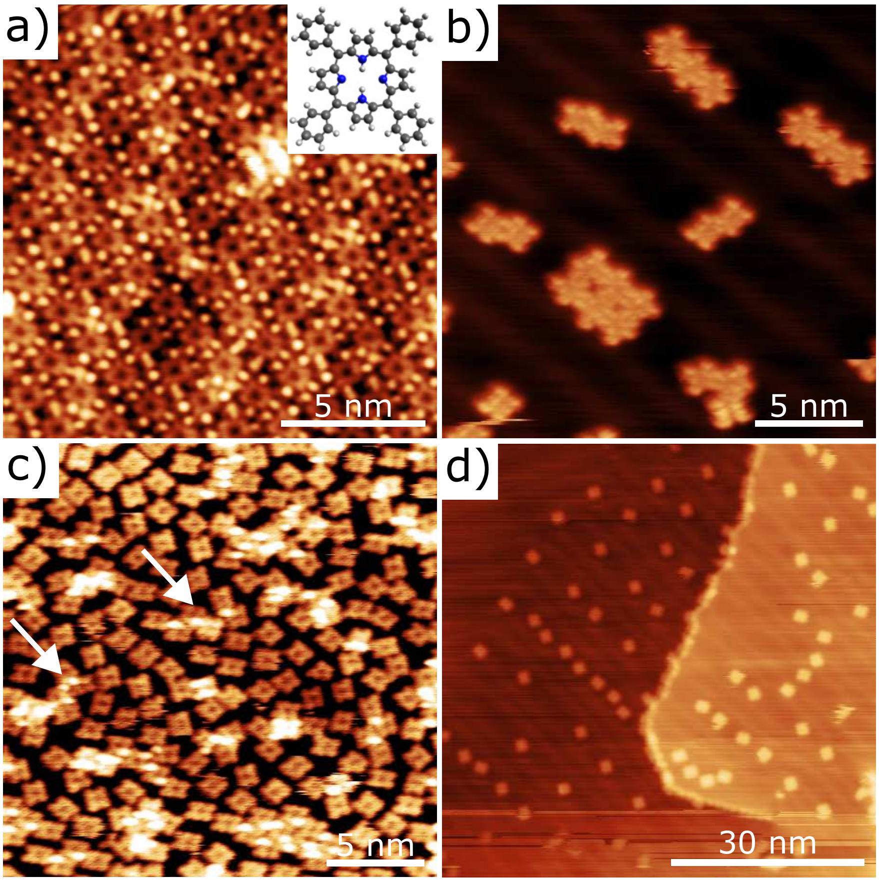

Figure 6.1: Close-packed TPP in both (a) monolayer and (b) sub-monolayer coverages on Au(111). Following an anneal to 580±50 K, the TPP were no longer close-packed and were now disordered for (c) monolayer and (d) sub-monolayer coverages. Arrows in (c) highlight incomplete ring-closing reactions. See the inset for the chemical structure of 2H-TPP. (STM data acquired by Dr. Frampton.)

6.2 Photoelectron and LEED investigations

A clean Au(111) single crystal substrate was prepared via several sputter-anneal cycles under UHV conditions (sputter: 1 keV for 30 minutes, annealing to 690 K for 30 minutes) and was subsequently characterised by LEED and XPS. The clean Au(111) surface was then exposed to a flux of 2H-TPP produced via sublimation from a Knudsen-type evaporator (280°C for 30 minutes whilst the substrate was held at room temperature). LEED was used to determine the deposition time required for a monolayer coverage which gives rise to a close-packed 2H-TPP overlayer. STM measurements indicate that stable close-packed structures are not formed below $\sim$ 1ML coverage of TPP at room temperature. We monitored the XP spectra between short sequential depositions. The spectra obtained were characteristic of TPP and the peak area increased as more TPP was deposited. Prior to reaching $\sim$ 1ML, no LEED pattern was obtained and we attribute this to a sub-monolayer deposition. At approximately 1ML, a LEED structure from the molecular overlayer was obtained. Sample temperatures were estimated based on calibration data obtained from a thermocouple positioned on a dummy sample prior to the experiment; the associated uncertainty for temperature measurements is estimated to be ±50 K. All measurements, other than those explicitly stated, were carried out with the sample held at room temperature and were acquired at different locations on the sample to minimise beam damage.

The I09 beamline consists of two undulator light sources that separately cover 'soft' (100-2000 eV) and 'hard' (2100–15000 eV) X-ray energy ranges. XP spectra of the C 1*s* and N 1*s* BE regions were recorded using photons generated by the soft X-ray undulator on the I09 beamline with energies of 900 eV and 600 eV respectively. The beam was 'detuned' (reduced in intensity) to reduce beam damage, whilst also providing a high signal-to-noise ratio. The photoelectrons were detected using a VG Scienta EW4000 HAXPES analyser mounted perpendicular to the incident X-ray beam. All binding energies quoted below are referenced to the Fermi level of the Au surface.

6.2.1 LEED data: characterisation of close-packed and diffuse structures

LEED was used to confirm the formation of a close-packed monolayer (shown by an overlayer diffraction pattern). TPP was deposited and the structure was characterised using microchannel plate LEED (MCP-LEED). MCP-LEED was chosen as it has a lower beam current, which should minimise beam damage to the molecular overlayer. A close-packed ordered surface was obtained as shown by a diffraction pattern on the LEED optics (see Figure 6.2a).

Using lattice dimensions of the molecular overlayer (STM measurements from Dr. Frampton), the overlayer structure was determined to be approximately square, with a unit cell of 1.4±0.1 nm × 1.4±0.1 nm that is incommensurate with the underlying surface lattice [130]. An estimation of the expected overlayer matrix description could be developed and further refined using the LEED data. Using LEEDpat [146], this matrix description can be simulated as a LEED pattern (see Figure 6.2b) and this provides a good level of similarity between the experimental and theoretical model. The matrix description of the overlayer, as determined by iterating through some values given by STM, and the experimental LEED pattern, is given by:

$$\begin{pmatrix} 3.96 & 5.41 \\ -3.96 & 1.45 \end{pmatrix}.$$

To probe the thermal stability of the surface, the close-packed ordered TPP preparation was heated slowly heated in front of MCP-LEED optics. No change in the LEED pattern was observed below 580±50 K. Upon reaching this temperature the diffraction pattern was no longer well defined and displayed a characteristic ring (see Figure 6.2c).

This ring pattern is indicative of a characteristic separation between species but not a well-defined crystalline overlayer. We were able to determine the average molecule-molecule separation, using the diffuse LEED pattern, to be 1.52±0.1 nm. Those dimensions are larger than that of the close-packed structure, and in combination with the lack of directional alignment, indicates that we have replicated the ‘diffuse’ effect seen in the group’s previous STM studies. By comparing the molecule-molecule separation, we found that the molecular density on the surface reduced from 0.51±0.05 nm^2 to 0.43±0.04 nm^2 (molecules per nm^2) following the anneal indicating that some TPP desorbs from the surface. To make this comparison (as the diffuse LEED data only provides molecule-molecule separation), we assume a square unit cell for both close-packed and diffuse data. These data are shown in full in Table 6.1. Further surface annealing did not have any effect on the diffuse LEED pattern already obtained. The reduction in molecular density occurs at the same temperature that the transition to the diffuse phase occurs. It is likely that two rate-activated processes are occurring at a similar temperature, one where the TPP is desorbed from the surface and the other where TPP becomes ring-closed. Once ring-closed, the TPP is likely to have a stronger interaction with the surface and therefore may desorb from the surface at a different temperature or rate.

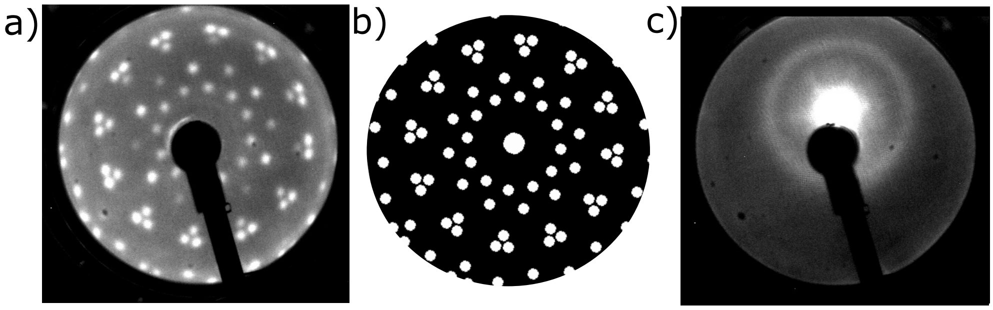

Figure 6.2: (a) The initial LEED pattern obtained for a close-packed monolayer of TPP on Au(111). Subsequent depositions using the same deposition parameters yielded the same diffraction pattern. LEED energy was 15.5 eV. (b) LEEDpat simulation using the matrix description of the overlayer (scaled to be similar to (a)). Edges of this simulation may differ from the experimental data due to distortion around the edges of experimental LEED optics not replicated by LEEDpat. (c) Following annealing to 580±50 K, no close-packed overlayer structure was present, with a characteristic ring pattern indicative of disorder shown. LEED energy was 6.5 eV.

Table 6.1: Molecule-molecule separations, obtained from LEED measurements, for TPP in the close-packed and diffuse phases. Estimated unit cell areas and molecular densities are calculated as described in the text.

Phase	Molecule-Molecule separation (nm)	Estimated unit cell area (nm^2)	Molecular density (molecules per nm^2)
Close-packed	1.4±0.1	2.0±0.2	0.51±0.05
Diffuse	1.52±0.1	2.3±0.2	0.43±0.04

6.2.2 XPS data: chemical environments

Following the deposition of TPP and formation of a close-packed monolayer, a wide XPS scan (BE 0-1000 eV) of the surface was carried out to provide elemental analysis, Au, N and C chemical signatures were detected. High resolution XP spectra were obtained by lowering the energy of the photons to provide a larger cross-section and more surface-sensitive readings within the C 1*s* and N 1*s* BE regions.

The C 1*s* carbon environments of the TPP molecule, shown in Figure 6.3a, were assigned based on work by Nardi *et al.* [147] that combined DFT and experimental spectra of TPP on a SiO_2/Si(100) surface. Our experimental C 1*s* spectra for the close-packed (ordered) 2H-TPP phase on Au(111) is shown in Figure 6.3b. Within our experimental data, the 4 phenyl rings (C_{Ph}) are assigned to the peak

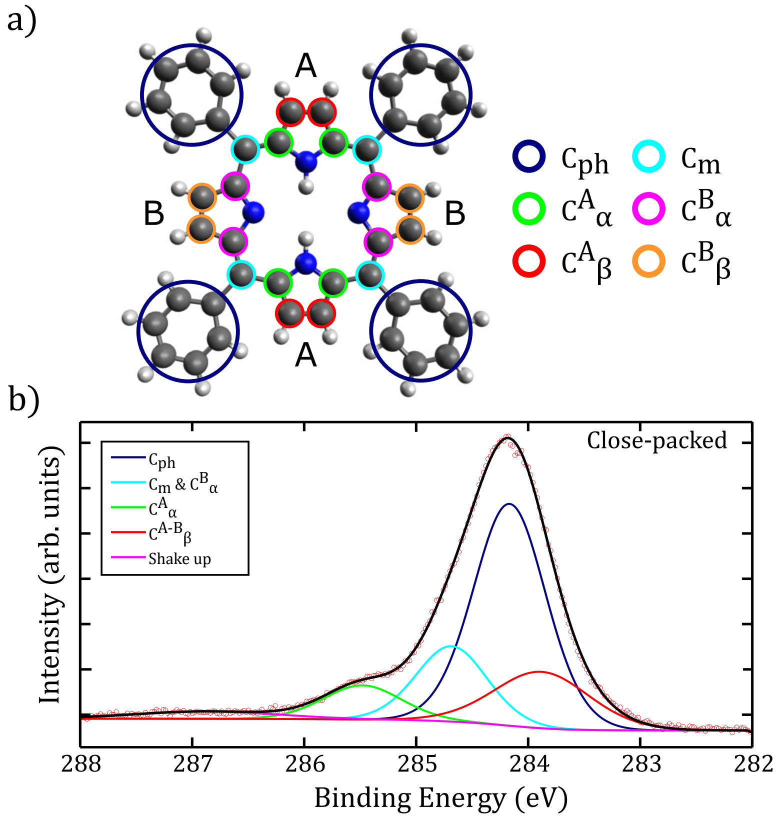

Figure 6.3: (a) Assignment of carbon environments based on work by Nardi *et al.* [147]. (b) C 1*s* XP spectra of the close-packed phase of 2H-TPP on Au(111). A Shirley background is fitted to the data, with the individual carbon environments fitted using Gaussian Lorentzian line shapes.

at 284.14 eV. The carbon environment at 284.68 eV is given by the *meso* (C_m) and C_α^B carbons. Furthermore, the peak at 285.48 eV is given by C_α^A. Finally, the peaks C_β^A and C_β^B are assigned to the 283.88 eV. A shake-up feature is visible but is negligible in our data set. The peak areas for each of these environments match the ratio for the molecule ($C_{Ph} : C_m + C_\alpha^B : C_\alpha^A : C_\beta^A + C_\beta^B$ the peak areas match 24:8:4:8). Unsurprisingly, due to different supporting substrates, our BE values differ from those reported by Nardi *et al.* (for a preparation of 2H-TPP on SiO_2/Si(100)), however, there is excellent agreement with respect to the relative shifts between the assigned carbon environments [147]. There was no change in the C 1*s* peak following heating the sample to 440±50 K.

N 1*s* XP spectra obtained for the close-packed TPP structure (shown in Figure 6.4a.), contains components assigned to iminic groups (=N-), at 397.2 eV BE, and pyrrolic (-NH-) groups, at 399.3 eV BE (with the expected ~2 eV shift between the two peaks observed). Additional features at 397.7 eV and 400.0 eV BE are also present. While these features may relate to multilayers of TPP [47], we observed an increase in the relative intensity of these peaks following annealing to 440±50 K. We, therefore, assign these features to an additional interaction between the iminic and pyrrolic nitrogens with a gold species. Based upon previous STM and density functional theory (DFT) studies of 2H-TPP on Au(111) the interaction can be assigned to gold adatom-2H-TPP species [37]. The co-existence of 2H-TPP and adatom-2H-TPP was confirmed using scanning tunnelling spectroscopy (STS) [37]. It is possible for the number of adatoms on the surface to vary, as they are known to diffuse freely on metal surfaces, including Au(111), with diffusion away from step-edges being a likely source of Au species [39, 148]. The ratio of the 2H-TPP to adatom-2H-TPP species (as identified within the N 1*s* XPS data) varied with sample preparation (sample temperature differed slightly between different preparations of the monolayer surfaces) and upon surface annealing to 440±50 K, in line with the expectation that the availability of Au adatoms is related to the surface temperature.

The anneal temperature for the transition to the diffuse phase was determined using LEED data. The C 1*s* and N 1*s* data were recorded again following the anneal to 580±50 K. XPS of the C 1*s* region showed evidence for two important

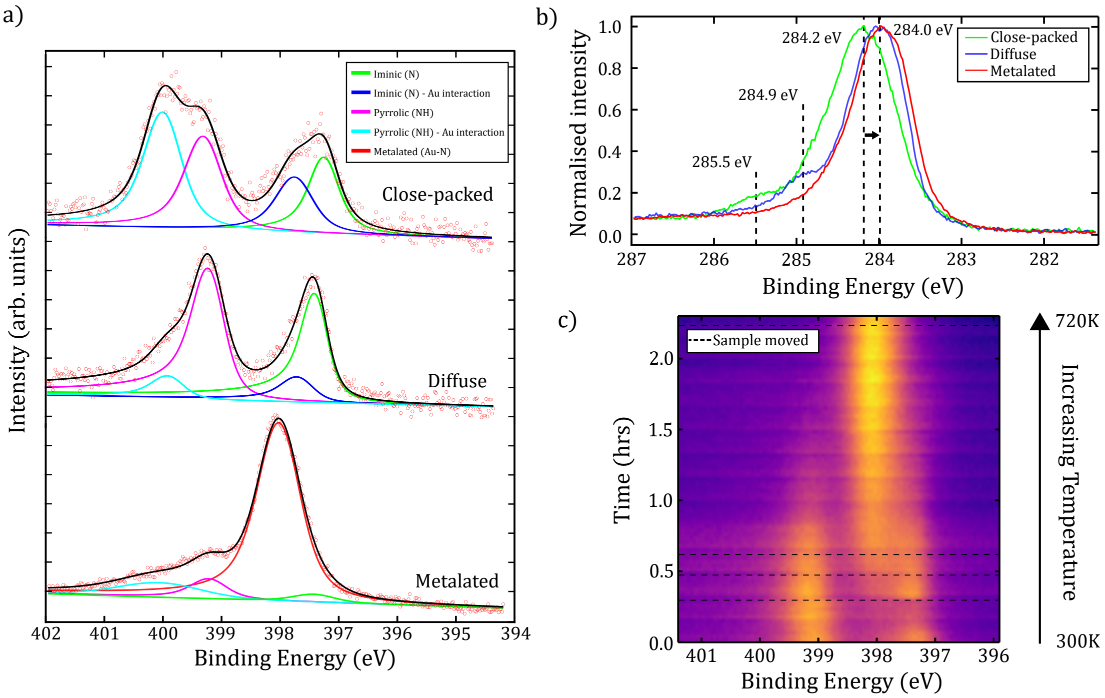

Figure 6.4: (a) XP spectra for the N 1*s* environment for each phase of TPP (close-packed/diffuse/metalated), as prepared by annealing. For both close-packed and diffuse spectra, iminic and pyrrolic groups are present with, in each case, additional peaks at slightly higher binding energies due to an interaction with Au adatoms. Further heating the diffuse phase produced a single nitrogen feature, indicative of a deprotonated environment within a metalated AuTPP species. Line shapes fitted using linear background and Doniach Sunjic line shapes. (b) C 1*s* XP spectra showing the shift to lower binding energies and loss of high BE features when annealing the surface. (c) Time-resolved N 1*s* XPS starting with the diffuse preparation at 0.0 hours. The sample was heated to 720±50 K over 2 hours (non-linear temperature change), resulting in a single metalated N 1*s* peak. The dotted lines correspond to movement of the sample whilst recording these spectra to reduce the effect of beam damage.

changes (see green to blue line in Figure 6.4b); a shift of the peak envelope to a lower binding energy (by ≈ 0.2 eV), indicating a change in the environment of the phenyl rings, and the loss of a feature at 285.5 eV (assigned to C_{α}^{A}). This is consistent with a 2H-TPP ring-closing reaction [46], and agrees with our STM observations of 'distorted' 2H-TPP species (see Figure 6.1c-d and Figure 5.16) following annealing. Related studies discussing fluorinated TPP species on Au(111) [49], 2H-TPP on Au(111) [38] and 2H-TPP on Ag(111) [46], report that phenyl rings are likely to react with the iminic part of the porphine ring due to DFT energy barrier analysis (whereas the loss of the C_{α}^{A} feature in our XPS data suggests a reaction via the pyrrolic part of the ring). Our study is consistent with a ring-closing reaction, and we propose that this is the on-surface process underpinning the observed order-disorder transition. The N 1*s* region of the XP spectra for the diffuse phase (Figure 6.4a) shows a reduction in the intensity of the peaks assigned to adatom-2H-TPP (399.9 eV and 397.7 eV BE), which is in agreement with an interpretation that flattening of the porphyrin species results in a reduction of conformation flexibility (e.g. switching from 'saddle' to a more 'planar' conformation), and hence reduces the interaction between Au adatoms and the nitrogen species within the porphyrin core.

Previous reported investigations characterising the heating of 2H-TPP on metallic substrates have shown that self-metalation of the porphyrin may be initiated by annealing to hotter temperatures than the ring-closing reaction [49]. By utilising time-resolved XPS measurements the effect of annealing the Au(111) surface to explore changes to the chemical environment of the molecule can be performed in real-time. The measurements (shown in Figure 6.4c) for the N 1*s* region were acquired while annealing to 720±50 K over 2.2 hours with non-linear increases in temperature. To check the effect of 'beam damage' the sample was periodically moved relative to the incident X-rays (indicated as dashed lines). We attribute the peak observed to grow at 398.0 eV to a strong interaction between four dehydrogenated nitrogen atoms, within the porphyrin core, and a Au species. This single nitrogen environment is indicative of full self-metalation of TPP. The partial metalation of TPP, due to interaction with Au adatoms or the substrate, would be expected to result in a slight increase in BE [40], compatible with the observed shift in BE from 397.7 eV to 398.0 eV. However, although metalated porphyrin species typically have nitrogen BEs in the range of 398.6-398.9 eV, it is known that this may be lowered as a result of interaction with the surface [149], or as an effect of localised charge on the molecule (e.g. AuTPP has previously been reported to exist in the 3+ oxidation state [150]), and as such our results are compatible with the formation of a AuTPP species.

6.2.3 NEXAFS data: a 'fingerprint' of self-metalation

NEXAFS data was acquired for the nitrogen K-edge for the three phases (close-packed, diffuse and metalated - data is shown in Figure 6.5) for the beam at three angles relative to the surface: normal incidence (0°), 'magic angle' (55°) and grazing incidence (85°). The raw data was normalised using methods described by Watts *et al.* [151]. This normalisation process involved: 1) Removing the vertical offset from the data, 2) normalising photon flux recorded from the soft X-ray drain current (as the flux of photons can change throughout the measurement due to the lifetime of electron beam and/or the topup of beam over time) and 3) subtraction of the background (clean Au) to provide a 'flat' lowest photon energy section.

NEXAFS data may be used to provide a 'fingerprint' of the TPP species in each preparation (information on the unoccupied states of the molecular species under study). When comparing the π^* states (first peak at the lowest photon energy), of the close-packed and diffuse phase, the photon energy of this peak is the same at 397.8 eV. Following metalation, there is a clear change in the dichroism of the first π^* state peak for the normal incidence spectra. This indicates that the macrocycle is tilted slightly following metalation [141]. Furthermore, the close-packed/diffuse π^* peak at 397.8 eV shifts to 398.4 eV for the metalated species.

Figure 6.6 shows a comparison between our studies of 2H-TPP on Au(111) and previous work on the self-metalation of 2H-TPP on the Cu(111) surface reported by Diller *et al.* [47]. When comparing the pre-annealed Au(111) and Cu(111) experimental data, the π^* transition at 397.8 eV and 397.6 eV for each preparation match well. The calculated NEXAFS data (Figure 6.6e - sum of

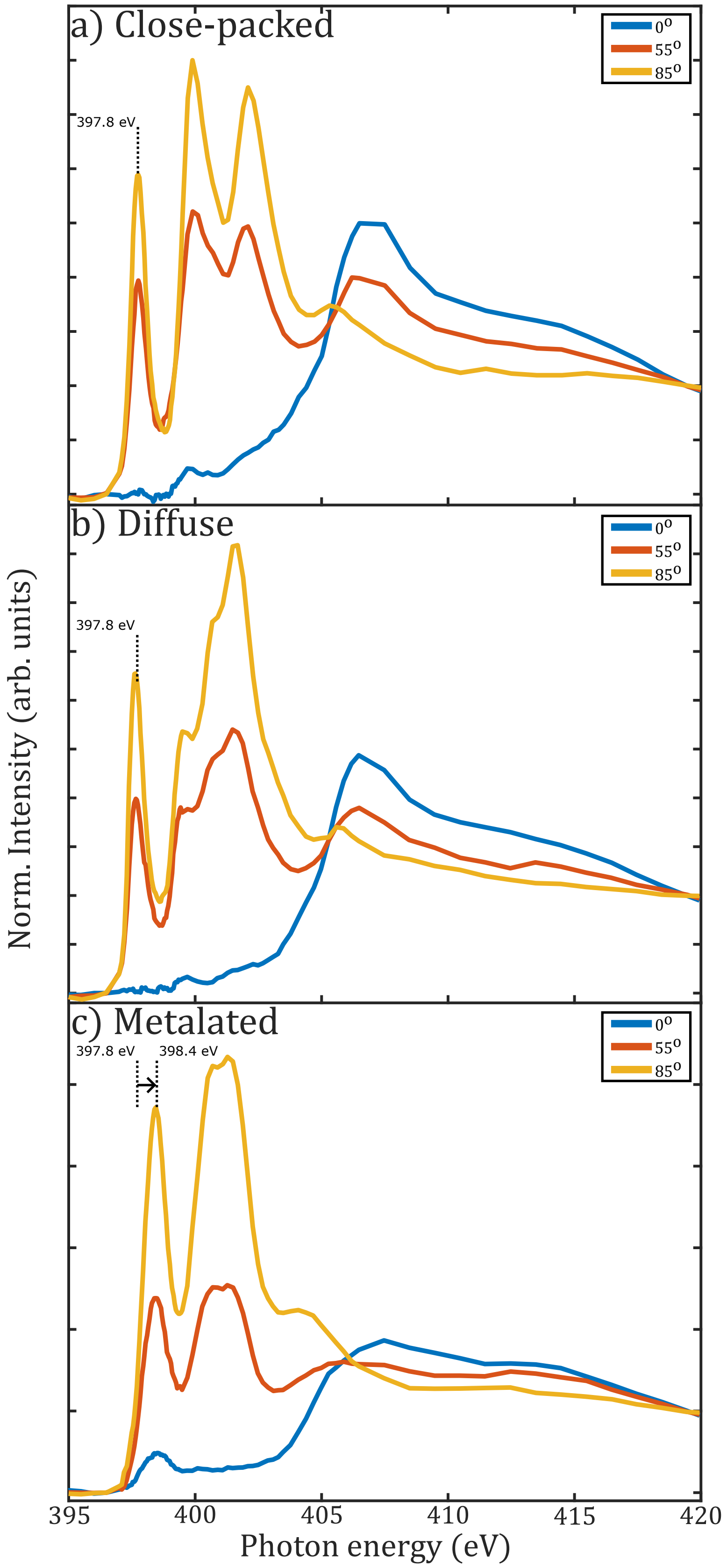

Figure 6.5: NEXAFS spectra acquired at normal incidence (0°), 'magic angle' (55°) and grazing incidence (85°) orientations for (a) the close-packed phase, (b) the diffuse phase, and (c) the metalated phase.

Table 6.2: NEXAFS peak positions [# This work, * Data reproduced from Diller *et al.* [47]].

Phase	Source	Peak 1	Peak 2	Peak 3	Peak 4
Close-Packed	Au(111) Exp#	397.8	399.9	401.9	406.5
	Cu(111) Exp*	397.6	399.8	401.6	
	Cu(111) DFT*	398.0	400.0	402.2	
Metalated	Au(111) Exp#	398.4	400.7	401.3	407.5
	Cu (111) Exp*	398.4	400.7	401.3	405.3
	Cu (111) DFT*	398.5	400.7	401.3	404.1

the peaks shown in Figure 6.6g where each nitrogen environment is considered separately) is also in good agreement with our experimental data, showing broad peaks at ∼400 eV and ∼402 eV and a σ^* feature at ∼407 eV.

We also observe a good agreement between the metalated CuTPP species and the species which we label as AuTPP (compare Figure 6.6b and 6.6d), where the π^* transition peak shifts to a higher photon energy. This π^* transition peak behaviour is replicated in the calculated NEXAFS data for a CuTPP species (see Figure 6.6f). Importantly, there is little to no agreement with the calculated spectra for a deprotonated TPP species (Figure 6.6h), which shows a shift to lower photon energy for the π^* transition peak. This indicates that the single nitrogen environment observed within the XPS data (Figure 6.4a) may be more readily attributed to AuTPP and not a deprotonated TPP species. The peaks present in our NEXAFS data and the Cu(111) experiment/DFT peaks are displayed in Table 6.2.

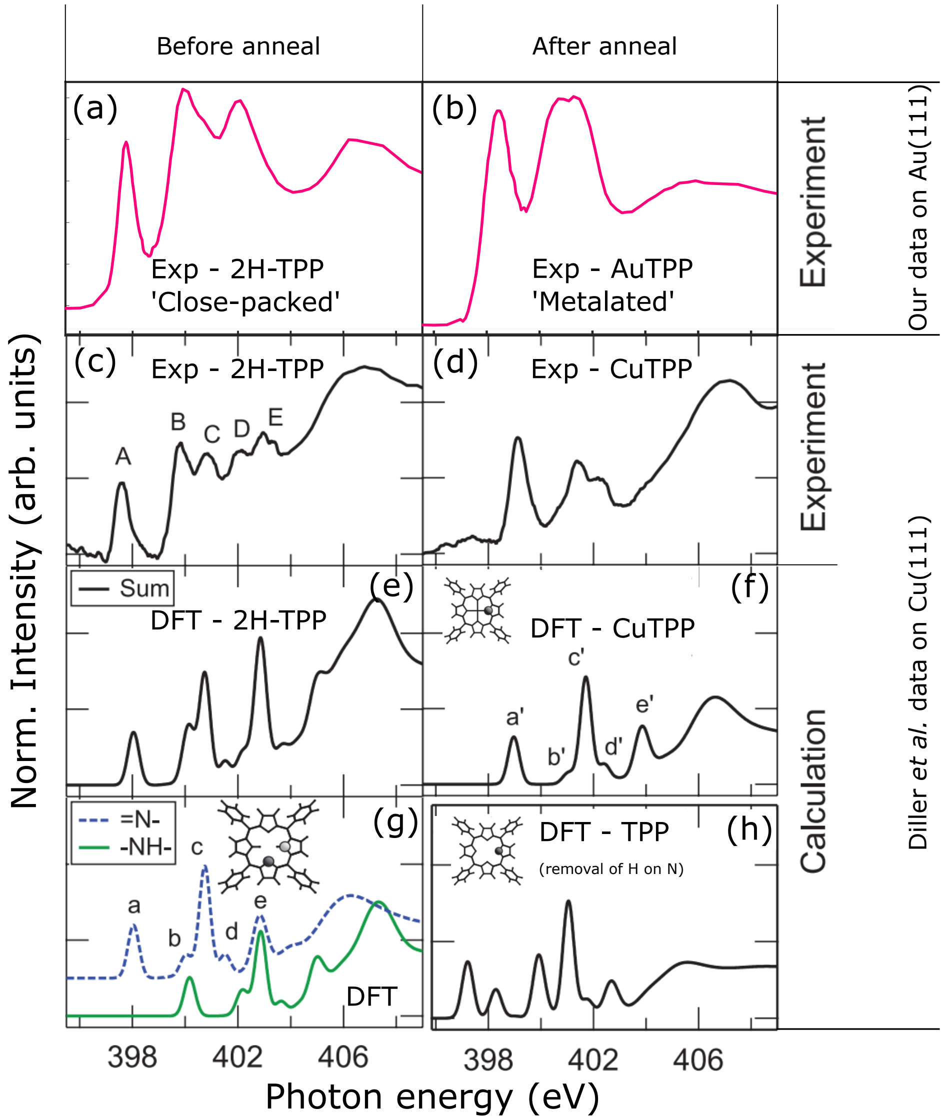

Figure 6.6: NEXAFS for the nitrogen K-edge region acquired for 2H-TPP on Au(111) with an angle of incidence of (55°), for (a) a close-packed phase, and (b) a metalated phase. (c-h) Experimentally obtained and DFT calculated nitrogen K-edge NEXAFS reproduced from Reference [47]: Experimental data for (c) 2H-TPP on Cu(111) and (d) CuTPP on Cu(111). Calculated spectra for (e) 2H-TPP (sum of g), (f) CuTPP, (g) 2H-TPP with contribution from iminic (N) and pyrrolic (NH) nitrogen species indicated, and (h) the deprotonated TPP species. [Figure 6.6(c-h) reprinted from Diller, K.; Klappenberger, F.; Marschall, M.; Hermann, K.; Nefedov, A.; Wöll, Ch.; Barth, J. V. *J. Chem. Phys.* 2012, 136 (1), 014705, with the permission of AIP Publishing.]

6.2.4 XSW data: structural characterisation

Normal incidence X-ray standing wave spectra were taken using (111) and $(\bar{1}11)$ planes of the Au(111) crystal. Here we show the (111) plane due to the low signal acquired in the $(\bar{1}11)$ plane. The mosaicity of the crystal was mapped by the reflected X-ray beam intensity at the Bragg energy for various crystal positions to determine a sufficiently good local crystalline structure position for the NIXSW. We used different areas of the crystal for each NIXSW data set to reduce the effect of beam damage. The incoming X-ray was detuned (attenuated) to reduce beam damage. We also recorded the hard XPS (taken using a photon energy ∼10 eV lower than Bragg condition photon energy) of the N 1*s* and C 1*s* spectra before and after NIXSW data collection to determine if beam damage had occurred. The C 1*s* peaks are considered within this work, see Dr. Frampton's thesis for N 1*s* NIXSW information [130].

6.2.4.1 Considerations whilst fitting NIXSW data

The NIXSW photoelectron yield data is generated by fitting environmental peaks based on known binding energies for specific elements, (determined for close-packed, diffuse and metalated) to individual hard XP spectra and monitoring the change in the area of that peak for each photon energy about the Bragg energy (see Chapter 3.2.4 for more details). The photoelectron yield data for each photon energy can then be plotted, once normalised such that the yield far away from the standing wave condition equals 1, and fitted to the function given by Equation 3.29. The fitting is carried out by a least squares fitting routine, giving associated errors for the fit related to the fitting parameters of the coherent position C_p and coherent fraction C_f. In the most basic of interpretations, the coherent position can be seen as the 'average height' of the environment within the reflection plane, and the coherent fraction as the level of 'order' of the environment at that coherent position (if the fraction was 1, then all of this environment would be at that coherent position). A better, but more detailed analysis, requires the use of an Argand diagram with modelled positions (angle) and fractions (radius) which form vectors, that sum together to give the coherent position and fractions vector as determined from experimental data given by the fitting program.

Within this dataset, we fitted XPS peaks that related to each environment the carbon atoms could be within the close-packed TPP species. These environments were discussed in the context of Figure 6.3. For completeness, these environments are $\mathrm{C}_a = \mathrm{C}_{ph}$, $\mathrm{C}_b = \mathrm{C}_m$ & C^B_α, $\mathrm{C}_c = \mathrm{C}^A_\alpha$ and $\mathrm{C}_d = \mathrm{C}^{A-B}_\beta$. These environments are shown in Figure 6.7a. These peaks were fitted using a combination of Gaussian and Doniach-Sunjic line shapes, in conjunction with a step function. The approximate photon energy of the Bragg condition for the (111) plane was 2631 eV.

When recording the NIXSW data, we inspected hard XP spectra of the C 1s and N 1s regions before and after to determine if beam damage was observed. From our initial inspection at the synchrotron, there was no obvious beam damage present on the surface. Further analysis later showed that there may be a linear shift of the peak envelope by $\sim$ 0.10-0.25 eV over the course of the NIXSW. This indicates that beam damage is causing some environments to alter under the photon flux resulting in a shift in BE. An example of the spectra envelope shift is shown in Figure 6.7b taken at the same photon energy before and after the NIXSW measurements.

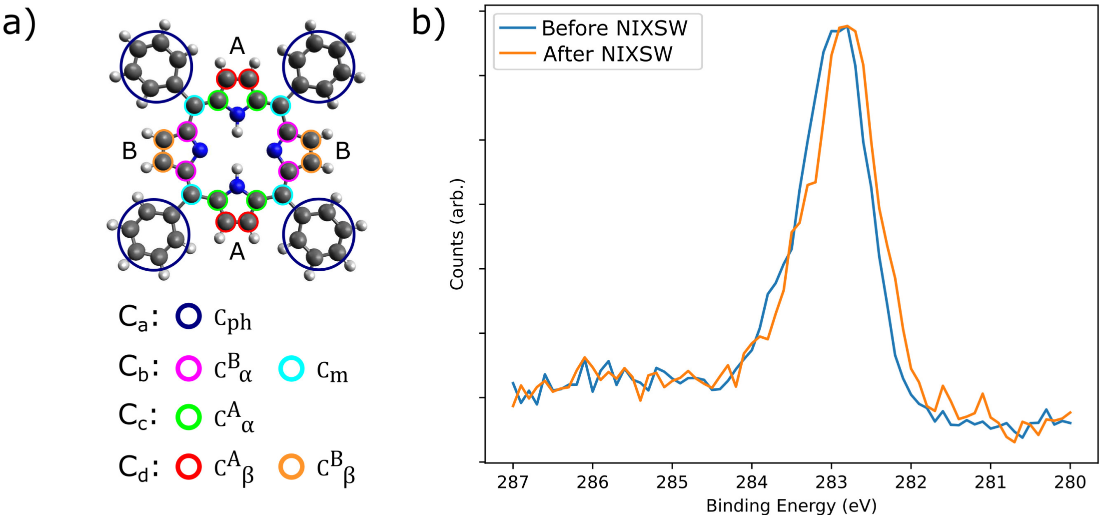

Figure 6.7: (a) Shows the environments for the C 1s NIXSW peak fitting. (b) The C 1s spectra obtained for the metalated TPP before and after NIXSW data collection. There is a clear shift to a lower binding energy. This is also replicated in the NIXSW data, where at each photon energy the envelope appears to shift to a lower binding energy. Photon energy was 2620 eV.

In the case where no beam damage is exhibited, it is expected that the photoelectron yields far away from the reflectivity/standing wave photon energy conditions are equal to 1. When beam damage is present in the data, and therefore shifts the peak envelope occur, the photoelectron yields may differ away from the reflectivity/standing wave (as seen in Figure 6.8b). This will lead to errors in the fitting program as the model on which the fit relies is no longer an accurate representation of the physical system under study.

6.2.4.2 Close-packed structural analysis

Shown in Figure 6.8 are the NIXSW photoelectron yield fits of the (111) reflection for the close-packed phase of TPP on Au(111). The resultant close-packed NIXSW coherent positions/fractions are displayed in Table 6.3. As determined by the LEED pattern and STM analysis, the TPP molecular overlayer is likely incommensurate with the atomic surface lattice. This means that low coherent fractions are expected, however, this in turn means that the interpretation of the data can be difficult. The results are compared in Section 6.2.5.

The phenyl rings (Figure 6.8a) show a well-defined NIXSW fit with low noise due to the high signal strength of this feature. Peaks labelled C_b (Figure 6.8b) show a reduction in adsorption at a photon energy of >2 eV than the Bragg energy, due to a loss of peak area likely as a result of beam damage. Due to low peak area, the C_c (Figure 6.8c) peak has high levels of noise related to the photoelectron yield. The C_d peak (Figure 6.8d) shows an increase of the photoelectron yield at a photon energy of >2 eV above the Bragg energy, likely due to the C 1s envelope shifting due to beam damage, however, it is difficult to see this as the fitted NIXSW intensity shows a plausible coherent position/fraction (compared to the effect seen in Figure 6.8b).

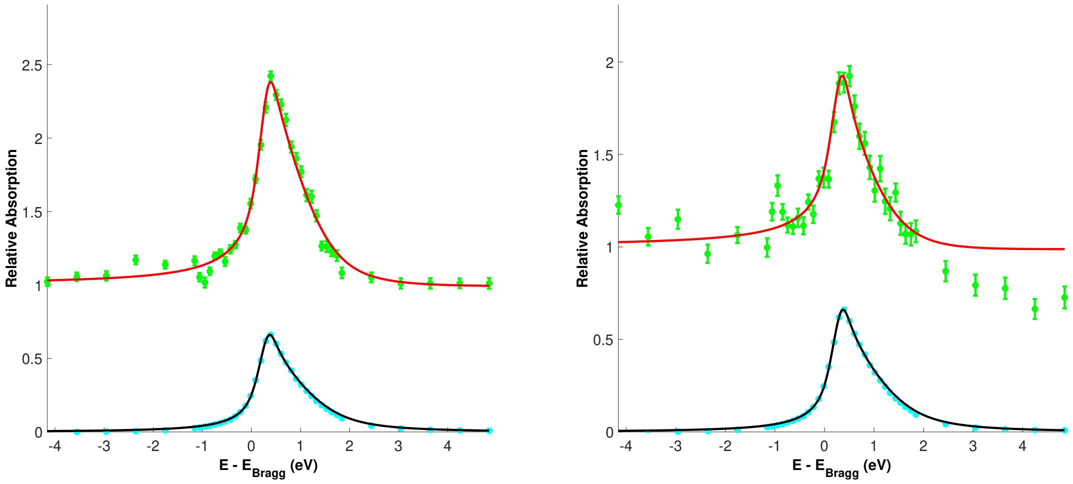

(a) C$_a$: C_f = 0.38±0.04, C_p = 0.40±0.03 (b) C$_b$: C_f = 0.13±0.08, C_p = 0.53±0.09

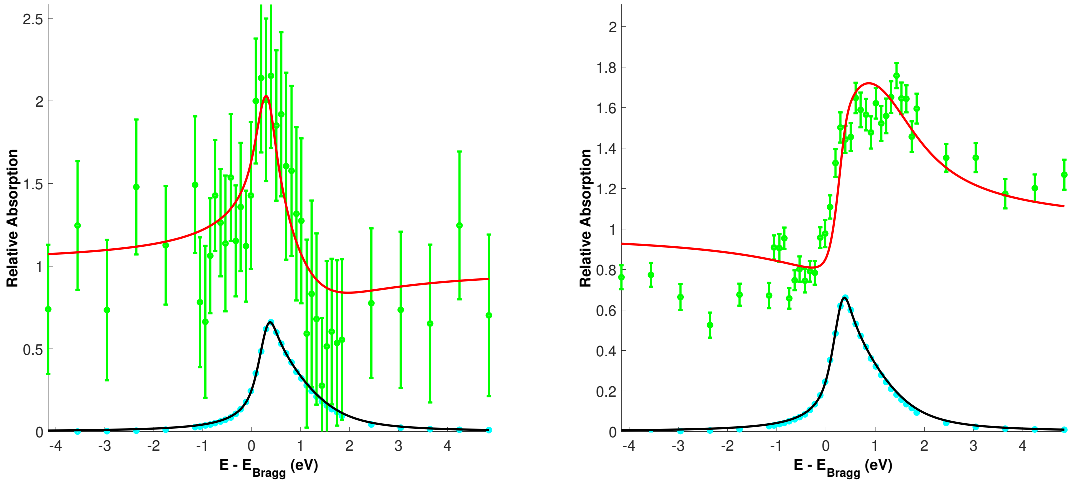

(c) C$_c$: C_f = 0.43±0.22, C_p = 0.63±0.12 (d) C$_d$: C_f = 0.50±0.11, C_p = 0.12±0.06

Figure 6.8: The fitted photoelectron yield (top of each sub-figure) to obtain a coherent fraction (C_f) and coherent position (C_p) for the (111) plane of the close-packed TPP preparation. These data were obtained by averaging three NIXSW data collections. The detected reflectivity is plotted on the bottom of each sub-figure.

Table 6.3: All the results from the close-packed NIXSW fitting for both (111) and ($\bar{1}$11) planes. It is unlikely that the positions of C_b-C_d are accurate due to beam damage.

	(111) plane		($\bar{1}$11) plane	
Carbon Environment	Coherent Fraction	Coherent Position	Coherent Fraction	Coherent Position
C_a	0.38±0.04	0.40±0.03	0.15±0.06	0.99±0.07
C_b	0.13±0.08	0.53±0.09	0.32±0.08	0.95±0.06
C_c	0.43±0.22	0.63±0.12	0.33±0.13	0.94±0.10
C_d	0.50±0.11	0.12±0.06	0.53±0.15	0.04±0.08

6.2.4.3 Diffuse structural analysis

As seen within the XP spectra the transition to the diffuse phase shifts the C 1s peak envelope over to lower BE (see Figure 6.4). This is the result of the formation of bonds between the phenyl rings and the outer carbons on the porphine ring. Shown in Figure 6.9 are the NIXSW photoelectron yield fits for the (111) reflection of the diffuse phase of TPP on Au(111). All the averaged diffuse NIXSW coherent positions/fractions are displayed in Table 6.4. As determined by the LEED pattern and STM analysis, there is no clear adsorption position of the diffuse TPP species. The results are compared in Section 6.2.5. Beam damage can be seen in Figure 6.9b, with the loss of absorption signal towards the higher photon energies.

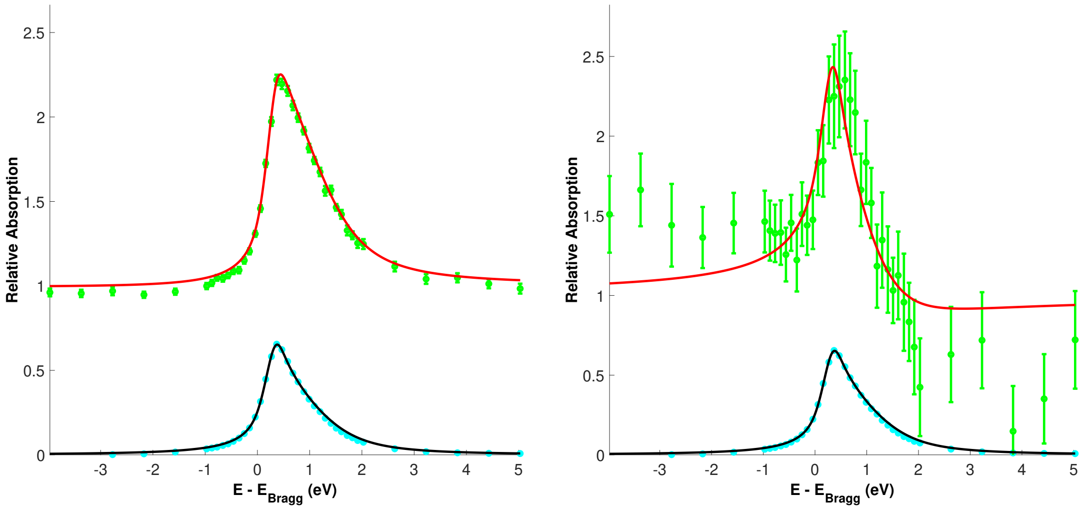

(a) C_a+C_d: $C_f = 0.38 \pm 0.02$, $C_p = 0.32 \pm 0.02$ (b) C_b+C_c: $C_f = 0.47 \pm 0.21$, $C_p = 0.51 \pm 0.12$

Figure 6.9: The fitted photoelectron yield (top of each sub-figure) to obtain a coherent fraction (C_f) and coherent position (C_p) for the (111) plane of the diffuse TPP preparation. These data were obtained by averaging two NIXSW data collections. The detected reflectivity is plotted on the bottom of each sub-figure.

Table 6.4: All the results from the diffuse NIXSW fitting for both (111) and ($\bar{1}$11) planes. It is unlikely that the positions of C_b+C_c are accurate due to beam damage.

	(111) plane		($\bar{1}$11) plane	
Carbon Environment	Coherent Fraction	Coherent Position	Coherent Fraction	Coherent Position
$C_a + C_d$	0.38±0.02	0.32±0.02	0.22±0.02	1.00±0.01
$C_b + C_c$	0.47±0.21	0.51±0.12	0.22±0.09	0.94±0.08

6.2.4.4 Metalated structural analysis

As seen within the XP spectra for the transition to the metalated phase, there are changes in the C 1s peak envelope as some features in the spectrum are no longer present (see Figure 6.4). Shown in Figure 6.10 are the NIXSW photoelectron yield fits for the (111) direction of the metalated phase of TPP on Au(111). All the averaged diffuse NIXSW coherent positions/fractions are displayed in Table 6.5. The results are compared in Section 6.2.5. Beam damage can be seen in Figure

6.10b, with the loss of absorption of the standing wave towards the higher photon energies. Unlike the other surface preparations, the ‘rocking curve’ (reflectivity curve as determined by a camera) did not correctly centre the Bragg photon energy position, resulting in the detailed section of the photon energy not being around the peak position. There is a very poor signal/noise ratio for the C_c curve, so we do not consider it further.

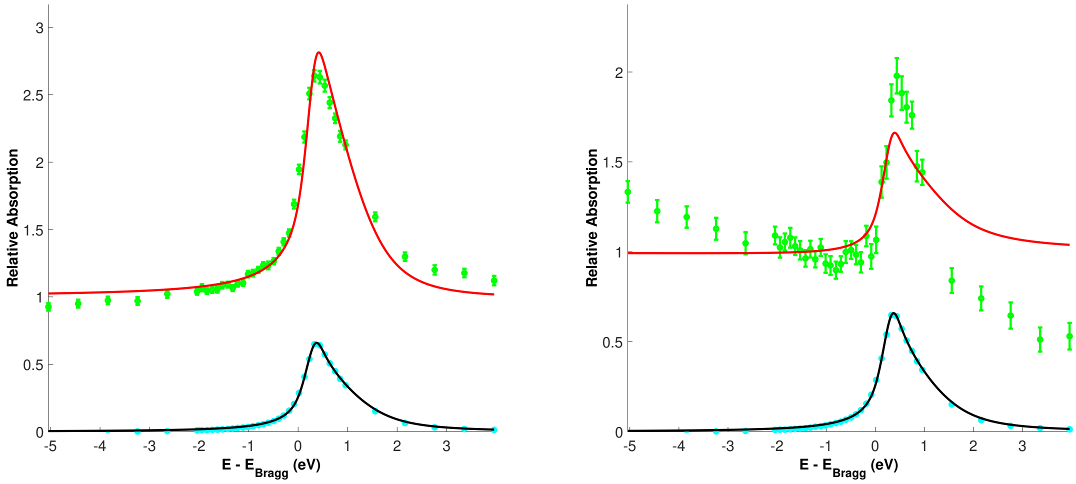

(a) C_a+C_d: $C_f = 0.67 \pm 0.06$, $C_p = 0.37 \pm 0.04$

(b) C_b: $C_f = 0.09 \pm 0.16$, $C_p = 0.06 \pm 0.21$

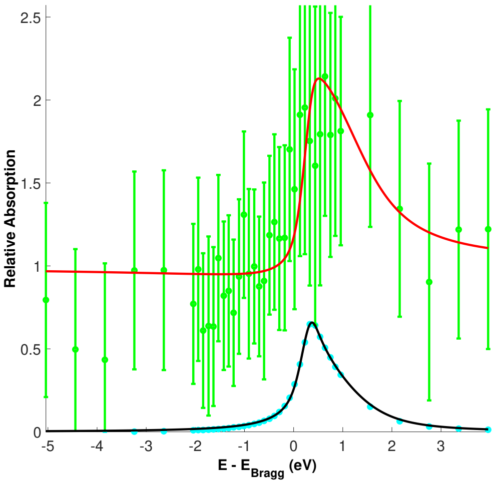

(c) C_c: $C_f = 0.45 \pm 0.22$, $C_p = 0.24 \pm 0.11$

Figure 6.10: The fitted photoelectron yield (top of each sub-figure) to obtain a coherent fraction (C_f) and coherent position (C_p) for the (111) plane of the metalated TPP preparation. These data were obtained by averaging three NIXSW data collections. The detected reflectivity is plotted on the bottom of each sub-figure.

Table 6.5: All the results from the metalated NIXSW fitting for both (111) and ($\bar{1}11$) planes. It is unlikely that the positions of C_b and C_c are accurate due to beam damage.

	(111) plane		($\bar{1}11$) plane	
Carbon Environment	Coherent Fraction	Coherent Position	Coherent Fraction	Coherent Position
C_a + C_d	0.67±0.06	0.37±0.04	0.24±0.02	0.01±0.02
C_b	0.09±0.16	0.06±0.21	0.39±0.15	0.92±0.11
C_c	0.45±0.22	0.24±0.11	0.72±0.19	0.00±0.09

6.2.5 Comparison of NIXSW data

Shown in Figure 6.11 is the position of the C 1*s* chemical environments, relative to the projected d_{111} planes. The minimum 'height' a carbon atom could be positioned at is shown by the dotted line given by the Van der Waals radius (as calculated at the 3-fold hollow site for Au and C atoms). Within the close-packed phase, it is expected that the TPP is adsorbed on the surface in a saddle-shaped conformation. The NIXSW results for the close-packed phase show various heights of the carbon environments. The carbon atoms bonded to the iminic nitrogen are closer to the surface than the carbon atoms bonded to the pyrrolic nitrogen. The carbons on the periphery of the nitrogen-carbon rings are higher than the other carbons, pointing the nitrogen features towards the surface. It could be expected from these results that the iminic nitrogen are closer to the surface than the pyrrolic nitrogen, which is the result obtained by the nitrogen NIXSW (see Dr. Frampton's analysis [130]). Adsorbed closer to the surface are the phenyl rings, which makes this consistent with a saddle-shape adsorption onto the Au(111) surface. Upon annealing, cyclodehydrogenation and ring-closing reactions occur which 'flattens' the molecule. The NIXSW results for the diffuse phase show evidence of a flattening of the molecule, compared to the saddle-shaped confirmation (the carbon environments C_a and C_d are closer together). Upon metalation of the TPP species, the conformation changes possibly to incorporate a Au atom within the macrocycle cavity, as all carbon atoms

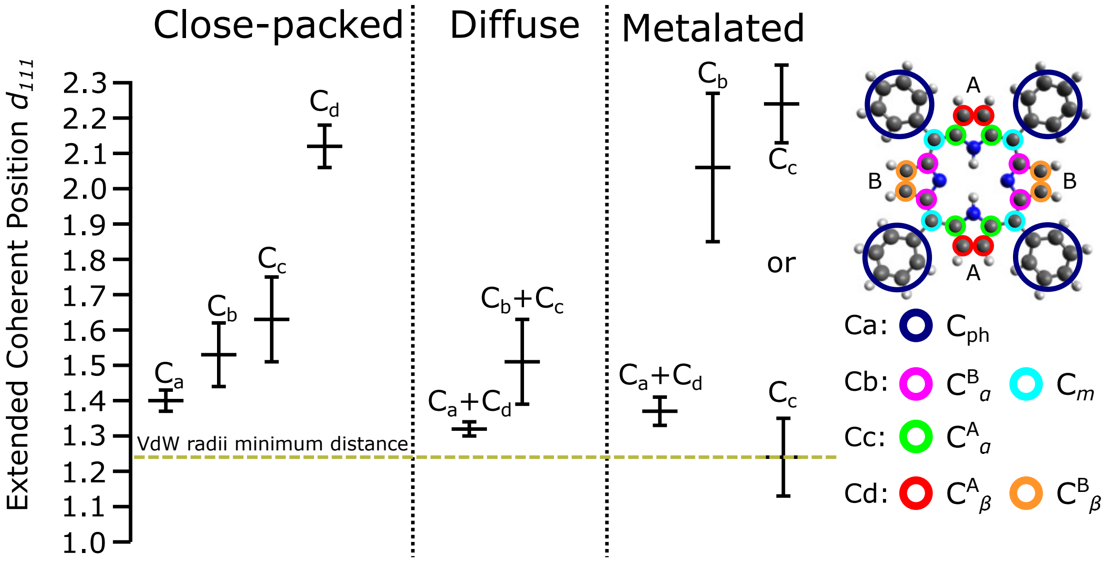

Figure 6.11: Average positions of the carbon environments within the extended surface planes d_{111}, as determined by NIXSW analysis. Low coherent fractions obtained in conjunction with the coherent positions mean that these positions can only be interpreted as the average position of the carbons environments. The associated errors in the positions are plotted as error bars. See right for the chemical structure and assignment of chemical environments. The minimum position a carbon atom could be positioned is shown by the dotted line given by the Van der Waals radius of the Au surface.

are adsorbed closer to the surface than the close-packed phase.

We should note that the loss of photoelectron yield and subsequent poor fitting performance for the C_b and C_c features in the diffuse and metalated make this challenging to properly assess. Furthermore, since not all TPP species form the same ring-closed product, these differences in structure may result in uncertainties in the fitted XP spectra to form NIXSW fitted peaks. It should also be noted that the low coherent fractions obtained make it difficult to interpret these heights as the absolute height of a carbon environment, but more as an average height of all of the carbons within that environment. However, this work shows how detailed structural information can be obtained at three stages within the on-surface self-metalation reaction of TPP.

6.3 Conclusion

We have utilised a combination of STM, LEED, XPS, NIXSW and NEXAFS to characterise an order to disorder transition of TPP on Au(111). The surface-sensitive techniques provided information on the chemical and order-disorder changes that occurred during this on-surface process. The observed transition from an ordered close-packed phase to a disordered diffuse phase was found to be correlated with a cyclodehydrogenation ring-closing reaction, which resulted in the 'flatter' porphyrin. Analysis of N 1*s* XPS data allowed us to identify two distinct porphyrin species within the close-packed phase, 2H-TPP and adatom-2H-TPP (a 2H-TPP species which forms a strong interaction with a Au adatom); in agreement with previous STM studies of the 2H-TPP Au(111) system. Further annealing of the diffuse phase resulted in the formation of a single nitrogen environment which, supported by previous studies and our own NEXAFS measurements, is indicative of the formation of a fully metalated AuTPP species. The NIXSW analysis provides a structural characterisation of the TPP molecule specific to each carbon environment for each phase in the reaction. Within the close-packed phase, there is evidence of saddle-shaped adsorption, in the diffuse phase the NIXSW shows a flattening of the TPP and in the metalated phase, the TPP appears to change conformation to incorporate the Au atom into the macrocycle cavity.

Chapter 7

Near ambient pressure gas dosing on iron phthalocyanine on Ag(111)

In this chapter, we explore the behaviour of iron phthalocyanine (FePc) on Ag substrates when exposed to specific gases (CO, H_2O and O_2). Two crystallographic planes of silver were used to support the FePc deposition. The Ag(111) plane was used to explore the effect of the exposure of CO, H_2O and O_2 to FePc in the 1-10 mbar pressure region. Here we show, via STM characterisation, that we can reliably create monolayer coverages using thermal sublimation of the FePc molecules by either setting a specific deposition time or by annealing multilayers of FePc to create a monolayer. We found that there was no clear interaction between the gases and the FePc-Ag(111) surface under the pressures accessed here. We discuss issues relating to contamination (Ni co-deposition with CO) and find that H_2O does not interact with the FePc/Ag(111) system at room temperature - in contrast to low-temperature studies. In Appendix B, we discuss the adsorption of FePc on a Ag(110) surface and characterise this surface with NIXSW and XPS.

7.1 Motivation

Transition metal phthalocyanines are of particular interest due to their potential use in light-emitting diodes, field-effect transistors and even solar cells [152,153]. The magnetic properties of a phthalocyanine due to the metal centre potentially allows for nano spintronic devices [154,155]. One of the key challenges faced by science more broadly is the capture, storage and processing of 'greenhouse gas emissions' as a result of burning fossil fuels. An approach to tackling this problem is with the use of functional surfaces prepared with bespoke chemical species, containing active sites, for the adsorption of small gaseous molecules. The formation of self-assembled close-packed structures of porphyrins and phthalocyanines on metallic surfaces at cryogenic temperatures is well studied, with some focusing on the ligation of gaseous species onto the core of various metalated phthalocyanine species [33].

Iron phthalocyanine (FePc) has been the subject of many gas-based experiments. The iron core of the FePc can ligate with carbon monoxide and the spin state of the iron core may be altered (where the substrate is held at cryogenic temperatures) [156,157]. FePcs have also been exposed to gaseous H_2O, on Ag(111) surfaces held at 60 K, where the ligation was shown to provide proof of the surface-*trans* effect [61]. FePc on Ag(110) has also been reported to interact with O_2 to change the chemical state of the iron core and also alter the spin exhibited by the iron atom [62,158].

Dosing of gases onto molecular species is typically carried out at relatively low pressures ($<10^{-6}$ mbar), where 'Langmuir dosing' of the gas is used to consider the relative exposure that the surface gets to the gas. The field of near-ambient pressures for gas exposure on molecular systems has been less extensively explored. An example of CO dosing using near ambient pressures up to 12 mbar, is shown by Corva *et al.* where CO is dosed on a monolayer of FePc on Ir(111), showing ligation with the iron core when characterised by IR vibrational spectroscopy at room temperature [159].

In our experiments, we aim to first characterise the surface topography of FePc on Ag(111) via UHV-STM. Then using near ambient pressure gas dosing, simultaneously expose FePc to various gases whilst recording the XP spectra to determine changes to the chemical environments. We can then transport the samples back to a UHV-STM system for post-gas dosing characterisation to inspect how the self-assembled structures have evolved and to determine if any changes to the electronic states of the molecules have occurred.

In Appendix B, we discuss the adsorption of FePc on a Ag(110) surface and characterise this surface with NIXSW and XPS. The O_2 adsorption between FePc-Ag(110) reported by Sedona *et al.* showed interesting behaviour in STM, where the bright Fe core of the FePc molecule is dulled upon exposure to O_2. The bright feature is reported to return upon annealing of the surface. The oxygen is expected to be underneath the FePc (between the FePc and Ag(110) surface), and using NIXSW we are able to determine any changes in the adsorption height of the FePc molecule.

7.2 Experimental methods

All STM measurements were made using an Omicron STM-1 ambient temperature UHV STM system. The STM chamber had a base pressure of less than 5×10^{-9} mbar, with a deposition chamber base pressure of 2×10^{-8} mbar. All experiments were carried out on Ag(111)/mica substrate that had been degassed prior to use, and cleaned with at least two sputter and anneal cycles between preparations. Surface heating was achieved by passing a current through a doped Si sample behind the Ag/mica sample.

Iron (II) phthalocyanine was deposited from a Knudsen cell within the deposition chamber, via thermal sublimation, onto Ag(111)/mica substrate held at room temperature. FePc was purchased from Sigma Aldrich, with a quoted purity of ∼90%; this is common amongst most other publications [156, 160]. The molecules required many days of thermal purification, 10-50°C below the deposition temperature (∼400°C). Various coverages of FePc were deposited onto the silver surface by varying the deposition time.

XPS characterisation of the sample was performed with a Specs NAP-XPS system; AlKα source with a characteristic photon energy of 1486.6 eV. Gas dosing of the surface was carried out in a near ambient pressure cell, within the vacuum chamber, whereby gas leaked into the cell and exposes the surface to ∼mbar levels of pressure. Gases dosed were of at least a 5.0 purity standard. The photoelectrons generated by the incident X-ray spot escape the NAP-cell to the hemispherical analyser via a cone placed close to the surface. The gas flow is controlled by mass flow control valves, providing excellent control of the pressure exerted by the gas when leaked into the cell. The gas lines used to transport the gas to the NAP cell are flushed thoroughly prior to their use. Samples were transported between the STM and NAP-XPS systems via vacuum suitcase.

7.3 Characterisation of deposited FePc using scanning tunnelling microscopy

Sub-monolayer coverages of FePc were prepared and characterised at room temperature using STM. However, stable islands of FePc were not observed at room temperature for sub-monolayer coverages. Stable multilayer coverages of FePc were prepared on Ag(111) as shown in Figure 7.1a. Step edges of the underlying surface are evident, indicating that the multilayer film is not thick enough to cover surface features or become insulating with respect to STM tunnelling. The top layer of the multilayer film has a square-type packing arrangement, however, insufficient resolution was obtained to characterise this top layer structure.

Monolayer coverages of FePc are obtained in this investigation by sequentially depositing on previous depositions until a close-packed overlayer is seen in room-temperature STM. At monolayer coverages, the FePc forms well-ordered regions, over 40 nm^2, with few defects (see Figure 7.1b). Multilayer coverages could be reduced to a monolayer by annealing the sample to 250-300°C (see Figure 7.1c). Comparing the two preparation methods of forming a monolayer (Figure 7.1b - depositing until close-packed structures are obtained, and Figure 7.1c - multilayer deposition is then annealed to a monolayer), the structure of FePc film layer is similar. Additional defects in the surface overlayer are more numerous following the 250-300°C anneal, in the form of larger ‘blobs’ and brighter individual FePc species when compared to a monolayer (Figure 7.1b). In Figure 7.1d, annealed

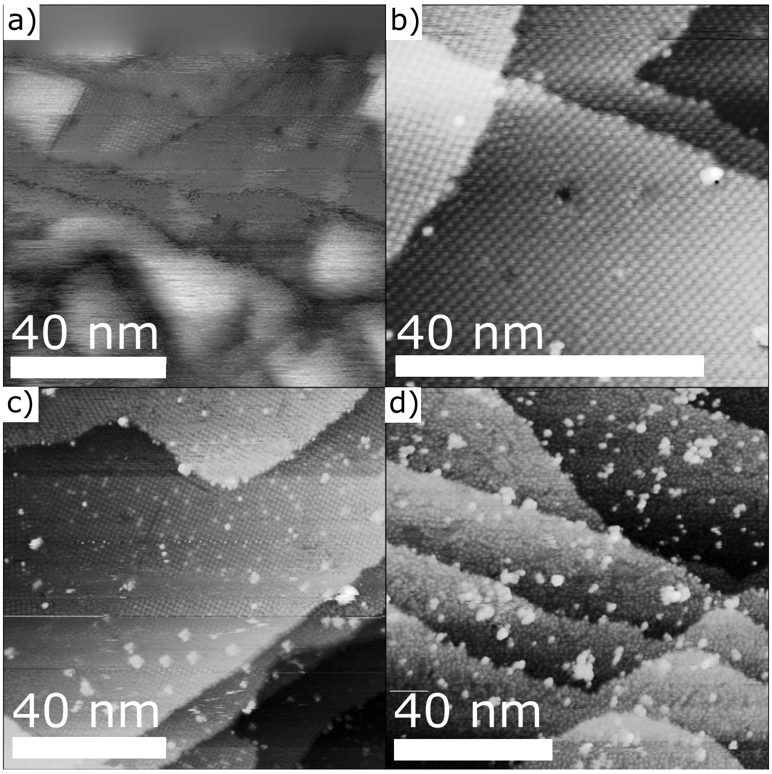

Figure 7.1: Different thicknesses of FePc films before and after annealing. (a) A multilayer of FePc, prior to annealing. (b) A monolayer after an anneal at 120°C. No changes to order structure were seen following this anneal. (c) A monolayer formed from annealing a multilayer at 250-300°C. (d) A monolayer of disordered FePc after an anneal above 300°C. STM image parameters V_{sample} = 1.5-1.8 V, I_{set} = 15-30 pA.

to > 300°C, it is clear that the surface is no longer ordered with many more large 'blobs' present on the surface. We attribute this to molecular reactions between FePc molecules, through temperature-induced homocoupling reactions as the isoindole rings become dehydrogenated [161].

High-resolution images of FePc within close-packed structures were obtained as shown in Figure 7.2a; showing the self-assembled structure formed. An overlay of a scaled FePc molecule is included, and it clearly shows the structure of the FePc molecule: a bright Fe centre and four isoindole rings making a 'plus' shape. As this image was acquired at room temperature, high levels of noise and drift can be seen. To obtain the unit cell dimension, as shown in Figure 7.2b, we average over several backward/forward and up/down scans. The vectors of the unit cell are: a_1 = 1.36±0.02 nm, a_2 = 1.37±0.02 nm with an angle between the two vectors of θ = 81±5°. These values are similar to those reported by

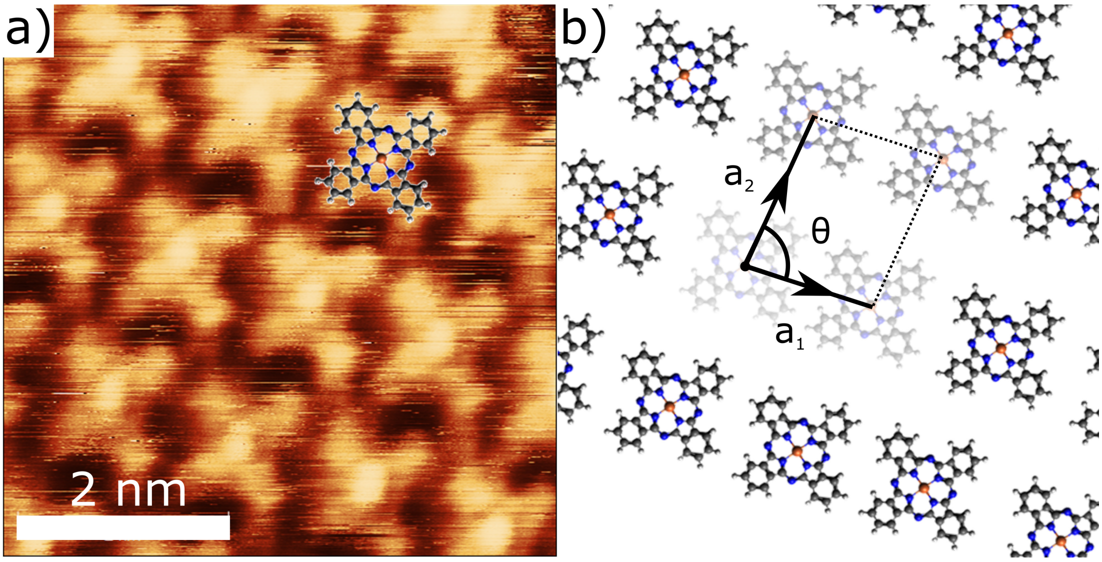

Figure 7.2: (a) High-resolution image of FePc on Ag(111)/mica with a scaled overlay of the FePc chemical structure. (b) Overlay structure of FePc showing the unit cell. STM image parameters V_{sample} = 1.4 V, I_{set} = 30 pA.

Takami *et al.* [162]. The molecular overlayer is incommensurate with the surface as reported previously [61].

An overview of a monolayer of FePc is shown in Figure 7.3a. Three clear domains of the self-assembled close-packed structure exist in this image, rotated by ~60° reflecting the symmetry of the underlying surface. This ~60° domain structure is also seen by Grand *et al.* in the epitaxial growth of CuPc on Ag(111) [163]. Two of the domains are observed to be separated by a boundary (see arrow). Also present on the surface are bright features, that line-spectra show to be much higher than the close-packed surface FePc molecules (see Figure 7.3b). These features appear sporadically over the surface and we attribute these features to 2nd layer FePc molecules. It was very difficult to scan this second layer for more detail, due to tip and/or surface instability whilst imaging. Multilayer FePc molecules are reported to rotate their adsorption axis, potentially providing a rationale for the difficulty in imaging these features [164]. Additional features that appear 'less bright' than the second layer bright FePc molecule can also be seen (see line-profile in Figure 7.3b), which we attribute to adatoms underneath the molecule, which has similarly been seen in TPP on Au(111) [37]. The next step is to characterise these structures using XP spectroscopy to provide chemical sensitivity of the FePc film.

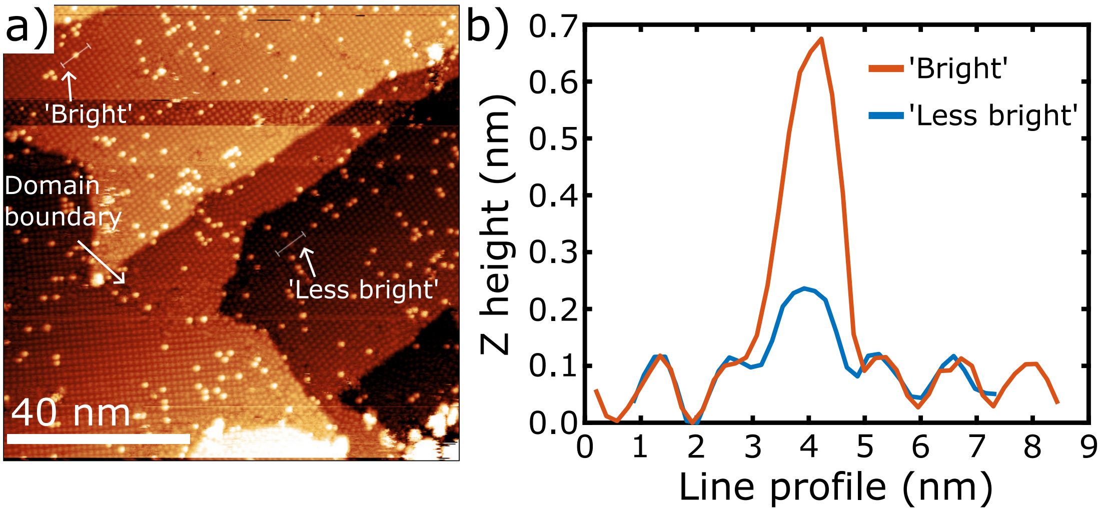

Figure 7.3: (a) STM topograph of a FePc monolayer. Brighter features correspond to the second layer. Less bright features are attributed to adatoms under the FePc monolayer. There are also three different directions of FePc, corresponding to different ordering domains rotated ∼60° from each other. A domain boundary is highlighted with an arrow. (b) Line profiles of the two features labelled in (a). STM image parameters: $V_{\text{sample}} = 1.8$ V, $I_{\text{set}} = 16$ pA.

7.4 X-ray photoelectron spectroscopy

In this section, we show the XPS characterisation of C 1s, N 1s and Fe 2p for various preparations of FePc on Ag(111). The binding energy of the data recorded was calibrated with respect to the Ag 3$d_{5/2}$ peak (368.2 eV). The regions measured were exported for analysis to CasaXPS [82], where background and peaks were fitted to the regions corresponding to the elemental environment. C 1s regions are clearly observed compared to the N 1s region, as the latter peaks sit on a loss feature of Ag 3d, and the Fe signal is weak due to the small quantity of iron on the surface [165, 166]. All peaks were fitted using a Gaussian:Lorentzian curve (0.7:0.3) [82]. Several samples were prepared, however, here we discuss the spectra for a multilayer, annealed monolayer (multilayer is annealed to form a monolayer) and a monolayer formed without annealing.

7.4.1 C 1*s* Spectra

FePc has two main carbon environments (benzene and pyrrole). Carbon atoms in aromatic compounds have $\pi - \pi^*$ transitions, which also contribute a shake-up feature for every carbon environment [167]. This means that there may be 4 peaks visible. It may be technically possible to fit 5 peaks [166], by differentiating further between inter-benzene environments, or vibrational coupling within the C-H stretching mode, but our data does not have the resolution to support this analysis.

7.4.1.1 Multilayer

The C 1*s* XP spectra for a multilayer of FePc can be seen in Figure 7.4, where 6 peaks have been fitted (4 peak fit + 2 peaks). The C 1*s* spectrum shown is similar to previous studies of phthalocyanines [156, 165, 166]. The 24 benzene carbons (B C 1*s*) produce a peak centred at 284.5 eV, creating a shake-up feature (B SU) at 286.7 eV on the tail of the 8 pyrrole carbons at 285.9 eV. The pyrrole shake-up feature is attributed to the peak located at 287.8 eV. Furthermore, the energy shift between the B C 1*s* and B SU peaks and P C 1*s* and P SU (2.2 eV and 1.9 eV) is attributed to the excitation of an electron from the HOMO to the LUMO state, in line with an experiment of FePc on Ag(110) by Palmgren *et al.* [164,168]. Our data, for the multilayer film, is typical for bulk phthalocyanines, or weak interactions between phthalocyanines and the surfaces [160, 164, 166].

There are a further two peaks at 289.3 eV and 291.8 eV. The two additional peaks have previously been attributed to background structures, however, in most publications the features have been too small to notice or assign a peak [165]. These features may appear in our data due to interactions between FePc in bulk structures, and therefore, we have access to additional loss features. The full-width half maximum of the B C 1*s* and P C 1*s* equal 1.08 and 1.10 and the corresponding shake-up features FWHM values are 1.27 and 1.28 respectively.

The area ratio of B C 1*s* and P C 1*s* is 2.4, lower than the predicted value of 3 and lower than 2.7-3 reported previously [164, 165]. Previous literature attempts to obtain the ratio of 3, were unsuccessful because the pyrrole peak was artificially large due to the unresolved benzene shake-up feature [165]. In our case, the

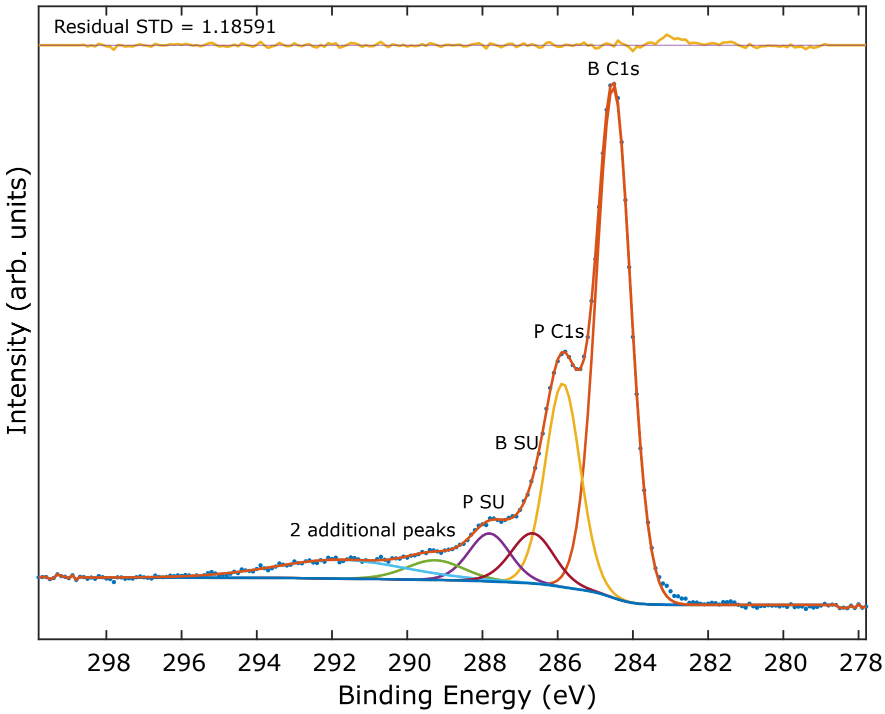

Figure 7.4: C 1*s* XP spectra of a multilayer of FePc. A Shirley background was fitted, followed by 6 peaks, made up of benzene C 1*s* and shake-up features (B C 1*s* and B SU), pyrrole C 1*s* and shake-up features (P C 1*s* and P SU) and 2 additional peaks. The residual of the fitted curve to the data is plotted at the top of the figure, with the associated residual standard deviation (STD).

benzene shake-up feature has been accounted for, however, less resolution in our data and the larger presence of additional peaks provide greater challenges in fitting. In Figure 7.4 the fit at 283 eV is poor, showing that there may be an additional unresolved peak present, an asymmetry or beam damage. Previous experiments have attributed contamination within the source material to binding energies around 282 eV [164].

7.4.1.2 Annealed monolayer

This surface was created following a 10-minute deposition and subsequent anneal to 530 K; resulting in a significant decrease in the carbon peak. The C 1*s* spectra of this surface can be seen in Figure 7.5; 6 peaks have been fitted (4 peak fit + 2 additional peaks). In the C 1*s* spectra, the carbon environments of B C 1*s*, P C 1*s*, B SU and P SU are assigned to peaks of 284.3 eV, 285.4 eV, 286.4 eV and 287.8 eV respectively. Surfaces such as Al and Ag interact strongly with phthalocyanines [164] and cause a reduction in the shake-up features, this is clear in the P SU peak in Figure 7.5 compared to Figure 7.4, showing a less well-defined feature. One of the arguments made by Ruocco *et al.* was that intermediate films (approximately 2 layers of phthalocyanines) may produce C 1*s* spectra with a superposition of peaks between a single layer and bulk [164]. These results are consistent with other work involving surfaces that interact strongly with phthalocyanines, lowering the binding energy of most of the peaks compared to the bulk [164, 168].

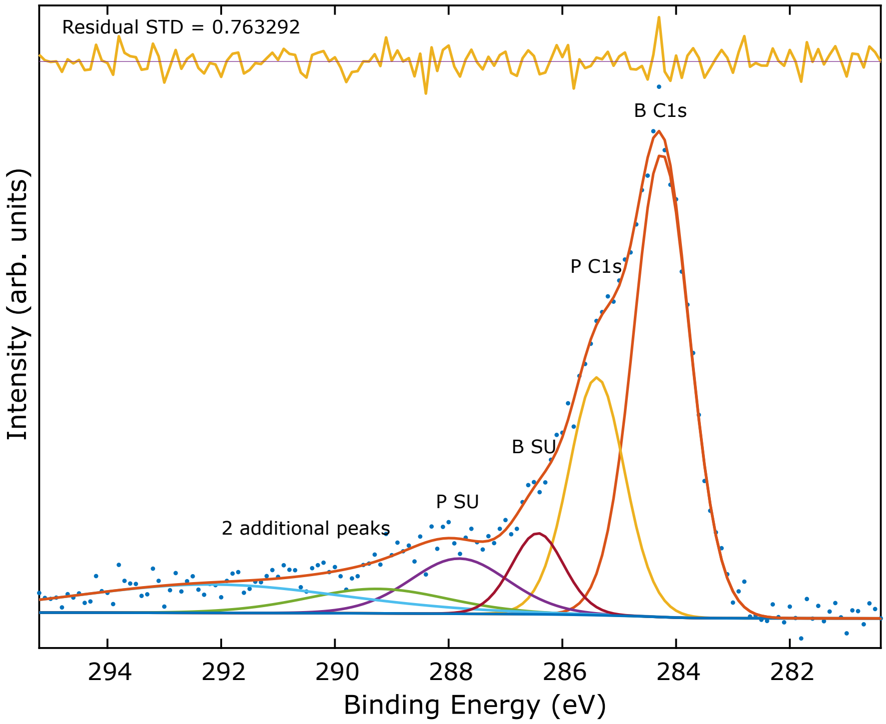

Figure 7.5: C 1*s* XP spectra of an annealed monolayer. A Shirley background was fitted, followed by 6 peaks, made up of benzene C 1*s* and shake-up features (B C 1*s* and B SU), pyrrole C 1*s* and shake-up features (P C 1*s* and P SU) and 2 additional peaks. The residual of the fitted curve to the data is plotted at the top of the figure, with the associated residual standard deviation (STD).

7.4.1.3 Monolayer

This surface was created ex-situ and transferred by vacuum suitcase to the NAP-XPS system. The deposition was characterised by STM prior to the transfer and was determined to be approximately one monolayer of FePc molecules. This provided a rough estimate of what a monolayer of FePc would look like in XPS without relying upon the annealing of multilayers to a monolayer.

When comparing the fit and the peaks plotted for the monolayer C 1*s* XP spectra (Figure 7.6), to those in Figures 7.4 and 7.5, it is clear that they are different. The XP spectra envelope has lost the clear definition of a pyrrole peak, as the envelope becomes more asymmetric. This behaviour seems to be normal for Ag surfaces and FePc [168]. Other experiments carried out at lower temperatures and photon energies have had greater success in differentiating the two main peaks (benzene and pyrrole); they can see that their main peaks have become asymmetric [164, 168]. Our data does not have the resolution to make that distinction between the main peaks at this surface preparation thickness. Palmgren *et al.* suggest that the asymmetry is due to the shifting of shake-up features, due to the strong coupling effect and the promotion of electrons to new unoccupied states in Ag above the Fermi energy [168]. The carbon environments of B C 1*s*,

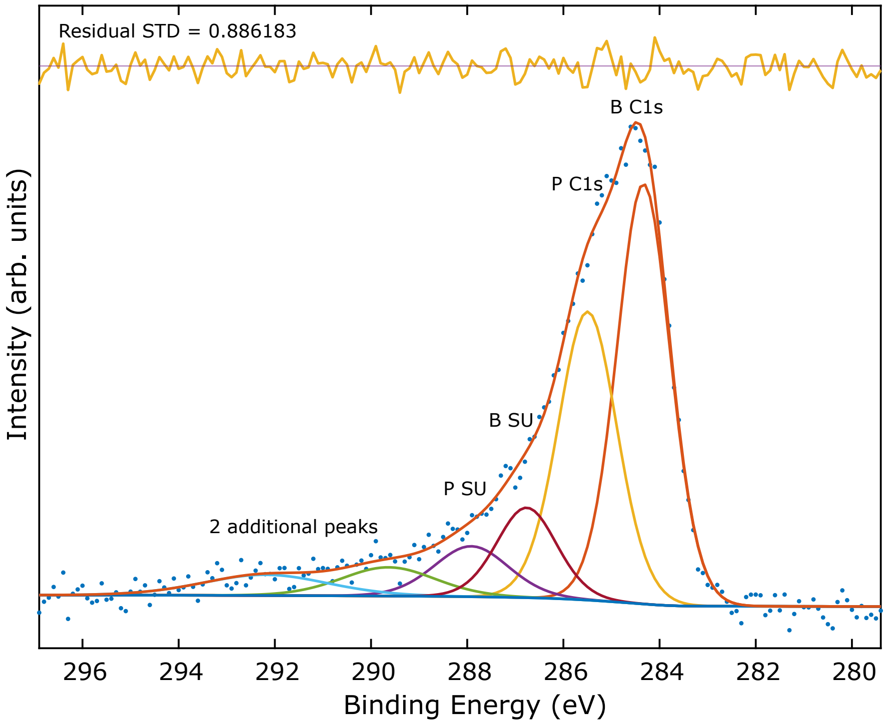

Figure 7.6: C 1*s* XP spectra of a monolayer of FePc. A Shirley background was fitted, followed by 6 peaks, made up of benzene C 1*s* and shake-up features (B C 1*s* and B SU), pyrrole C 1*s* and shake-up features (P C 1*s* and P SU) and 2 additional peaks. The residual of the fitted curve to the data is plotted at the top of the figure, with the associated residual standard deviation STD.

P C 1*s*, B SU and P SU have had peaks assigned to 284.3 eV, 285.5 eV, 286.8 eV and 287.9 eV. The additional features have also been assigned to 289.6 eV and 292.2 eV. These data are consistent with the other deposition thicknesses.

7.4.2 N 1*s* Spectra

Acquisition of data within the N 1*s* region is complicated by the presence of loss features from Ag 3*d* peaks (observed at 385-405 eV). Therefore, a sufficiently thick layer of FePc (>2ML) is required to provide the required signal-to-noise ratio. We remove the background Ag 3*d* loss features from the N 1*s* spectra by comparison with a clean Ag 3*d* loss feature spectra; this will increase the noise and error on the data points. The N 1*s* spectra of the three preparations are displayed in Figure 7.7. In the case of the multilayer, Ag 3*d* loss feature background subtraction is not performed on that dataset.

The ex-situ prepared monolayer has a main peak centred at 398.5 eV, with weaker features at 401.1 eV and 404.2 eV. The annealed monolayer had a main peak centred at 398.7 eV, with weaker features at 401.2 eV and 403.4 eV. The main peak for the multilayer is centred at 398.9 eV, with weaker features at 400.6 eV and 403.3 eV. These results are almost identical to those reported for a thin film of FePc on Si(100) [160], with features at 398.7 eV, 400.4 eV, 402.5 eV and a broad feature at 405.2 eV. The monolayers have a less well-defined 2nd peak (400-401 eV feature) compared to the multilayer sample. There is a shift of 0.4 eV between the multilayer and monolayers, which could be attributed to the stronger interaction between the substrate and the FePc compared to the bulk FePc-FePc interactions.

7.4.3 Fe 2*p* Spectra

The Fe 2*p* peak is located on top of the wide Ag 3*s* peak. Peaks are not fitted to the Fe 2*p* spectra as the features are asymmetric and complicated due to the valence open shell structure of Fe [160]. There needs to be a sufficient quantity of Fe to see this peak, due to the relatively low cross-section of Fe with this photon energy. The Fe 2*p* spectra shown in Figure 7.8 have had the Ag peak background removed prior to plotting. It is clear that it is only possible to see the Fe $2p_{1/2}$ and

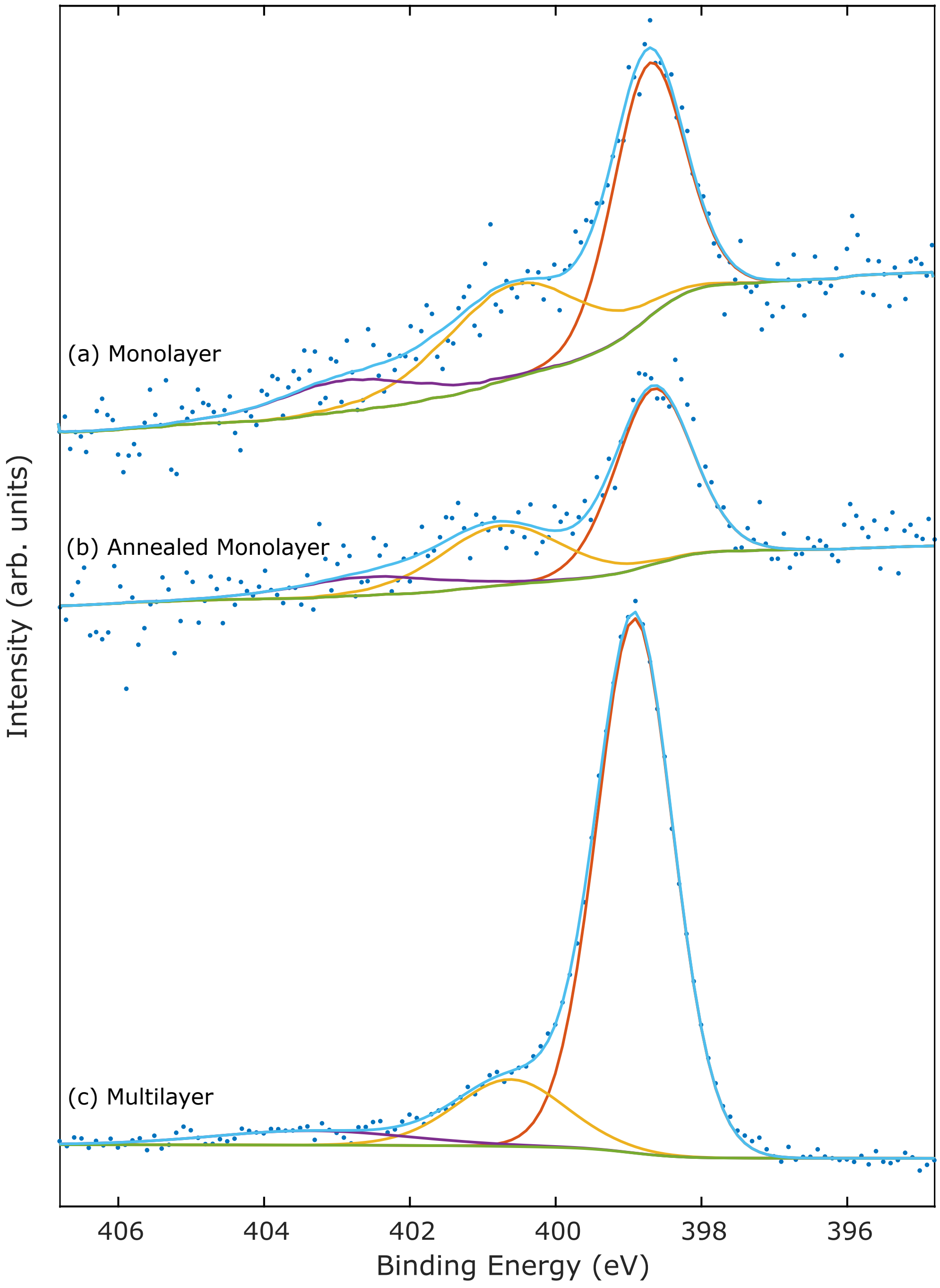

Figure 7.7: N 1s XP spectra of (a) monolayer, (b) annealed monolayer and (c) multilayer. A Shirley background has been applied, but not removed from the data. Data shown in (a) and (b) have had the Ag 3d loss feature background removed from the data prior to plotting, (a) and (b) have also been scaled in the y-axis to show peaks clearly.

Fe 2$p_{3/2}$ spectra in the multilayer. The Fe 2$p_{3/2}$ peak of the multilayer (situated at 709 eV) is in line with other experiments [160].

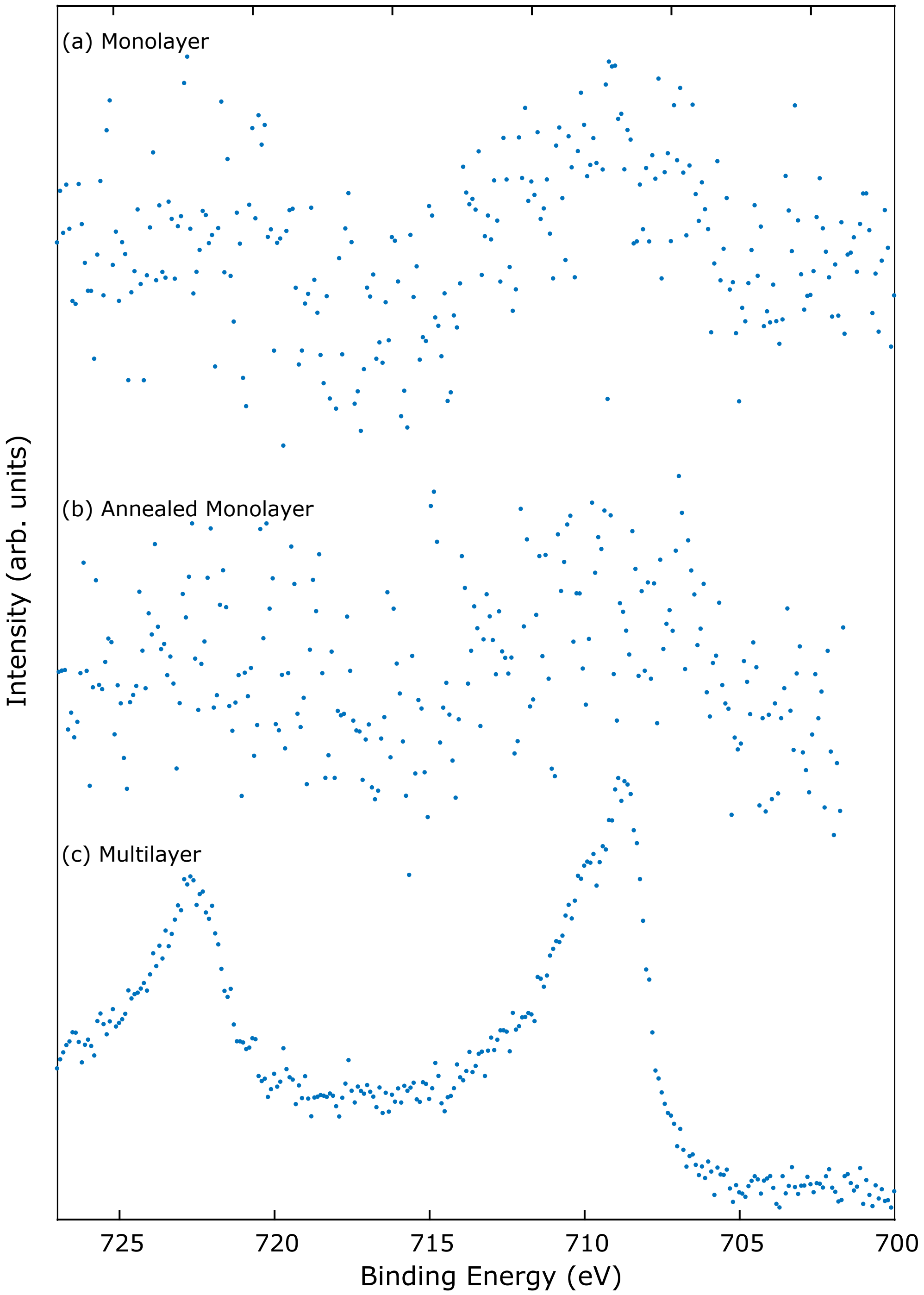

Figure 7.8: Fe $2p$ XP spectra of (a) monolayer, (b) annealed monolayer and (c) multilayer. The spectra displayed are the result of removing the Ag peak from the Fe $2p$ peak since they occupy the same binding energy. The Fe $2p_{3/2}$ is the peak located at the lower BE, the other peak is the Fe $2p_{1/2}$ environment.

7.4.4 Near ambient pressure of gas dosing

The near ambient pressure cell within the NAP-XPS system can simultaneously expose a sample to ∼10 mbar of a gas whilst recording the XP spectra of the sample, providing a chemical characterisation of the interaction of gas with the surface. The pressure, and the temperature of the samples, were recorded during XPS and NAP-XPS measurements. For these experiments, non-annealed monolayer coverages of FePc on Ag(111) were produced and dosed with gas. Three gases (CO, H_2O and O_2) were chosen for dosing onto the FePc/Ag(111) monolayer as they have all been previously shown to interact with related systems. Carbon monoxide has previously been dosed onto FePc on Au(111) held at cryogenic temperatures and high vacuum pressures [156, 157]. CO has also been dosed on to FePc/Ir(111) in NAP conditions (up to 12 mbar), and the gas is shown using IR vibrational spectroscopy to interact Fe core of the phthalocyanine [159]. Water has been reported in the surface-*trans* effect experiment to interact with Fe core (whilst dosing at high vacuum) [61]. Oxygen has been reported to interact with the FePc on Ag(110), such that the oxidation state of the iron is altered [62].

7.4.4.1 CO dosing

The carbon monoxide gas was dosed onto the FePc monolayer surface. Shown in Figure 7.9 are the fast XP spectra taken during CO gas dosing up to 12 mbar. The low signal produced by the Fe $2p$ and N $1s$ states would be attenuated further in the NAP cell, therefore, we only record the C $1s$ and O $1s$ spectra as this should indicate any interaction with the FePc and the surface. In the C $1s$ spectra (Figure 7.9a), the gaseous CO peak can be seen at ~292 eV, with the C $1s$ features from the FePc molecule between 284-286 eV. As the gas pressure is increased the gaseous CO feature becomes more prominent, and the FePc features become less clear due to the attenuation of the photoelectrons from the surface molecules. Similarly, the O $1s$ spectra shows an increasing gaseous CO feature at ~538 eV as the pressure is increased, however, there is no clear CO-surface interaction peak in the O $1s$ data.

Following the dosing, the sample was removed from the NAP cell and XP spectroscopy of the surface was carried out. The before and after CO dosing XP spectra are shown in Figure 7.10a-d. Comparing the C $1s$ spectra (Figure 7.10a), there is little difference in the overall peak shape, with a slight shift in the envelope peak to a lower binding energy. The O $1s$ spectra (Figure 7.10b)

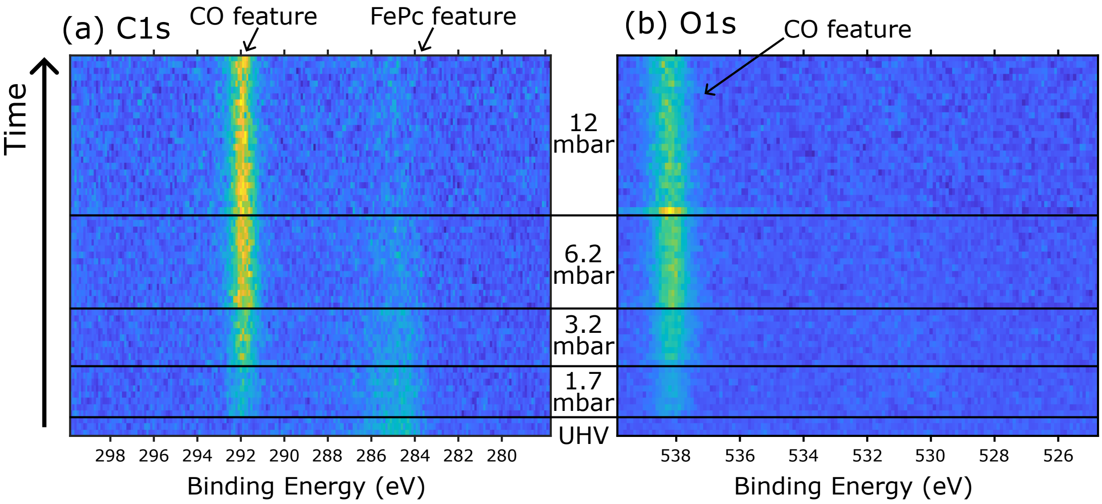

Figure 7.9: Fast XPS measurements of the FePc/Ag(111) surface as CO gas was leaked into the NAP cell up to 12 mbar. (a) C 1*s* spectra shows the gas phase CO gas at ~292 eV that increases in intensity as the pressure is increased. The FePc features at 284-286 eV appear to reduce in intensity due to attenuation of the photoelectrons by the CO gas. (b) O 1*s* spectra shows the gas phase CO feature that increases with pressure increases. No clear O 1*s* surface feature formed in this spectra. All individual spectra in the heat maps were normalised using the median value making the background appear at the same intensity.

shows a clear indication that an oxygen species has been left on the surface with a peak at ~538 eV. The N 1*s* spectra (Figure 7.10c) shows no change in position for the peak at ~399 eV between the spectra, as expected, since the interaction with CO should be localised to the Fe atom. Interestingly, the loss features (due to Ag 3*d* peaks) in the N 1*s* peak are less distinct following CO dosing; this may indicate additional surface coverage of a species which attenuates the loss feature photoelectrons.

Surprisingly, we found that the dosing of CO in the NAP-cell causes the co-deposition of nickel onto the surface. A control experiment (CO on Ag(111)) showed nickel contamination following the dosing (Figure 7.10d). According to Williams *et al.* a concentration of 100 ppm of $Ni(CO)_4$ can exist in the highest purity CO canisters due to the reversible reaction between CO and Ni found in stainless steel [169]. It is therefore likely we expose FePc to $Ni(CO)_4$ and not only CO as intended.

This CO-dosed monolayer was transported back to the STM by vacuum suit-

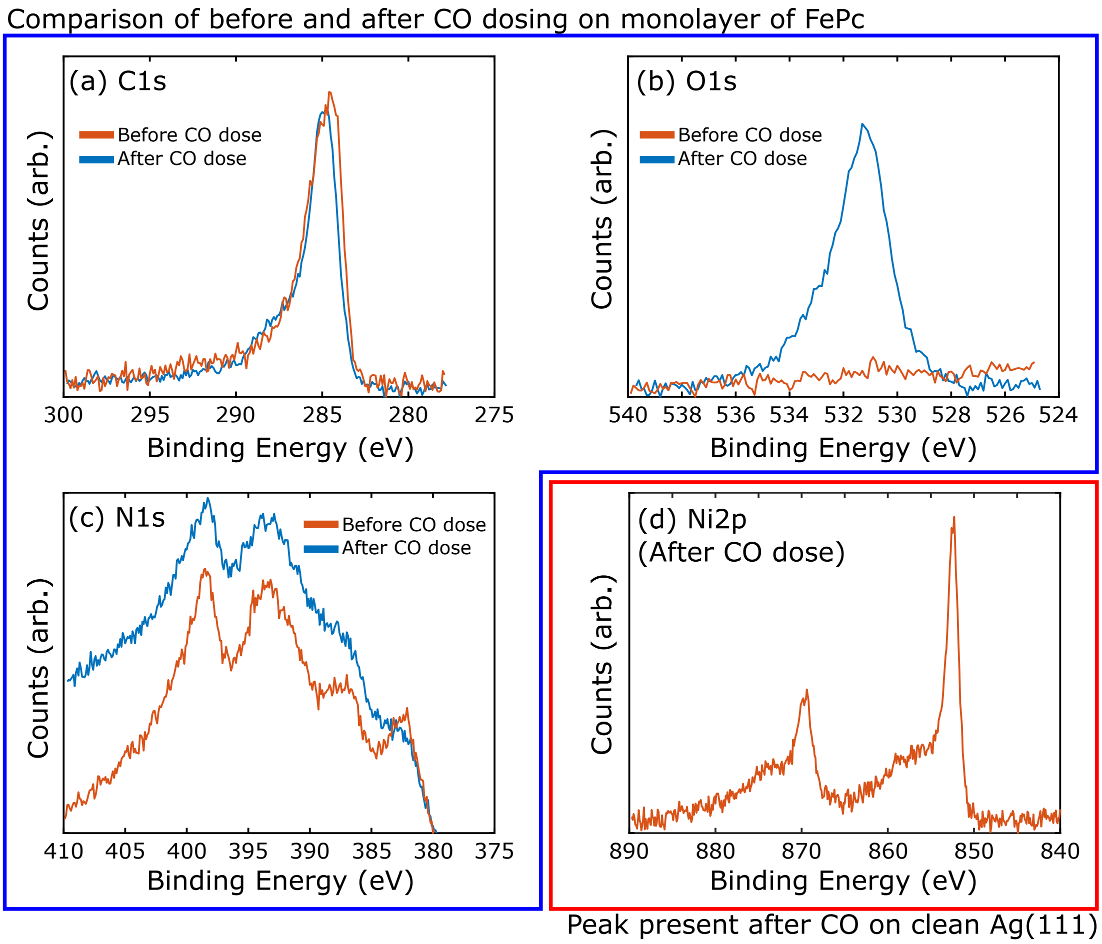

Figure 7.10: (a-c) XP spectra of before and after the CO dosing on (a) C 1*s*, (b) O 1*s* and (c) N 1*s* features of the surface. (d) CO dosing of clean Ag(111) caused the deposition of nickel on the surface. This is shown in the Ni 2*p* features shown here.

case. This surface was then characterised by STM, as shown in Figure 7.11a, with a loss of the ordered FePc structure clearly observed. The XPS measurements revealed that the elements that constitute iron phthalocyanine are still present on the surface (therefore we expect FePc to be present). As shown in Figure 7.11b, it is clear that FePc molecules are not easily identified. The size of the features observed are larger than the expected dimensions of FePc and the characteristic '+' shape of the phthalocyanine is not present. We attribute this appearance to nickel deposition from the Ni(CO)$_4$ contamination present within the CO gas.

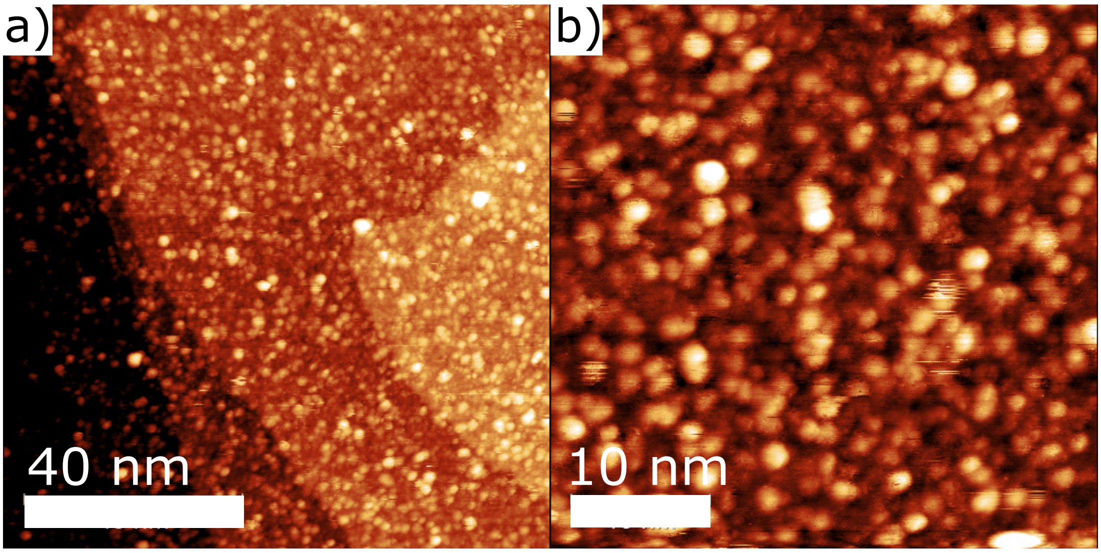

Figure 7.11: STM images from a monolayer of FePc on Ag(111)/mica, after CO dosing. (a) shows a 100x100 nm image of the surface and (b) is a zoomed-in area of the surface to try to provide extra detail. It was not possible to identify molecular features which could be assigned to FePc.

7.4.4.2 H_2O dosing

To dose H_2O, a vial of distilled water is placed under vacuum; water evaporates and the resultant gas is dosed onto the sample within the NAP cell. Shown in Figure 7.12a is the fast XP spectra as H_2O was exposed to the FePc monolayer on Ag(111) up to 7.2 mbar. The O 1*s* spectra shows an increase in the gaseous H_2O signal at ~535.5 eV as the pressure is increased in the NAP-cell (see pressure in NAP-cell in Figure 7.12b). In the inset, spectra before and after the dosing of H_2O are shown, which indicates that there was no interaction with the surface due to the H_2O. Our experiment was performed at room temperature, in contrast to the sample temperature of 60 K for the surface-*trans* effect paper where H_2O was shown to interact with the FePc molecule [61]. It is clear from these results that H_2O does not interact and/or adsorb on the FePc/Ag(111) monolayer at these temperatures and pressures.

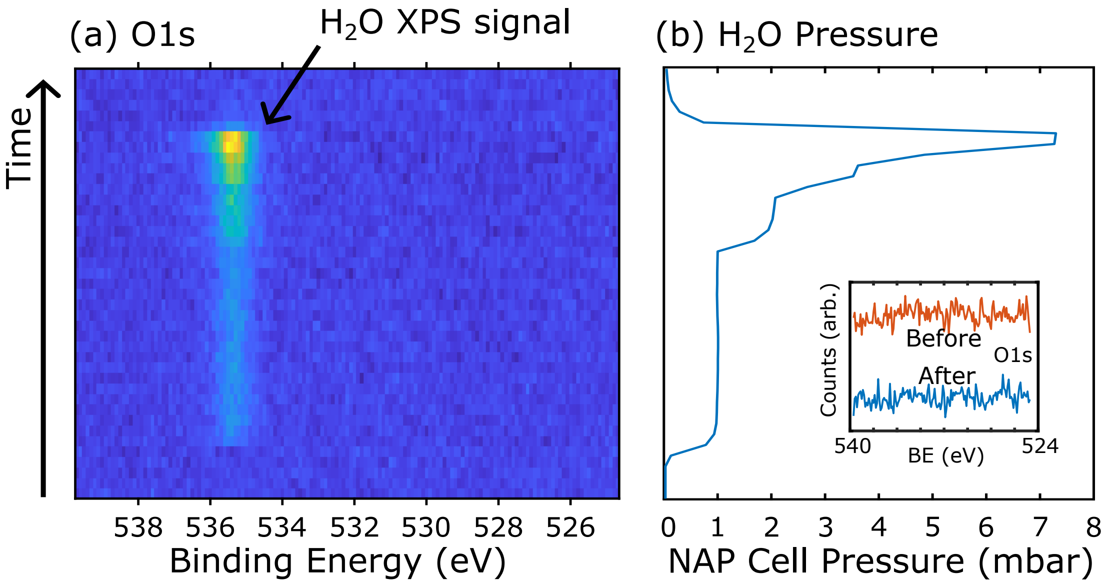

Figure 7.12: (a) Fast XP spectra measurements of the O 1s states as H_2O was dosed onto a monolayer of FePc/Ag(111). The gaseous H_2O peak at ~535.5 eV increases as the pressure of water is increased. There are no other peaks visible. (b) The pressure in the NAP-cell due to H_2O leaked into the chamber. The inset shows no change in the O 1s features of the surface as a result of the H_2O dosing.

7.4.4.3 O_2 dosing

It is well reported that O_2 adsorbs on Ag(111), where it forms a variety of surface structures depending upon the pressure of dosing [170,171]. O 1s features due to oxygen adsorption on Ag(111) have been reported to be at 528.2 eV which seems to be constant regardless of coverage [171]. Those reported results were carried out in a low-pressure regime (~10^{-6} mbar), whereas our NAP-cell measurements will be performed in the 1-10 mbar region. In the first experiment, we dose O_2 onto clean Ag(111) to see if there is any effect due to the many order of magnitudes larger pressure of oxygen.

In Figure 7.13a-b, fast XP spectra of the O 1s and C 1s regions of the surface whilst O_2 is dosed into the NAP-cell are shown (pressure within NAP-cell is shown in Figure 7.13c). As expected, the O 1s features show a strong gaseous phase O_2 peak, with a surface peak appearing instantaneously as oxygen is present in the NAP-cell (see Figure 7.13d for a snapshot at 3.5 mbar). The gaseous oxygen peaks (see Figure 7.13d) are present at 538.5 eV (main) and 539.8 eV (smaller peak) somewhat differs from that reported previously. Avval *et al.* report that gaseous oxygen has peaks at 539.3 eV (main) and 540.4 eV (smaller peak) [172], whereas Held *et al.* report that the peaks are 537.3 eV (main) and 538.4 eV (smaller peak) [173].

Interestingly, the C 1*s* spectra shows the formation of two peaks (see Figure 7.13e obtained after gas dosing), which may not be expected from a high-purity oxygen supply. The oxygen on the surface is too high in binding energy to be molecular oxygen (our recorded value 530.5 eV - see Figure 7.13f). This is in comparison to the value reported by Martin *et al.* of 528.2 eV [171]. Our surface oxygen value is closer to that of the OH group reported at 530.0 eV [171].

We also performed the same experiment on a monolayer of FePc on Ag(111), however, a similar result was obtained where an oxygen feature was present at 530.5 eV. It is not clear, when considering the carbon contamination and the binding energy of the oxygen peak, what oxygenated species we are depositing on the surface. While it is disappointing that we were unable to determine any interaction between the oxygen and the FePc species, our methodology shows a route to complementary studies between NAP-XPS and STM, which gives spatial and chemical characterisations of surfaces.

7.5 Summary

The results in this chapter show that we can produce various coverages of FePc on Ag(111), that show similar characteristics to those previously reported for both self-assembled structures and chemically sensitive photoelectron spectroscopy. The use of near-ambient pressure dosing of gases is shown to be more susceptible to contamination, compared to more traditional methods of gas doing of samples (Langmuir dosing). This contamination makes it difficult to disentangle the chemical shifts and/or states resulting from either the contamination or gas interaction with the FePc overlayer.

Regardless, this investigation has highlighted the complexities of a NAP-XPS gas dosing experiment. We have shown that we can transfer samples between the NAP-XPS and STM systems to provide spatial and chemical characterisations of surfaces; the H_2O dosing showed that there is no interaction with the FePc film at the temperature and pressures that we explore.

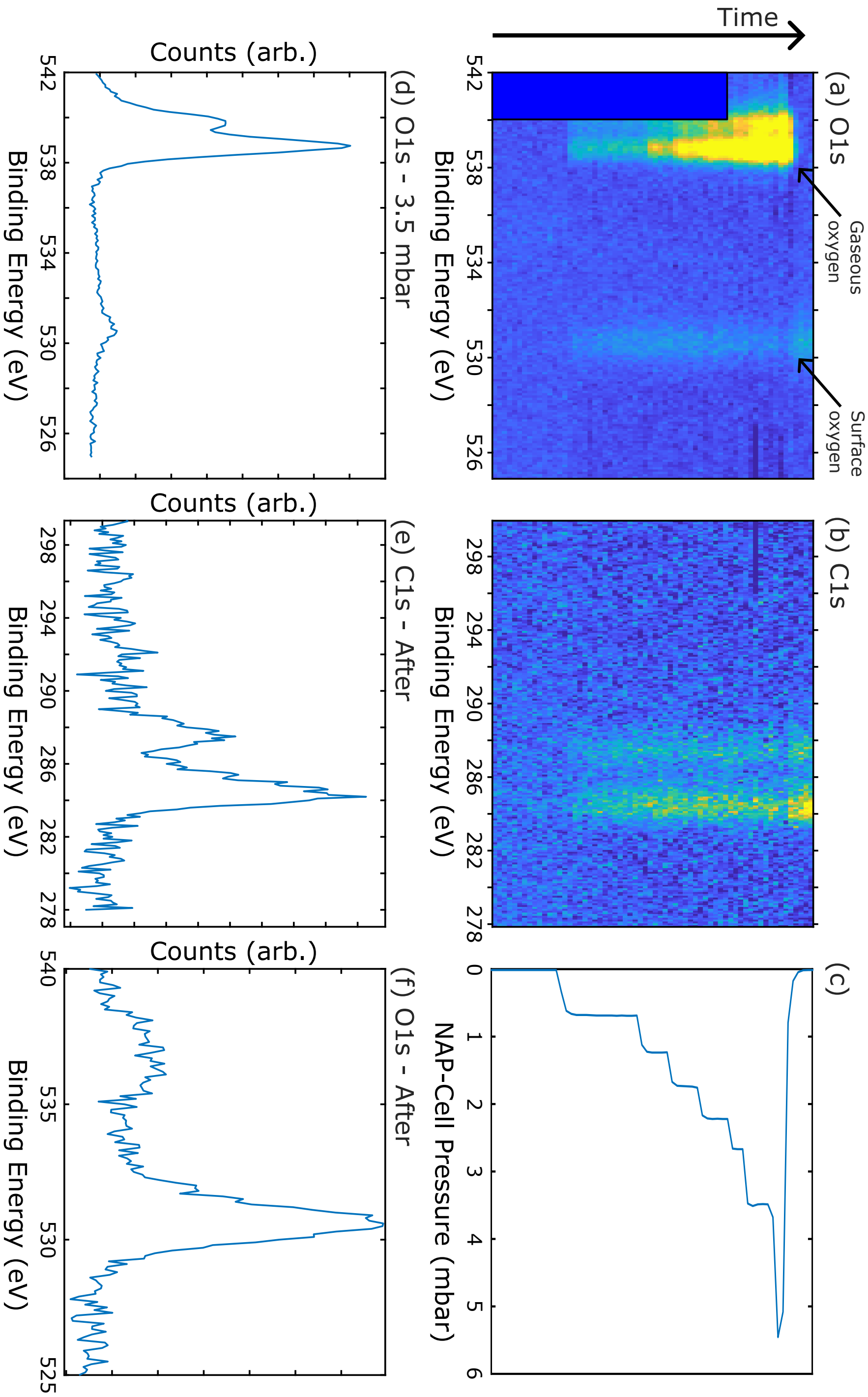

Figure 7.13: (a) Fast XPS of the O 1s region when O_2 is leaked into the NAP-cell. The gaseous oxygen feature is visible and a surface oxygen feature is present at a lower BE. (b) Fast XPS of the C 1s region when O_2 is leaked into the NAP-cell, two peaks are formed. (c) Shows the pressure in the NAP-cell over time. (d) The XP spectra of the O 1s region when 3.5 mbar of O_2 was in the NAP-cell. (e) C 1s region after the O_2 dosing. (f) O 1s spectra after the O_2 dosing.

Chapter 8

Conclusion

In this chapter, a summary of the findings that are reported in this thesis is presented.

8.1 Summary of findings

The work detailed in this thesis has focused on the interactions and reactions of porphyrins and phthalocyanines confined to the surface of metallic substrates. The molecules have been observed to self-assemble and form structures that depend upon their supporting substrate topography, or react with themselves and other molecules to act as 'building blocks' in the formation of new species (including complex polymeric architectures). An understanding of these nanoscale processes is a fundamental prerequisite to designing bespoke chemical pathways to form new nanoscale materials from the 'bottom up'.

Within this thesis, tetraphenylporphyrin (TPP) on Au(111) has been extensively studied. When deposited onto Au(111), TPP was shown to self-assemble into close-packed islands once cooled to 4.7 K. The islands had preferential positions to form these islands with *fcc* sites at elbows within the herringbone surface reconstruction. This shows a difference in surface interaction between the TPP and the different surface sites (*fcc* and *hcp*) that drive molecular ordering. The structural difference between the *fcc* and *hcp* sites is small; a small change in the registry of the top surface atom relative to the underlying bulk atoms, and the observed effect on molecular ordering is fascinating. Using variable temperature

STM, we can cool down the TPP/Au(111) preparation much slower than usual, viewing the surface as it cools. We can view the formation and evolution of islands at elevated temperatures. At lower temperatures, we observe individual TPP diffusion events and characterise this by Arrhenius analysis to show differences in the energy barrier to diffusion when the TPP is adsorbed at *fcc* or *hcp* sites. Importantly, the larger diffusion barrier within *fcc* which we observe may underlie the preference for island formation within *fcc* sites. Variable temperature STM measurements are not limited to viewing on-surface diffusion events, for example, chemical reactions could also be characterised as a function of temperature. Many reactions may occur within our range of available temperatures and the energy barrier to these interactions may be obtained by a similar Arrhenius analysis. This type of experiment should form the basis for future research in the field of on-surface synthesis.

When annealing TPP on Au(111), we observe a transition from order (self-assembled close-packed structures) to disorder. This transition was first characterised with STM by other members of the group, which showed a change in the structure of the molecule. Within this thesis, we use photoelectron spectroscopy in conjunction with SPM studies, to show that the periphery of the molecule interacted with itself, where dehydrogenation of the phenyl rings occurred and covalent bonds were formed between the rings and the inner porphine macrocycle. This reaction resulted in the disorder of the close-packed structures since self-assembly was no longer possible, likely due to the weakening of the CH-π bonding that drives assembly order between TPP. Further annealing showed the formation of a metallic species, formed by the sequestration of a surface Au atom into the TPP macrocycle cavity. The NEXAFS measurement provided further evidence that the single nitrogen N 1s feature was metalation and not simply dehydrogenation. Using NIXSW, we were able to obtain a structural characterisation of the molecule with higher spatial resolution than can be obtained with SPM. This reaction shows novel ways of using on-surface chemistry to form molecular species and alternatives to solution-phase chemistry. Further research could be undertaken to understand the ring-closing reaction, as currently the only evidence of which phenyl ring interacts with (either the pyrrole or aminic ring) is by DFT analysis, and nc-AFM may further elucidate the reaction pathway.

The addition of bromine atoms to the phenyl rings of the TPP species allows for covalently coupled polymer chains to be formed via an Ullmann-type coupling reaction. Prior to this reaction, brominated TPP species are shown to self-assemble into close-packed islands that form similarly to non-brominated versions of the molecule. The bromine atoms are electronegative and may be expected to alter the electronic states of the molecules. We explored the molecular states of brominated TPP and found that bromines shift the highest occupied molecular states to more negative values. We use this information to be able to identify Br_xTPP species based on the number of bromine atoms attached to the molecule using differential conductance mapping (for $x = 1, 2, 3, 4$). Annealing the surface results in Ullmann-type coupling, with longer covalently bonded chains being formed. The self-assembled structure also now differed from that previously reported. Further annealing created longer chains where we show that electronic molecular states do not show a clear difference between coupled and non-coupled states. We also find that the ring-closing reaction previously reported also happens to TPP incorporated within the polymer chain, and this occurs without disruption of the chain bonds. Annealing to higher temperatures shows that we can form Au-TPP species, within the molecular chain, shown by the macrocycle cavity becoming bright indicating an increase in the LDOS at that region as a direct result of a Au atom becoming incorporated within the porphyrin macrocycle. Further research in this area could focus on the charge localisation of the bromine atoms on the TPP molecule, as well as the charge of the Au within self-metalated TPP species; this could be achieved by Kelvin probe microscopy. It would be interesting to see if chemical differentiation between molecular species could be achieved spectroscopically, which would turn SPM into a highly chemically sensitive characterisation technique, by providing more information on the products within a reaction pathway.

The interaction of iron phthalocyanines on Ag surfaces with gases at near ambient pressures was explored. Initially, we verified that ordered FePc surfaces were able to be produced by characterising the surfaces using STM. Using XPS, we characterised preparations of varying thicknesses and showed how gases interact with the molecular overlayer. Unfortunately, due to surface/gas contamination, the CO and O_2 exposure did not show any clear result, however, we did not see any interaction between the H_2O and FePc overlayer.

This work has demonstrated, and characterised, the complex interactions and chemistry of porphyrins and phthalocyanines on metallic surfaces. The analysis within this thesis has helped to further the understanding of the nanoscale interactions of these systems. Combining the sub-molecular spatial resolution of SPM techniques, the chemical sensitivity of photoelectron spectroscopy, and the kinetic analysis of Arrhenius analysis provides an in-depth picture of on-surface reactions and processes. Such techniques will continue to provide fundamental insights into the mechanism underlying on-surface processes, and the use of near-ambient pressure techniques allows us to move towards a point where the properties of bespoke molecular structure may be incorporated with functional devices.

Appendix A

Diffusion TPP

A.1 Surface features alter herringbone reconstruction

Shown in Figure A.1 is the Au(111) herringbone reconstruction on several narrow terraces. The narrow terrace width is likely to drive a change in the surface reconstruction, creating larger *fcc* regions on the surface.

A.2 Full sized image of TPP 1000 nm

Shown in Figure A.2 is the larger image that is cropped to create Figure 4.5.

A.3 Full sized images of TPP VT-STM measurements

The STM LHe bath cryostat was cooled to 4.3 K whilst a sample (at 293 K) was inserted into the STM. Under normal conditions, the sample would cool to 4.7 K within 1 hour (see blue line in Figure 4.3). To keep the sample at ∼285 K, the sample was counter-heated to maintain a set temperature (see Figure 4.9) and the temperature was then reduced in stages. The images shown in Figure A.3 are larger version images in the inset of Figure 4.9.

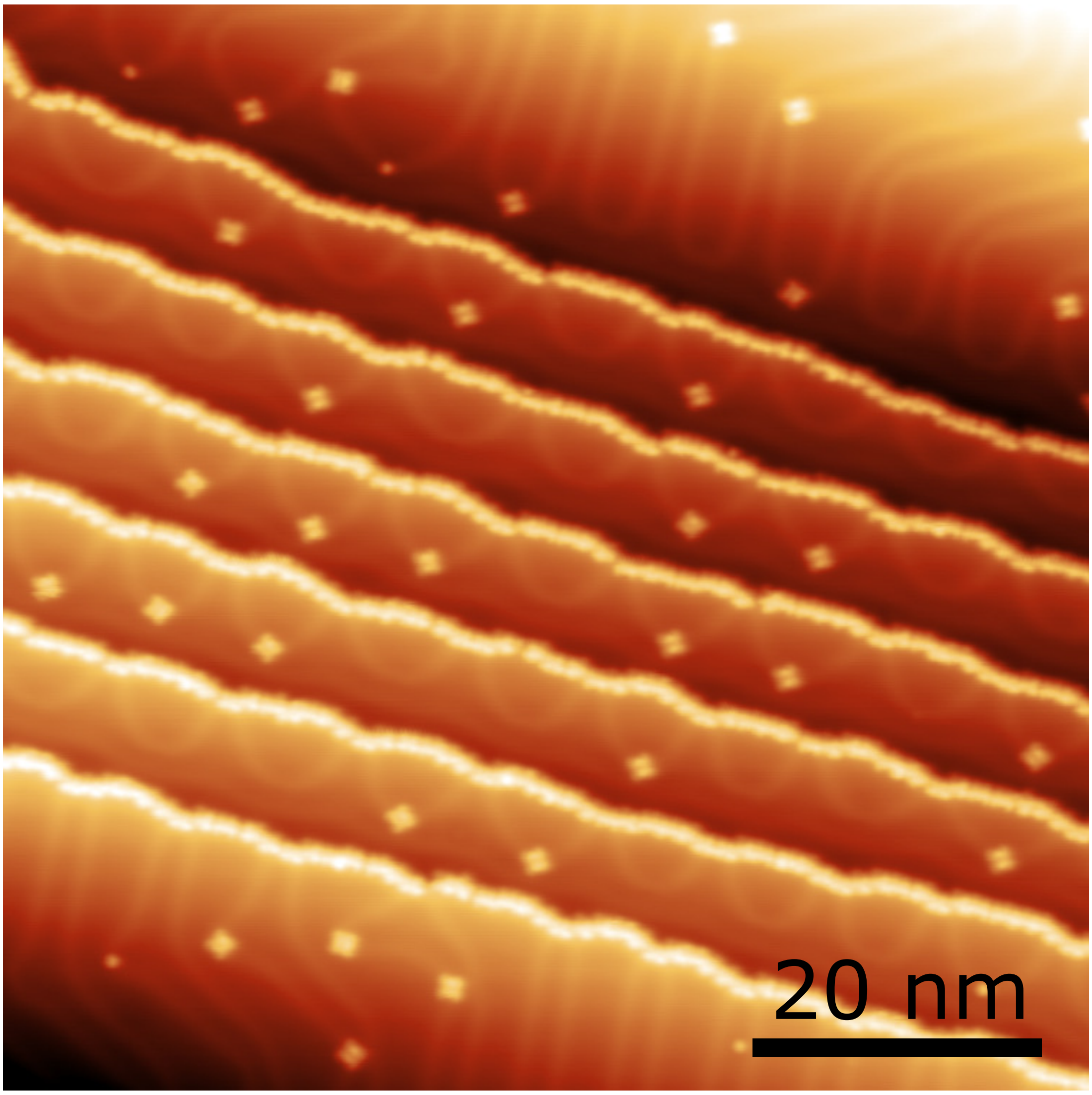

Figure A.1: Shows the variation in the herringbone reconstruction that is driven by narrow terraces on a ∼0.04ML coverage of TPP/Au(111) sample. Image parameters: ($V_{\text{bias}} = -1.8$ V, $I_{\text{set}} = 50$ pA, $T_{\text{sample}} = 4.7$ K)

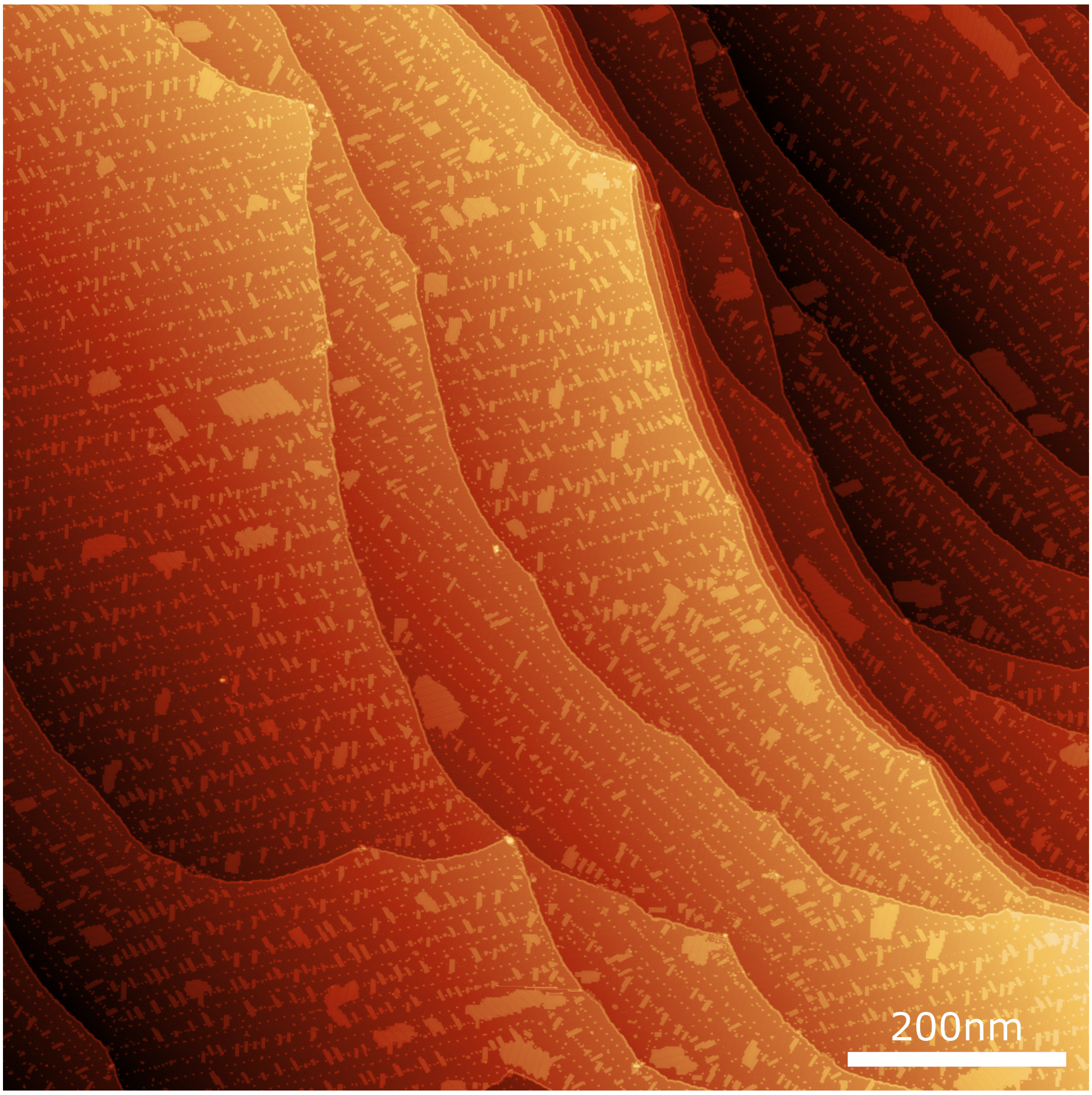

Figure A.2: Large overview (4000x4000 pixel image) showing the sub-monolayer close-packed growth of TPP on Au(111). Image parameters: ($V_{\text{bias}} = 2.0$ V, $I_{\text{set}} = 20$ pA, $T_{\text{sample}} = 4.7$ K)

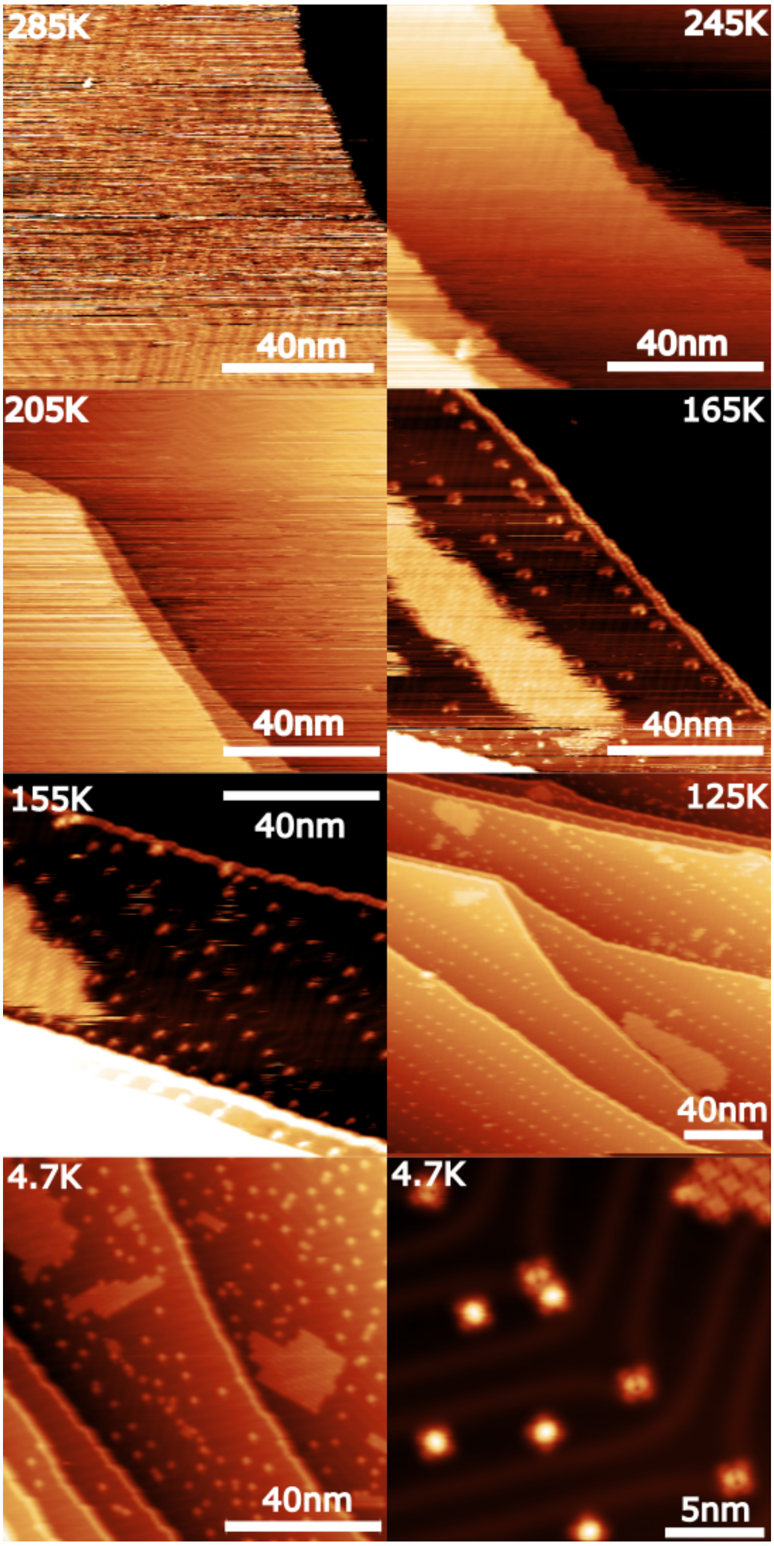

Figure A.3: STM images from each temperature measured. VT-STM image settings: $V_{\text{bias}} = 0.5$ V, $I_{\text{set}} = 10$ pA. Image settings for left 4.7 K image: $V_{\text{bias}} = 0.5$ V, $I_{\text{set}} = 10$ pA and right 4.7 K image: $V_{\text{bias}} = 0.4$ V, $I_{\text{set}} = 630$ pA.

Appendix B

FePc on Ag(110)

B.1 Introduction and Motivation

Porphyrins and phthalocyanines (Pc) have been commonly studied within the surface science community as monolayer and sub-monolayer coverages. These are generally adsorbed upon metallic surfaces prepared under ultra-high vacuum (UHV) [33]. Often these macrocycles are functionalised with metal atoms providing an active site available for ligation and, in principle, catalytic reactions [33]. This approach of transferring the functional properties of molecules to a surface confined low-dimensional structure is a promising route towards functional materials [139].

Many of the ligation studies involving Pc species have been carried out at cryogenic temperatures. Research conducted at room temperature has shown the adsorption of O_2 with a low-density phase of iron phthalocyanine (FePc) on Ag(110) [62]. Density functional theory (DFT) calculations for this system predicted that the adsorption site of O_2 is beneath the FePc overlayer (sandwiched between the FePc and Ag(110) surface). It was also suggested that the Fe within the ligated phthalocyanine is pulled towards the surface (see Figure B.1a for a schematic). This model of oxygen adsorption is in contrast to related systems (e.g. NH_3-FePc/Ag(111) [61]) where the ligand species is modelled as attaching in an axial geometry (in a *trans*-position relative to the surface plane – see Figure B.1b for a schematic diagram).

The O_2 adsorption between FePc-Ag(110) reported by Sedona *et al.* showed

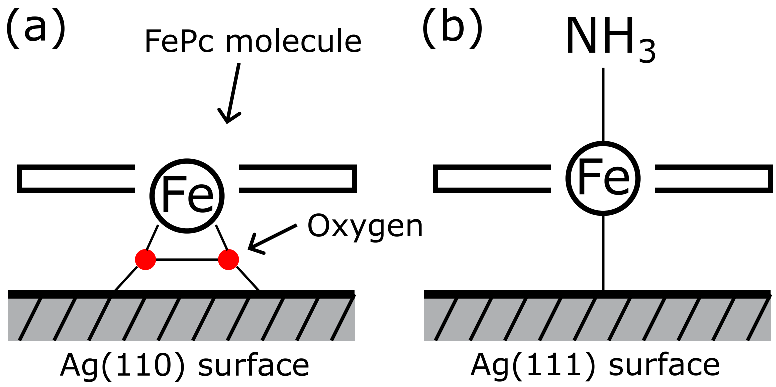

Figure B.1: (a) Interaction of the oxygen species with the Fe molecule following dosing of the gas onto a specific preparation of FePc. It is reported that the Fe atom is pulled closer to the surface. See references [62,158]. (b) Interaction of ammonia with the FePc molecule from the surface-*trans* effect experiment. The ligation of ammonia results in an alteration of the Ag-Fe distance. See reference [61].

interesting behaviour in STM; the bright iron core in STM became dulled upon O_2 dosing on the surface (see Figure B.2a-b) [62]. This indicates a strong interaction with the iron core that changes the electronic properties of the atom. Further evidence of the strength of this interaction was shown by Bartolome *et al.*, where the magnetic properties (spin) of the iron atom were turned on as the O_2 interacts with the molecule, due to the crossover from metallic Fe to oxidised Fe(III) [158]. The oxygen dosing reaction could be reversed by heating the sample to 370 K, whereby the bright iron core of the FePc would now be visible (see Figure B.2b-c) [62]. The reaction could also be reversed via the dosing of H_2 gas [158].

As reported by Sedona *et al.*, O_2 adsorption between FePc-Ag(110) is only possible under a specific close-packing arrangement of FePc. Shown in Figure B.2d are the published STM and LEED patterns of FePc on Ag(110) as reported by Bartolome *et al.* that depend upon the density of the FePc molecular overlayer [158]. The required phases for O_2 adsorption are those labelled R1, R2 and R3 with a rectangle unit cell and the OB2 phase that does not have rectangular symmetry. Originally, Sedona *et al.* only reported on the R1, R2 and OB1 phases within their work (see Figure B.2d). The differences between the phases is related to their adsorption position with respect to the Ag(110) surface. The R1 phase FePc iron core is centered atop a Ag atom. The R2 phase FePc iron core is centered on the short bridge site between two Ag atoms. Interestingly, the

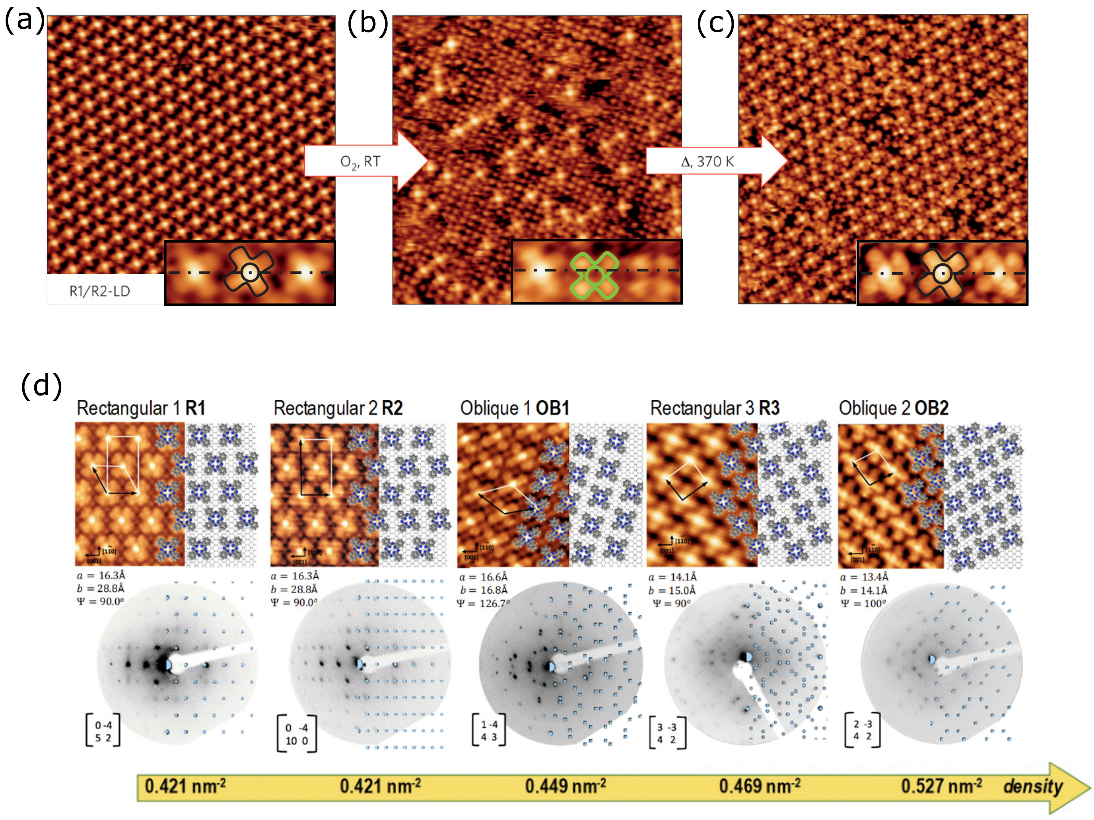

Figure B.2: (a) STM image showing close-packed FePc on Ag(110) in the R2 phase. The iron cores are visible as bright features (see inset). (b) STM image showing close-packed FePc on Ag(110) in the R2 phase following O_2 dosing. The iron cores are dark features (see inset). (c) STM image showing close-packed FePc on Ag(110) in the R2 phase following O_2 dosing and annealing to 370 K. The iron cores are now bright features again (see inset). (d) Reported packing modes of FePc on Ag(110) with the STM and LEED patterns shown for increasing molecular density left to right. Figures (a)-(c) taken from Sedona *et al.* [62] and (d) taken from Bartolome *et al.* [158].

adsorption of the iron within the OB1, R3 and OB2 phases is the same as the R2 phase.

The published results relating to different potential adsorption sites for gaseous ligands [61, 62] provide the opportunity to perform a combined XPS/NIXSW study to facilitate structural characterisation of adsorbed O_2 on the FePc/Ag(110) surface. Such an approach may allow us to characterise the adsorption geometry of the O_2 species as well as the position of the Fe species (which is of relevance to the previously reported surface-*trans* effect [61]). The additional X-ray brightness, energy resolution and cross-section provided by synchrotron light is required for the resolution of the Fe energy shifts that occur as a result of the O_2 interactions and is essential for NIXSW experiments.

B.2 Experimental methods

A clean Ag(110) substrate was prepared via several sputter-anneal cycles under UHV conditions and was subsequently characterised by low-energy electron diffraction and X-ray photoelectron spectroscopy. The clean Ag(110) surface was then exposed to a flux of FePc (triply-thermally purified prior to use) via sublimation from a Knudsen-type evaporator. The deposition time and temperature were varied during our work in order to produce several distinct arrangements of FePc on Ag(110) (365°C - 380°C, for between 15 and 36 minutes, with the substrate held at room temperature). Characterisation was performed using LEED, XPS (C 1*s*, N 1*s*, and Fe 2*p* regions), and NIXSW (N 1*s* and C 1*s* signatures measured using the (220) Bragg reflection). Due to COVID-19 restrictions, this work was performed remotely with all experimental work being performed by members of the I09 research team (led by David Duncan).

High-resolution C 1*s*, N 1*s* and Fe 2*p* XPS measurements were acquired using the soft X-ray (SXR) undulator on the I09 beamline, acquired at 450 eV, 550 eV, and 850 eV respectively. NIXSW measurements utilised the (200) Bragg plane of the crystal (switching to the hard X-ray undulator on I09, Bragg energy of ∼4270 eV). All measurements were carried out with the sample held at RT. Measurements were acquired at different locations on the sample in order to reduce the effects of beam damage. This procedure allows us to ascertain the coherent position and coherent fraction for key atomic species within the molecule.

B.3 Results

Following each deposition, a LEED image was acquired of the surface in order to characterise the geometric arrangement present. In addition, XPS data was obtained for the Fe 2*p*, C 1*s*, and N 1*s* regions.

To obtain the required R1/R2 phase a series of sequential depositions of FePc were performed onto a clean Ag(110) crystal. We observe similar features in the XP spectra for a range of sample preparations (varying deposition time and temperature, and hence varying the molecular coverage). Figure B.3 shows XPS data for the three phases obtained (Diffuse, R3 and OB2 - see LEED data in Figure B.4). The C 1*s* region can be resolved into two distinct features, with peaks at ∼285.5 eV and ∼284.5 eV binding energy; assigned to aryl carbons (within the outer benzene rings) and pyrrole carbons (within the inner rings), respectively [174]. A single broad nitrogen environment is resolved within the N 1*s* region, centred at ∼399 eV which may contain components at ∼400 eV and ∼398 eV previously assigned to bridging nitrogen species and those coordinated with the Fe core, respectively [174]. The Fe 2*p* region shows a single peak at ∼707 eV, consistent with monolayer/sub-monolayer coverage of FePc, with the lack of a peak at ∼708.5 eV also supporting the absence of second layer growth [175]. It can be seen that there is no significant change in peak positions with respect to the three phases characterised, although the normalised peak intensities increase (Diffuse $<$ R3 $<$ OB2) as expected for the molecular densities previously reported (shown in Figure B.2d) [158].

As the R1/R2 phase is expected to be a prerequisite for successful oxygen adsorption, significant effort was devoted to obtaining this phase [62]. A systematic approach was taken whereby a diffuse LEED pattern was obtained, and subsequent depositions (for 2 minutes in duration) were performed with LEED data acquired at each point. Numerous attempts were made but none of the low-density phases previously reported (R1, R2, OB1) were obtained. The first observable LEED pattern obtained corresponds to the R3 phase (see Figure B.4a), indicating that this approach of sequential deposition does not allow access to the lower density phases previously reported.

Attempts were also made with depositions at a high evaporation temperature (to assess the effect of varying the flux of impinging FePc). However, such an approach resulted in the formation of the higher density OB2 structure (see Figure B.4b); as one might expect for an increased exposure to FePc. Annealing the Diffuse, R3, and OB2 structures did not result in significant changes (annealed OB2 structure shown in Figure B.4c)

Based upon the systematic studies outline above it is clear that there is a

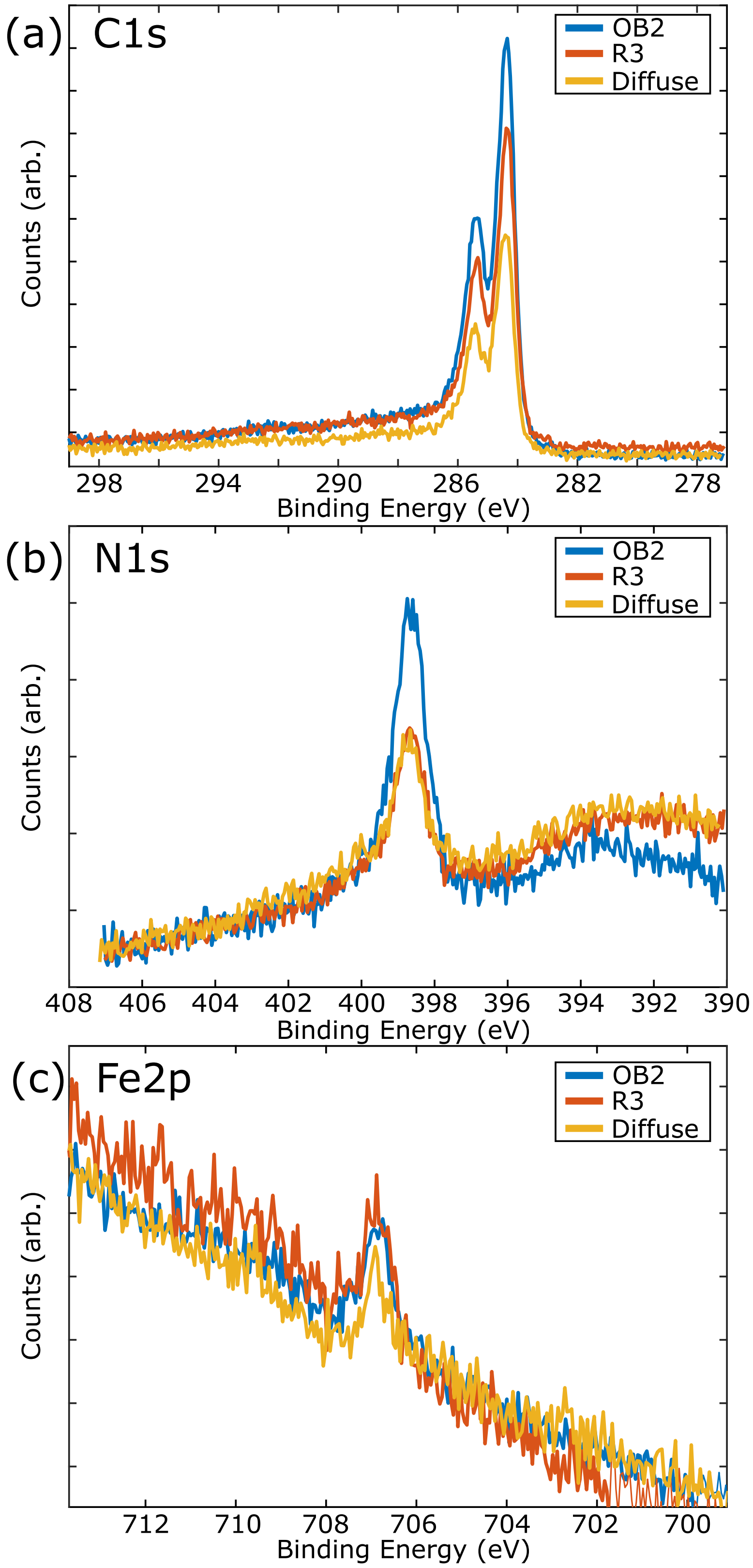

Figure B.3: XPS data showing the N 1*s*, C 1*s*, and Fe 2*p* regions for three characteristic FePc/Ag(110) phases obtained here (Diffuse, R3, and OB2).

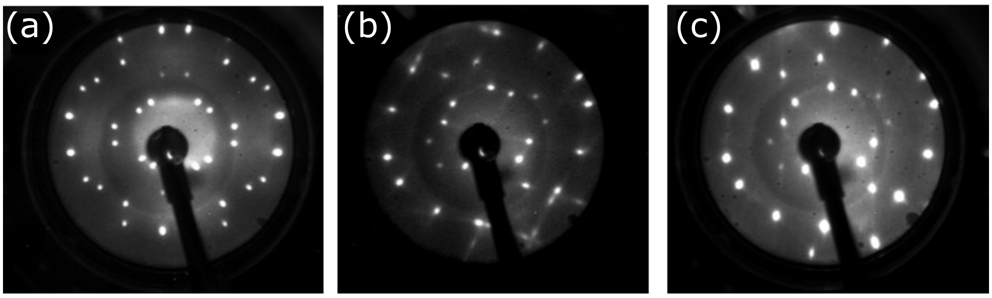

Figure B.4: LEED data acquired for two phases of FePc obtained. After, (a) 30 minute deposition at 365°C - assigned to a R3 structure, 15.5 eV. (b) 15 minute deposition at 380°C - assigned to an OB2 structure, 14.5 eV. (c) 15 minute deposition at 380°C and subsequent anneal to ~480°C - assigned to an OB2 structure, 14.5 eV.

significant difference between the molecular assemblies we are able to produce by following previously published procedures [62, 158]. This could indicate that the FePc structures are highly sensitive to specific deposition parameters (e.g flux rate or sample temperature) that are not documented in the published work.

In order to utilise the experimental time we acquired chemically sensitive NIXSW measurements for the three FePc phases that we were able to reproduce (Diffuse, R3 and OB2). Utilising the (220) Bragg reflection and the chemical environments identified for the carbon and nitrogen species in the XPS analysis above, we are able to obtain two structural parameters, the coherent fraction (Cf) and coherent position (Cp), which provide information on the adsorption position of these species relative to the (220) planes of the bulk substrate [85,86]. Figure B.5 shows the adsorption yields and corresponding Cf and Cp values for carbon and nitrogen environments within the three distinct phases (these values are collated in Table B.1).

The coherent fractions obtained are in the range (0.53–0.72) indicating an appreciable level of order, but with multiple adsorption heights expected for each species. The similar coherent positions for each species within a given phase indicate, as expected, that the FePc species is relatively flat. The slightly lower Cp value for the C 1*s* Peak 2 (corresponding to the outer benzene rings of FePc), indicates that these groups may lie closer to the substrate than the nitrogen and carbon atoms within the inner core (where the adsorption position may be driven by the presence of the bulky Fe atom). Due to the requirement to use the (220)

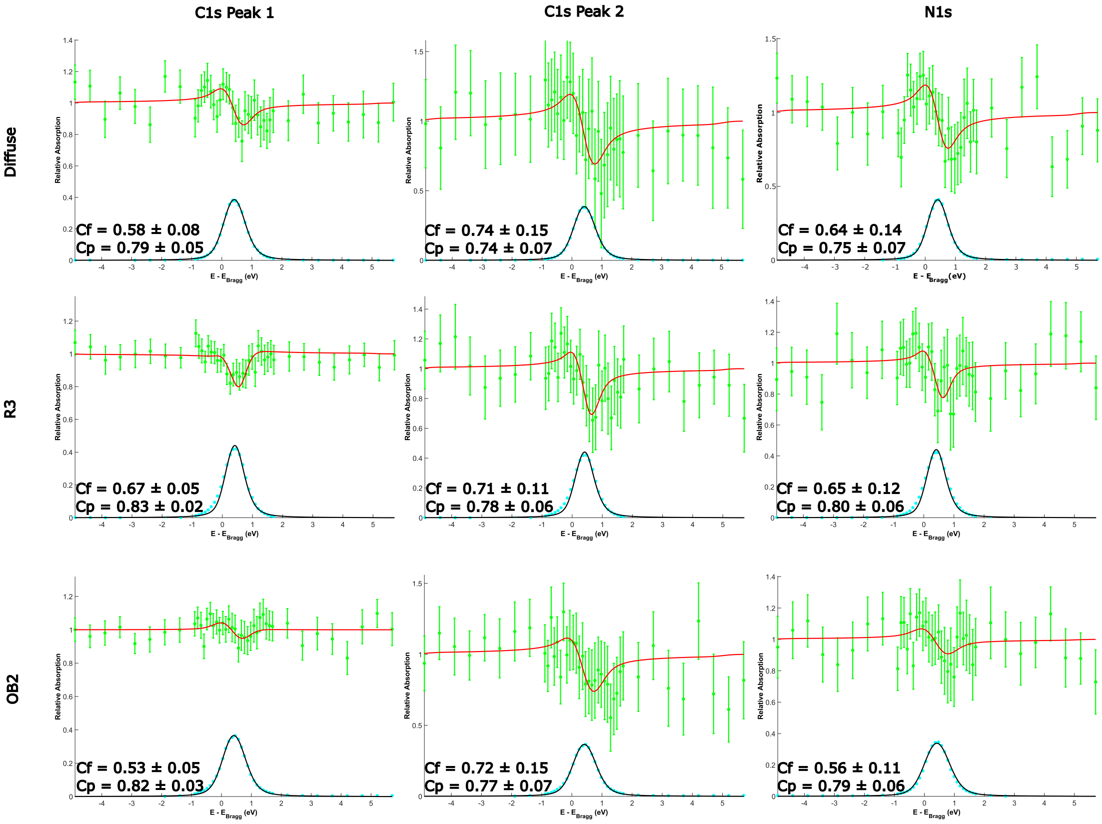

Figure B.5: XSW photoelectron yield and reflectivity fits for each of the three FePc phases prepared. The data was collected using the (220) reflection of the Ag(110) surface with a photon energy of ∼4270 eV. The coherent fraction and position for each of the core levels for carbon (C 1*s*) and nitrogen (N 1*s*) are shown. Peak 1 of the C 1*s* NIXSW corresponds to the lower BE peak in the XPS data. Absorption profiles are based on 3, 12, and 4 NIXSW data sets for each species within the Diffuse, R3, and OB2 phases, respectively.

plane of the NIXSW, the cross-section of the features is very low, which prevented the NIXSW of the Fe atom from being captured.

The data presented in Table B.1 demonstrates that we can obtain accurate adsorption geometries for FePc on Ag(110). This is a vital prerequisite to allow one to investigate the effect of oxygen adsorption upon the FePc/Ag(110) structure. Although we were unable to proceed to measurements of oxygen adsorption, due to time constraints, the data here suggests that we would be able to distinguish between the two modes of adsorption, as outlined in the introduction, within future experiments. That is to say that structural information, following dosing of oxygen on the three phases shown here, would allow us to investigate

Table B.1: Coherent fraction (Cf) and coherent position (Cp) of the three preparations of FePc on Ag(110)

Sample Preparation	Coherent fraction (Cf)	Coherent position (Cp)
Dep 25min (365°C) - Diffuse	C 1s Peak 1 = 0.58±0.08	C 1s Peak 1 = 0.79±0.05
	C 1s Peak 2 = 0.74±0.15	C 1s Peak 2 = 0.74±0.07
	N 1s Peak = 0.64±0.14	N 1s Peak = 0.75±0.07
Dep 36min (365°C) - R3	C 1s Peak 1 = 0.67±0.05	C 1s Peak 1 = 0.83±0.05
	C 1s Peak 2 = 0.71±0.11	C 1s Peak 2 = 0.78±0.06
	N 1s Peak = 0.65±0.12	N 1s Peak = 0.80±0.06
Dep 15min (380°C) - OB2	C 1s Peak 1 = 0.53±0.05	C 1s Peak 1 = 0.82±0.03
	C 1s Peak 2 = 0.72±0.15	C 1s Peak 2 = 0.77±0.07
	N 1s Peak = 0.56±0.11	N 1s Peak = 0.79±0.06

whether (i) oxygen adsorption at the Ag(110)/FePc interface, or (ii) ligation to Fe at the FePc/vacuum interface, is the preferred route to ligation.

B.4 Conclusion

The work outlined above has provided valuable insight into the complexities of reproducing specific phases of FePc upon Ag(110). The ligation of gaseous molecules upon metal functionalised macrocycles (e.g. porphyrins and phthalocyanines) is a potentially important mechanism for solid-state ‘gas capture’ devices. The question of the specific structure, and adsorption geometry, for the ligated species (and indeed the oxygen ligand) is still an open question.

References

[1] Richard P. Feynman. There's Plenty of Room at the Bottom. *Engineering and Science*, 23(5):22–36, 1960.

[2] D. M. Eigler and E. K. Schweizer. Positioning single atoms with a scanning tunnelling microscope. *Nature*, 344(6266):524–526, 1990.

[3] A. J. Heinrich, C. P. Lutz, J. A. Gupta, and D. M. Eigler. Molecule Cascades. *Science*, 298(5597):1381–1387, 11 2002.

[4] Fabian D. Natterer, Kai Yang, William Paul, Philip Willke, Taeyoung Choi, Thomas Greber, Andreas J. Heinrich, and Christopher P. Lutz. Reading and writing single-atom magnets. *Nature*, 543(7644):226–228, 3 2017.

[5] J. M. Lehn. Supramolecular Chemistry—Scope and Perspectives Molecules, Supermolecules, and Molecular Devices (Nobel Lecture), 1 1988.

[6] George M. Whitesides and Bartosz Grzybowski. Self-Assembly at All Scales. *Science*, 295(5564):2418–2421, 3 2002.

[7] Johannes V. Barth, Giovanni Costantini, and Klaus Kern. Engineering atomic and molecular nanostructures at surfaces. *Nature*, 437(7059):671–679, 9 2005.

[8] Jacob N. Israelachvili. *Intermolecular and Surface Forces.* Elsevier, 2011.

[9] Hong Ying Gao, Hendrik Wagner, Philipp Alexander Held, Shixuan Du, Hong Jun Gao, Armido Studer, and Harald Fuchs. In-plane Van der Waals interactions of molecular self-assembly monolayer. *Applied Physics Letters*, 106(8):081606, 2 2015.

[10] Chris J. Judd, Neil R. Champness, and Alex Saywell. An On-Surface Reaction Confined within a Porous Molecular Template. *Chemistry - A European Journal*, 24(1):56–61, 2018.

[11] James A. Theobald, Neil S. Oxtoby, Michael A. Phillips, Neil R. Champness, and Peter H. Beton. Controlling molecular deposition and layer structure with supramolecular surface assemblies. *Nature*, 424(6952):1029–1031, 8 2003.

[12] L. M. A. Perdigão, E. W. Perking, J. Ma, P. A. Staniec, B. L. Rogers, N. R. Champness, and P. H. Beton. Bimolecular networks and supramolecular traps on Au(111). *Journal of Physical Chemistry B*, 110(25):12539–12542, 2006.

[13] Gabriella Cavallo, Pierangelo Metrangolo, Roberto Milani, Tullio Pilati, Arri Priimagi, Giuseppe Resnati, and Giancarlo Terraneo. The Halogen Bond. *Chemical Reviews*, 116(4):2478–2601, 2 2016.

[14] Jalmar Tschakert, Qigang Zhong, Daniel Martin-Jimenez, Jaime Carracedo-Cosme, Carlos Romero-Muñiz, Pascal Henkel, Tobias Schlöder, Sebastian Ahles, Doreen Mollenhauer, Hermann A. Wegner, Pablo Pou, Rubén Pérez, André Schirmeisen, and Daniel Ebeling. Surface-controlled reversal of the selectivity of halogen bonds. *Nature Communications*, 11(1), 2020.

[15] Lei Dong, Zi'Ang A. Gao, and Nian Lin. Self-assembly of metal–organic coordination structures on surfaces, 2016.

[16] Alexandre Dmitriev, Hannes Spillmann, Nian Lin, Johannes V. Barth, and Klaus Kern. Modular assembly of two-dimensional metal-organic coordination networks at a metal surface. *Angewandte Chemie - International Edition*, 42(23):2670–2673, 6 2003.

[17] Carlo Sambiagio, Stephen P. Marsden, A. John Blacker, and Patrick C. Mcgowan. Copper catalysed Ullmann type chemistry: from mechanistic aspects to modern development. *Chem. Soc. Rev*, 43:3525, 2014.

[18] Todd D. Nelson and R. David Crouch. Cu, Ni, and Pd Mediated Homocoupling Reactions in Biaryl Syntheses: The Ullmann Reaction. In *Organic Reactions*, pages 265–555. John Wiley & Sons, Ltd, 1 2004.

[19] Lei Dong, Pei Nian Liu, and Nian Lin. Surface-Activated Coupling Reactions Confined on a Surface. *Accounts of Chemical Research*, 48(10):2765–2774, 10 2015.

[20] Marco Di Giovannantonio, Massimo Tomellini, Josh Lipton-Duffin, Gianluca Galeotti, Maryam Ebrahimi, Albano Cossaro, Alberto Verdini, Neerav Kharche, Vincent Meunier, Guillaume Vasseur, Yannick Fagot-Revurat, Dmitrii F. Perepichka, Federico Rosei, and Giorgio Contini. Mechanistic Picture and Kinetic Analysis of Surface-Confined Ullmann Polymerization. *Journal of the American Chemical Society*, 138(51):16696–16702, 2016.

[21] J. Björk. Reaction mechanisms for on-surface synthesis of covalent nanostructures. *Journal of Physics Condensed Matter*, 28(8):083002, 2016.

[22] Jonas Björk, Felix Hanke, and Sven Stafström. Mechanisms of halogen-based covalent self-assembly on metal surfaces. *Journal of the American Chemical Society*, 135(15):5768–5775, 2013.

[23] Qitang Fan, Cici Wang, Yong Han, Junfa Zhu, Julian Kuttner, Gerhard Hilt, and J. Michael Gottfried. Surface-assisted formation, assembly, and dynamics of planar organometallic macrocycles and zigzag shaped polymer chains with C-Cu-C bonds. *ACS Nano*, 8(1):709–718, 2014.

[24] Weihua Wang, Xingqiang Shi, Shiyong Wang, Michel A. Van Hove, and Nian Lin. Single-molecule resolution of an organometallic intermediate in a surface-supported ullmann coupling reaction. *Journal of the American Chemical Society*, 133(34):13264–13267, 2011.

[25] Gianluca Galeotti, Marco Di Giovannantonio, Josh Lipton-Duffin, Maryam Ebrahimi, Stefano Tebi, Alberto Verdini, Luca Floreano, Yannick Fagot-Revurat, Dmitrii F. Perepichka, Federico Rosei, and Giorgio Contini. The role of halogens in on-surface Ullmann polymerization. *Faraday Discussions*, 204:453–469, 2017.

[26] Thomas A. Baker, Efthimios Kaxiras, and Cynthia M. Friend. Insights from Theory on the Relationship Between Surface Reactivity and Gold Atom Release. *Topics in Catalysis*, 53(5-6):365–377, 5 2010.

[27] Alex Saywell, Wojciech Greń, Grégory Franc, André Gourdon, Xavier Bouju, and Leonhard Grill. Manipulating the conformation of single organometallic chains on Au(111). *Journal of Physical Chemistry C*, 118(3):1719–1728, 2014.

[28] Joseph W. Lauher and James A. Ibers. Structure of Octaethylporphyrin. A Comparison with Other Free Base Porphyrins. *Journal of the American Chemical Society*, 95(16):5148–5152, 8 1973.

[29] Karl Walter. Bock, Francesco De Matteis, and W. Norman. Aldridge. *Heme and hemoproteins.* Springer-Verlag, 1978.

[30] Isao Mochida, Katsuya Suetsugu, Hiroshi Fujitsu, and Kenjiro Takeshita. Enhanced catalytic activity of cobalt tetraphenylporphyrin on titanium dioxide by evacuation at elevated temperatures for intensifying the complex-support interaction. *Journal of Physical Chemistry*, 87(9):1524–1529, 1983.

[31] Bharath R. Takulapalli, Gez M. Laws, Paul A. Liddell, Joakim Andréasson, Zach Erno, Devens Gust, and Trevor J. Thornton. Electrical detection of amine ligation to a metalloporphyrin via a hybrid SOI-MOSFET. *Journal of the American Chemical Society*, 130(7):2226–2233, 2008.

[32] Lu Lin Li and Eric Wei Guang Diau. Porphyrin-sensitized solar cells. *Chemical Society Reviews*, 42(1):291–304, 12 2012.

[33] J. Michael Gottfried. Surface chemistry of porphyrins and phthalocyanines. *Surface Science Reports*, 70(3):259–379, 2015.

[34] Angela Rosa, Giampaolo Ricciardi, and Evert Jan Baerends. Synergism of Porphyrin-Core Saddling and Twisting of meso -Aryl Substituents. *The Journal of Physical Chemistry A*, 110(15):5180–5190, 4 2006.

[35] Johannes V. Barth. Molecular architectonic on metal surfaces. *Annual Review of Physical Chemistry*, 58:375–407, 2007.

[36] Florian Buchner, Ina Kellner, Wolfgang Hieringer, Andreas Görling, Hans-Peter Steinrück, and Hubertus Marbach. Ordering aspects and intramolecular conformation of tetraphenylporphyrins on Ag(111). *Physical Chemistry Chemical Physics*, 12(40):13082, 2010.

[37] Johannes Mielke, Felix Hanke, Maike V. Peters, Stefan Hecht, Mats Persson, and Leonhard Grill. Adatoms underneath single porphyrin molecules on Au(111). *Journal of the American Chemical Society*, 137(5):1844–1849, 2015.

[38] Jianchen Lu, Binbin Da, Wei Xiong, Renjun Du, Zhenliang Hao, Zilin Ruan, Yong Zhang, Shijie Sun, Lei Gao, and Jinming Cai. Identification and electronic characterization of four cyclodehydrogenation products of H2TPP molecules on Au(111). *Physical Chemistry Chemical Physics*, 23(20):11784–11788, 2021.

[39] D. R. Peale and B. H. Cooper. Adsorbate-promoted mass flow on the gold (111) surface observed by scanning tunneling microscopy. *Journal of Vacuum Science & Technology A: Vacuum, Surfaces, and Films*, 10(4):2210–2215, 6 1992.

[40] J. P. Macquet, M. M. Millard, and T. Theophanides. X-Ray Photoelectron Spectroscopy of Porphyrins. *Journal of the American Chemical Society*, 100(15):4741–4746, 7 1978.

[41] Florian Buchner, Jie Xiao, Elisabeth Zillner, Min Chen, Michael Röckert, Stefanie Ditze, Michael Stark, Hans Peter Steinrück, J. Michael Gottfried, and Hubertus Marbach. Diffusion, rotation, and surface chemical bond of individual 2 H-tetraphenylporphyrin molecules on Cu(111). *Journal of Physical Chemistry C*, 115(49):24172–24177, 2011.

[42] H. Marbach and H. P. Steinrück. Studying the dynamic behaviour of porphyrins as prototype functional molecules by scanning tunnelling microscopy close to room temperature. *Chemical Communications*, 50(65):9034–9048, 2014.

[43] J. A. Venables, G. D. T. Spiller, and M. Hanbucken. Nucleation and growth of thin films. *Reports on Progress in Physics*, 47(4):399–459, 4 1984.

[44] Grazyna Antczak and Gert Ehrlich. Jump processes in surface diffusion. *Surface Science Reports*, 62(2):39–61, 2007.

[45] S. Ovesson, G. Wahnström, B. I. Lundqvist, and A. Bogicevic. Neglected adsorbate interactions behind diffusion prefactor anomalies on metals. *Physical Review B - Condensed Matter and Materials Physics*, 64(12), 2001.

[46] Alissa Wiengarten, Julian A. Lloyd, Knud Seufert, Joachim Reichert, Willi Auwärter, Runyuan Han, David A. Duncan, Francesco Allegretti, Sybille Fischer, Seung Cheol Oh, Özge Salam, Li Jiang, Saranyan Vijayaraghavan, David Écija, Anthoula C. Papageorgiou, and Johannes V. Barth. Surface-Assisted Cyclodehydrogenation; Break the Symmetry, Enhance the Selectivity. *Chemistry - A European Journal*, 21(35):12285–12290, 2015.

[47] K. Diller, F. Klappenberger, M. Marschall, K. Hermann, A. Nefedov, Ch. Wöll, and J. V. Barth. Self-metalation of 2H-tetraphenylporphyrin on Cu(111): An x-ray spectroscopy study. *Journal of Chemical Physics*, 136(1):014705, 2012.

[48] C. Bürker, A. Franco-Cañellas, K. Broch, T. L. Lee, A. Gerlach, and F. Schreiber. Self-metalation of 2H-tetraphenylporphyrin on Cu(111) studied with XSW: Influence of the central metal atom on the adsorption distance. *Journal of Physical Chemistry C*, 118(25):13659–13666, 2014.

[49] Borja Cirera, Bruno De La Torre, Daniel Moreno, Martin Ondráček, Radek Zbořil, Rodolfo Miranda, Pavel Jelínek, and David Écija. On-Surface Synthesis of Gold Porphyrin Derivatives via a Cascade of Chemical Interactions: Planarization, Self-Metalation, and Intermolecular Coupling. *Chemistry of Materials*, 31(9):3248–3256, 2019.

[50] Michael Röckert, Stefanie Ditze, Michael Stark, Jie Xiao, Hans Peter Steinrück, Hubertus Marbach, and Ole Lytken. Abrupt coverage-induced enhancement of the self-metalation of tetraphenylporphyrin with Cu(111). *Journal of Physical Chemistry C*, 118(3):1661–1667, 2014.

[51] Samuel Jarvis. Resolving Intra- and Inter-Molecular Structure with Non-Contact Atomic Force Microscopy. *International Journal of Molecular Sciences*, 16(8):19936–19959, 8 2015.

[52] C. Joachim, J. K. Gimzewski, and A. Aviram. Electronics using hybrid-molecular and mono-molecular devices. *Nature*, 408(6812):541–548, 11 2000.

[53] James R. Heath and Mark A. Ratner. Molecular electronics. *Physics Today*, 56(5):43–49, 5 2003.

[54] Abraham Nitzan, Mark A. Ratner, George M. Whitesides, Bartosz Grzybowski, J. V Barth, G Costantini, K Kern, C. Joachim, J. K. Gimzewski, and A. Aviram. Electron transport in molecular wire junctions. *Nature*, 408(5624):671–679, 11 2003.

[55] Leonhard Grill, Matthew Dyer, Leif Lafferentz, Mats Persson, Maike V. Peters, and Stefan Hecht. Nano-architectures by covalent assembly of molecular building blocks. *Nature Nanotechnology*, 2(11):687–691, 2007.

[56] Karl M. Kadish, Kevin M. Smith, Â Sciences Gabriel, and Roger Guilard. *The Porphyrin Handbook*, volume 7. 2000.

[57] Alexander B. Sorokin. Phthalocyanine metal complexes in catalysis. *Chemical Reviews*, 113(10):8152–8191, 2013.

[58] Peter Gregory. Industrial applications of phthalocyanines. *Journal of Porphyrins and Phthalocyanines*, 4(4):432–437, 6 2000.

[59] J. Blochwitz, M. Pfeiffer, T. Fritz, and K. Leo. Low voltage organic light emitting diodes featuring doped phthalocyanine as hole transport material. *Applied Physics Letters*, 73(6):729–731, 8 1998.

[60] Raymond Bonnett. Photosensitizers of the porphyrin and phthalocyanine series for photodynamic therapy. *Chemical Society Reviews*, 24(1):19–33, 1995.

[61] Peter S. Deimel, Reda M. Bababrik, Bin Wang, Phil J. Blowey, Luke A. Rochford, Pardeep K. Thakur, Tien-Lin Lee, Marie-Laure Bocquet, Johannes V. Barth, D. Phil Woodruff, David A. Duncan, and Francesco Allegretti. Direct quantitative identification of the "surface trans-effect". *Chemical Science*, 7(9):5647–5656, 8 2016.

[62] F. Sedona, M. Di Marino, D. Forrer, A. Vittadini, M. Casarin, A. Cossaro, L. Floreano, A. Verdini, and M. Sambi. Tuning the catalytic activity of Ag(110)-supported Fe phthalocyanine in the oxygen reduction reaction. *Nature Materials*, 11(11):970–977, 2012.

[63] G. Binnig, H. Rohrer, C. Gerber, and E. Weibel. Tunneling through a controllable vacuum gap. *Applied Physics Letters*, 40(2):178–180, 1982.

[64] Gerd Binnig and Heinrich Rohrer. Scanning Tunneling Microscopy—from Birth to Adolescence (Nobel Lecture). *Angewandte Chemie International Edition in English*, 26(7):606–614, 1987.

[65] J. Tersoff and D. R. Hamann. Theory and application for the scanning tunneling microscope. *Physical Review Letters*, 50(25):1998–2001, 1983.

[66] A. Baratoff. Theory of scanning tunneling microscopy - methods and approximations. *Physica B+C*, 127(1-3):143–150, 12 1984.

[67] C. Julian Chen. *Introduction to scanning tunneling microscopy.* Oxford University Press, 2021.

[68] A.P. French and Edwin F. Taylor. *An Introduction to Quantum Physics.* Routledge, 1st edition, 5 1978.

[69] Roland Wiesendanger. *Scanning Probe Microscopy and Spectroscopy.* Cambridge University Press, 9 1994.

[70] J. Bardeen. Tunnelling from a many-particle point of view. *Physical Review Letters*, 6(2):57–59, 1 1961.

[71] C. Julian Chen. Origin of atomic resolution on metal surfaces in scanning tunneling microscopy. *Physical Review Letters*, 65(4):448–451, 1990.

[72] Franz J. Giessibl. The qPlus sensor, a powerful core for the atomic force microscope. *Review of Scientific Instruments*, 90(1):011101, 1 2019.

[73] S-2000A Stabilizer™ Top Performance Pneumatic Vibration Isolators with Automatic Re-Leveling, URL: https://www.newport.com/f/pneumatic-vibration-isolators-with-automatic-re-leveling.

[74] H. Hertz. Ueber einen Einfluss des ultravioletten Lichtes auf die electrische Entladung. *Annalen der Physik*, 267(8):983–1000, 1887.

[75] A. Einstein. Über einen die Erzeugung und Verwandlung des Lichtes betreffenden heuristischen Gesichtspunkt, 1905.

[76] John F. Watts and John Wolstenholme. *An Introduction to Surface Analysis by XPS and AES*. John Wiley & Sons, Ltd, Chichester, UK, 3 2003.

[77] Gianangelo Bracco and Bodil Holst, editors. *Surface Science Techniques*, volume 51 of *Springer Series in Surface Sciences*. Springer Berlin Heidelberg, Berlin, Heidelberg, 2013.

[78] Kai Siegbahn. Electron spectroscopy for atoms, molecules, and condensed matter. *Reviews of Modern Physics*, 54(3):709–728, 7 1982.

[79] C. W. Oatley. The measurement of contact potential difference. *Proceedings of the Royal Society of London. Series A - Mathematical and Physical Sciences*, 155(885):218–234, 6 1936.

[80] Kai Siegbahn. Electron spectroscopy for atoms, molecules and condensed matter - an overview. *Journal of Electron Spectroscopy and Related Phenomena*, 36(2):113–129, 1985.

[81] Perry Sprawls. *Physical Principles of Medical Imaging. 2nd ed*, volume 200. 8 1996.

[82] Neal Fairley. *CasaXPS Manual 2.3.15.* 2009.

[83] Dhananjay I. Patel, Tuhin Roychowdhury, Varun Jain, Dhruv Shah, Tahereh G. Avval, Shiladitya Chatterjee, Stephan Bahr, Paul Dietrich, Michael Meyer, Andreas Thißen, and Matthew R. Linford. Introduction to near-ambient pressure x-ray photoelectron spectroscopy characterization of various materials. *Surface Science Spectra*, 26(1):016801, 6 2019.

[84] Joachim Stöhr. *NEXAFS Spectroscopy.* Springer Berlin, Heidelberg, 1992.

[85] Robert G. Jones, A. S. Y. Chan, M. G. Roper, M. P. Skegg, I. G. Shuttleworth, C. J. Fisher, G. J. Jackson, J. J. Lee, D. P. Woodruff, N. K. Singh, and B. C. C. Cowie. X-ray standing waves at surfaces. *Journal of Physics Condensed Matter*, 14(16):4059–4074, 2002.

[86] D. P. Woodruff. Surface structure determination using x-ray standing waves. *Reports on Progress in Physics*, 68(4):743–798, 2005.

[87] Tien Lin Lee and David A. Duncan. A Two-Color Beamline for Electron Spectroscopies at Diamond Light Source. *Synchrotron Radiation News*, 31(4):16–22, 7 2018.

[88] Research Using Synchrotron Light, URL: https://www.diamond.ac.uk/industry/Industry-News/Latest-News/Synchrotron-Industry-News-Automotive-Research.html.

[89] The fundamentals of high, ultra-high and extreme high vacuum, URL: https://www.vacuumscienceworld.com/ultra-and-extreme-high-vacuum.

[90] Pfeiffer vacuum: Know how, URL: https://www.pfeiffer-vacuum.com/en/know-how/.

[91] Felix Hanke and Jonas Björk. Structure and local reactivity of the Au(111) surface reconstruction. *Physical Review B - Condensed Matter and Materials Physics*, 87(23):1–6, 2013.

[92] N. C. Bartelt and K. Thürmer. Structure and energetics of the elbows in the Au(111) herringbone reconstruction. *Physical Review B*, 104(16):165425, 2021.

[93] Xuechao Li, Haitao Ge, Renjie Xue, Minghui Wu, and Lifeng Chi. Anchoring and Reacting On-Surface to Achieve Programmability. *JACS Au*, 2(1):58–65, 2022.

[94] Lander Verstraete and Steven De Feyter. 2D Self-assembled molecular networks and on-surface reactivity under nanoscale lateral confinement. *Chemical Society Reviews*, 50(10):5884–5897, 2021.

[95] Adam Sweetman, Neil R. Champness, and Alex Saywell. On-surface chemical reactions characterised by ultra-high resolution scanning probe microscopy. *Chemical Society Reviews*, 49:4189, 2020.

[96] Chris J. Judd, Filipe L.Q. Junqueira, Sarah L. Haddow, Neil R. Champness, David A. Duncan, Robert G. Jones, and Alex Saywell. Structural characterisation of molecular conformation and the incorporation of adatoms in an on-surface Ullmann-type reaction. *Communications Chemistry*, 3(1):1–8, 2020.

[97] Lukas Grossmann, David A. Duncan, Samuel P. Jarvis, Robert G. Jones, Soumen De, Johanna Rosen, Michael Schmittel, Wolfgang M. Heckl, Jonas Björk, and Markus Lackinger. Evolution of adsorption heights in the on-surface synthesis and decoupling of covalent organic networks on Ag(111) by normal-incidence X-ray standing wave. *Nanoscale Horizons*, 7(1):51–62, 2022.

[98] Matthew Edmondson, Eleanor S. Frampton, Chris J. Judd, Neil R. Champness, Robert G. Jones, and A. Saywell. Order, disorder, and metalation of tetraphenylporphyrin (2H-TPP) on Au(111). *Chemical Communications*, 58(42):6247–6250, 2022.

[99] J. V. Barth. Transport of adsorbates at metal surfaces: From thermal migration to hot precursors. *Surface Science Reports*, 40(3):75–149, 2000.

[100] Shammi Rana, Kristen N. Johnson, Kirill Gurdumov, Ursula Mazur, and K. W. Hipps. Scanning Tunneling Microscopy Reveals Surface Diffusion of Single Double-Decker Phthalocyanine Molecules at the Solution/Solid Interface. *Journal of Physical Chemistry C*, 126(8):4140–4149, 2022.

[101] M. Schunack, T. R. Linderoth, F. Rosei, E. Lægsgaard, I. Stensgaard, and F. Besenbacher. Long Jumps in the Surface Diffusion of Large Molecules. *Physical Review Letters*, 88(15):4, 2002.

[102] J. C. Gehrig, M. Penedo, M. Parschau, J. Schwenk, M. A. Marioni, E. W. Hudson, and H. J. Hug. Surface single-molecule dynamics controlled by entropy at low temperatures. *Nature Communications*, 8:1–8, 2017.

[103] Alex Saywell, Jutta Schwarz, Stefan Hecht, and Leonhard Grill. Polymerization on stepped surfaces: Alignment of polymers and identification of catalytic sites. *Angewandte Chemie - International Edition*, 51(21):5096–5100, 5 2012.

[104] Dingyong Zhong, Jörn Holger Franke, Santhosh Kumar Podiyanachari, Tobias Blömker, Haiming Zhang, Gerald Kehr, Gerhard Erker, Harald Fuchs, and Lifeng Chi. Linear alkane polymerization on a gold surface. *Science*, 334(6053):213–216, 2011.

[105] Chris J. Judd, Dmitry V. Kondratuk, Harry L. Anderson, and Alex Saywell. On-Surface Synthesis within a Porphyrin Nanoring Template. *Scientific Reports*, 9(1):9352, 12 2019.

[106] Qitang Fan, J. Michael Gottfried, and Junfa Zhu. Surface-Catalyzed C-C Covalent Coupling Strategies toward the Synthesis of Low-Dimensional Carbon-Based Nanostructures. *Accounts of Chemical Research*, 48(8):2484–2494, 2015.

[107] J. V. Barth, H. Brune, G. Ertl, and R. J. Behm. Scanning tunneling microscopy observations on the reconstructed Au(111) surface: Atomic structure, long-range superstructure, rotational domains, and surface defects. *Physical Review B*, 42(15):9307–9318, 1990.

[108] Shobhana Narasimhan and David Vanderbilt. Elastic stress domains and the herringbone reconstruction on Au(111). *Physical Review Letters*, 69(10):1564–1567, 1992.

[109] J. A. Meyer, I. D. Baikie, E. Kopatzki, and R. J. Behm. Preferential island nucleation at the elbows of the Au(111) herringbone reconstruction through place exchange. *Surface Science*, 365(1):647–651, 1996.

[110] M. M. Dovek, C. A. Lang, J. Nogami, and C. F. Quate. Epitaxial growth of Ag on Au(111) studied by scanning tunneling microscopy. *Physical Review B*, 40(17):11973–11975, 1989.

[111] Matthias Böhringer, Karina Morgenstern, Wolf Dieter Schneider, Richard Berndt, Francesco Mauri, Alessandro De Vita, and Roberto Car. Two-dimensional self-assembly of supramolecular clusters and Chains. *Physical Review Letters*, 83(2):324–327, 1999.

[112] Z. H. Cheng, L. Gao, Z. T. Deng, Q. Liu, N. Jiang, X. Lin, X. B. He, S. X. Du, and H. J. Gao. Epitaxial growth of iron phthalocyanine at the initial stage on Au(111) surface. *J. Phys. Chem. C*, 111(6):2656–2660, 2007.

[113] David Écija, Roberto Otero, Luis Sánchez, José María Gallego, Yang Wang, Manuel Alcamí, Fernando Martín, Nazario Martín, and Rodolfo Miranda. Crossover site-selectivity in the adsorption of the fullerene derivative PCBM on Au(111). *Angewandte Chemie - International Edition*, 46(41):7874–7877, 2007.

[114] Robert J. Madix and Cynthia M. Friend. Gold's enigmatic surface. *Nature*, 479(7374):482–483, 11 2011.

[115] Jascha Repp, Gerhard Meyer, Karl-Heinz Rieder, and Per Hyldgaard. Site Determination and Thermally Assisted Tunneling in Homogenous Nucleation. *Physical Review Letters*, 91(20):206102, 11 2003.

[116] Cesar Moreno, Markos Paradinas, Manuel Vilas-Varela, Mirko Panighel, Gustavo Ceballos, Diego Peña, and Aitor Mugarza. On-surface synthesis of superlattice arrays of ultra-long graphene nanoribbons. *Chemical Communications*, 54(68):9402–9405, 2018.

[117] Leif Lafferentz, Francisco Ample, Hao Yu, Stefan Hecht, Christian Joachim, and Leonhard Grill. Conductance of a single conjugated polymer as a continuous function of its length. *Science*, 323(5918):1193–1197, 2 2009.

[118] D. D. Chambliss, R. J. Wilson, and S. Chiang. Nucleation of ordered Ni island arrays on Au(111) by surface-lattice dislocations. *Physical Review Letters*, 66(13):1721–1724, 1991.

[119] L. Lafferentz, V. Eberhardt, C. Dri, C. Africh, G. Comelli, F. Esch, S. Hecht, and L. Grill. Controlling on-surface polymerization by hierarchical and substrate-directed growth. *Nature Chemistry*, 4(3):215–220, 2012.

[120] Jacques G. Amar and Fereydoon Family. Critical Cluster Size: Island Morphology and Size Distribution in Submonolayer Epitaxial Growth. *Physical Review Letters*, 75(10):2069–2069, 9 1995.

[121] Takashi Yokoyama, Shiyoshi Yokoyama, Toshiya Kamikado, and Shinro Mashiko. Nonplanar adsorption and orientational ordering of porphyrin molecules on Au(111). *The Journal of Chemical Physics*, 115(8):3814, 8 2001.

[122] Grazyna Antczak and Gert Ehrlich. Long jumps in surface diffusion. *Journal of Colloid and Interface Science*, 276(1):1–5, 2004.

[123] M. Eichberger, M. Marschall, J. Reichert, A. Weber-Bargioni, W. Auwärter, R. L. C. Wang, H. J. Kreuzer, Y. Pennec, A. Schiffrin, and J. V. Barth. Dimerization boosts one-dimensional mobility of conformationally adapted porphyrins on a hexagonal surface atomic lattice. *Nano Letters*, 8(12):4608–4613, 2008.

[124] Shi Chao Yan, Nan Xie, Hui Qi Gong, Qian Sun, Yang Guo, Xin Yan Shan, and Xing Hua Lu. Mapping the diffusion potential of a reconstructed Au(111) surface at nanometer scale with 2D molecular gas. *Chinese Physics Letters*, 29(4):046803, 4 2012.

[125] J. V. Barth, H. Brune, B. Fischer, J. Weckesser, and K. Kern. Dynamics of Surface Migration in the Weak Corrugation Regime. *Physical Review Letters*, 84(8):1732–1735, 2 2000.

[126] Fischer Bjørn, Brune Harald, Johannes V. Barth, Fricke Alexander, and Kern Klaus. Nucleation kinetics on inhomogeneous substrates: Al/Au(111). *Physical Review Letters*, 82(8):1732–1735, 2 1999.

[127] Pierre Martin Dombrowski, Stefan R. Kachel, Leonard Neuhaus, J. Michael Gottfried, and Gregor Witte. Temperature-programmed desorption of large molecules: Influence of thin film structure and origin of intermolecular repulsion. *Nanoscale*, 13(32):13816–13826, 2021.

[128] Donato Civita, Marek Kolmer, Grant J. Simpson, An Ping Li, Stefan Hecht, and Leonhard Grill. Control of long-distance motion of single molecules on a surface. *Science*, 370(6519):957–960, 2020.

[129] Adrien P. Cote, Annabelle I. Benin, Nathan W. Ockwig, Michael O'Keeffe, Adam J. Matzger, and Omar M. Yaghi. Porous, Crystalline, Covalent Organic Frameworks. *Science*, 310(5751):1166–1170, 11 2005.

[130] Eleanor S. Frampton. *Self-assembly and on-surface chemistry of tetraphenylporphyrin*. PhD thesis, University of Nottingham, 2021.

[131] Gaël Reecht, Benjamin W. Heinrich, Hervé Bulou, Fabrice Scheurer, Laurent Limot, and Guillaume Schull. Imaging isodensity contours of molecular states with STM. *New Journal of Physics*, 19(11):113033, 2017.

[132] Thomas Andreev, Ingo Barke, and Heinz Hövel. Adsorbed rare-gas layers on Au(111): Shift of the Shockley surface state studied with ultraviolet photoelectron spectroscopy and scanning tunneling spectroscopy. *Physical Review B - Condensed Matter and Materials Physics*, 70(20), 2004.

[133] Matthew Edmondson and Alex Saywell. Molecular Diffusion and Self-Assembly: Quantifying the Influence of Substrate hcp and fcc Atomic Stacking. *Nano Letters*, 22(20):8210–8215, 10 2022.

[134] Geoffrey Rojas, Xumin Chen, Cameron Bravo, Ji Hyun Kim, Jae Sung Kim, Jie Xiao, Peter A. Dowben, Yi Gao, Xiao Cheng Zeng, Wonyoung Choe, and Axel Enders. Self-assembly and properties of nonmetalated tetraphenyl-porphyrin on metal substrates. *Journal of Physical Chemistry C*, 114(20):9408–9415, 2010.

[135] Stefan Müllegger, Mohammad Rashidi, Wolfgang Schöfberger, and Reinhold Koch. Single-molecule chemical reduction induced by low-temperature scanning tunneling microscopy: A case study of gold-porphyrin on Au(111). *Surface Science*, 678:157–162, 12 2018.

[136] Johannes Mielke, Jesús Martínez-Blanco, Maike V Peters, Stefan Hecht, and Leonhard Grill. Observing single-atom diffusion at a molecule-metal interface. *PHYSICAL REVIEW B*, 94:35416, 2016.

[137] Bas Hulsken, Richard Van Hameren, Jan W. Gerritsen, Tony Khoury, Pall Thordarson, Maxwell J. Crossley, Alan E. Rowan, Roeland J. M. Nolte, Johannes A .A. W. Elemans, and Sylvia Speller. Real-time single-molecule imaging of oxidation catalysis at a liquid-solid interface. *Nature Nanotechnology*, 2(5):285–289, 2007.

[138] Cyrille Costentin, Hachem Dridi, and Jean Michel Savéant. Molecular Catalysis of O_2 Reduction by Iron Porphyrins in Water: Heterogeneous versus Homogeneous Pathways. *Journal of the American Chemical Society*, 137(42):13535–13544, 2015.

[139] Willi Auwärter, David Écija, Florian Klappenberger, and Johannes V. Barth. Porphyrins at interfaces. *Nature Chemistry*, 7(2):105–120, 2015.

[140] Everly B. Fleischer and Andrei Laszlo. Synthesis of a gold porphyrin. *Inorganic and Nuclear Chemistry Letters*, 5(5):373–376, 1969.

[141] D. A. Duncan, P. S. Deimel, A. Wiengarten, M. Paszkiewicz, P. Casado Aguilar, R. G. Acres, F. Klappenberger, W. Auwärter, A. P. Seitsonen, J. V. Barth, and F. Allegretti. Bottom-Up fabrication of a metal-supported oxo-metal porphyrin. *Journal of Physical Chemistry C*, 123(51):31011–31025, 2019.

[142] Ken Flechtner, Andreas Kretschmann, Liam R. Bradshaw, Marie Madeleine Walz, Hans Peter Steinrück, and J. Michael Gottfried. Surface-confined two-step synthesis of the complex (ammine)(meso-tetraphenylporphyrinato)-zinc(II) on Ag(111). *Journal of Physical Chemistry C*, 111(16):5821–5824, 2007.

[143] Andrea Goldoni, Carlo A. Pignedoli, Giovanni Di Santo, Carla Castellarin-Cudia, Elena Magnano, Federica Bondino, Alberto Verdini, and Daniele Passerone. Room temperature metalation of 2H-TPP monolayer on iron and nickel surfaces by picking up substrate metal atoms. *ACS Nano*, 6(12):10800–10807, 2012.

[144] Catherine M. Doyle, Sergey A. Krasnikov, Natalia N. Sergeeva, Alexei B. Preobrajenski, Nikolay A. Vinogradov, Yulia N. Sergeeva, Mathias O. Senge, and Attilio A. Cafolla. Evidence for the formation of an intermediate complex in the direct metalation of tetra(4-bromophenyl)-porphyrin on the Cu(111) surface. *Chemical Communications*, 47(44):12134–12136, 2011.

[145] Isabelle Toubia, Christophe Nguyen, Stéphane Diring, Lamiaa M. A. Ali, Ludivine Larue, Rabab Aoun, Céline Frochot, Magali Gary-Bobo, Marwan Kobeissi, and Fabrice Odobel. Synthesis and Anticancer Activity of Gold Porphyrin Linked to Malonate Diamine Platinum Complexes. *Inorganic Chemistry*, 58(18):12395–12406, 2019.

[146] Klaus Hermann and M. A. Van Hove. LEEDpat4 - LEED pattern analyzer, URL: https://www.fhi.mpg.de/958975/LEEDpat4, 2022.

[147] Marco Nardi, Roberto Verucchi, Claudio Corradi, Marco Pola, Maurizio Casarin, Andrea Vittadini, and Salvatore Iannotta. Tetraphenylporphyrin electronic properties: A combined theoretical and experimental study of thin films deposited by SuMBD. *Physical Chemistry Chemical Physics*, 12(4):871–880, 2010.

[148] Margret Giesen. Step and island dynamics at solid/vacuum and solid/liquid interfaces. *Progress in Surface Science*, 68(1-3):1–154, 9 2001.

[149] Katharina Diller, Anthoula C. Papageorgiou, Florian Klappenberger, Francesco Allegretti, Johannes V. Barth, and Willi Auwärter. In vacuo interfacial tetrapyrrole metallation. *Chemical Society Reviews*, 45(6):1629–1656, 2016.

[150] Stefan Müllegger, Wolfgang Schöfberger, Mohammad Rashidi, Lorenz M. Reith, and Reinhold Koch. Spectroscopic STM studies of single gold(III) porphyrin molecules. *Journal of the American Chemical Society*, 131(49):17740–17741, 2009.

[151] B. Watts, L. Thomsen, and P. C. Dastoor. Methods in carbon K-edge NEXAFS: Experiment and analysis. *Journal of Electron Spectroscopy and Related Phenomena*, 151(2):105–120, 2006.

[152] M. Pfeiffer, K. Leo, X. Zhou, J. S. Huang, M. Hofmann, A. Werner, and J. Blochwitz-Nimoth. Doped organic semiconductors: Physics and application in light emitting diodes. *Organic Electronics*, 4(2-3):89–103, 9 2003.

[153] M. Victoria Martínez-Díaz, Gema De La Torre, and Tomás Torres. Lighting porphyrins and phthalocyanines for molecular photovoltaics. *Chemical Communications*, 46(38):7090–7108, 2010.

[154] Mirko Cinchetti, Kathrin Heimer, Jan Peter Wüstenberg, Oleksiy Andreyev, Michael Bauer, Stefan Lach, Christiane Ziegler, Yongli Gao, and Martin Aeschlimann. Determination of spin injection and transport in a ferromagnet/organic semiconductor heterojunction by two-photon photoemission. *Nature Materials*, 8(2):115–119, 2 2009.

[155] Emilia Annese, Jun Fujii, Ivana Vobornik, Giancarlo Panaccione, and Giorgio Rossi. Control of the magnetism of cobalt phthalocyanine by a ferromagnetic substrate. *Physical Review B - Condensed Matter and Materials Physics*, 84(17):174443, 11 2011.

[156] Cristina Isvoranu, Bin Wang, Evren Ataman, Jan Knudsen, Karina Schulte, Jesper N. Andersen, Marie-Laure Bocquet, and Joachim Schnadt. Comparison of the Carbonyl and Nitrosyl Complexes Formed by Adsorption of CO and NO on Monolayers of Iron Phthalocyanine on Au(111). *J. Phys. Chem. C*, 115:24718–24727, 2011.

[157] C. Isvoranu, B. Wang, K. Schulte, E. Ataman, J. Knudsen, J. N. Andersen, M. L. Bocquet, and J. Schnadt. Tuning the spin state of iron phthalocyanine by ligand adsorption. *Journal of Physics: Condensed Matter*, 22(47):472002, 12 2010.

[158] E. Bartolomé, J. Bartolomé, F. Sedona, J. Lobo-Checa, D. Forrer, J. Herrero-Albillos, M. Piantek, J. Herrero-Martín, D. Betto, E. Velez-Fort, L. M. García, M. Panighel, A. Mugarza, M. Sambi, and F. Bartolomé. Enhanced Magnetism through Oxygenation of FePc/Ag(110) Monolayer Phases. *Journal of Physical Chemistry C*, 124(25):13993–14006, 2020.

[159] M. Corva and E. Vesselli. Room temperature carbonylation of iron-phthalocyanines adsorbed on a single crystal metal surface: An in situ SFG investigation at near-ambient pressure. *Journal of Physical Chemistry C*, 120(39):22298–22303, 10 2016.

[160] John Åhlund, Katharina Nilson, Joachim Schiessling, Lisbeth Kjeldgaard, Simon Berner, Nils Mårtensson, Carla Puglia, Barbara Brena, Mats Nyberg, and Yi Luo. The electronic structure of iron phthalocyanine probed by photoelectron and x-ray absorption spectroscopies and density functional theory calculations. *J. Chem. Phys*, 125:9780, 2006.

[161] Olesia Snezhkova, Felix Bischoff, Yuanqin He, Alissa Wiengarten, Shilpi Chaudhary, Niclas Johansson, Karina Schulte, Jan Knudsen, Johannes V Barth, Knud Seufert, Willi Auwärter, and Joachim Schnadt. Iron phthalocyanine on Cu(111): Coverage-dependent assembly and symmetry breaking, temperature-induced homocoupling, and modification of the adsorbate-surface interaction by annealing. *J. Chem. Phys*, 144:94702, 2016.

[162] Tomohide Takami, Clarisa Carrizales, and K. W. Hipps. Commensurate ordering of iron phthalocyanine on Ag(111) surface. *Surface Science*, 603(21):3201–3204, 2009.

[163] J.-Y. Grand, T. Kunstmann, D. Hoffmann, A. Haas, M. Dietsche, J. Seifritz, and R. Möller. Epitaxial growth of copper phthalocyanine monolayers on Ag(111). *Surface Science*, 366(3):403–414, 11 1996.

[164] A. Ruocco, F. Evangelista, A. Attili, M. P. Donzello, M. G. Betti, L. Giovanelli, and R. Gotter. Copper-phthalocyanine ultra thin films grown onto Al(100) surface investigated by synchrotron radiation. *Journal of Electron Spectroscopy and Related Phenomena*, 137-140:165–169, 7 2004.

[165] Barbara Brena, Yi Luo, Mats Nyberg, Stéphane Carniato, Katharina Nilsson, Ylvi Alfredsson, John Åhlund, Nils Mårtensson, Hans Siegbahn, and Carla Puglia. Equivalent core-hole time-dependent density functional theory calculations of carbon 1s shake-up states of phthalocyanine. *Physical Review B - Condensed Matter and Materials Physics*, 70(19):1–6, 2004.

[166] A. Cossaro, D. Cvetko, G. Bavdek, L. Floreano, R. Gotter, A. Morgante, F. Evangelista, and A. Ruocco. Copper-Phthalocyanine Induced Reconstruction of Au(110). *J. Phys. Chem. B*, 108:14671–14676, 2004.

[167] David J. Morgan. X-Ray Photoelectron Spectroscopy (XPS): An Introduction. Technical report.

[168] P. Palmgren, T. Angot, C. I. Nlebedim, J.-M. Layet, G. Le Lay, and M. Göthelid. Ordered phthalocyanine superstructures on Ag(110). *J. Chem. Phys.*, 128:9780, 2008.

[169] Timothy C. Williams and Christopher R. Shaddix. Contamination of carbon monoxide with metal carbonyls: implications for combustion research. *Combustion Science and Technology*, 179(6):1225–1230, 5 2007.

[170] R. Reichelt, S. Günther, M. Rößler, J. Wintterlin, B. Kubias, B. Jakobi, and R. Schlögl. High-pressure STM of the interaction of oxygen with Ag(111). *Physical Chemistry Chemical Physics*, 9(27):3590–3599, 2007.

[171] N. M. Martin, S. Klacar, H. Grönbeck, J. Knudsen, J. Schnadt, S. Blomberg, J. Gustafson, and E. Lundgren. High-coverage oxygen-induced surface structures on Ag(111). *Journal of Physical Chemistry C*, 118(28):15324–15331, 7 2014.

[172] Tahereh G. Avval, Shiladitya Chatterjee, Grant T. Hodges, Stephan Bahr, Paul Dietrich, Michael Meyer, Andreas Thißen, and Matthew R. Linford. Oxygen gas, O_2(g), by near-ambient pressure XPS. *Surface Science Spectra*, 26(1):014021, 6 2019.

[173] Georg Held, Federica Venturini, David C. Grinter, Pilar Ferrer, Rosa Arrigo, Liam Deacon, Wilson Quevedo Garzon, Kanak Roy, Alex Large, Christopher Stephens, Andrew Watts, Paul Larkin, Matthew Hand, Hongchang Wang, Linda Pratt, James J. Mudd, Thomas Richardson, Suren Patel, Michael Hillman, and Stewart Scott. Ambient-pressure endstation of the Versatile Soft X-ray (VerSoX) beamline at Diamond Light Source. *Journal of Synchrotron Radiation*, 27(5):1153–1166, 9 2020.

[174] Jaspreet Singh, R. K. Sharma, U. K. Goutam, U. S. Sule, Jagannath Gupta, S. C. Gadkari, and P. N. Rao. Orientation study of iron Phthalocyanine (FePc) thin films deposited on silicon and gold surfaces. *Materials Research Express*, 6(1):016411, 10 2019.

[175] F. Petraki, H. Peisert, U. Aygül, F. Latteyer, J. Uihlein, A. Vollmer, and T. Chassé. Electronic structure of FePc and interface properties on Ag(111) and Au(100). *Journal of Physical Chemistry C*, 116(20):11110–11116, 2012.